Programa de Doctorado en Biotecnología Sanitaria

Na_V and thermosensitive TRP ion channels as a key molecular and functional landmark for neuropathic pain transduction in subsets of somatosensory neurons

Angela Lamberti

Director/a de la tesis: **Dr. D. Antonio Ferrer Montiel**
Codirector/a de la tesis: **Dra. Dña. Asia Fernández Carvajal**

UNIVERSIDAD MIGUEL HERNÁNDEZ DE ELCHE

Instituto de Investigación, Desarrollo e Innovación en Biotecnología Sanitaria de Elche (IDiBE)

-2025-

La presente Tesis Doctoral, titulada "**Na_V and *thermos TRP ion channels as a key molecular and functional landmark for neuropathic pain transduction in subsets of somatosensory neurons***", se presenta bajo la modalidad de **tesis por compendio** de la siguiente publicación:

- Lamberti, A., Aprile, S., Cabañero, D., Travagin, F., Butron, L., Fernández-Ballester, G., Tron, G.C., Fernández-Carvajal, A., Ferrer-Montiel, A. and Galli, U. (2025), An adamantane-based ligand as a novel chemical tool for thermosensory TRPM8 channel therapeutic modulation. FEBS J. doi: https://doi.org/10.1111/febs.70065. (Q1; Factor de impacto: 5.62).

El Dr. D. Antonio Ferrer Montiel, director, y la Dra. Dña. Asia Fernández Carvajal , codirectora de la tesis doctoral titulada "**Na_V and *thermos TRP ion channels as a key molecular and functional landmark for neuropathic pain transduction in subsets of somatosensory neurons*".**

INFORMA/N:

Que D./Dña. Angela Lamberti ha realizado bajo nuestra supervisión el trabajo titulado **"Na_V and *thermos TRP ion channels as a key molecular and functional landmark for neuropathic pain transduction in subsets of somatosensory neurons*"** conforme a los términos y condiciones definidos en su Plan de Investigación y de acuerdo al Código de Buenas Prácticas de la Universidad Miguel Hernández de Elche, cumpliendo los objetivos previstos de forma satisfactoria para su defensa pública como tesis doctoral.

Lo que firmo/firmamos para los efectos oportunos, en Elche a ……. de …….. de 2025

Director de la tesis	Codirectora de la tesis
Dr. D. Antonio Ferrer Montiel	Dra. Dña. Asia Fernández Carvajal

El Dr. D. Gregorio Fernández Ballester, Coordinador del Programa de Doctorado en **Biotecnología Sanitaria**

INFORMA:

Que Dña. *Angela Lamberti* ha realizado bajo la supervisión de nuestro Programa de Doctorado el trabajo titulado "**Na_V and *thermos TRP ion channels as a key molecular and functional landmark for neuropathic pain transduction in subsets of somatosensory neurons***" conforme a los términos y condiciones definidos en su Plan de Investigación y de acuerdo al Código de Buenas Prácticas de la Universidad Miguel Hernández de Elche, cumpliendo los objetivos previstos de forma satisfactoria para su defensa pública como tesis doctoral.

Lo que firmo para los efectos oportunos, en Elche a ……. de …….. de 2025

Prof. Dr. D. Gregorio Fernández Ballester
Coordinador del Programa de Doctorado en **Biotecnología Sanitaria**

La presente tesis doctoral, realizada en el Instituto de Investigación, Desarrollo e Innovación en Biotecnología Sanitaria de Elche (IDiBE), ha sido financiada por European Union's Horizon 2020 research and innovation program under the Marie Skłodowska-Curie Actions [No 956477] y por Generalitat Valenciana [GVA-PROMETEO/2021/031].

Además, durante este periodo Dña. Angela Lamberti ha realizado dos estancias de investigación de 3 meses cada una en la Universitá del Piemonte Orientale, Novara (Italia) y en Polypure AS, Oslo (Noruega) financiada por European Union's Horizon 2020 research and innovation program under the Marie Skłodowska-Curie Actions [No 956477].

INDEX

LIST OF ABBREVIATIONS

2-AG: 2-arachidonoylglycerol

AEA: Anandamide

AHP: Afterhyperpolarization phase

AB9: N-(4-hydroxy-2-iodo-5-methoxybenzyl)dodecanamide (C20H32IN03)

AITC: Allyl isothiocyanate

AG1529: 2-((4-hydroxy-2-iodo-5-methoxybenzyl) amino)-2-oxoethyl dodecanoate

AMBER: Assisted model building with energy refinement

AMG333: (S)-6-(((3-Fluoro-4-(trifluoromethoxy)phenyl)(3-fluoropyridin-2-yl)methyl)carbamoyl)nicotinic acid

AMTB: N-(3-aminopropyl)-2-{[(3-methylphenyl)methyl]oxy}(20)-N-(2-thienylmethyl)benzamide

AP: Action potential

CaV: Voltage-gated calcium channels

Caps: Capsaicin

CBG: Cannabigerol

CGRP: Calcitonin-gene related peptide

CIPN: Chemotherapy-Induced Peripheral Neuropathy

CNG: Cyclic nucleotide-gated channel

CNS: Central nervous system

Cpd: Compound

Cryo-EM: Cryogenic-electron microscopy

CNV10114802: Raxatrigine; 4-Amino-1-((2S,3R)-2-(2,4-difluorophenyl)-1-oxo-3-(2-thienylmethyl)butyl)-cyclohexane carboxamide

DMSO: Dimethyl sulfoxide

DIV: Days in vitro

DPBS: Dulbecco's phosphate-buffered saline

DRG: Dorsal root ganglion

EC: Endocannabinoid

EC_{50}: Half maximal effective concentration

EMEM: Earle’s minimum essential medium

Et2O: Diethyl ether

EtOAc: Ethyl acetate

EV: Endovanilloid

FBS: Fetal bovine serum

GSH: Glutathione

G-V: Conductance–Voltage relationship

HaCaT: Immortalized nontumorigenic human epidermal cells

HCN: Hyperpolarization-activated cyclic nucleotide-gated channel

hDRG: Human dorsal root ganglion

HEK: Human embryonic kidney 293 cells

IASP: International Association for the Study of Pain

IB4: Isolectin B4

IBD: Inflammatory bowel disease

IC_{50}: Concentration to reach half maximal inhibitory activity

IENF: Intra-epidermal nerve fiber

IEM: Inherited erythromelalgia

iPSC: Induced pluripotent stem cells

IQR: Interquartile range

J-V: Current density–Voltage relationship

K2P: Two-pore K+ channel

KA: Fast-inactivating potassium current

KCl: Potassium chloride

KDR: Delayed rectifier potassium current

Kir: Inward rectifier channels

KO: Knockout

K_v: Voltage-gated potassium channels

MCP-1: Monocyte chemoattractant protein-1

MEA: Microelectrode/multielectrode array

MFC: Microfluidic chamber

MPTP: 1-Methyl-4-phenyl-1,2,3,6-tetrahydropyridine (neurotoxin)

NADA: N-arachidonoyl-dopamine

Na_V: Voltage-gated sodium channels

NP: Neuropathic pain

OLDA: N-oleoyl-dopamine

OIPN: Oxaliplatin-induced peripheral neuropathy

OSN: Olfactory sensory neuron

PAR2: Protease-activated receptor 2

PE: Petroleum ether

PF-05105679: (R)-3-[(1-(4-fluorophenyl)ethyl)(quinolin-3-ylcarbonyl)amino]methylbenzoic acid

PIPN: Paclitaxel-induced peripheral neuropathy

ProtxII: Peptide toxin targeting sodium channels

RMP: Resting membrane potential

ROS: Reactive oxygen species

SA: Spontaneous activity

SEM: Standard error of the mean

TBDMS: Tert-butyldimethylsilyl

TEBA: Benzyltriethylammonium chloride

TENS: Transcutaneous electrical nerve stimulation

TGFα: Tumor growth factor alpha

THC: Delta-9-tetrahydrocannabidiol

TLR4: Toll-like receptor 4

TRP: Transient receptor potential

TRPA1: Transient receptor potential cation channel subfamily A member 1

TRPM8: Transient receptor potential cation channel subfamily M member 8

TRPV1: Thermosensory channel TRP vanilloid 1

TTX: Tetrodotoxin

UPO: Università del Piemonte Orientale

VSD: Voltage-sensing domain

VGSC: Voltage-gated sodium channels

WS12: (1R,2S,5R)-N-(4-Methoxyphenyl)-5-methyl-2-(propan-2-yl)cyclohexane-1-Carboxamide

RESUMEN - ABSTRACT

RESUMEN

El dolor crónico, especialmente el dolor neuropático, afecta aproximadamente a 1.500 millones de personas en todo el mundo, causando un sufrimiento intenso e imponiendo importantes cargas económicas a través de los costes de atención médica, pagos por discapacidad y pérdida de productividad. A pesar de su prevalencia, los tratamientos disponibles muestran una efectividad variable debido a la falta de herramientas diagnósticas y terapéuticas. Esta investigación forma parte del proyecto PIANO, un gran consorcio internacional cuyo objetivo es mejorar nuestra comprensión y tratamiento del dolor neuropático que afecta a unos 1.500 millones de personas en todo el mundo. PIANO tiene como objetivo superar estos obstáculos focalizando el tratamiento en las primeras etapas de la vía del dolor, los ganglios de la raíz dorsal (DRG), minimizando los efectos secundarios.

Entre los objetivos de PIANO destaca la neuropatía periférica inducida por quimioterapia (CIPN), un efecto secundario grave producido por los medicamentos contra el cáncer como el paclitaxel, para la que no se ha encontrado un tratamiento eficaz. Esta tesis se alinea con investigaciones en curso dentro de PIANO para explorar el papel de los canales termo TRP (TRPV1, TRPM8, TRPA1) en la sensibilización de las neuronas sensitivas, crucial para comprender la fisiopatología molecular de la neuropatía. Estos canales actúan como detectores moleculares de estímulos térmicos y químicos y son potenciados por agentes proinflamatorios, un proceso que aumenta el reclutamiento de canales TRP a la membrana y modifica sus propiedades de activación. La investigación sobre estos canales ha abierto nuevas vías para el desarrollo de analgésicos innovadores. En esta tesis se estudian los efectos de la exposición secuencial al paclitaxel sobre la excitabilidad y la integridad de las neuronas sensitivas utilizando un cultivo primario a largo plazo de neuronas nociceptivas de ratón (15 DIV). Se realizaron dos aplicaciones de paclitaxel de 24 horas, administradas de manera cíclica para imitar los ciclos de quimioterapia en humanos. Se observo un aumento en la actividad espontánea y la frecuencia de disparo de los potenciales de acción en neuronas sensitivas IB4(+) e IB4(-). Los efectos neurotóxicos tras la primera exposición al agente quimioterapéutico fueron notorios y persistentes 96h después de la segunda dosis. Se observaron cambios significativos en el

umbral de disparo y en la fase de hiperpolarización posterior, junto con una mayor actividad de los canales Na_V y TRP termo sensibles (TRPV1, TRPM8, TRPA1). Además, se observó una notable retracción axonal tras la segunda dosis, subrayando el impacto duradero del paclitaxel en la estructura y la función neuronal.

Este estudio avanza el estado del arte al investigar cómo la neuropatía inducida por paclitaxel altera la expresión y función de TRPV1, TRPM8 y de los canales de sodio, con el objetivo de mapear los cambios de activación en las vías de dolor, lo cual podría dirigir nuevas terapias para la CIPN y otras formas de dolor neuropático.

Adicionalmente, se han probado diversos moduladores de TRPV1 y TRPM8 para evaluar su capacidad de aliviar la neuropatía periférica inducida por quimioterapia. Los moduladores se seleccionaron específicamente por su potencial para disminuir la hipersensibilidad y mejorar los efectos neuroprotectores en los DRG afectados. Estos moduladores buscan estabilizar el estado inactivo de los canales TRP y reducir la actividad anómala de las neuronas sensitivas, lo que podría resultar en un tratamiento más eficaz y menos invasivo para el dolor neuropático.

ABSTRACT

Chronic pain, especially neuropathic pain, affects approximately 1.5 billion people worldwide, causing intense suffering and imposing significant economic burdens through healthcare costs, disability payments, and lost productivity. Despite its prevalence, available treatments show variable effectiveness due to the lack of diagnostic and therapeutic tools. This research is part of the PIANO project, a large consortium aimed at improving our understanding and treatment of neuropathic pain affecting about 1.5 billion people worldwide. PIANO aims to overcome these obstacles by localizing treatment at the first stations of the pain pathway, the dorsal root ganglia (DRG), minimizing side effects.

Among PIANO's objectives is chemotherapy-induced peripheral neuropathy (CIPN), a severe and poorly resolved side effect of cancer drugs like paclitaxel, for which no effective treatment has been found. This thesis aligns with ongoing PIANO research to explore the role of thermo TRP channels (TRPV1, TRPM8, TRPA1) in sensory neuron sensitization, crucial for understanding the molecular pathophysiology of neuropathy. These channels act as molecular detectors of thermal and chemical stimuli and are potentiated by proinflammatory agents, a process that increases TRP channel recruitment and modifies their activation properties. Research on these channels has opened new avenues for developing innovative analgesics. This project studies the effects of sequential paclitaxel exposure on the excitability and integrity of sensory neurons using a long-term primary culture of mouse nociceptive neurons (15 DIV). Two 24-hour applications of paclitaxel, administered cyclically to mimic chemotherapy cycles, increased spontaneous activity and action potential firing frequency in IB4(+) and IB4(-) sensory neurons. Although the neurotoxic effects of the first exposure were noticeable, they persisted 96 hours after the repeated dose, with significant changes observed in firing threshold and the second phase of after-hyperpolarization, along with increased activity in thermo-sensitive Na_V and TRP channels (TRPV1, TRPM8, TRPA1). Additionally, notable axonal retraction was observed after the second dose, underscoring the lasting impact of paclitaxel on neuronal structure and function.

This project advances the state of the art by investigating how paclitaxel-induced neuropathy alters the expression and function of TRPV1, TRPM8, and sodium channels,

aiming to map activation changes in pain pathways, which could lead to new therapies for CIPN and other forms of neuropathic pain. In this study, various modulators of TRPV1 and TRPM8 were examined to evaluate their ability to relieve chemotherapy-induced peripheral neuropathy. Modulators of these ionotropic channels, which regulate sensory neuron excitability, were specifically selected for their potential to decrease hypersensitivity and improve neuroprotective effects in affected DRG. These modulators aim to stabilize the inactive state of TRP channels and reduce abnormal sensory neuron activity, potentially resulting in a more effective and less invasive treatment for neuropathic pain.

INTRODUCTION

1. INTRODUCTION

1.1 Somatosensory system

The nervous system is an exciting, highly complex network in animals that coordinates sensory actions and processes by transmitting signals between different parts of the body. One of its major divisions, the peripheral nervous system, includes the somatosensory system, which is specifically responsible for processing tactile, pain, temperature, and proprioceptive information from the body. This system enables organisms to perceive and respond to mechanical forces, thermal changes (cold or hot), and noxious stimuli. In contrast, other specialized sensory systems, such as the visual, auditory, olfactory, and gustatory systems, are dedicated to detecting light, sound waves, chemical molecules in air or food, respectively (1). This network necessitates some mechanism known as *sensory transduction* where specific types of cells are adapted to detect particular stimuli via sensory receptors. In other words, they regulate the somatosensory system that detects external and internal stimuli. External perception includes mechanoreceptors (touch), nociceptors (pain) and thermal receptors (temperature) (2). Multiple receptors (i.e. chemoreceptors, central chemoreception, arterial chemoreceptors, and nuclear receptors) are responsible for modulating the internal stimuli. These receptors are located in the neurons from dorsal root ganglia (DRG) which are located immediately outside the dorsal side of the spinal cord (3). Sensory neurons are pseudo-unipolar, having a process from which the axon from the cell body branches in two directions: one branch travels into the spinal nerves while the other travels through the dorsal root. An ascending pathway from the dorsal column is a main pathway by which sensory information is sent to processing areas of the cortex (4).

1.2 General pathways

The transmission of perception is regulated by two principal pathways: the dorsal column-medial lemniscus pathway and trigeminal pathways (5). These two pathways converge on the same area in the primary somatosensory cortex - located in brain areas within the parietal lobe of the cerebral cortex. The pathway of the dorsal lemniscus detects peripheral stimuli from the body and neck via the spinal nerve. It sends signal to the dorsal

root ganglion just outside of the spinal cord, from where it ascends to the brainstem, as well as up to the thalamus through the ventral posterior lateral nucleus. Finally, third-order neurons in the thalamus project to the primary somatosensory cortex. In contrast, the trigeminal pathway transmits peripheral stimulus from face and head through the cranial nerve V to the trigeminal ganglion and trigeminal nucleus in the brainstem (6). The stimulus is relayed to the ventral posterior medial nucleus (VPM) in the thalamus terminating in the parietal lobe of cerebral cortex (7). The cell bodies of somatosensory receptor neurons are mainly located at the DRGs, that hold a collection of neuronal cell bodies. These neurons give rise to primary afferent fibers- axons which originate in peripheral target organs and travel into the DRG where their cell bodies are located. Primary afferent axon types differ according to conduction velocity and receptor density: as group I, II, III and IV fibers depending also on the genesis (8). The fastest one, the heavily myelinated fibers are found in group I (Aα, which is of a large diameter). The Aβ and Aδ are the group II and III respectively, with a thinner diameter and slower conduction. Group IV are unmyelinated, small diameter, and slow conductors of action potentials (0.5-2 m/sec) also called C fibers. Pain, temperature and itch sensation are conveyed by receptor Aδ and C fibers (**Fig. 1**- (9)).

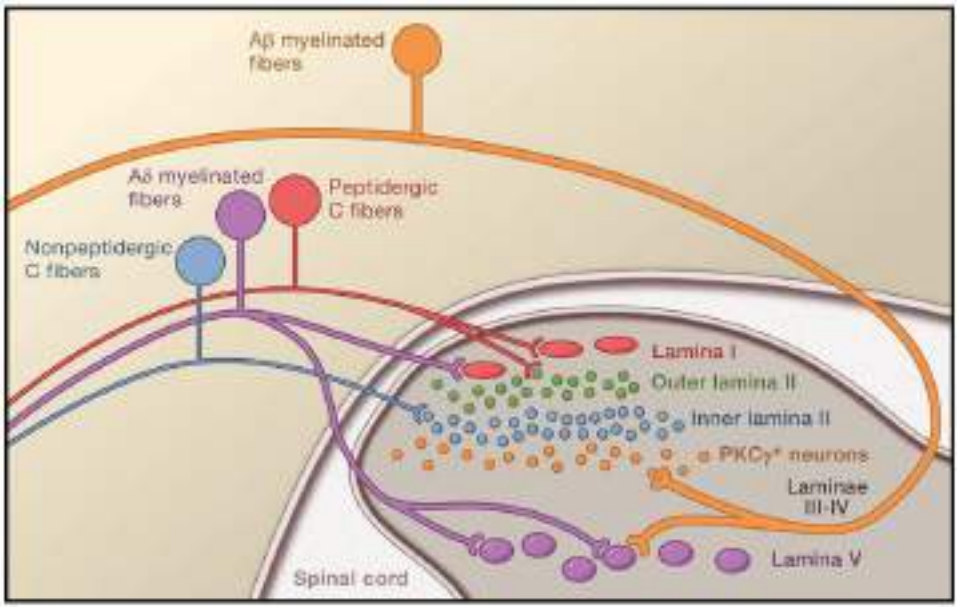

Figure 1: Primary afferent fibers connect within the spinal cord dorsal horn. Adapted from https://pubmed.ncbi.nlm.nih.gov/19837031/. (9), it highlights the dorsal horn structured laminar arrangement, where specific types of sensory fibers connect with distinct spinal neurons. Unmyelinated peptidergic C fibers and myelinated Aδ nociceptors link to large projection neurons in lamina I and outer lamina II interneurons. Nonpeptidergic unmyelinated nociceptors interact with interneurons in inner lamina II, while myelinated Aβ fibers, responsible for non-painful sensory signals, connect with PKCγ-expressing interneurons in the ventral part of inner lamina II. Lamina V projection neurons receive overlapping input from both Aδ and Aβ fibers.

1.3 Somatosensory receptors

Sensory signals from the periphery are sensed by mechanoreceptors, thermoreceptors and nociceptors. These tactile receptors are situated on the skin at different parts of the body and have their own functions:

- ***Mechanoreceptors***: Proprioceptive receptors sensors that provide feedback about limbs and position of other body parts. Such as the Meissner's corpuscles (low-frequency vibrations and light touch), Merkel cells (pressure and touch), Pacinian corpuscles (rapid changes in vibrations & pressure) (10).
- ***Thermoreceptors:*** These receptors are sensitive to changes in temperature. They are classified into cold receptors and hot receptors. They are free nerve endings (cold Aδ fibers; hot C fibers) right below the epidermis (11).
- ***Nociceptors:*** According to Woolf and Ma, nociceptors are pain receptors that detect noxious stimuli and protect the body from damage (12).

Finally, there are also ***proprioceptors*** (detectors of position and movement of the body)

and ***chemoreceptors*** (respond to chemical stimulation). The somatosensory receptors set off action potentials that travel through the nerve fibers, into the spinal cord and up to the brain for processing the stimulus.

1.4 Pain

Although it is heavily tied with tissue damage, pain is a complex and subjective experience that serves as an important and protective function in the body by alerting the presence of noxious stimuli (13). It signals to the individual that an aversive stimulus may cause harm, and thus acts as a protective mechanism. People insensitive to pain are prone to hurting themselves and have more persisting infections, which usually lead to a shorter lifespan (14). According to the *International Association for the Study of Pain* (IASP), which made its last update in January 2022, pain is defined as: "An unpleasant sensory and emotional experience associated with, or resembling that associated with, actual or potential tissue damage"(15). Pain can be classified in acute, when it is transient (<3 months) and only remains to signal warning pathology, or chronic pain, when pain persists for longer than 3–6 months, which is a class of lesions that take many forms (**Table 1**) (16). Chronic pain, on the other hand, is present with no current or imminent noxious stimulus. It represents a maladaptation of the sensory system, recognized by a disease rather than a symptom.

Physiologic change	Acute pain	Chronic pain
Vital signs	May vary consistently with degree of pain severity	No or minimal change
Purpose of pain	Useful	Inhibits function and not useful
Central sensitization	Short term; improves with healing of injury	Remains present despite absence of ongoing injury
Neuropathic pain	Increases likelihood of chronic pain when present in acute phase	Common etiology of chronic pain
Nociceptive pain	Often found during acute pain state	Commonly presents with some neuropathic pain

Table 1: Differences between acute and chronic pain.

https://www.lecturio.com/concepts/physiology-of-pain/.

1.5 Chronic pain

Chronic pain is considered a complex disease involving biological, psychological and social aspects. It impacts millions of people throughout the world, a major challenge to both the individual and healthcare systems (17). Chronic pain is not a sign of illness or injury, it is a disease entity in its own right that persists for more than 3 months, frequently associated with high levels of mental health conditions. Analgesic treatment is the principal medication used to manage chronic pain, whereas antidepressants and anticonvulsants are the principal medications for depression treatment which occur as a secondary effect to chronic pain. To tailor the treatment of chronic pain for each individual, a comprehensive picture that considers the physical, emotional, and social dimensions is necessary such as nutritional methods, exercise and physiological activity or motion therapy like acupuncture and mind–body therapies (18). The economic component must not be overlooked as chronic pain represents a considerable burden on health care costs and work absenteeism associated with reduced ability to function at full capacity (19)

There are various types of chronic pain, based on its source and nature, however the categories are not mutually exclusive, as a person with one type of chronic pain can have

elements of several different ones. There are three main forms of chronic pain (20,21):

i. ***Nociceptive pain***: It originates from real or potential tissue injury, serves as a warning system of our body to harmful stimuli or injury. This can be divided into somatic nociceptive pain (well-defined, arising from injuries, fractures, cuts and burns) and visceral pain (from internal organs where it is more difficult to localize).

ii. ***Neuropathic pain***: It originates from damage or dysfunction of the nervous system. Damage to either the peripheral nervous system or central nervous system, as well as nerve dysfunction, are the common cause of neuropathic pain resulting in abnormal signaling. Such pain may occur spontaneously or in response to stimuli that would not normally be painful (allodynia), or it can be induced by noxious stimulation (hyperalgesia).

iii. ***Inflammatory pain***: It is associated with inflammation in the body, typically caused by an infection or autoimmune disorder, or tissue damage. It is due to the release of inflammatory mediators including prostaglandins, bradykinin and cytokines which increase sensitivity and excite nerve endings (nociceptors), in the area involved.

1.6 Pain pathway

Pain, which is evoked by harmful stimuli, represents a complex phenomenon that corresponds to neural processing itself (nociception) involving transduction, transmission, and modulation (22). *Transduction* occurs as noxious stimuli are transformed into electrical signals through chemical processes that generate action potential once a threshold is achieved. These signals are carried through nociceptive pathways across synapses, with neurotransmitters such as glutamate and substance P released by nociceptors to signal transmission through the dorsal roots of the spinal cord (23).

The dorsal horn of the spinal cord is essential for pain signal processing and *transmission* via ascending pathways. A layered structure, with nociceptors terminating in multiple laminae at the spinal cord, increases the complexity of pain processing, which is initiated with neurotransmission by nociceptors within each lamina where second-order neurons are activated. More limited in the sense that Aδ nociceptors terminate at both laminae I

and V and C nociceptors terminate at both superficial laminae (I, II). Knowledge of the dorsal horn and its role in pain processing is an essential foundation for any intervention aimed at treating pain (24).

Gate-control theory, which was developed by Melzack and Wall, postulated that non-painful sensory inputs close a "gate" in the dorsal horn and inhibits pain signal transmission to the brain (**Fig. 2**– https://basicmedicalkey.com/pain-4/) (25). The theory has changed over the years, but it is still a valid model for pain transmission. The theory suggests that there are control systems, or "gates," in the normal pain pathways of the body that can affect the entry of pain stimuli into the spinal cord and brain. These gates situated at the synapses of nerves, can open and let through pain impulses into your brain or close to dampen or change those signals. Competing sensory stimuli can lead to gate closure, e.g., applying ice to an area of pain diverts awareness from a painful stimulus and over the cold sensation.

Transcutaneous electrical nerve stimulation (TENS) is a therapeutic tool that produces peripheral sensory stimulation at the level of first-order afferents which occludes the activity of pain transmission (26). Furthermore, efferent transmissions from the reticular formation allow the brain to augment incoming pain signals. This control system can be activated by factors such as prior conditioning, emotional state and distraction. For instance, a person might not feel pain from an injury until later when they are no longer busy, thus reacting to the situation. While neurons themselves cannot replenish with new tissues, neuroplastic changes can occur in the dorsal horn giving rise to sensitized neurons that are conduits of pain signals (27).

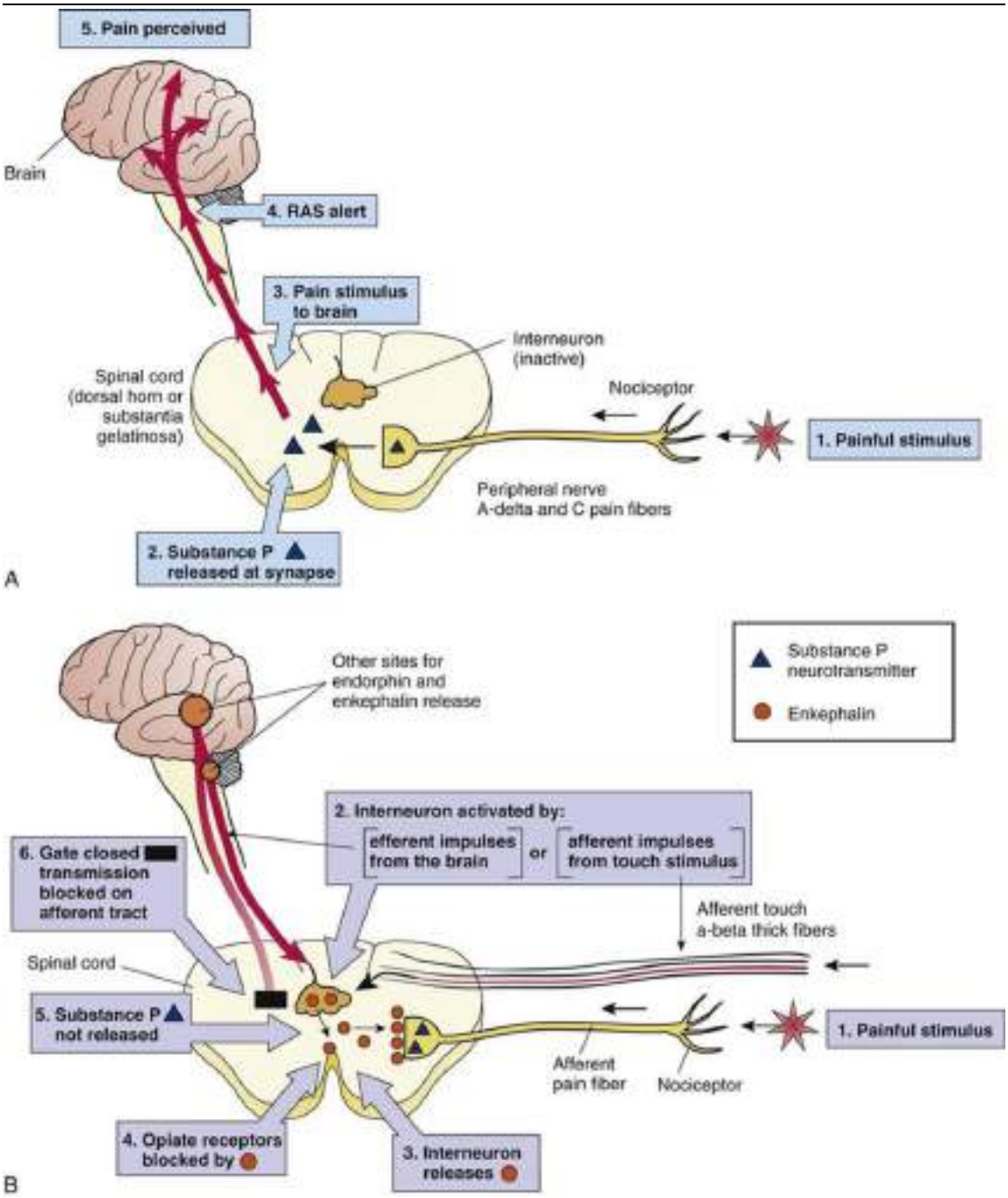

Figure 2: The gate-control theory of pain. (A) When the gate is open, pain messages are allowed through. (B) When the gate is shut, pain messages are stopped. The body has natural mechanisms- referred to as "gates"- that help manage how pain signals reach the spinal cord and brain. If these gates remain open, signals from peripheral nerves pass into the spinothalamic pathway and continue upward toward the brain. Image from https://basicmedicalkey.com/pain-4/ (25).

1.7 Nociceptors

These specialized sensory receptors, known as nociceptors, convert signals that may indicate danger into a sensation of pain to inform the body of impending threats. Such stimuli are mechanical, thermal and chemical compounds released during inflammation. Recent transcriptomic profiling studies have expanded the traditional classification of sensory neurons, identifying more than ten distinct subtypes based on gene expression patterns, beyond the classical peptidergic and non-peptidergic categories (28). Nevertheless, for the purposes of this section, we focus on the well-established distinction between peptidergic and non-peptidergic nociceptors, which remain functionally relevant in pain researchs (**Fig. 3-**(29)).

Non-peptidergic neurons- commonly identified as IB4(+) in rodent models- arise from unmyelinated C-fibers and transmit signals at slower conduction velocities. They typically respond to mechanical stimuli and high-threshold pressure, showing rapid adaptation to sustained stimuli. While they are not usually linked with inflammatory responses, they are crucial contributors to several chronic pain states. By contrast, **peptidergic** neurons (IB4(-) in some rodent models) play a role in slower, more prolonged pain transmission and release neuropeptides including substance P and calcitonin gene-related peptide (CGRP). Although peptidergic neurons are exclusively associated with myelinated Aδ fibers (30), they can also be unmyelinated. They are quickly able to send messages when attached with myelinated fibers and respond to other stimuli — thermal, chemical, and mechanical stimuli. These nociceptors show reduced adaptation and are generally more involved in inflammatory responses and neurogenic inflammation, but also chronic pain states (31).
IB4(+) and IB4(-) neurons are characterized based on their reactivity to Isolectin B4 (IB4), a lectin that binds surface specific carbohydrates. The knowledge of the IB4(+) (non-peptidergic) and IB4(-) (peptidergic) neuronal types of properties and functions will be beneficial to better understand the mechanisms underlying sensory processing, nociception, and pain (32). Indeed, to better target pain treatment and similar interventions, we study these populations in this thesis.

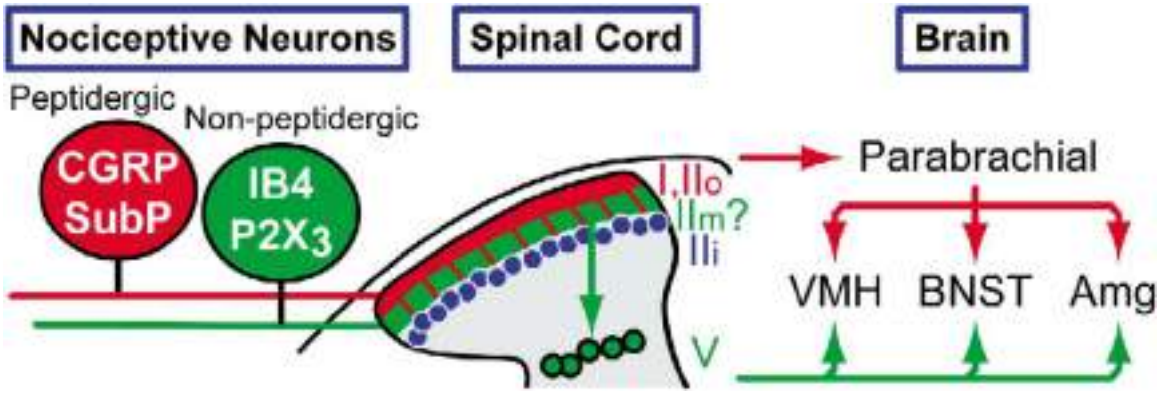

Figure 3. Different types of nociceptors. The way pain signals reach emotional centers in the brain involves two main types of nociceptive neurons. Nonpeptidergic ones (shown in green) take an indirect, multisynaptic route through neurons located in spinal cord laminae II and V, avoiding PKCγ-positive interneurons (depicted as blue circles). In contrast, peptidergic nociceptors (red) transmit to limbic structures by way of lamina I neurons and the parabrachial nucleus. Lamina II itself is further categorized into outer (IIo), inner (IIi), and a possible middle (IIm) layer—identified as a subregion of IIi in mice. Key limbic targets include the ventromedial hypothalamic nucleus (VMH), bed nucleus of the stria terminalis (BNST), and the amygdala (Amg). Image from https://doi.org/10.1016/j.neuron.2005.09.003. (29)

1.8 Ion channels in pain

Ion channels are specialized protein structures found in the membranes of virtually all cell types, including neurons, where they regulate the flow of ions across cellular membranes. They are located not only on the plasma membrane but also on intracellular membranes such as those of the endoplasmic reticulum and mitochondria. In the context of sensory neurons, various ion channel types play essential roles in detecting and transmitting pain signals and are heavily implicated in the mechanisms underlying chronic pain. This has made ion channels a prime target to find analgesic drugs (33). As of right now, ion channels are targeted by nearly 21% of all analgesic therapies. Most noteworthy of these are sodium (Na^+), calcium (Ca^{2+}) and transient receptor potential (TRP) channels, all strong contenders as they play impactful roles in the inhibition of pain (34).

The action potential (AP) is achieved mainly by sodium (Na^+) and potassium (K^+) channels to elicit fast and slow flow of current in neurons. Fast depolarizing Na^+ channels are responsible for the rapid upstroke of action potentials, while slower repolarization K^+ channels bring resting membrane potential back to normal. In neurons, the resting membrane potential (RMP) is -70mV, and its maintenance relies on the selective permeabilities of cell membranes to different ions (**Fig. 4**-(35)).

A stimulus received by a neuron will result in the opening of voltage-gated Na^+ channels (Na_v), which depolarizes the cell and increases intracellular sodium ion (Na^+) concentrations. Na^+ influx boosts the membrane potential quickly. When the potential passes a certain threshold, additional Na_v open, and an ever-increasing positive feedback loop finishes off the job of depolarizing the membrane. In response, voltage-gated potassium channels (K_v) open during the repolarization phase and, as a result, K^+ moves out of the intracellular space; however, this process also works at a slower velocity compared to sodium influx (36). The resulting change can in turn trigger hyperpolarization, making the membrane potential more negative than it is at rest, and that renders the neuron less able to respond to further stimuli, forming unidirectional propagation of action potentials.

Specialized sensory neurons called nociceptors turn painful stimuli into electrical signals via their ion channels. When exposed to harmful stimuli or products of the host response, Na_v and Ca_v, as well as members of the transient receptor potential (TRP) subfamily, become activated (37). As a result, this activation permits ions to flow into the cell, depolarizing it by increasing its membrane potential. This depolarization is then sufficient to induce a rapid and large influx of Na^+ due to the opening of Na_v channels which leads to an even larger depolarization phase of action potential (AP). Na_V channels inactivate, preventing additional entry of K_v channels open and begin to allow K^+ out of the cell, returning membrane potential to resting. Since the closure of K_v channels is slower, it leads to a brief undershoot below resting potential called hyperpolarization. The Na^+-K^+ ATPase in turn restores ionic balance by pumping out Na^+ and bringing in K^+, recalibrating the membrane potential.

Various other ion channels facilitate nociceptor excitability and pain modulation, including Ca_v, "two-pore domain" potassium channels (K2P), hyperpolarization-activated cyclic nucleotide-gated (HCN) channels, acid-sensing ion channels (ASICs), Piezo channels, and purinergic P2X receptors (38).

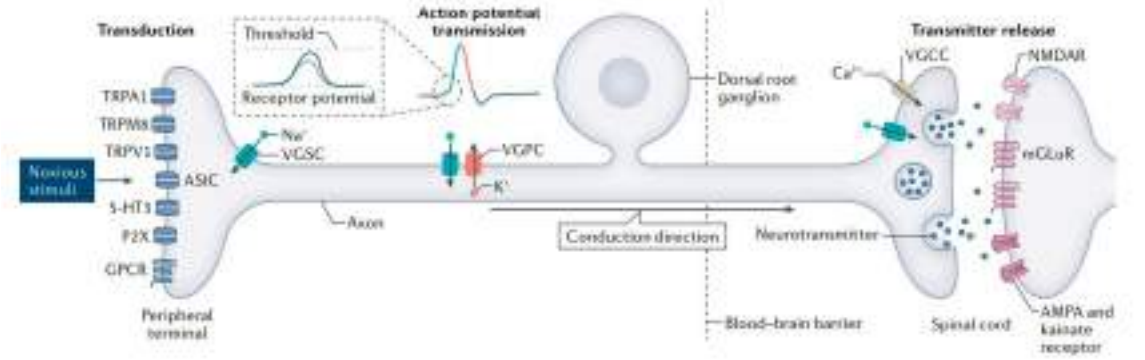

Figure 4: The process of nociception through ion channels pain. Image from **https://doi.org/10.1038/s41583-021-00444-w** (35)

1.9 TRPs channels

Transient receptors potential ion channels (TRP) belong to a superfamily of ion channels that mediate the transduction of diverse sensory signals, including pain. The TRP channels permit the passive passing of ions, including Na^+ and $Ca^{2+,}$ resulting in depolarization of the cell membrane, which are triggered by a range of stimuli: temperature, pressure, and chemicals (39). The depolarization produced by these channels in response to noxious stimuli can also lead to action potential and therefore pain signal.

Structurally, TRP channels are composed of six transmembrane segments (S1–S6), with the ion-conducting pore formed by a loop between the fifth and sixth segments (S5–S6). This architecture is conserved across most subtypes, although variations in other structural domains contribute to the functional diversity within the family. The C-terminal region contains a conserved TRP domain, which plays a crucial role in channel gating, interaction with intracellular proteins, and regulation of channel activity (40). Many TRP subtypes also feature ankyrin repeat domains (ARDs) in their N-terminal region, which facilitate protein–protein interactions important for channel modulation. The remainder of the N-terminus is more variable and is believed to be involved in subtype-specific regulatory mechanisms and signaling pathways (**Fig.5**-(41)). Through their structural versatility and sensitivity to multiple stimuli, TRP channels serve as key molecular sensors that transduce environmental and pathological signals into cellular responses.

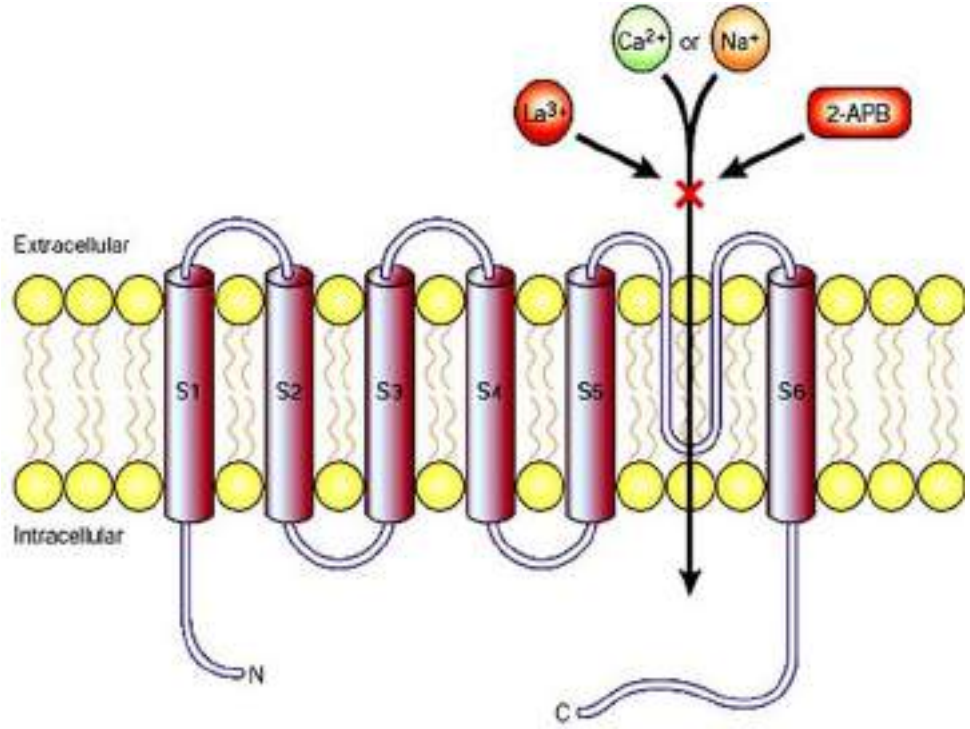

Figure 5. TRP channel's structure. Adapted from https://doi.org/10.1038/35077544 (41)

A well-characterized subset of the transient receptor potential (TRP) channel family is the group known as thermoTRPs, which are specialized in detecting changes in temperature. These channels respond to a broad range of thermal stimuli- from noxious heat to painful cold- and play a key role in thermosensation and pain perception. Beyond temperature detection, TRP channels are also involved in sensing a variety of noxious stimuli, including chemical irritants and mechanical stress (**Fig.6**-(42). As a family of non-selective cation channels, TRPs are central mediators of sensory transduction, and several of their subtypes have been strongly implicated in pain pathways:

- ***TRPV1 (Transient receptor potential vanilloid 1):***

TRPV1 is known as the "capsaicin receptor" because it is activated by capsaicin, the agonist mediating pain sensation induced by heat-bearing chili peppers causing burning sensations. High temperature (more than 43°C, 109°F) also switches on TRPV1 and is activated by diverse chemical stimuli such as protons (acidic conditions), endogenous ligands and inflammatory mediators (43).

It was first localized in medium and small diameter sensory neurons of dorsal root ganglion (DRGs) and trigeminal ganglion (TG); however, later studies localized this

channel in the brain as well as non-neuronal tissues. TRPV1 plays a key role in both inflammatory and neuropathic pain. It contributes to peripheral sensitization, a process where nociceptors become more responsive to stimuli following tissue injury. In neuropathic pain conditions- such as diabetic neuropathy or nerve injury- TRPV1 is involved in abnormal pain signaling that leads to heightened pain sensitivity. At sites of inflammation, TRPV1 can be activated by a wide range of mediators released in the damaged tissue, including protons, bradykinin, prostaglandins, and nerve growth factor (NGF), which further enhance its excitability and contribute to pain hypersensitivity (44). The role of TRPV1 in migraine, a neurological disorder characterized by paroxysms of recurrent headache, is suggested to contribute to pathophysiology (45).

Due to its role in pain disorders, TRPV1 has been proposed as a possible therapeutic target for the modulation of different kinds of acute and chronic pain. Capsaicin patches and other TRPV1 modulators are used in medication practice for symptom alleviation of pain associated with multiple diseases (46). The role of this channel in the transduction of pain has led to TRPV1-targeted therapeutic interventions designed to selectively activate or inhibit TRPV1-mediated pathways that may provide analgesic relief against different forms of pain. It should be noted that while targeting TRPV1 for the treatment of pain shows promise, it is important to adopt a cautious approach in order to balance therapeutic efficacy with side effects (47). This caution is important because TRPV1 plays a role in many physiological functions outside perception of pain, such as regulating body temperature, controlling bladder function, and modulating inflammation. There are endless ongoing explorations and clinical trials to bring new modifications of TRPV1 in our management of pain more safely and effectively (48).

- ***TRPM8 (Transient receptor potential melastatin 8):***

Background TRPM8, also known as cold and menthol receptor 1, is a nonselective cation channel that is expressed largely in sensory neurons. It is important for the perception of temperature, touch, and pain. TRPM8 is activated in the temperature range of 8–28 degrees Celsius and by cooling agents like icilin, menthol and its derivates (including WS12) (49). TRPM8-expressing sensory neurons are scattered in the skin and other tissues and are known as thermoreceptors (50). Upon triggering by menthol, TRPM8 channels activate and permeabilize to cations (such as calcium (Ca^{2+}) and sodium ions (Na^{+})),

causing depolarization of the neuron and action potential transmission to the nervous system where it is perceived as cold.

Despite being known to participate in several physiological functions like pain and immune response modulations, overactivity of TRPM8 might be connected to different pathophysiology (51). Indeed, it is also involved in inflammation, including stimulation of inflammatory mediators from pulmonary epithelial cells, thereby contributing to dysregulation of immune response and chronic inflammation (52). TRPM8 is expressed in the airways (where its activation promotes bronchodilation) and the urinary bladder (where it affects bladder function). In asthma, TRPM8 inhibition has been proven to reduce respiratory hyperresponsiveness (53).

Due to its high expression in prostate tumor cells, an increase of TRPM8 activity through different trigger elements such as agonists has been investigated regarding cancer cell proliferation, migration, and apoptosis leading to the proposition that it is a potential target for cancer therapy when combined with other treatment options (54,55). Relevance of TRPM8 receptor has been associated to pathophysiological problems such as dry eye syndrome, itch-associated neural signaling, neuropathic pain disorders and migraines Modulation of TRPM8 has been investigated as a potential therapeutic approach to manage pain states like cold allodynia triggered by oxaliplatin (56).

Knowing the chronic TRPM8 associated diseases like neuropathic pain, inflammatory disorders and cancers would greatly benefit from modulators of these channels with possible therapeutic applications. Therefore, use modulators of TRPM8 may provide analgesic effects in chronic pain states and can be envisaged as a novel site for anticancer therapy (57).

- ***TRPA1 (Transient receptor potential ankyrin 1)***

Ca^{2+} permeant nonselective cation channel, TRPA1 is primarily expressed in sensory neurons and it is induced by a range of chemical irritants as well as environmental stimuli relevant to pain and cool sensation. Among the main agonists are allyl isothiocyanate (AITC) from mustard and wasabi; cinnamaldehyde from cinnamon; and reactive oxygen species. Additionally, it is also involved in the detection of noxious cold temperatures (58). TRPA1 is closely associated with inflammation, as its sensitization by inflammatory mediators that increases pain sensitivity. For instance, it has been implicated in

inflammatory bowel disease (IBD), arthritis and asthma (59). TRPA1 is not so cold-sensation specific as TRPM8, but can still be activated by a range of cold temperatures through diverse mechanisms (60). In particular, it is stimulated by noxious cool temperatures below 17°C, mimicking a pain sensation. In fact, the function of TRPA1 as cold receptor is controversial because of the overlapping temperature range of TRPM8 vs. TRPA1 signalling (61). Additionally, a few studies also confirmed that cold activates TRPA1 probably more slowly than TRPM8. In contrast, several studies confirmed the involvement of TRPA1 in pain perception associated with noxious stimuli that potentially relies on membrane-bound second messenger system coupling noxious cold temperature to perceived pain (62).

TRPA1 activation triggers action potential that are transmitted to the central nervous system to detect pain or discomfort. There are few cases where the aberrant expression and function of TRPA1 may play a role in disease, one of which is neuropathic pain due to diabetes or nerve injury. Cold hypersensitivity arises from neuropathic pain involvement, leading to heightened pain sensitivity (63).

Because of its role in diseases related to hyper-algesia, TRPA1 has recently become an attractive drug target. Despite considering the involvement of this channel in other distinct physiological processes, drugs that modulate TRPA1 activity are likely useful in ameliorating neuropathic pain manifestations; however, further investigation will be necessary to correct therapeutic strategies to reduce side effects (64).

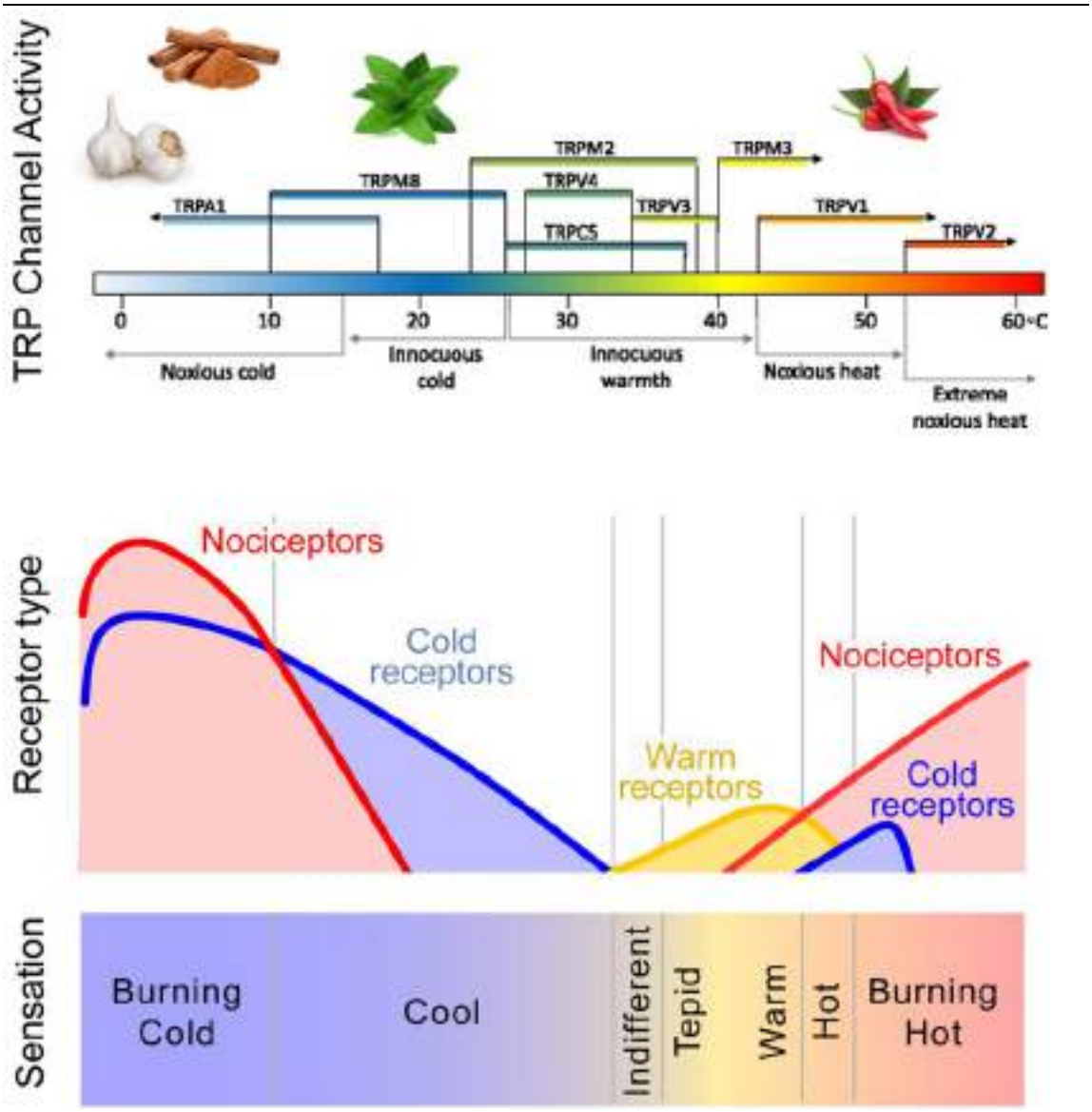

Figure 6. Hypothetical relationship between TRP channel activation, body surface temperature, and corresponding sensations. theoretical link between TRP channel activation, body surface temperature, and related sensations. The top section shows the thermal and molecular activation patterns of various TRP channels observed in recombinant systems. The middle section displays the activity of cutaneous sensory receptors when their receptive fields encounter specific temperatures. The bottom section outlines the sensations humans perceive at different skin temperatures (figure modified from https://doi.org/10.1186/1744-8069-4-14)(42).

1.10 Sodium channels (Na_v channels)

Sodium channels work to generate electrical impulses, using the surrounding sodium ions (Na^+) as electrolytes between cells– It is necessary for electrical signalling and especially relevant here as the target of action potential circuitry in nerve fibers such as sensory

neurons involved in pain transduction (35). Voltage-gated sodium channels (VGSCs) are membrane proteins that activate and propagate action potentials in excitable cells, like neurons. Every VGSC consists of a chief alpha (α) subunit, which forms part of the pore that conducts ions, and auxiliary beta (β) subunits that modulate the channel's proteostasis, localization, gating, and kinetics. These modulatory effects are influenced by intracellular signaling pathways, including those mediated by kinases such as protein kinase C (PKC), protein kinase A (PKA), and mitogen-activated protein kinases (MAPKs), which can phosphorylate channel subunits and affect their function (65).

VGSCs can be altered in states of injury, inflammation or in certain diseases which lead to sensitization of the pain pathways. These channels could become more sensitive and require less stimulation to open and propagate action potential leading to hyperexcitability. VGSCs may be in a state of persistent activation (e.g., activated and open for prolonged periods) within chronic pain conditions, which can enhance pain (66).

The expression of different sodium channel subtypes associated with pain are found on sensory neurons (**Table 2; Fig. 7**- (66)):

- ***$Na_V1.7$ (Sodium voltage-gated channel alpha subunit 1.7)***: $Na_V1.7$ is primarily found in small sensory nerve cells and plays a key role in boosting pain signals and increasing nociceptor responsiveness to harmful stimuli. People with non-functional $Na_V1.7$ channels are unable to feel pain (67), while gain-of-function mutations lead to heightened pain. Compared to $Na_V1.8$, $Na_V1.7$ has distinct channel kinetics and a much greater sensitivity to the sodium channel blocker tetrodotoxin (TTX); it responds to very low nanomolar doses, while $Na_V1.8$ remains unaffected even at high concentrations (68). $Na_V1.7$ has a lower activation threshold, allowing it to respond to small, slow depolarizations and amplify the signal, playing a critical role in initiating action potentials. It is particularly important in the upstroke phase of action potentials (69). Overexpression of $Na_V1.7$ in injured neurons, likely triggered by increased protein kinase activity, such as protein kinase A (PKA) or protein kinase C (PKC), contributes to ectopic discharges and enhances its role in pain signaling. Additionally, mutations in the SCN9A gene, which encodes $Na_V1.7$, are linked to hereditary pain disorders,

including congenital insensitivity to pain (CIP) and inherited erythromelalgia (IEM), highlighting $Na_V1.7$'s central role in neuropathic pain (70). $Na_V1.7$ is one of the most critical voltage-gated sodium channels in the peripheral nervous system (PNS), especially in small nociceptors of peripheral sensory neurons and DRG neurons. $Na_V1.7$ is also expressed in the vagus nerve, where its activation can lead to parasympathetic responses such as bronchospasm and mucus secretion, and in olfactory sensory neurons (OSNs) of the central nervous system (CNS), contributing to the sense of smell. Interestingly, loss-of-function mutations in $Na_V1.7$ can lead to anosmia, or the loss of the sense of smell (71,72). Due to its significant role in NP, $Na_V1.7$ remains a prime target for developing selective blockers. These blockers are expected to provide pain relief with fewer side effects compared to non-selective sodium channel blockers, which can limit therapeutic options due to their broader effects (73). For instance, ANP-230 (previously DSP-2230), in development for peripheral neuropathic pain, inhibits $Na_V1.7$, $Na_V1.8$, and $Na_V1.9$ with minimal effect on $Na_V1.5$. ANP-230 has also shown potential in reducing hyperexcitability of DRG neurons by altering gating kinetics and achieving state-independent $Na_V1.7$ blocking (74)

- ***$Na_V1.8$ (Sodium voltage-gated channel alpha subunit 1.8)***:

  $Na_V1.8$ has long been recognized for its involvement in inflammatory pain, where its upregulation plays a significant role. More recently, its contribution to neuropathic pain (NP) has come under scrutiny, with growing evidence supporting its relevance (75).

  $Na_V1.8$ is widely expressed in nociceptors, especially in small-diameter DRG neurons and somatosensory afferent fibers. The complexity of its role in NP is reflected in the observed patterns of both downregulation and upregulation following nerve injury (76). Initially, $Na_V1.8$ expression decreases in affected afferent neurons; however, it is later upregulated in uninjured nociceptive fibers near the injury site, likely due to inflammatory cytokines. This redistribution of $Na_V1.8$ contributes to ectopic activity and persistent hypersensitivity, marking it as a potential therapeutic target for NP management (77). $Na_V1.8$, like other sodium channel isoforms such as $Na_V1.6$ and $Na_V1.7$, contributes to the rising phase of the

action potential in sensory neurons. However, $Na_V1.8$ stands out as the predominant isoform in nociceptive neurons and is characterized by slower inactivation kinetics and the ability to support high-frequency firing. These properties make it especially important for sustaining repetitive action potentials and maintaining neuronal excitability in pain pathways. Moreover, SCN10A gene polymorphisms, which encode $Na_V1.8$, are associated with variations in pain sensitivity and are implicated in conditions such as painful diabetic neuropathy (78). While inhibitors of $Na_V1.8$ have been identified (79), many lack the necessary selectivity, affecting other sodium channels and limiting their therapeutic potential. Local anesthetics like lidocaine, benzocaine, and tetracaine can temporarily block $Na_V1.8$ and relieve pain, but their use is accompanied by side effects such as seizures, ataxia, confusion, and sedation. This highlights the need for more selective and safer treatment options. Actually, selective sodium channel inhibitors targeting $Na_V1.8$, such as suzetrigine, have been shown to effectively reduce neuropathic pain, including chemotherapy-induced neuropathy, by blocking pain signal transmission in peripheral sensory neurons. These compounds represent a promising therapeutic approach for managing chemotherapy-induced peripheral neuropathy, providing a non-opioid alternative for pain control (80).

- ***$Na_v1.9$ (Sodium voltage-gated channel alpha subunit 1.9)****:* $Na_V1.9$ is mainly located in small-diameter neurons within the dorsal root ganglia (DRG) and trigeminal ganglia, where it contributes significantly to pain perception. Similar to $Na_V1.7$, it activates at low voltage thresholds. However, $Na_V1.9$ also produces a continuous sodium current, which stabilizes the resting membrane potential and influences how these neurons react to depolarizing inputs. (81). Mutations in the SCN11A gene, which encodes $Na_V1.9$, have been associated with various pain disorders, making this channel a potential target for treating(82). Additionally, $Na_V1.9$ influences the action potential threshold and firing frequency in nociceptors, despite being less studied than $Na_V1.7$ and $Na_V1.8$, $Na_V1.9$ is still considered a promising target for managing chronic pain. Although there are not

highly selective $Na_V1.9$ blockers currently available, clinical trials are actively investigating modulators of this channel (83). Ongoing trials are exploring its potential to treat infantile episodic limb pain syndrome, a condition linked to gain-of-function mutations in SCN11A, underscoring the potential for targeting genetic pain disorders. The advancement of stable $Na_V1.9$ expression systems, supported by co-expression with β-subunits, further facilitates high-throughput screening, offering new opportunities for developing $Na_V1.9$-targeted therapies for NP (84). Additionally, both $Na_V1.8$ and $Na_V1.9$ are resistant to TTX, highlighting their roles in action potential firing and pain signaling (85).

Channel	TTX Sensitivity	Activation Threshold	Kinetics	Expression	Pain Relevance	Selective Blockers
$Na_V1.7$	High (nanomolar)	Low	Fast activation/ inactivation	Small DRG neurons, nociceptors, OSNs, vagus nerve	Initiation/amplification of action potentials; hereditary pain syndromes	PF-05089771, CNV1014802
$Na_V1.8$	Resistant	Higher than NaV1.7	Slow inactivation, supports high-frequency firing	Small-diameter DRG neurons, nociceptive fibers	Inflammatory and neuropathic pain; high-frequency firing	Suzetrigine (Journavx™), Lidocaine (non-selective)
$Na_V1.9$	Resistant	Very Low	Persistent current, stabilizes resting potential	Small DRG and trigeminal ganglia neurons	Chronic pain modulation; genetic pain disorders	Currently under investigation

Table 2. Biophysical and pharmacological properties of DRG Na_V channels.

VGSCs exist in three distinct conformational states, i.e., resting (closed), activated (open), and inactivated (closed). During resting state, VGSCs impede the ion flux of Na^+. When depolarized, the voltage-sensing domain (VSD) senses change in membrane potential and induces a rotatory movement that opens the activation gate to permit Na^+ influx that initiates action potentials. VGSCs then rapidly enter a fast-inactivated state and remain unresponsive until the membrane potential is re-established (86). It may also involve slow inactivation, which occurs following sustained depolarization (although its mechanism is less clearly defined).

Sodium channels are the subject of several drugs that have been developed for pain and neurological disorders. Examples of sodium channel blockers that are used in research, because they induce paralysis and possibly death, include Tetrodotoxin (TTX) and Saxitoxin (87). By contrast, the experimental drugs PF-05089771 and CNV1014802 selectively block $Na_V1.7$. The serious side effects associated with these drugs have prompted continual research into finding more selective and effective pain medications (88,89). As mentioned, Suzetrigine, marketed as Journavx™, is a highly selective $Na_V1.8$ inhibitor recently approved by the FDA for managing moderate-to-severe acute pain in adults. This non-opioid analgesic offers a novel approach to pain relief by targeting peripheral pain pathways, potentially reducing the risks associated with opioid use.

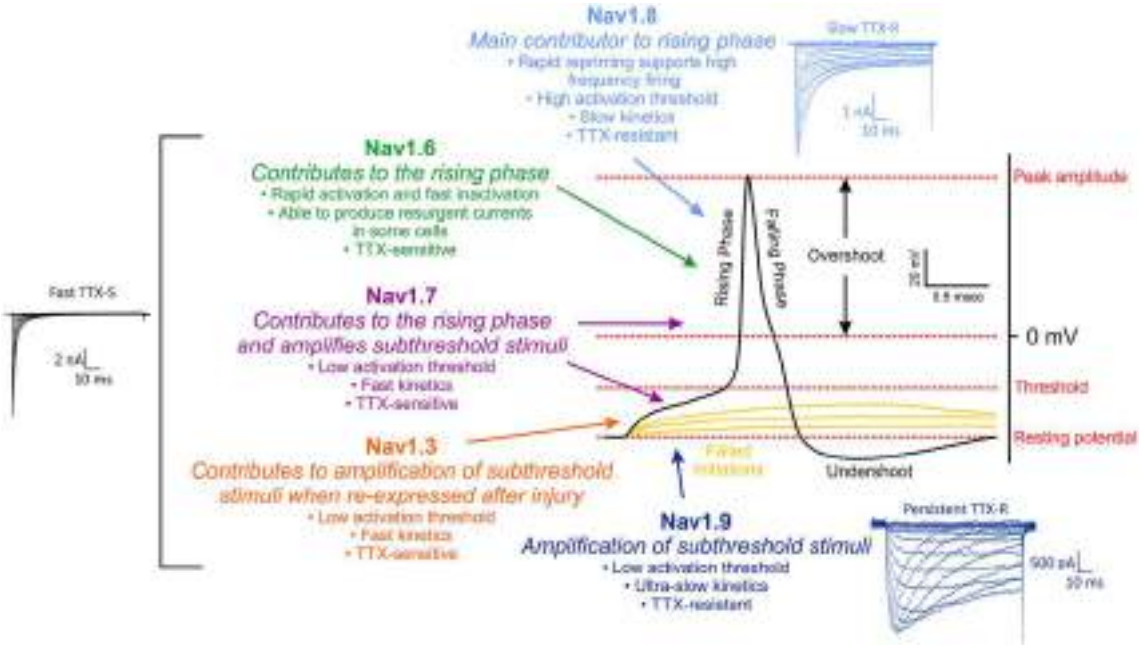

Figure 7. The role of voltage-gated sodium channels (VGSCs). Voltage-gated sodium channels (VGSCs) are essential for initiating and propagating action potentials in nociceptive neurons. The figure depicts a typical action potential recorded from a small-diameter dorsal root ganglion neuron following a 200-pA depolarizing current. Various VGSC subtypes contribute to different phases of the spike. The inset illustrates examples of sodium currents: rapid, tetrodotoxin (TTX)-sensitive currents linked to $Na_V1.3$, $Na_V1.6$, and $Na_V1.7$; slower, TTX-resistant currents generated by $Na_V1.8$; and a sustained, TTX-resistant current mediated by $Na_V1.9$. (adapted from https://doi.org/10.1016/j.bioorg.2024.107605 (66)).

1.11 Potassium channels (K_V)

Potassium channels (K^+) are a large and diverse family of ion channels that regulate membrane potential, repolarization, and overall cellular excitability across many cell types, including sensory neurons and glial cells (90). Among them, voltage-gated potassium channels (K_V channels) represent just one subfamily characterized by their activation in response to changes in membrane potential. Other major K^+ channel families include inwardly rectifying potassium channels (Kir), two-pore domain potassium channels (K2P), and calcium-activated potassium channels (KCa), each contributing differently to neuronal function. K_v channels play a particularly important role in setting the resting membrane potential and modulating excitability in both neurons and supporting cells, especially in the context of pain processing. Those are a family of ion channels with various subtypes, based on their structure, capacity and opening attributes. They consist of four α-subunits containing six transmembrane segments (S1–S6). K_v are classified into K_v1 to K_v12 with multiple members in each subfamily (e.g., $K_v1.1$, $K_v1.$ 2, etc.) (91). K_V contributes to repolarization phase following the action potential and likewise prevents excessive neuronal hyperexcitability. In fact, the way they function can affect how long these pain signals stick around. K_V channels can be broadly classified according to their inactivation kinetics and current properties: Fast-inactivating A-type (IKA) currents channels generate a fast-activating, rapidly inactivating current. Essential early in the action potential, main subtype: $K_V1.4$, $K_V3.4$, $K_V4.1$, and $K_V4.3$. Other subtypes are Delayed-rectifying slowly inactivating (IKDR) current channels, including $K_v2.1$, $K_V2.2$, $K_V7.2$, $K_V7.3$, and $K_V7.5$, resulting in a slow inactivating delayed-rectifying current that can keep them open longer (92). Several K_V channels subtypes are present in sensory neurons, such as the $K_V1.1$, $K_V1.2$, and $K_V1.6$, which are important for the transmission of pain signals from the periphery to spinal cord. They are also able to be influenced by the secretion of inflammatory mediators during inflammatory conditions and alterations in their expression and function have been involved in neuropathic pain. Modulation of these channels and the ability to study the unique properties of IKA- and IKDR-like currents in nociceptors suggest that such currents play a critical role in pain perception, which may provide a basis for focused novel therapies (93).

1.12 Chemotherapy-induced peripheral neuropathy (CIPN)

Chemotherapy Induced Peripheral Neuropathy (CIPN) is a well-documented side effect of peripheral nerve damaging by chemotherapeutic agents. It has multiple varying symptoms such as ache, numbness and motor impaired condition. It is caused by different chemotherapy drugs, such as platinum-based drugs (cisplatin, oxaliplatin), taxanes (paclitaxel, docetaxel) and vinca alkaloids (vincristine, vinblastine and others) (94). The symptoms occur during or up to several days after the course of chemotherapy, at which point the treatment may be modified or discontinued for the patient. Obviously, this affects the survival of the patients. In addition, the symptoms of CIPN impact cancer survivors on quality of life (QoL) in aspects such as daily activities, mobility and overall health status. CIPN can last long after treatment based on the type of chemotherapy, total amount and individual vulnerability (95). Although the mechanisms involved in CIPN are not completely elucidated, damage to peripheral nerves and changes in ion channel function, inflammatory processes, and oxidative stress are being investigated as contributing pathways (96), but at this time no therapeutic options exist to prevent or treat CIPN. In addition, some risk factors that may be involved when it comes to an individual becoming susceptible to CIPN are things such as having diabetes, genetic components and by the medications being received that have neurotoxic activity (97). Pharmacologic management of symptoms that could be related to CIPN includes analgesics, physical therapy and vigilant long-term monitoring together with supportive care utilizing lifestyle modification to augment treatment (98).

Although exact pathways are still being researched, it is thought that nerve damage results from several mechanisms used by chemotherapy agents (99). This may consist of a direct neurotoxicity to axonal fibers, an inflammatory mediated response, and/or manipulation of peripheral nerve molecular environment. During this process, a key player is a family of ion channels referred to as Transient Receptor Potential (TRP) channels (**Fig. 8**).

Evidence highlights a central role for TRP channels in pain-related pathways that emerge during neurotoxicity induced by chemotherapy, with a focus on TRPV1, TRPA1 and TRPM8. (100) Paclitaxel, oxaliplatin and cisplatin (chemotherapy drugs) induce changes

in TRP function and sensitivity that underlie enhanced pain behavior in CIPN. Damaged and injured nerve fibers following chemotherapy may lead to a stronger expression and response of TRP channels that excite sensory neurons. As an example, TRPV1 that is usually triggered by heat or capsaicin, may become hypersensitized post-chemotherapy (101). Therefore, even innocuous stimuli like gentle touch or minimal changes in temperature may be enough to trigger the pain pathways and cause the patient to perceive heightened pain- termed hyperalgesia (102,103).

TRP channels also contribute to mechano-sensation, or the perception of mechanical stress/injury (104). Chemotherapy can increase the sensitivity of these channels, which makes it more sensitive for these patients in touch or pressure. This can lead to extreme tenderness or pain when performing daily activities, like walking around or holding something.

Furthermore, chemotherapy induces an inflammatory response in the peripheral nervous system. Inflammatory mediators, including cytokines activate TRP channels e.g., TRPA1 and TRPV1 that may lead to a pain-inflammatory vicious cycle (44,105). This should be noted as this aspect in CIPN is even more troublesome because the presence of inflammatory mediators clearly sensitizes sensory nerves that further contribute to nociceptive pain (106)

However, many chemotherapy agents, including but not limited to oxaliplatin, are known to cause serious cold hypersensitivity in patients. The proposed mechanism is that the damage caused by these agents makes TRPM8 channels more sensitive hence they respond to cold temperatures that rarely cause pain under normal circumstances. This might lead to severe pain in response to chilling stimuli, worsening the discomfort under CIPN. CIPN mechanism involving TRP channels could provide therapeutic targets. If so, modulating the activity of these channels might help with chemotherapy-induced nerve-damaging pain and discomfort. A recent clinical study using a nociceutical formulation targeting TRP channels resulted in a less incidence of CIPN in hand during chemotherapy (107). TRPV1 modulators and TRPM8 inhibitors are being studied in this thesis for possible treatment of patients with CIPN (108–110).

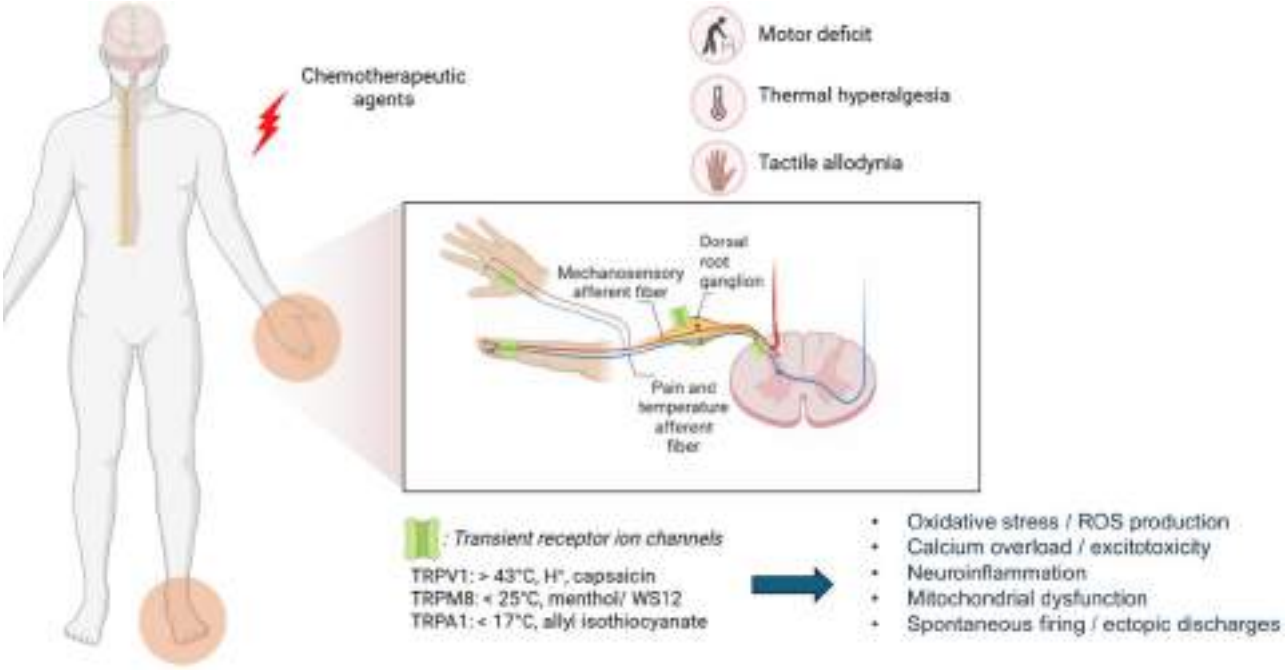

Figure 8. Drugs used in chemotherapy, including cisplatin, oxaliplatin, and paclitaxel, influence TRP channels- such as TRPA1, TRPM8, TRPV1- in neurons of the dorsal root ganglia (DRG), leading to a range of effects. These agents can trigger the activation of these channels, altering their expression and contributing to pain-related responses, oxidative damage, and increased sensitivity to mechanical pressure, temperature, and cold. *Created in Biorender.com.*

1.12.1 Paclitaxel-induced peripheral neuropathy (PIPN)

PIPN in the clinic is bilateral and characterized by tingling, numbness, and burning pain, in a length-dependent fashion, i.e., affecting the longest axons first (111). In extreme cases, patients can have muscle weaknesses and loss of vibratory sensation (112). Symptoms may become acute or continue weeks to months after treatment, a phenomenon referred to as coasting (113). This delayed progression may pose a challenge to the management of patients since the susceptibility to chronic PIPN remains unpredictable (114). PIPN has a considerable impact on quality of life with the potential for long-lasting disability. Further studies are necessary to develop risk stratification, investigational approaches for early diagnosis, and possible neuroprotective measures in patients treated with paclitaxel.

1.12.2 Paclitaxel in cancer therapy

Paclitaxel (commercially known as Taxol®) is a microtubule-stabilising agent extensively used in the treatment of cancer. It is most often indicated for ovarian and breast cancer

but also has been shown useful in the treatment of small cell lung cancer and Kaposi's sarcoma (115–117). Paclitaxel's history began in the 1960s when the National Cancer Institute (NCI) and the United States Department of Agriculture (USDA) began a screening program to search for natural anti-tumor agents. Paclitaxel cytostatic activity is primarily attributed to an ester group found at C-13 (118). It has cytotoxic effects on cells by interfering with the balance of cell cycle and by preventing the depolymerization of the microtubules through binding to the β -subunit of tubulin (119) At higher concentrations, it is a polymerizing agent that stabilizes the microtubule network. Neurotoxicity is a common adverse effect of paclitaxel, which has been well described. Although initially the exact cause was unknown, researchers soon suspected the drug's excipient Cremophor EL- which is required to dissolve the poorly water-soluble paclitaxel- as a leading cause of the development of this debilitating side-effect, however studies have shown that paclitaxel is also a contributing factor to peripheral neuropathy (120). Paclitaxel dosage and administration route depend on cancer type, stage, and past treatments. The traditional route is i.v. infusion. With its potent anti-tumor activity, paclitaxel for decades continued to be a cornerstone in cancer therapy. Crucial research is still underway to further develop its delivery and formulations, even though there exist numerous challenges concerning drug solubility, toxicity, and neuropathy. Such a comprehensive understanding of paclitaxel's mechanisms and side effects will facilitate the optimization of its therapeutic application, while limiting its complications.

1.12.3 Distribution of paclitaxel

Paclitaxel is widely distributed in the systemic circulation following systemic administration and determined paclitaxel levels in the heart, lungs, liver, kidneys, and skeletal muscles of mice receiving 2–22.5 mg/kg paclitaxel by intravenous (i.v.) injection and in most cases, brain tissue was found to contain no trace of paclitaxel (121) In a series of studies, rats were given 0.03 mg/kg of tritium-labeled paclitaxel, and it was found that while the drug was present in the heart, liver, spleen, and lungs, it was not present in the brain and peripheral nerves (122) This indicates that lower doses may not behave in the same way as higher doses (i.e., 30 mg/kg), which have been found in peripheral nerves (123), evidenced by the inability to pass blood-brain and blood-nerve barriers. Paclitaxel accumulation in the peripheral nerves has been studied showing persistence after repeated dosing. Paclitaxel was found to accumulate in dorsal root ganglia (DRG) and sciatic nerve in mice that received a single i.v. 30 mg/kg injection or were dosed repeatedly every 2 weeks (drug detectable up to 26 days in the repeated-dose group (123)). Similar observations were made in a rat model of peripheral neuropathy following treatment with paclitaxel (5 mg/kg) on alternate days; paclitaxel was found in the DRG and sciatic nerve (124). In a separate regimen (2 mg/kg on days 0, 2, 4, and 6), paclitaxel was detected in the DRG, dorsal roots, ventral roots and sciatic nerve by liquid chromatography-mass spectrometry (LC-MS/MS), with small amounts also detected in the brain and spinal cord (125) The carrier used to administer paclitaxel also influences its distribution and efficacy. These findings reflect the intricacy of paclitaxel pharmacokinetics, whose distribution is not only determined by dose, route of administration and formulation, but also has consequences in terms of its efficacy and toxicity.

1.12.4 Paclitaxel effects on immune system and ion channels

Paclitaxel is a well-established chemotherapeutic treatment; however, its advantages are commonly diminished by dose-dependent neurotoxicity and the resultant paclitaxel-induced peripheral neuropathy (PIPN) (126). PIPN occurs in 22–100% of patients treated with doses over 250 mg/m^2 and may present as paresthesia, numbness and burning pain, especially in the extremities (127). This demonstrates that the severity of neuropathy is directly proportional to cumulative dosing and/or duration of infusion, serving to

underscore the need for more individualized treatment regimens (128). At the molecular level, PIPN is mediated by axonal degeneration and inflammatory processes. Paclitaxel can trigger inflammatory cascades through direct interactions with macrophages and Toll-like receptor 4 (TLR4) (122), with the involvement of Langerhans cells and the subsequent release of IL-6, IL-8, IL-10, and MCP-1. Moreover, oxidative stress has a direct impact on Schwann cells, microglia, and DRG neurons, resulting in mitochondrial malfunction and the liberation of damage-associated molecular patterns (DAMPs), further promoting inflammation (123,124). Furthermore, paclitaxel affects both ion channel activity and sensory and autonomic system function, leading to neuronal hyperexcitability and neuropathic pain. Changes in $Na_V1.3$, $Na_V1.7$, $Na_V1.8$, and $Na_V1.9$ sodium channels are observed that ameliorate the effect on the propagation of action potential (129) ProTx II and similar inhibitors have been demonstrated to reduce these effects (125). Moreover, dysfunction in specific voltage-gated potassium (K_v) channels contributes to the hyperexcitability of sensory neurons observed in neuropathic pain. For instance, reduced activity of $K_v1.2$ and $K_v11.3$ channels has been linked to increased neuronal firing and heightened pain sensitivity. Additionally, $K_v7.2/K_v7.3$ (KCNQ2/3) channels play a crucial role in stabilizing the resting membrane potential; pharmacological openers such as retigabine have demonstrated therapeutic potential by enhancing these channels' activity and reducing neuronal excitability (124,129). Another important factor in PIPN is the transient receptor potential (TRP) family; among them, TRPV1 mediates thermal hyperalgesia. In animal models, TRPV1 antagonists like ruthenium red have mitigated this symptom (130). In the case of TRPA1 and TRPM8, it is still debated whether (or not) these were their roles since their inhibition has been associated with increased cold and mechanical hypersensitivity (131). Notably, TRP channel activity has also been assayed in human DRG neurons, underlining its clinical relevance (132).

1.12.5 Current treatments for PIPN

Despite the emergence of promising tools to screen and diagnose of PIPN, the absence of standard assessments as well as effective preventive interventions and therapeutic agents is a critical barrier (133) These pharmacological treatments are limited, and non-pharmaceutical approaches, such as exercise, have been successfully employed to

manage cancer-related symptomatic conditions recurring in clinical populations, including those related to thermal sensitivity, numbness, and tingling (134). Regarding the pharmaceutical options, there is insufficient effectiveness in available drugs for PIPN prevention or treatment. Thus far, biological targets have proven to be promising when tested in vivo in animal models (135), but many of these preclinical findings have failed to translate to successful clinical trials. Most initial studies underpowered meta-analyses or non-randomized, highlighting the need for better structured clinical trials to accurately assess drug efficacy (135). Vitamin E, an antioxidant that exhibited neuroprotective effects (136) in small trials, failed a later double-blind, placebo-controlled trial showing significant prevention in patients treated with platinum- or taxane-based agents (137). Likewise, in a clinical trial acetyl-L-carnitine (ALC), which demonstrated beneficial effects in animal models did not prevent taxane-induced neuropathy and worsened symptoms in some patients (138). In clinical trials PIPN symptoms were not substantially alleviated by drugs that effectively treat diabetic neuropathy (139), such as gabapentin and lamotrigine. Indeed, rest and topical medications such as ketamine and amitriptyline did not reduce pain levels in established PIPN (140). The only drug with modest activity in a randomized, double-blind, placebo-controlled crossover trial was the serotonin and norepinephrine reuptake inhibitor (133). Its effectiveness, most notably, was affected by the type of chemotherapy agent used.

In the end, PIPN is still not managed well, as results are poorly reported and there are no effective treatments (133). In view of the unsatisfactory patient responses to existing therapies, this often necessitates dose reduction or total discontinuation of chemotherapy, with possibly detrimental effects on the management of malignant disease. A more comprehensive understanding of the underlying mechanisms of this relatively under-researched condition is paramount to the development of effective therapies to prevent/manage PIPN, ensuring that patients may be provided with adequate symptom relief and not hinder their cancer treatment in the process.

1.12.6 Animal model and in vitro model of PIPN

The mechanisms involved in the development and persistence of PIPN are investigated actively by researchers in animal models. These models are useful for understanding underlying mechanisms and testing possible therapies. Several classes of

chemotherapeutics have been studied in animals and have been shown to reproduce a pain-like phenotype that is similar to what has been reported in patients, such as taxanes, platinum agents and proteasome inhibitors (141).

In order to create a useful model, it is important to replicate patient symptoms along with quantifiable endpoints, such as structural, electrical, or behavioral changes.

Researchers translate human doses into clinically relevant doses using body surface area and weight-based calculations (142). Research findings suggest that regimens of paclitaxel at low doses, such as 2 mg/kg at alternating days (cumulative 8 mg/kg), induce sustained mechanical hypersensitivity (a key feature of PIPN), with the absence of severe adverse events, like loss of body mass or alopecia (143). This dosing schedule also reduces severe motor incoordination and heat hypersensitivity.

Researchers are expanding upon current data to determine optimal dosing regimens and a better grasp of the mechanistic pathways behind PIPN to design targeted countermeasures for the prevention or attenuation of chemotherapy-induced neuropathy without compromising anti-cancer efficacy.

In contrast, in vitro models based on animal-derived cells have been extensively used for studying paclitaxel neuropathy, enabling investigation in controlled environments devoid of inter-organ influences found in whole organisms. In particular, cultures of rodent dorsal root ganglion (DRG) neurons have proven useful in studying paclitaxel-induced axonal degeneration, mitochondrial dysfunction, and altered ion channel activity (129). These models facilitate rigorous control over drug concentrations and time-course experiments, permitting examination of dose-dependent impacts on neuron viability and function. Furthermore, co-culture systems involving Schwann and glial cells can help to clarify the role of non-neuronal compartments in PIPN (144).

1.13 Sex dimorphism in CIPN

In recent years, interest in how pain differs between sexes has increased considerably. A large body of research suggests that pain perception is not the same in men and women, with women generally exhibiting heightened sensitivity to pain and a greater likelihood of developing chronic pain disorders (145). Variations in responses to both pharmacological and non-pharmacological pain treatments have been noted, although

these differences are inconsistent and seem to depend on the type of treatment and the specifics of the pain and provider. The exact mechanisms behind these sex differences remain unclear but are likely due to a combination of biological and psychosocial factors (146). Emerging evidence points to the roles of genotype and endogenous hormones, particularly sex hormones, in these differences, though the precise influence of sex hormones on pain requires more investigation. Psychosocial factors like pain perception and stress exposure may also contribute to sex disparities in pain experiences. Population studies consistently show that women report pain more frequently than men. Large-scale epidemiological research across different regions supports this finding (147). More research is needed to understand these mechanisms better and to develop sex-specific treatments. In the context of the CIPN model, there is evidence of sex differences in pathophysiology. Cabañero et al., conducted a bibliographic review of clinical and preclinical studies, revealing more severe peripheral neuropathy symptoms in women (**Table 3**-(148)). However, due to the varied chemotherapeutic regimens, information on individual drugs is limited. A recent study by Mizrahi et al. found higher neuropathic scores in women in a cohort of 333 patients treated with paclitaxel and/or oxaliplatin (149). Furthermore, pharmacology to treat PIPN was adapted to the patients taking into account the sex with promising results. Additionally, pharmacological treatments for PIPN have been tailored to patients' sex with promising outcomes.

Using an in vitro model of rat CIPN, Villalba et al. discovered higher sensitivity and lower rheobase in female DRG neurons. They also found increased TRPM8 currents in female rats (150). Moreover, paclitaxel treatment may activate the IL23/IL-17A/TRPV1 axis exclusively in female mice, with sex hormone differences being a key mechanism in the sexual dimorphism observed in chronic pain (151). As demonstrated by Luo et al. (2019), sex differences significantly influence the modulation of immune toll-like receptors (TLR) signaling, particularly through the modulation of transient receptor potential (TRP) channels (152). For example, they found that using a TLR9 antagonist effectively reduced mechanical pain induced by paclitaxel treatment in male mice but not in female mice. This reduction was linked to the enhancement of functionality in the transient receptor potential vanilloid 1 (TRPV1) channel. Further emphasizing the sex-specific nature of

immune response modulation, Forsyth et al. (2024) observed that TLR4 mediated inflammatory and neuropathic pain responses in male mice but not in female mice (153). Beyond the involvement of TRP channels, various physiological differences contribute to sex disparities in pain perception and drug response. For instance, females generally exhibit increased epidermal nerve fiber density compared to males, as noted in studies by Gøransson et al. (2004) (154). In addition to these physiological differences, variations in drug pharmacokinetics also play a role in sex-specific responses to pain treatment. Understanding these multifaceted factors is crucial for developing tailored pain management strategies that consider sex differences and optimize therapeutic outcomes. Findings from in vitro studies can inform subsequent in vivo experiments and clinical trials. Understanding the cellular mechanisms underlying sex-specific responses can guide the design and interpretation of preclinical and clinical studies, ultimately improving translation to patient care. The evidence of sex differences in pain sensation and development led us to investigate the potential sex dimorphism in our in vitro PIPN mouse model, advancing our understanding of this condition and highlighting the importance of developing more effective and personalized treatments for patients.

Chemothera-peutic Drug	Potential thermoTRPs Involved	Sex differences observed	Reference
Taxanes			
Paclitaxel	TRPV1 TRPM8 TRPV4 TRPA1	Reduced rheobase, higher sensitivity in female rat DRG neurons exposed to paclitaxel	(150)
		Cold allodynia more robust in female mice	(155)
		Greater magnitude of paclitaxel hyperalgesia in female rats	(156)
		Higher TRPM8 expression in male rat DRG neurons	(150)
		Mechanical pain produced through estrogen dependent IL-23/IL-13/TRPV1 signaling axis only in female mice	(151)
		No significant sex difference in the response to mechanical stimuli for male and female rats	(157)
Docetaxel	TRPV1	Not investigated alone	
Platinum-based compounds			
Oxaliplatin	TRPV1, TRPM8, TRPA1	Reduction in nerve conduction amplitude in female mice	(158)
Cisplatin	TRPV1 TRPV2 TRPA1 TRPM8	Tendency in women with advanced non-small cell lung cancer to have more neurosensory deficits than men (clinical trials)	(159)
		More persistent tactile allodynia in male than in female mice	(160)
		Bigger incidence of prolonged heat latency in male rats	(161)
Carboplatin	TRPA1	Not investigated alone	
Vinca-alkaloids			
Vincristine	TRPV1 TRPV4	Mechanical hyperalgesia was higher in female than in male rats	(162)
		Statistically significant reduced mechanical sensitivity threshold only in male rats	(163)
Proteasome inhibitor			
Bortezomib	TRPA1 TRPV1	The prevalence of peripheral neuropathy was nearly double in women treated with bortezomib (65.3%) compared to men (36%) (retrospective study using clinical data)	(164)
		Significant lower threshold of mechanical sensitivity at day 30 in female but not in male Sprague-Dawley rats	(163)
		S1PR1 antagonists prevented bortezomib mechano-allodynia and mechano-hyperalgesia in male but not in female rats	(165)
		Male sex was a predictor of bortezomib-induced CIPN development (retrospective analysis using clinical data)	(166)
Alkylating agents			
Ifosfamide	TRPA1?	Higher neurotoxicity in females	(167)

Antibody-Drug Conjugates (ADC)			
Brentuximab-vedotin Enfortumab-vedotin	Not investigated	Not disclosed, but likely similar to vincristine as auristatin E as both share a similar inhibitory mechanism	
Bevacizumab	Not investigated	More abdominal pain in females than males with advanced-stage non-small cell lung cancer (clinical trials)	(168)
Hormonal therapies: Aromatase inhibitors			
Anastrozole	TRPA1	Not studied in male (breast cancer)	
Immunomodulatory drugs			
Thalidomide	TRPA1 TRPV4	Not investigated	
Antimetabolites			
5-Fluorouracil (Capecitabine)	Not investigated	Female patients with advanced colorectal cancer had significantly higher risk for hand-foot syndrome (clinical trials)	(169)
Epothilones			
Ixabepilone	Not investigated	Not studied in male, only in female	
Combination therapies			
leucovorin + fluorouracil + oxaliplatin (FOLFOX)	Not investigated	Higher incidence of peripheral neuropathy and hand-foot syndrome in female patients with colorectal cancer (clinical trials) (Wagner et al., 2021)	(170)
Combined (not mentioned)	Not investigated	Increased I-III grade neurological toxicities in female patients (clinical trials database, $N = 23256$ patients)	(171)
Combined	Not investigated	Female sex associated with higher neuropathy sum score after treatment of Hogkin's lymphoma (clinical trials)	(172)
Combined (ECF, ECX, EOF or EOX)	Not investigated	Males showed higher incidence of all-grade peripheral neuropathy in oesophagogastric cancer	(173)
FOLFOX/ bevacizumab	Not investigated	No differences for grade ≥ 3 sensory neuropathy in patients with unresectable advanced or recurrent metastatic colorectal cancer	(174)
Paclitaxel and/or Oxaliplatin	Not disclosed, but likely TRPV1, TRPA1 and TRPM8	Female associated with higher neuropathy score (cohort study of 333 patients)	(149)

Table 3. Sex differences found in CIPN pain symptoms after treatment with different chemotherapeutic agents in diverse clinical and/or pre-clinical studies. Taken from https://doi.org/10.1016/j.pharmthera.2022.108297 (148)**.** E: Epirubicin; C: Cisplatin; F: Fluorouracil; X: Capecitabine; O: Oxaliplatin. L: Leucovorin.

1.14 Modulation of TRP ion channels in pain treatments

Transient receptor potential (TRP) channels form a broad group of ion channels essential for sensory processing, particularly in the context of pain. Due to their involvement in multiple pain-related pathways, they are being explored as promising therapeutic targets for managing various painful conditions. The wide range of biological roles and regulatory controls governing TRP channels contributes to their involvement in both inherited and acquired channelopathies (175). Modulating the activity of specific TRP channels offers potential relief in several disorders (176). Ongoing research and drug development efforts have increasingly focused on TRP channels, driven by advances in understanding their structure and function. While initial studies emphasized pain management, recent progress has broadened their therapeutic potential to include areas such as respiratory diseases, neurological and psychiatric disorders, metabolic conditions like diabetes, and cancer (177,178).

In pain disorders, such as PIPN, several TRP channels are targeted due to their involvement in sensory signaling and pain perception, in particular TRPV1, TRPM8 and TRPA1 (175). In this context, targeting TRPV1 with antagonists or modulators may offer a potential strategy for alleviating chemotherapy-induced neuropathic pain. However, clinical translation of TRPV1 antagonists for pain management has faced challenges due to off-target effects and lack of efficacy in some cases (179). While TRPM8 has not been as extensively studied in the context of CIPN compared to TRPV1, its involvement in sensory signaling suggests a potential role in neuropathic pain modulation. Modulating TRPM8 activity with agonists or antagonists may influence cold-induced neuropathic pain associated with certain chemotherapeutic agents (180). Finally, targeting TRPA1 with antagonists may represent a therapeutic approach for alleviating neuropathic pain associated with chemotherapy (64). While treatments targeting TRPM8 and TRPV1 channels for pain relief in CIPN are in preclinical and clinical development stages, there are currently no TRPA1-specific clinical studies for pain relief in CIPN, although research into targeting TRPA1 channels for pain management is ongoing and shows promise.

1.14.1 TRPV1 based pain-treatments

TRPV1 agonist, capsaicin, is a natural compound found in chili peppers that has been

widely used for pain relief. In neuropathic pain, it is commonly used in topical formulations, such as creams, gels, and patch. These formulations are applied directly to the affected area to provide localized pain relief. Beyond capsaicin, numerous other vanilloids have been identified as activators of the TRPV1 channel. Resiniferatoxin (RTX), a diterpene phorbol ester akin to capsaicin, is a potent analogue found in the Euphorbia resinifera cactus, noted for its heightened irritant potency (181). Additionally, several chemical compounds activate TRPV1, including 4-(thiophen-2-yl) butanoic acid, camphor, 2-aminoethoxydiphenyl borate (2-APB), and hydroxyl alpha sanshool, the active component of Sichuan pepper (182). Compounds in garlic and onion, particularly allicin, can activate TRPV1 channels. Similarly, zingerone from ginger, piperine from black pepper, and other related molecules have shown the ability to stimulate TRPV1 (183). Although a wide range of substances can act as TRPV1 agonists, capsaicin is still the most widely used for therapeutic pain management. The mechanism is based on prolonged TRPV1 activation (> 60 min) that induces significant alterations in membrane potential, reducing neuronal excitability, impairing neurotrophic factor production (e.g., Substance P), and leading to the retraction of epidermal and dermal nerve fiber terminals (184). Capsaicin is a useful agent to reduce pain but side effects, such as the initial pungency, irritation, and variable efficacy observed in some clinical trials have prompted exploration into TRPV1 antagonists (185). Pharmaceutical companies endeavor to develop TRPV1 antagonists capable of treating pathological pain while mitigating the adverse effects associated with TRPV1 agonists.

Emerging research suggests a profound interplay between the endovanilloid (EV) and endocannabinoid (EC) systems, giving rise to the concept of a unified system governed by a shared repertoire of endogenous ligands and regulatory mechanisms (186). This EV/EC system encompasses key components such as the ion channel TRPV1, the G protein-coupled receptors CB1 and CB2, their endogenous ligands, and the enzymes responsible for biosynthesis and inactivation (187). Pathological conditions involving disruptions in EV/EC interactions span inflammation, pain, neurodegenerative disorders, and ailments affecting bones and skin (188,189). The Passerini reaction was employed in a diversity-oriented strategy to synthesize a series of α-acyloxycarboxamides featuring diverse structural motifs at both the head and tail ends (190). These compounds were

systematically screened for their activity on TRPV1, CB1, and CB2 receptors, along with assessments of their metabolic stability in skin cells, microsomes, and plasma. This comprehensive protocol enabled the identification of compounds exhibiting varied activity profiles on TRPV1, CB1, and CB2 receptors, as well as diverse metabolic stability patterns. Notably, compared to natural mediators, these agents display improved drug-like properties. Compound **41** was signalled as an agonist with balanced activity on both TRPV1 and CB2 receptors. Compound **41** exhibited high selectivity over TRPM8, TRPA1, and CB1 receptors, coupled with favorable in vitro metabolic stability, synthetic accessibility, and low promiscuity. This discovery underscores the potential of compound **41** as a promising candidate for further exploration in the modulation of the EV/EC system and its therapeutic implications (191).

The other class of TRPV1 based pain-treatments are the antagonists, starting with the discovery of capsazepine, initially proclaimed for their potential to selectively block TRPV1 channels activated by chemical stimuli (192). However, subsequent investigations revealed an unexpected broad-spectrum effect, as capsazepine also inhibited the cold-activated TRPM8 channel, voltage-activated calcium channels, and nicotinic acetylcholine receptors (193). Despite their promise, competitive TRPV1 antagonists faced setbacks due to significant side effects, including hyperthermia and impaired sensitivity to noxious heat in humans, leading to their withdrawal from clinical trials (194). The mechanisms underlying these adverse effects remain unclear, but probably the high-affinity, and almost irreversible competitive mechanism of designed antagonists may be implicated. Interestingly, compounds that specifically prevented TRPV1 activation by capsaicin, but not by changes in pH or temperature, did not elicit the same hyperthermic response. However, the exact relationship between these conditions requires further elucidation.

Subsequently, researchers pursued alternative strategies to develop TRPV1 inhibitors with improved safety profiles. Three key approaches emerged in TRPV1 pharmacology:

- Allosteric Modulation: Researchers have focused on the TRP domain- a key region involved in channel gating- as a target for novel therapeutics. This led to the creation of TRPducins, a class of short peptides that mimic sequences from the N-terminal portion of the TRP domain. These peptides specifically inhibit TRPV1 activity by binding to intracellular interaction sites (195)

- Inhibition of TRPV1 Overexpression: Another approach uses peptides such as DD04107, modeled after the SNAP25 protein, to interfere with the inflammatory recruitment of TRPV1 to the cell surface by blocking its membrane insertion. These compounds show strong and lasting pain-relieving effects in preclinical models of neuropathic and inflammatory pain and are currently in Phase II clinical testing (196).
- Non-Competitive Antagonists: A different tactic involves designing TRPV1 blockers that act in a state-dependent manner, targeting the receptor only when it is activated or bound to an agonist (197,198).

Nikolaeva and colleagues recently identified **AG1529**, a TRPV1 antagonist capable of competitively inhibiting capsaicin-triggered activation of human TRPV1 with micromolar effectiveness (199). While it moderately influenced acid-induced activation, it did not impact responses driven by voltage or temperature. **AG1529** showed limited selectivity, slightly affecting human TRPA1 and TRPM8 channels(199). In cultured rat dorsal root ganglion (DRG) neurons, **AG1529** significantly suppressed neuronal activity triggered by capsaicin. Its effectiveness was reduced when tested against acid-induced TRPV1 activation and TRPA1-driven nociceptive responses. Additionally, **AG1529** completely prevented TRPV1 sensitization caused by histamine and inflammatory mediators in DRG cultures. When applied to the skin in either an acetone solution or a water-free ointment, **AG1529** reduced histamine-induced itch in rodents in a dose-dependent fashion. These preclinical findings clarify how **AG1529** interacts with TRPV1 channels and reinforce its potential as a capsaicinoid-derived soft drug for topical treatment of itch and inflammation, however, it exhibited poor stability in water and underwent hydrolysis when free or encapsulated in liposomes. This chemical instability prevented us from using a traditional water-based encapsulation system. Consequently, we developed a stable **AG1529** derivative suitable for encapsulation for a delivery system (**AB9**). The difference in stability between the hard drug (**AB9**) and the soft drug (**AG1529**) in water can be attributed to their chemical properties and molecular structures. In general, the term "hard drug" is used to describe a compound that is more chemically and metabolically stable and less prone to degradation or hydrolysis in various environments, including water.

For this reason, we investigated the compound **AB9**, the hard drug of **AG1529**, conducting pharmacological experiments to ensure that the efficacy, potency, and selectivity of the hard derivative was similar to the original parental soft drug. Thereafter, we aimed to PEGylate the compound. PEGylation has been used as a delivery vehicle for various drugs and compounds due to its biocompatibility and ability to improve the pharmacokinetic properties of the encapsulated substances (200). It can help enhance the targeted delivery of **AB9**, potentially reducing systemic side effects and increasing its efficiency in a pain relief model.

1.14.2 TRPM8 based pain-treatments

TRPM8 channel is involved in pain treatment in different pathologies. TRPM8 agonists have gained attention in pain treatment due to their potential to activate the channel, which is involved in the sensation of cold and plays a role in pain modulation (180). By activating TRPM8, these agonists can induce a cooling sensation and attenuate pain signals, offering a novel approach to pain management. Some TRPM8 agonists that have been investigated for their analgesic properties include menthol, that is a well-known TRPM8 agonist found naturally in plants such as mint. It is commonly used in topical analgesic formulations due to its cooling effect, which can provide relief from pain associated with conditions like arthritis, muscle strains, and neuropathy. Furthermore, cooling agents, such as icilin and WS-12, have been identified as potent TRPM8 agonists (201–203). These compounds activate TRPM8 channels, leading to a sensation of cold and providing relief from pain. Icilin, in particular, has been studied for its potential use in topical analgesic formulations. Another commonly used TRPM8 agonist is the eucalyptol, also known as 1,8-cineole, a natural compound found in eucalyptus plants. It has been shown to activate TRPM8 channels, resulting in a cooling sensation. Eucalyptol-based formulations have been explored for their analgesic properties, particularly in the management of musculoskeletal pain (204,205). Finally, L-menthol synthetic derivatives have been developed to enhance its TRPM8 agonist activity and improve its therapeutic efficacy. These derivatives exhibit potent analgesic effects and may have potential applications in pain management. Like TRPV1, menthol-based gels and patches, are available commercially for the relief of various types of pain, including muscle aches, joint

pain, and neuropathic pain. These products provide localized cooling effects, which can help alleviate pain and discomfort. Overall, TRPM8 agonists represent a promising class of compounds for pain treatment, particularly for conditions where cooling-based analgesia is beneficial (206). Further research is needed to explore their full therapeutic potential and optimize their use in clinical practice.

The versatile involvement of TRPM8 in various physiological and pathological processes positions this channel as a promising therapeutic target. Particularly, the development of TRPM8 antagonists has garnered significant interest (207). Several compounds have been identified in this regard. For instance, capsazepine, the potent TRPV1 antagonist, also exhibits non-specific TRPM8 blocking properties, effectively attenuating cold allodynia induced by CCI (chronic constriction injury) (192). Similarly, (S)-1-phenylethyl (2-aminoethyl)(4-(benzyloxy)-3-methoxybenzyl)carbamate (PBMC), a novel TRPM8 antagonist, demonstrates efficacy in alleviating CCI-induced cold allodynia (208). However, akin to TRPV1 antagonists, critical side effects have been reported with TRPM8 antagonists. PBMC was found to induce a reduction in core body temperature of more than two degrees in mice. Additionally, many current TRPM8 antagonists exhibit activity on other ion channels, complicating their selectivity and introducing potential side effects. Capsazepine, despite its efficacy in treating cold allodynia, also affects voltage-gated calcium channels, nicotinic acetylcholine receptors, and TRPV1. Similarly, compounds like 4-(3-chloro-2-pyridinyl)-N-[4-(1,1-dimethylethyl)phenyl]-1-piperazinecarboxamide (BCTC) and clotrimazole, while inhibiting TRPM8, also activate TRPA1, leading to undesirable side effects such as irritation and burning (209). Moreover, SKF96365, a non-specific blocker of various calcium channels, receptor-operated channels, and inwardly rectifying potassium channels, exhibits inhibitory effects on TRPM8 in vitro (210). The lack of selectivity and side effects associated with existing TRPM8 antagonists not only limit their therapeutic utility but also hinder their use in investigating TRPM8 as a therapeutic target. Despite the challenges encountered in the search for TRPM8 antagonists, the significance of this ion channel as a therapeutic target remains undisputed. Consequently, the focus has shifted towards developing more selective antagonists using diverse modulation strategies for TRPM8. High-throughput screening assays of chemical libraries followed by structure-activity relationship studies have been conducted to identify

promising candidates. Furthermore, efforts have been directed towards enhancing the design of TRPM8 antagonist candidates based on the obtained knowledge. Additionally, understanding the mechanisms of action of TRPM8 antagonists is crucial for their development. Limited information exists regarding their mechanism of action, with only a few papers suggesting two main binding regions for antagonists. Competitive TRPM8 antagonists like SKF96365 bind to the Y745 region between S2 and S3 domains of one subunit, inhibiting conformational changes necessary for channel activation (210). An additional modulatory site involving segments S1 through S4, along with certain amino acids within the TRP domain, has been suggested to influence TRPM8 function—potentially through a mechanism of negative allosteric regulation. Continued research in this area is crucial to support the strategic development of antagonists aimed at minimizing common adverse effects.

OBJECTIVES

2. OBJECTIVES

The current doctoral dissertation aims to explore the molecular mechanisms involved in the sensitization and desensitization of nociceptors following 2-cycle exposure (24h each) to the chemotherapeutic agent paclitaxel. It also investigates the influence of sexual dimorphism and characterized novel modulators of TRP channels that may assist in attenuating CIPN.

To address this goal, the specific objectives are:

- To investigate the molecular and functional changes provoked by 2 cycles of paclitaxel on nociceptors using an in vitro preclinical model of chemotherapy-induced peripheral neuropathy.
- Evaluate the effect of paclitaxel on nociceptors excitability, and action potential waveform.
- Examine the peripheral impact of paclitaxel on nociceptor axons over a 10-day in vitro duration.
- Determine the effect of paclitaxel on the function and expression of TRP and Na_v genes.
- Design and test TRP modulators on attenuating neuropathic symptoms.

RESULTS

3. RESULTS

3.1 CHAPTER 1: Development of an in vitro preclinical model to study chemotherapy-induced peripheral neuropathy pathogenic mechanisms: the role of Na_V and TRP channels.

The results of the PIPN model are currently under review by the *FEBS Journal*.

Unpublished results from paper 1:

- Lamberti A, Fernández-Carvajal A, Ferrer Montiel A.

Paclitaxel-induced peripheral neuropathy in vitro model

In order to investigate the mechanisms of paclitaxel-induced peripheral neuropathy (PIPN), many preclinical models have been established, such as primary cultures of dorsal root ganglion (DRG) neurons. They have shown how these models form an effective platform to understand the precise acute and chronic effects of paclitaxel on nociceptors with alterations in neuronal excitability and pathways that signal pain perception (211–213). To investigate the time course of paclitaxel-induced excitability changes and potential sex differences in neuropathic responsiveness, we analyzed IB4(-) and IB4(+) neuronal subpopulations from both male and female adult mice. Using a long-term (15 days in vitro) primary culture of mouse DRG neurons, we examined the direct impact of two consecutive paclitaxel administrations on neural excitability, TRP channel activity and expression, and axonal effects post-treatment. These doses, administered at different intervals, mimic the cyclical nature of chemotherapy. Neuron activity was assessed at 0, 48, and 96 hours following each administration (PTX-1 or PTX-2) to capture the evolving effects of paclitaxel over time. This approach allowed us to elucidate the time course of excitability changes and explore sex-related differences in neuropathic responses.

a. Consecutive administrations of Paclitaxel led to a heightened neuronal excitability in DRG sensory neurons.

Villalba et al. demonstrated that Paclitaxel significantly elevated the spontaneous activity

of rat sensory neurons displaying spontaneous activity (SA), reaching a peak increase of 2.4-fold at 48 hours post-treatment before returning to nearly baseline levels by 96 hours (150). To mimic the clinical scenario of cancer patients undergoing multiple cycles of chemotherapy, we extracted DRG sensory neurons from adult mice, employing an experimental paradigm involving two consecutive administrations of 1μM Paclitaxel, at day 5 in vitro (DIV5) and day 10 in vitro (DIV10), for 24h each (**Fig.9A**). Spontaneous activity was evaluated at 0h, 24h and 96h post PTX treatments for PTX-1 or PTX-2. Sensory neurons treated with Paclitaxel showed an increase in excitability with the first administration of paclitaxel, reaching a massive spontaneous activity 48h after the second treatment (**Fig.9B**). Furthermore, the percentage of sensory neurons exhibiting spontaneous activity was evaluated overtime, resulting in a significant increase after the first treatment nearly returning to baseline levels at 96 hours (**Fig.9C**). Notably, IB4(-) neurons displayed a much higher level of spontaneous activity compared to IB4(+) neurons, indicating a differential response to treatment between these two subpopulations. The consecutive second administration of paclitaxel (PTX-2) induced a substantial increase in the percentage of spontaneous activity with no recovery at 96h. Spontaneous activity frequency (Hz) is significantly augmented in IB4(-) neurons with the second treatment (**Fig.9D**), leading to a significant increase of resting membrane potential (mV) in both treatments (**Fig.9E**). Taking together, these results showed that the excitability of neurons becomes more pronounced with increased exposure to paclitaxel, especially in IB4(-) neurons, without affecting the capacitance (pF) of the cells (**Fig.9F**). Due to their distinct receptor profiles and molecular composition, IB4(+) neurons exhibit reduced sensitivity to paclitaxel-induced alterations in excitability compared to other sensory neuron subtypes.

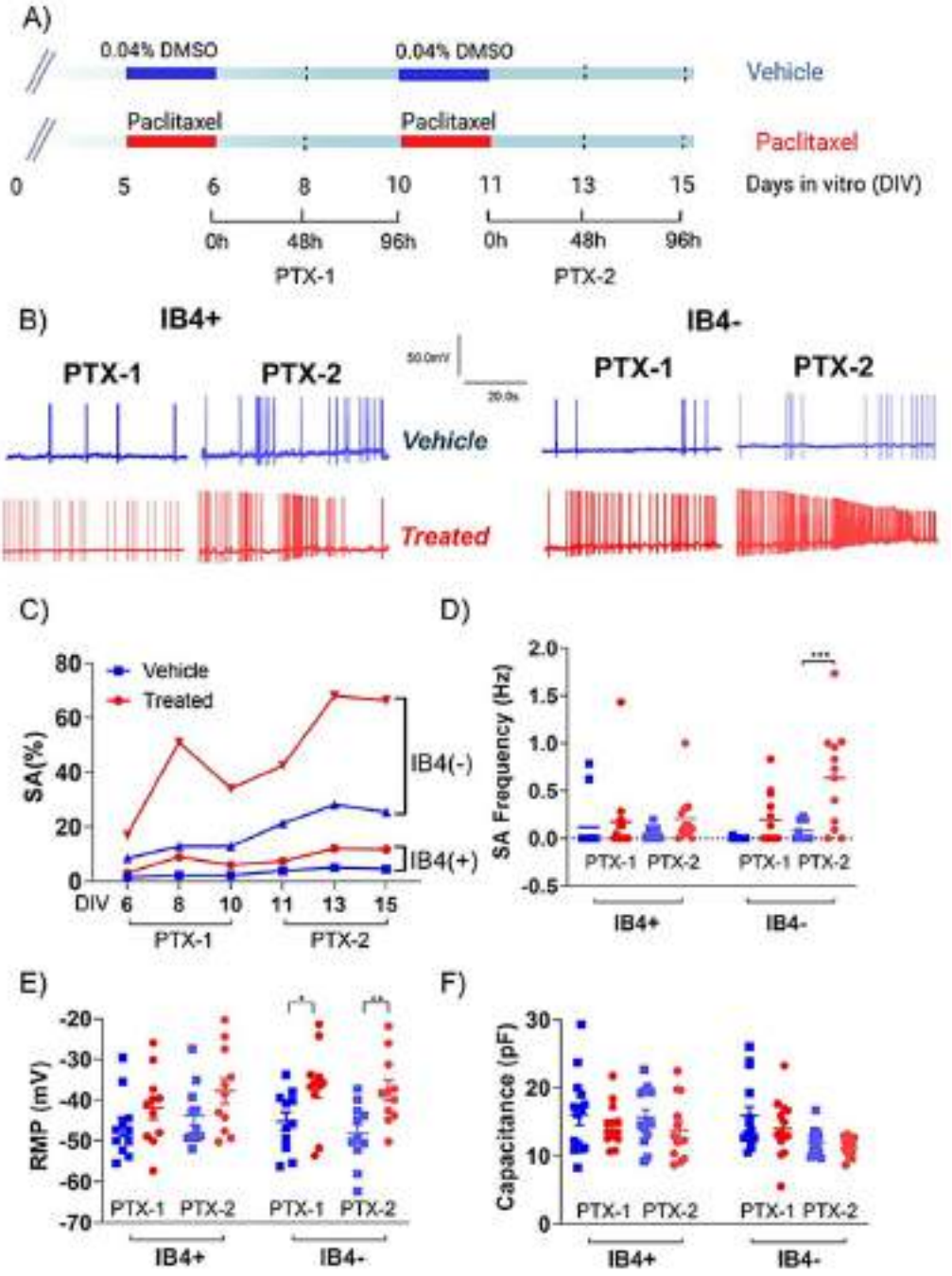

Figure 9. Administration of paclitaxel increases electrical activity in IB4(+) and IB4(-) nociceptors. A) Experimental design for investigating the effect of paclitaxel on DRG neuron activity. B) Representative recordings of the spontaneous activity after vehicle (top) or paclitaxel (bottom) treatment at 48h post-first treatment (PTX-1) or 48h post-second treatment (PTX-2). C) Percentage of DRG neurons exhibiting spontaneous activity (SA) at 0, 48 and 96 h after vehicle or paclitaxel treatments for IB4(+) and IB4(-). Data are given as percentage with N = 6, n = 10-15. D) Frequency of spontaneous AP firing in 60s recordings. Spontaneous activity was almost not detected in IB4(-) neurons treated with vehicle at DIV8. E) Resting membrane potential (RMP) in mV for IB4(-) and IB4(+) neurons at 48h after vehicle or paclitaxel treatments. F) Capacitance of the cells in vehicle and paclitaxel groups for IB4(-) and IB4(+). Results are shown as individual values with means ± SD. *P < 0.05, Fisher's exact test (C), unpaired t test (D, E and F).

b. Two consecutive treatments of Paclitaxel led to alterations in the electrical properties of both IB4(+) and IB4(-) action potentials.

To deep the investigation of the effects of two consecutive administrations of paclitaxel on DRG sensory neurons, we investigate its effects on the electrical properties of IB4(+) and IB4(-) action potentials. Paclitaxel-induced changes in IB4(+) neurons (**Fig 10A; Table 4**) included a significant reduction of the AHP amplitude by ≈ 5 mV at 48h post both treatments, as illustrated in **Figure 10B**. However, other action potential (AP) properties such as tpeak, threshold potential (Vth), overshoot, amplitude, and maximum upstroke slope remained unaltered following paclitaxel treatment (**Figure 10C-D-E**). It is important to note that while IB4(+) neurons represent a relatively homogenous group of non-peptidergic nociceptors, the IB4(−) population is more heterogeneous. This group includes various subtypes of peptidergic nociceptors, low-threshold mechanoreceptors, and other sensory neuron types, each with distinct electrophysiological profiles. Therefore, the observed responses in IB4(−) neurons may reflect an averaged effect across multiple subtypes. Similarly, in IB4(-) neurons (**Fig.11A; Table 5**), paclitaxel administration resulted in a significant depolarization of the AHP amplitude by 5 mV, as shown in **Figure 11B**. Also, no statistically significant differences were observed in other parameters such as tpeak, Vth, overshoot amplitude, and maximum upstroke slope after the first treatment (**11C-D-E**). However, the second administration of paclitaxel leads to a significant decrease in action potential parameters, such as Vth, tpeak, and tr (recovery time) (**Fig.11B-C**). Consequently, the increased electrical excitability observed in paclitaxel-treated IB4(−) and IB4(+) neurons is primarily attributed to a smaller AHP. Additionally, in IB4(−) neurons, faster repolarization and AHP recovery also contribute to this heightened excitability. These findings shed light on the specific effects of paclitaxel on the electrical properties of IB4(−) neurons, highlighting the importance of considering neuron subtype specificity in understanding the effects of chemotherapeutic agents on neuronal function.

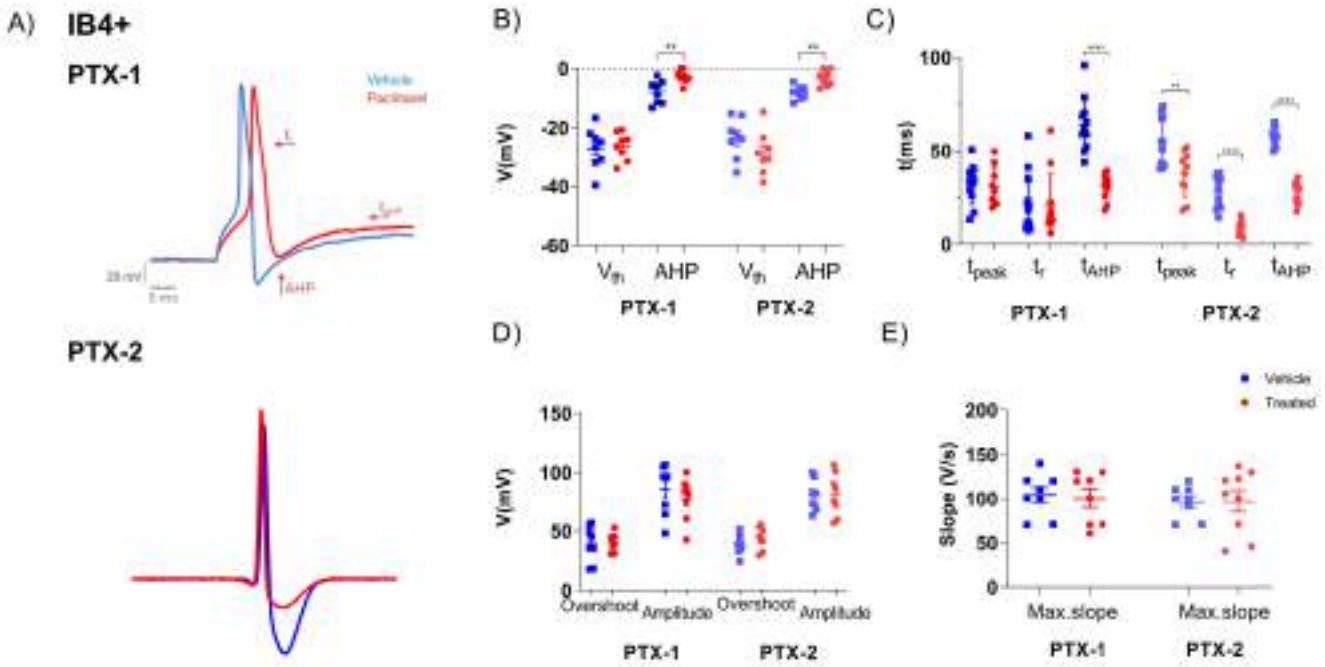

Figure 10. Paclitaxel influenced the action potential characteristics IB4(+) neurons. A) Representative action potentials (APs) of IB4(+) neurons exposed to either vehicle or paclitaxel, at 48h post-first treatment (PTX-1) and at 48h post-second treatment (PTX-2). Arrows indicate the parameters where significant statistical differences were observed, including repolarization time (tr), afterhyperpolarization (AHP) amplitude, and the duration of the half afterhyperpolarization (tAHP). APs were induced using 10 ms current pulses ranging from 0 to 300 pA and were analyzed at the current threshold. B) Action potential threshold (V_{th}) and AHP amplitude. C) Parameters for time to peak (tpeak), time to recovery (tr), and time to afterhyperpolarization (tAHP). D) Overshoot and amplitude measurements. E) The maximum upstroke slope (max. slope). Data were collected 48 hours post-treatments and are presented as mean ± SD. Sample sizes were N = 8, n = 9-14. ****P≤0.0001; ***P≤0.0001; **P≤0.005; *P≤0.01. Statistical tests used include unpaired t-test or Mann–Whitney test.

	PTX-1		PTX-2	
	Vehicle	Paclitaxel	Vehicle	Paclitaxel
Vth (mV)	−27.03 ± 2.49	−26.33 ± 1.68	−23.57 ± 2.43	−28.48 ± 2.60
AHP (mV)	−7.90 ± 1.37	−2.77 ± 0.78	−8.76 ± 1.15	−3.63 ± 1.01
T_{peak} (ms)	31.85 ± 3.19	30.70 ± 3.51	55.17 ± 3.96	37.36 ± 3.82
T_r (ms)	17.88 ± 3.35	20.91 ± 4.96	27.89 ± 2.60	8.45 ± 1.17
T_{AHP} (ms)	64.04 ± 4.37	30.45 ± 1.61	57.93 ± 1.57	27.11 ± 1.22
Overshoot (mV)	39.13 ± 5.38	40.66 ± 2.69	38.43 ± 2.88	43.07 ± 3.38
Amplitude (mV)	85.59 ± 7.55	77.76 ± 6.48	83.48 ± 3.82	80.32 ± 5.78
Max Slope (V/s)	107.13 ± 8.11	100.02 ± 8.97	99.84 ± 5.71	97.92 ± 10.87

Table 4. Action potential parameters for IB4(+).

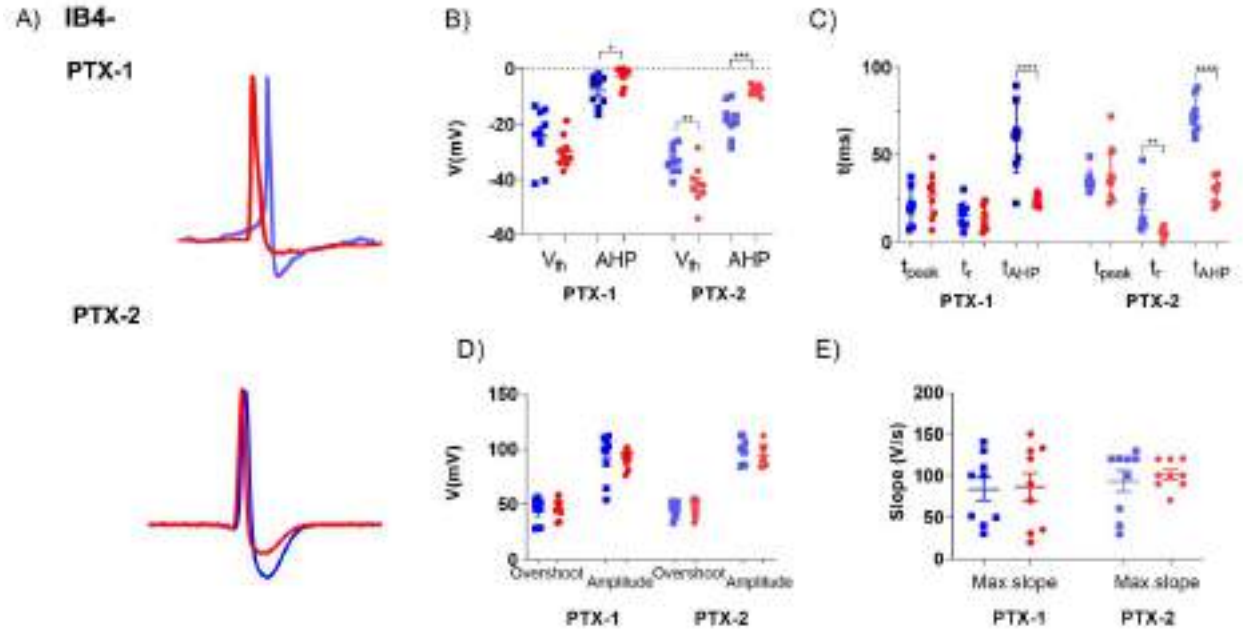

Figure 11. Paclitaxel influenced the action potential characteristics IB4(-) neurons. A) Representative action potentials (APs) of IB4(-) neurons exposed to either vehicle or paclitaxel, at 48h post-first treatment (PTX-1) and at 48h post-second treatment (PTX-2). Arrows indicate the parameters where significant statistical differences were observed, including repolarization time (tr), afterhyperpolarization (AHP) amplitude, and the duration of the half afterhyperpolarization (tAHP). APs were induced using 10 ms current pulses ranging from 0 to 300 pA and were analyzed at the current threshold. B) Action potential threshold (V_{th}) and AHP amplitude. C) Parameters for time to peak (tpeak), time to recovery (tr), and time to afterhyperpolarization (tAHP). D) Overshoot and amplitude measurements. E) The maximum upstroke slope (max. slope). Data were collected 48 hours post-treatments and are presented as mean ± SD. Sample sizes were N = 8, n = 9-14. ****P≤0.0001; ***P≤0.0001; **P≤0.005; *P≤0.01. Statistical tests used include unpaired t-test or Mann–Whitney test.

	PTX-1		PTX-2	
	Vehicle	Paclitaxel	Vehicle	Paclitaxel
Vth (mV)	−24.21 ± 3.46	−29.94 ± 1.90	−33.18 ± 1.62	−41.26 ± 2.40
AHP (mV)	−7.90 ± 1.79	−2.45 ± 1.08	−18.82 ± 2.14	−7.48 ± 0.53
T_{peak} (ms)	20.13 ± 3.19	24.84 ± 4.35	36.18 ± 2.29	40.39 ± 4.32
T_r (ms)	15.95 ± 2.25	14.32 ± 2.79	17.96 ± 3.01	5.57 ± 0.91
T_{AHP} (ms)	59.19 ± 6.68	24.34 ± 1.37	72.31 ± 3.15	28.40 ± 2.19
Overshoot (mV)	43.38 ± 3.91	45.41 ± 2.71	45.68 ± 2.26	47.61 ± 2.76
Amplitude (mV)	92.84 ± 6.84	90.87 ± 2.68	97.90 ± 3.23	95.53 ± 3.57
Max Slope (V/s)	83.99 ± 13.72	86.77 ± 16.55	93.67 ± 13.00	101.60 ± 5.63

Table 5. Action potential parameters for IB4(-).

c. Dual paclitaxel treatments augment electrical firing in IB4(+) and IB4(-) sensory neurons.

Next, we investigated the effect of two doses of paclitaxel on the firing of DRG sensory neurons at 48h post-first treatment (PTX-1) or post-second treatment (PTX-2). In the vehicle group, only few of IB4(+) nor IB4(−) neurons exhibited spontaneous action potential firing under resting conditions; in this case all responses were evoked through current injection. This confirms that the observed differences in firing behavior following paclitaxel treatment reflect changes in evoked excitability rather than baseline spontaneous activity. Paclitaxel elicited a notable increase in electrically evoked action potential firing in both neural subtypes (**Fig.12A-B**). Significantly, it doubled the firing frequency of IB4(+) neurons after the second administration (PTX-2) (**Fig.12D**) and it increased 4-fold the firing frequency (Hz) in IB4(-) in both treatments (**Fig.12E-F**). To further characterize these effects over time, we examined the same parameters at two distinct time points- 48 h after the first and second paclitaxel treatments (corresponding to PTX-1 and PTX-2, respectively). Paclitaxel tripled AP triggering AUC in IB4(-) neurons, accompanied by a notable decrease in the current rheobase post-drug treatments (**Fig.12G-I**). As shown in **Figure 12H**, in IB4(+) neurons, a trend toward increased tonic firing was observed at PTX-1, becoming statistically significant at PTX-2. In contrast, IB4(−) neurons already exhibited a significant increase at PTX-1, which was further maintained after the second treatment. This increase in firing frequency was observed across the entire range of currents from 10 to 300 pA, leading to a rise in the percentage of IB4(+) and IB4(−) neurons exhibiting tonic firing (**Fig.12G-H**). Furthermore, paclitaxel notably reduced the current rheobase in both subtypes of neurons (**Fig.12I**). Hence, paclitaxel treatment of DRG cultures amplified the electrogenic activity of both IB4(+) and IB4(-) neural subtypes.

These data suggest a cumulative sensitization effect, particularly in IB4(−) neurons. However, the most pronounced increase was observed 48h after the second dose (PTX-2), highlighting a dose- and time-dependent amplification of neuronal excitability. This stronger effect at PTX-2 likely reflects the cumulative impact of repeated paclitaxel exposure on ion channel modulation and intracellular signaling pathways, further lowering the threshold for repetitive firing and enhancing the overall responsiveness of

DRG neurons.

Collectively, these findings confirm that paclitaxel treatment enhances the electrogenic activity of both IB4(+) and IB4(−) sensory neurons, with a more rapid and sustained effect observed in IB4(−) subtypes. The progression of excitability changes over time suggests that repeated paclitaxel exposure exacerbates neuronal sensitization, potentially contributing to the development of neuropathic pain symptoms.

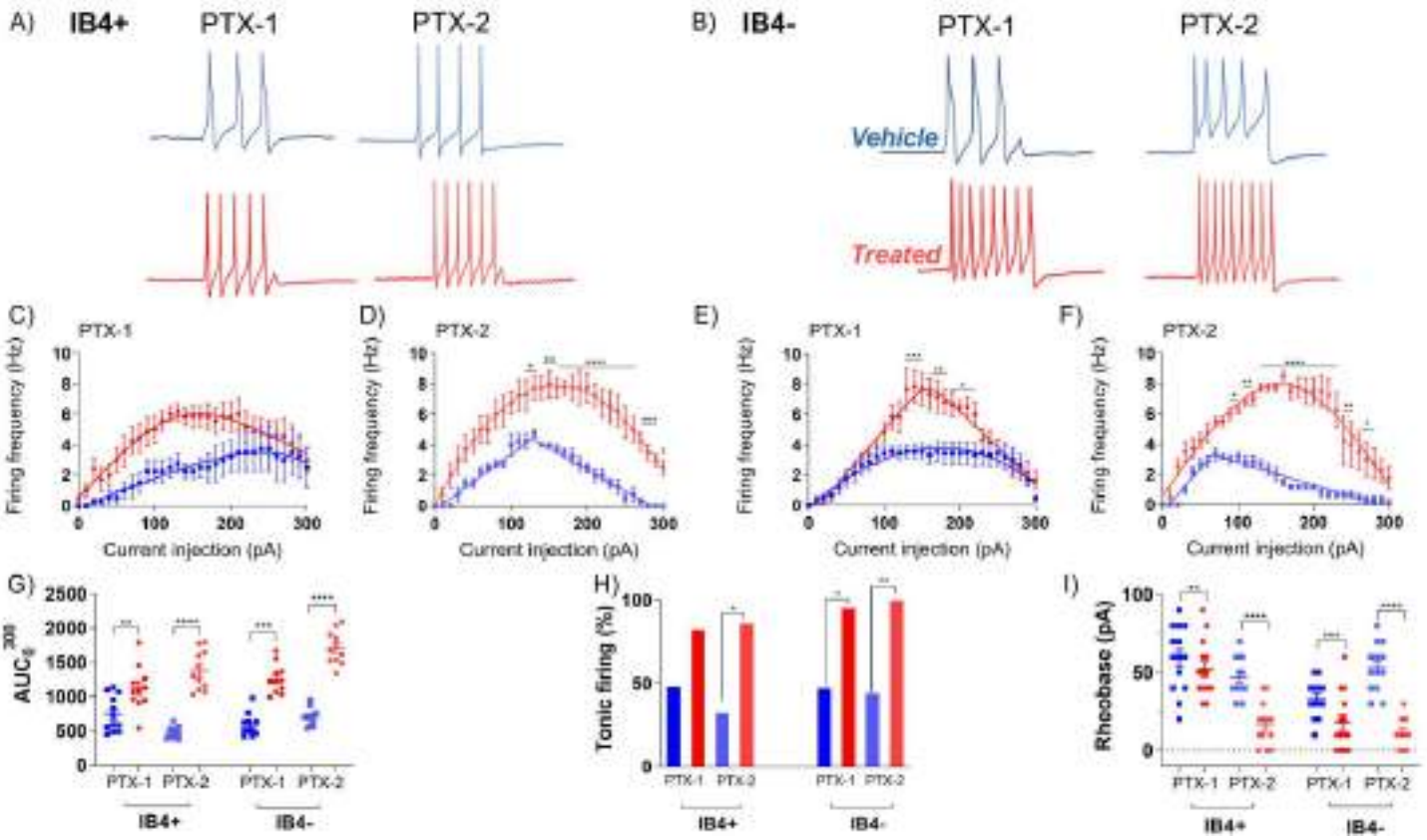

Figure 12. Paclitaxel enhanced the electrically-evoked action potential (AP) firing in both IB4(-) and IB4(+) dorsal root ganglion (DRG) neurons. A-B) Sample recordings of AP firing in response to a 1-second, 120 pA current injection pulse for IB4(+) and IB4(-) neurons, either treated with vehicle or paclitaxel, recorded 48 hours post first treatment (PTX-1) or post second treatment (PTX-2). C-F) The firing frequency (number of APs generated during the 1-second depolarizing pulse) was measured for each current injection from 0 to 300 pA in 10-pA increments for IB4(+) (C-D) and IB4(-) (E-F) neurons treated with two consecutive administrations of vehicle or paclitaxel. G) The area under the curve (AUC_{0-300}) was calculated by plotting firing frequency against the injected current across the 0 to 300 pA range. H) The percentage of neurons showing tonic firing after vehicle or paclitaxel exposure was recorded. I) Rheobase values were determined for IB4(-) and IB4(+) small DRG neurons exposed to vehicle or paclitaxel. Data are presented as column (H) or individual values with ±SD. Each dot represents the measurements for each recorded cell. Data were collected 48 hours post first treatment (PTX-1) or post second treatment (PTX-2). Sample sizes were N = 8; n = 10-15 *P < 0.05, Two way-ANOVA (for B) and Mann–Whitney test (for C, D, and E).

d. Sodium current is affected by two consecutive administrations of Paclitaxel in IB4(+) and IB4(-) neurons.

Previously, we found that paclitaxel augmented the expression and activity of $Na_V1.8$ in sensory neurons, with minor effects on K_V channels (150). Thus, we next recorded the Na_V currents 48h post-treatments in both neuronal populations using a depolarizing protocol

that preferentially records $Na_V1.8$ currents by inactivating other Na_V subtypes. The activating protocol consisted of a 500 ms depolarizing prepulse to -50 mV from a holding of -80 mV followed by a family of 30 ms of 10 mV depolarizing steps from -70 to 35 mV from the holding potential (214). In addition, to isolate the somatic Na_V currents and minimize space-clamp artifacts, we used the protocol described by Meents et al. (2019) (215), consisting of applying a 6-8 ms pre-pulse voltage step from -50 to -40 mV, followed of a 1 ms hyperpolarizing step to -120 mV before the activating protocol (**Fig. 13-14**).

As shown in **Figure 13 and 14**, paclitaxel significantly increased sodium current density in both neuronal subtypes. This enhancement was evident after the first treatment and became more pronounced following the second, particularly in IB4(−) neurons (**Fig.14C-D**). Representative current traces (**Fig.13A,C-14A,C**) illustrate the increased inward current amplitude following paclitaxel administration, while J–V and corresponding G–V plots (**Fig.13B,D-14B,D**) reveal that paclitaxel hyperpolarized the half-activation voltage ($V_{0.5}$) by 14-18 mV. This suggests a higher availability and sensitivity of the channels to depolarization. Importantly, the voltage-dependence of activation ($V_{1/2}$) was significantly hyperpolarized in IB4(+) neurons, indicating that a smaller depolarizing input is sufficient to activate sodium channels after paclitaxel treatment (**Fig.13B,D**). While a significant change was also observed in IB4(−) neurons, the shift occurred at more depolarized potentials compared to IB4(+), suggesting a less pronounced enhancement in excitability (**Fig.14B,D**). This differs from other parameters previously examined, where IB4(−) neurons appeared more sensitive to paclitaxel. These findings suggest that sodium channel gating is more finely modulated in IB4(+) neurons. This may be due to intrinsic differences in ion channel regulatory mechanisms, as IB4(+) nociceptors are enriched in $Na_V1.8$ and participate in broader signaling cascades involving ion channels such as TRPs, which may contribute to their increased susceptibility to excitability changes induced by paclitaxel.

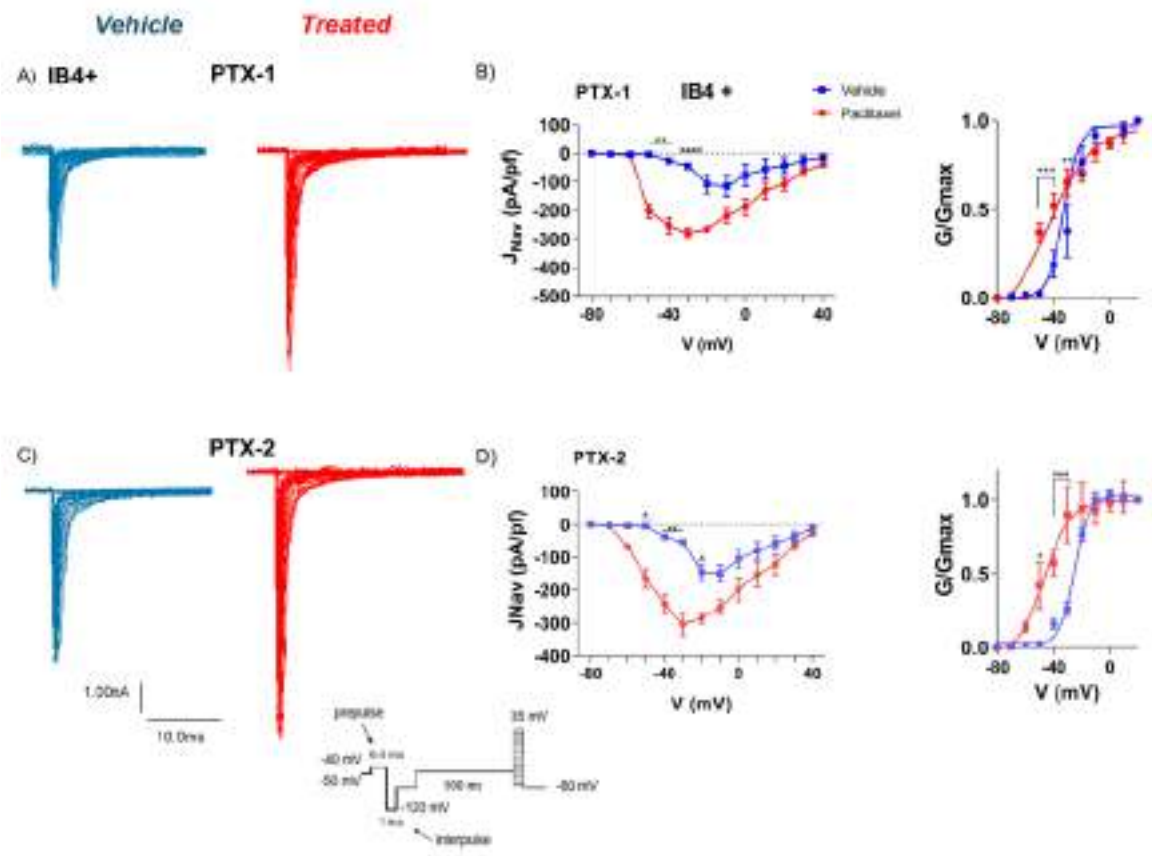

Figure 13. $Na_V1.8$ channel current is increased by two treatments of paclitaxel in IB4(+) neurons following treatment with either vehicle or paclitaxel. A,C) Representative recordings of a family of ionic currents were evoked using a 500 ms depolarizing protocol from -80 mV to 35 mV in 10 mV steps; to isolate somatic NaV currents, a short voltage prepulse (6–8 ms, -50 to -40 mV) followed by a 1 ms interpulse at -120 mV was applied prior to each voltage step 48h after vehicle or paclitaxel first-treatments (PTX-1) (A), or second-treatment (PTX-2) (C). B, D) The current-voltage (J-V) relationships for Na+ inward currents were plotted at PTX-1 or PTX-2, showing median current density values (pA/pF) with interquartile ranges. The right side displays G-V curves derived from the J-V curves, with reversal potentials interpolated from each J-V curve. The curves were fitted using the Boltzmann equation: G/Gmax = 1/(1 + e^(-zF(V1/2 - V)/RT)). Data are presented as medians with interquartile ranges. N=6, n=10. ****P≤0.0001; ***P≤0.0005; **P≤0.006; *P≤0.05 indicates a significant difference from the vehicle group; Two-way ANOVA.

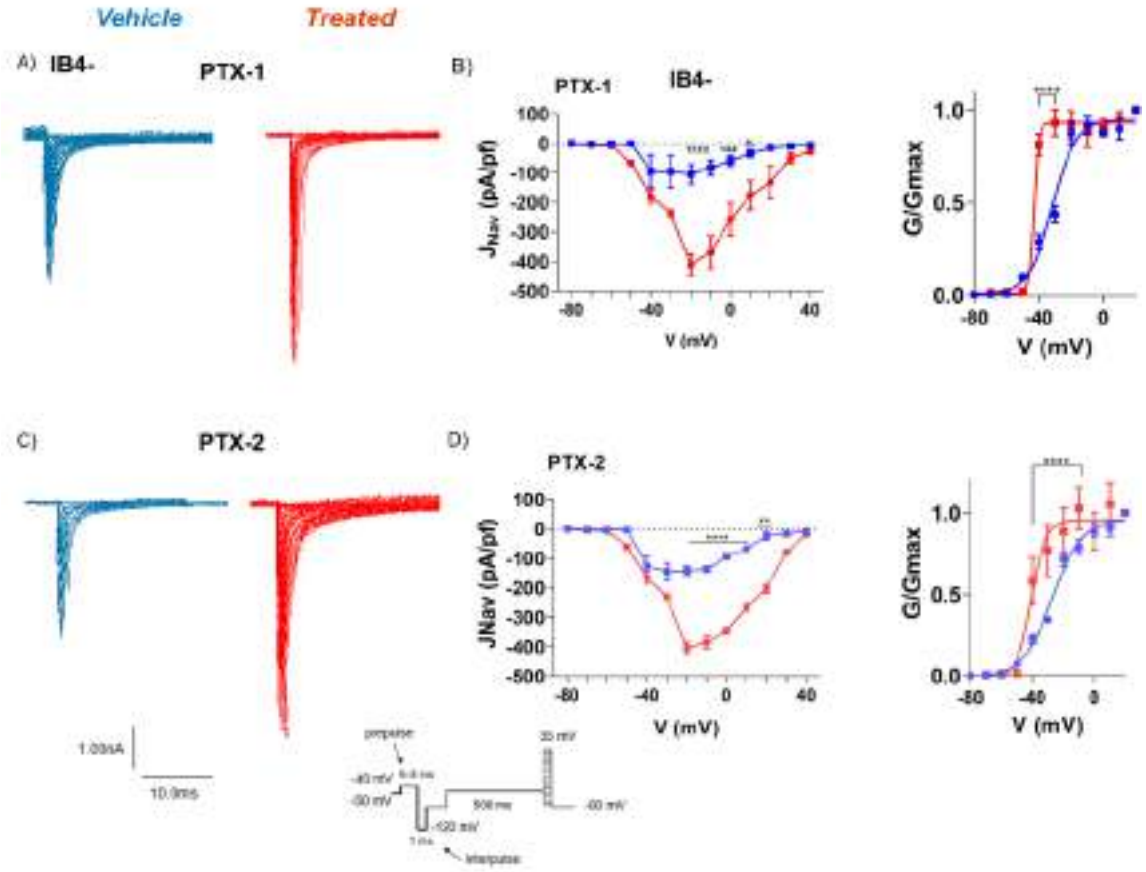

Figure 14. $Na_V1.8$ channel current is increased by two treatments of paclitaxel in IB4(-) neurons following treatment with either vehicle or paclitaxel. A,C) Representative recordings of a family of ionic currents were evoked using a 500 ms depolarizing protocol from -80 mV to 35 mV in 10 mV steps; to isolate somatic NaV currents, a short voltage prepulse (6–8 ms, -50 to -40 mV) followed by a 1 ms interpulse at -120 mV was applied prior to each voltage step 48h after vehicle or paclitaxel first-treatments (PTX-1) (A), or second-treatment (PTX-2) (C). B, D) The current-voltage (J-V) relationships for Na+ inward currents were plotted at PTX-1 or PTX-2, showing median current density values (pA/pF) with interquartile ranges. The right side displays G-V curves derived from the J-V curves, with reversal potentials interpolated from each J-V curve. The curves were fitted using the Boltzmann equation: G/Gmax = 1/(1 + e^(-zF(V1/2 - V)/RT)). Data are presented as medians with interquartile ranges. N=6, n=10. ****P≤0.0001; ***P≤0.0005; **P≤0.006; *P≤0.05 indicates a significant difference from the vehicle group; Two-way ANOVA.

To further elucidate which sodium channel subtypes were responsible for this effect, we assessed the relative expression levels of $Na_V1.7$, $Na_V1.8$, and $Na_V1.9$ using RT-qPCR (**Fig. 15**). Interestingly, only $Na_V1.8$ showed a significant upregulation at PTX-2 (48h post-second treatment), while $Na_V1.7$ and $Na_V1.9$ expression levels remained almost unchanged. This supports the hypothesis that paclitaxel-induced changes in excitability are mainly driven by $Na_V1.8$.

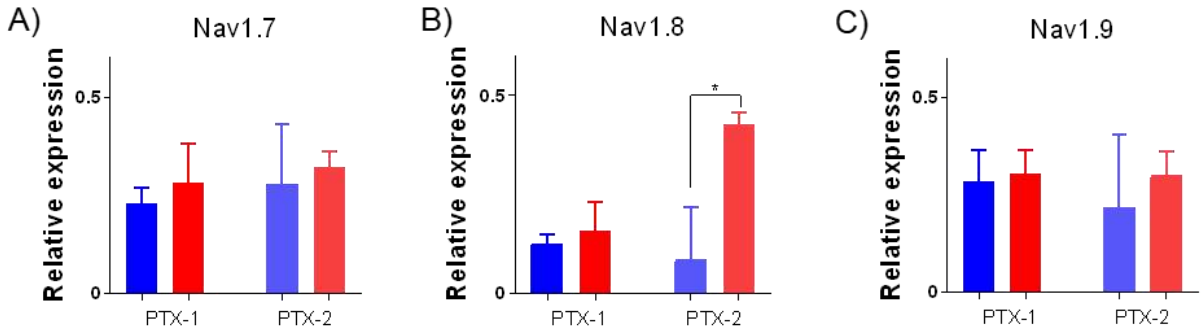

Figure 15. Paclitaxel increases Nav1.8 relative expression upon the second administration. A) Nav1.7 relative expression represented as column at DIV8 (48h post first treatment) and DIV13 (48h post second treatment). B) Nav1.8 relative expression represented as column at DIV8 (48h post first treatment) and DIV13 (48h post second treatment). C) Nav1.9 relative expression represented as column at DIV8 (48h post first treatment) and DIV13 (48h post second treatment). T-test, *P≤0.005. N=3.

To further characterize the subtype-specific contribution of sodium channels to the increased excitability induced by paclitaxel, we performed a pharmacological analysis using the selective blocker TTX (100 nM), at a concentration that blocks TTX-sensitive channels while sparing TTX-resistant subtypes such as $Na_V1.8$ and $Na_V1.9$. Although previous experiments and mRNA analysis strongly implicated $Na_V1.8$ in mediating the paclitaxel-induced increase in excitability, this analysis aimed to functionally isolate the contribution of TTX-resistant sodium currents and evaluate whether changes in their biophysical properties- such as voltage dependence of activation- also contributed to the observed phenotype (**Fig.16A**).

As shown in **Figure 16**, G–V curves were plotted for both IB4(+) (**panel B**) and IB4(−) (**panel C**) neurons at PTX-1 and PTX-2, allowing us to examine voltage-dependent activation profiles for $Na_V1.8/1.9$ currents in vehicle- and paclitaxel-treated conditions.

While $Na_V1.8$ expression was already known to be upregulated, the shift in voltage dependence of activation suggests additional modulatory mechanisms beyond expression levels. These could include changes in the relative abundance of $Na_V1.8$ versus $Na_V1.9$, post-translational modifications of the channel proteins, or alterations in β-subunit composition, all of which are known to affect sodium channel gating kinetics. Thus, the observed hyperpolarizing shift in $V_{1/2}$ may not only reflect an increase in total

channel number but also a change in the biophysical behavior of the sodium channel population present after paclitaxel treatment. At PTX-2, the effect of paclitaxel became more pronounced. In both IB4(+) and IB4(−) neurons (**panels B,C**), $Na_V1.8/1.9$-mediated currents displayed a significantly greater conductance and a stronger hyperpolarizing shift in $V_{1/2}$, reflecting increased channel availability and earlier activation thresholds. The enhancement was most evident in IB4(+) neurons, which aligns with the more robust excitability changes observed in this subtype following paclitaxel exposure. This is consistent with the enhanced mRNA upregulation of $Na_V1.8$ in our RT-qPCR data (**Fig. 15**), further suggesting that $Na_V1.8$ is the primary driver of the increased sodium current density observed.

These results suggest that paclitaxel-induced peripheral neuropathy involves subtype-specific remodeling of sodium channel function, with $Na_V1.8$ playing a central role in the altered excitability of both IB4(+) and IB4(−) neurons. Targeting $Na_V1.8$ could therefore represent a promising therapeutic strategy for the treatment or prevention of chemotherapy-induced peripheral neuropathy (CIPN).

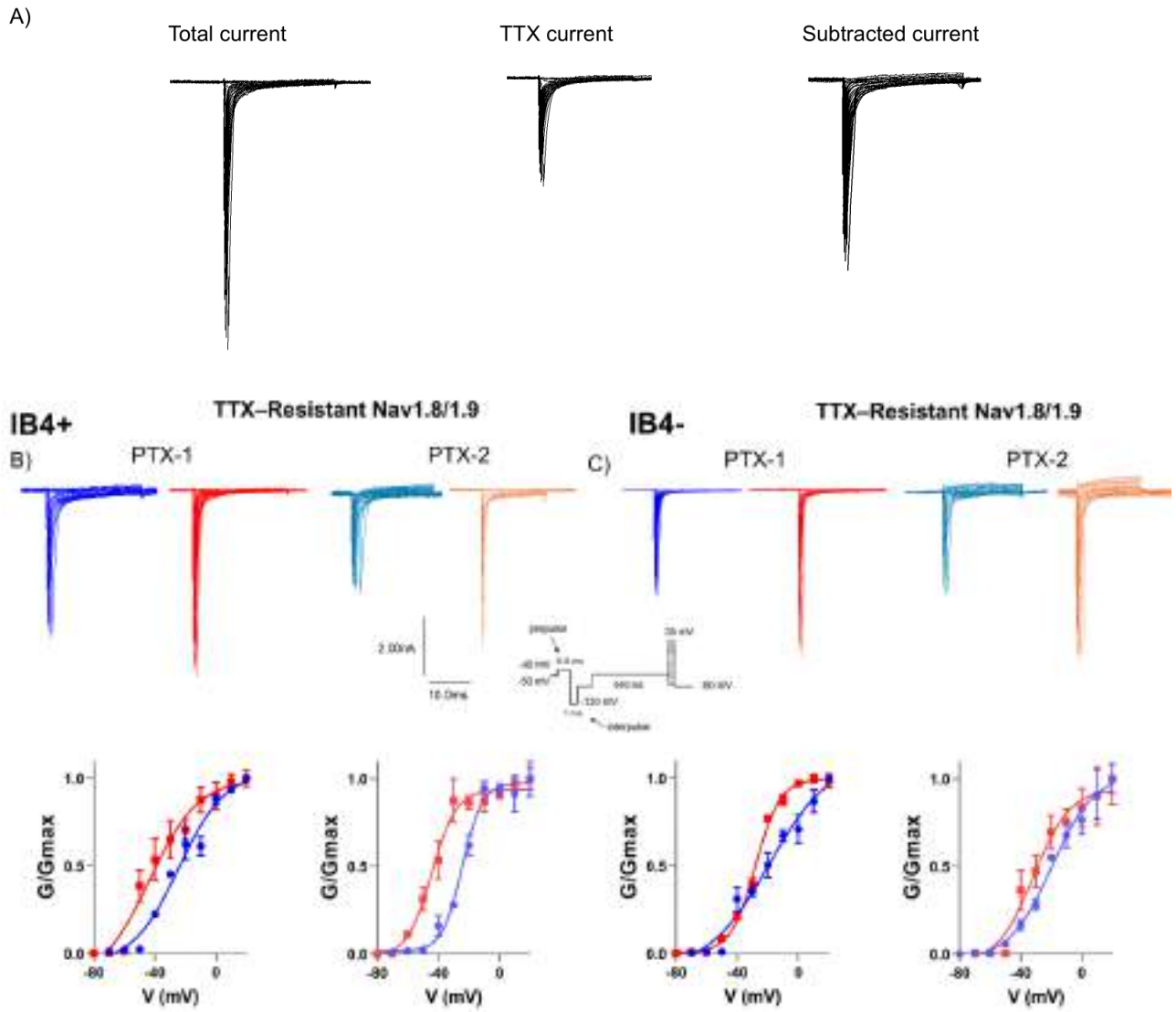

Figure 16. Paclitaxel increased TTX-resistant $Na_V1.8/1.9$ currents in both IB4(-) and IB4(+) sensory neurons. Pharmacological analysis of Na_V currents in vehicle- and paclitaxel-treated neurons was performed using the TTX (100 nM) to isolate $Na_V1.8/1.9$ channels. A) The remaining currents after TTX-blocking were subtracted from the total recorded current. B) G-V curves for IB4(+) at PTX-1 or PTX-2 derived from the J-V curves, with reversal potentials interpolated from each J-V curve. C) G-V curves for and IB4(-) at PTX-1 or PTX-2 derived from the J-V curves, with reversal potentials interpolated from each J-V curve. The curves were fitted using the Boltzmann equation: G/Gmax = 1/(1 + e^(-zF(V1/2 - V)/RT)). Data are represented as median±SEM. N=6, n=10.

e. Paclitaxel does not alter delayed rectifier (DR)-type potassium currents in both IB4(+) and IB4(-) neurons.

Our investigation delved then into the effects of paclitaxel on potassium (K^+) currents within IB4(-) and IB4(+) neurons. We used a voltage pulse ranging from -80 to 40 mV inducing a series of outwardly rectifying, non-inactivating K^+ currents known as K_{DR}. Upon

exposure to paclitaxel, these neurons exhibited distinct K^+ currents, featuring a rapid-inactivating A-type current (K_A) succeeded by K_{DR} currents, notably prominent at depolarizing potentials exceeding 30 mV. This distinct kinetic profile enabled a comprehensive analysis of both K_A and K_{DR} currents, even though it was not completely evident with the second administration of paclitaxel (PTX-2). Our investigation into the effects of paclitaxel on neuronal currents revealed distinct responses between IB4-positive (IB4+) and IB4-negative (IB4-) neurons. Specifically, after an initial treatment with paclitaxel, there was no significant impact on the A-type potassium currents (K_A) or the delayed rectifier potassium currents (K_{DR}) in either IB4(+) or IB4(-) neurons (**Fig.17-18**). However, in IB4(+) neurons, there was a slight enhancement in the G/Gmax ratio, suggesting a minor increase in the relative conductance of the K_A currents, though this effect did not reach statistical significance (**Fig.17B**). Following the second paclitaxel treatment (**Figure 17E**), the same voltage-clamp protocol was applied to assess potential cumulative effects. Representative traces (**Fig.17A,D-18A,D**) and the I–V relationships (**Fig.17-18, panels B, C, E, F**) again confirmed that neither K_A nor K_{DR} currents were significantly altered in amplitude or activation properties in paclitaxel-treated neurons compared to vehicle. Conductance analysis reinforced this finding, showing no significant differences in voltage sensitivity or maximal conductance in either IB4(+) (**Fig.17**) or IB4(-) (**Fig.18**) subtypes.

Together, these data demonstrate that paclitaxel does not significantly affect outward K^+ currents in DRG neurons, even after repeated exposure. Therefore, the increased excitability observed in treated neurons is unlikely to be mediated by a reduction in repolarizing K^+ currents, but rather through enhanced inward Na^+ conductance, as previously shown.

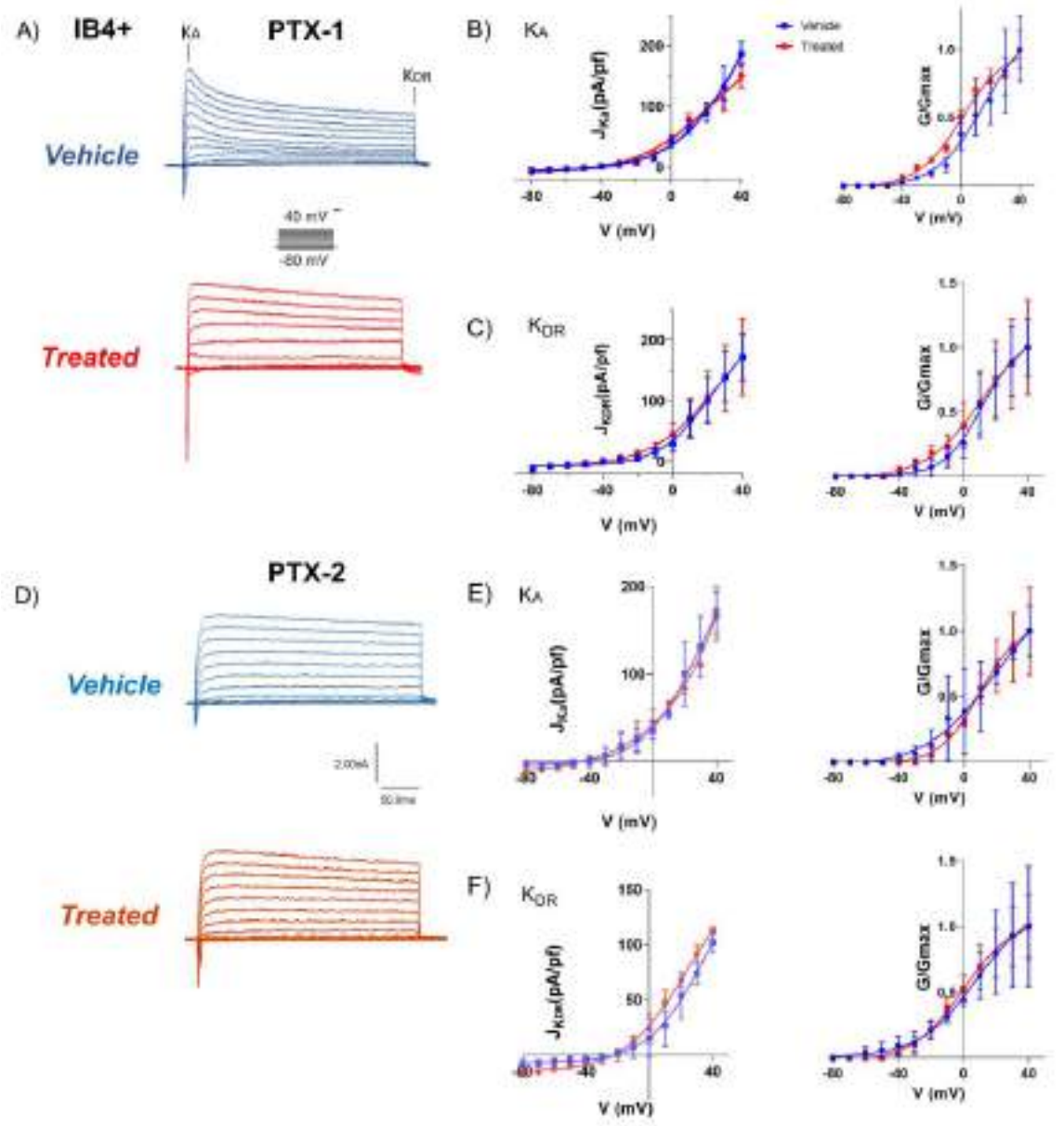

Figure 17. Paclitaxel doesn't affect the fast-inactivating (K_A) component and outward K+ currents (K_{DR}) in IB4(+) neurons after 48h post treatments. A,D) Representative current traces recorded in IB4(+) neurons following depolarization to 20 mV and -30 mV at 48h-PTX-1 (A) and 48h-PTX-2 (D). Both the fast-inactivating (K_A) and sustained (K_{DR}) components are indicated. B,C) Current-voltage (J-V) relationships for K_A (B) and K_{DR} (C) at 48h-PTX-1, presented as current density (pA/pF) with median values±SEM. On the right panel, conductance-voltage (G-V) curves derived from IV plots for K_A and K_{DR} at 48h-PTX-1, using VK+ = -92 mV. E,F) Current-voltage (J-V) relationships for K_A (E) and K_{DR} (F) at 48h-PTX-2, presented as current density (pA/pF) with median values±SEM. On the right panel, conductance-voltage (G-V) curves derived from IV plots for K_A and K_{DR} at 48h-PTX-2, using VK+ = -92 mV. Mean values with SEM are displayed, with Boltzmann equation fitting (see Figure 11 legend).

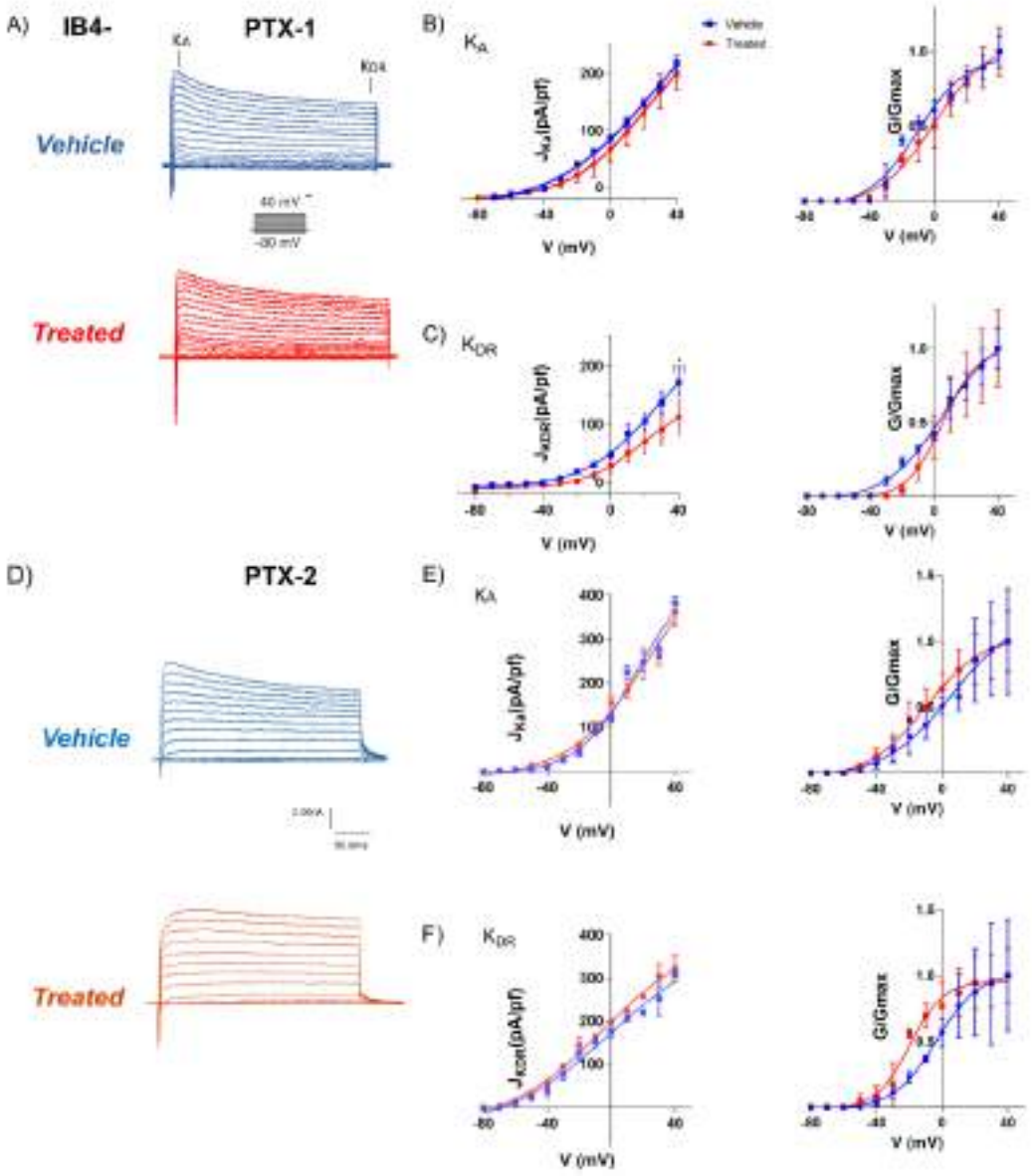

Figure 18. Paclitaxel doesn't affect the fast-inactivating (K_A) component and outward K+ currents (K_{DR}) in IB4(-) neurons after 48h post treatments. A,D) Representative current traces recorded in IB4(-) neurons following depolarization to 20 mV and -30 mV at 48h-PTX-1 (A) and 48h-PTX-2 (D). Both the fast-inactivating (K_A) and sustained (K_{DR}) components are indicated. B,C) Current-voltage (J-V) relationships for K_A (B) and K_{DR} (C) at 48h-PTX-1, presented as current density (pA/pF) with median values±SEM. On the right panel, conductance-voltage (G-V) curves derived from IV plots for K_A and K_{DR} at 48h-PTX-1, using VK+ = -92 mV. E,F) Current-voltage (J-V) relationships for K_A (E) and K_{DR} (F) at 48h-PTX-2, presented as current density (pA/pF) with median values±SEM. On the right panel, conductance-voltage (G-V) curves derived from IV plots for K_A and K_{DR} at 48h-PTX-2, using VK+ = -92 mV. Mean values with SEM are displayed, with Boltzmann equation fitting (see Figure 11 legend).

f. TRP currents and expression levels are elevated following a second round of Paclitaxel treatment.

Having established that paclitaxel induces a marked increase in the excitability of DRG sensory neurons- characterized by enhanced action potential firing, a reduced current threshold, and elevated $Na_V1.8$ activity- we next investigated whether Transient Receptor Potential (TRP) channels, key players in nociceptive signaling, also contribute to this hyperexcitable phenotype.

To assess this, we applied TRP channel agonists on cultured adult mouse DRG neurons, evaluating paclitaxel's effect on TRP-mediated ionic currents. As shown in **Figure 19**, the first treatment with paclitaxel did not significantly alter inward currents evoked by AITC (a TRPA1 agonist) or WS12 (a TRPM8 agonist). However, after the second administration, we observed a moderate increase in TRPA1 activity (**Fig. 19A-B-left panel**) and a substantial amplification of capsaicin-evoked currents, indicating a robust potentiation of TRPV1 function (**Fig. 19A-B, right panel**). On the other hand, the TRPM8 was significantly affected only after the second treatment (PTX-2) **(Fig.19A-B, middle panel)**. These findings suggest that paclitaxel's effect on TRP channel activity is dose- and time-dependent, becoming prominent only after repeated exposure.

To determine whether these functional changes were accompanied by transcriptional or protein-level regulation, we examined mRNA expression and performed immunocytochemical analysis. qPCR analysis showed no significant changes in TRPA1 or TRPM8 transcript levels after the first treatment (**Fig.19C**), in line with the lack of functional effects observed at this stage. However, protein-level analysis revealed a notable increase in TRPV1 expression following the second treatment (PTX-2), confirmed both biochemically and via immunocytochemistry (**Fig. 19C, right panel; Fig. 20C**). Importantly, TRP channel immunoreactivity was nearly undetectable in vehicle neurons across all subtypes tested, as shown in **Figure 20**. This likely reflects the low basal expression of TRP channels in non-injured DRG neurons, a well-documented feature under physiological conditions. TRP channels such as TRPA1, TRPV1, and TRPM8 are often upregulated in response to cellular stress, inflammation, or neurotoxic agents, and their

expression is typically minimal in the absence of such stimuli (216). In contrast, TRPA1 immunoreactivity remained relatively stable, with only a modest increase observed after repeated exposure (**Fig. 20A**), supporting the smaller changes in TRPA1-evoked currents. Additionally, TRPM8 immunoreactivity also increased after the second treatment (PTX-2) (**Fig. 20B**), despite no clear transcriptional upregulation, suggesting possible post-transcriptional or trafficking-related mechanisms.

Altogether, these results indicate that paclitaxel selectively enhances TRP channel activity and expression, particularly that of TRPV1 and TRPV1, following cumulative exposure. This TRP channel upregulation, along with $Na_V1.8$-driven hyperexcitability, likely plays a critical role in the development of chemotherapy-induced peripheral neuropathy (CIPN).

These findings expand our understanding of the molecular mechanisms underlying CIPN. Furthermore, by showing that repeated paclitaxel exposure leads to functional and structural sensitization of sensory neurons- through enhanced Na_V and TRP channel activity and axonal damage- we highlight new potential targets for therapeutic intervention aimed at preventing or reversing this debilitating condition.

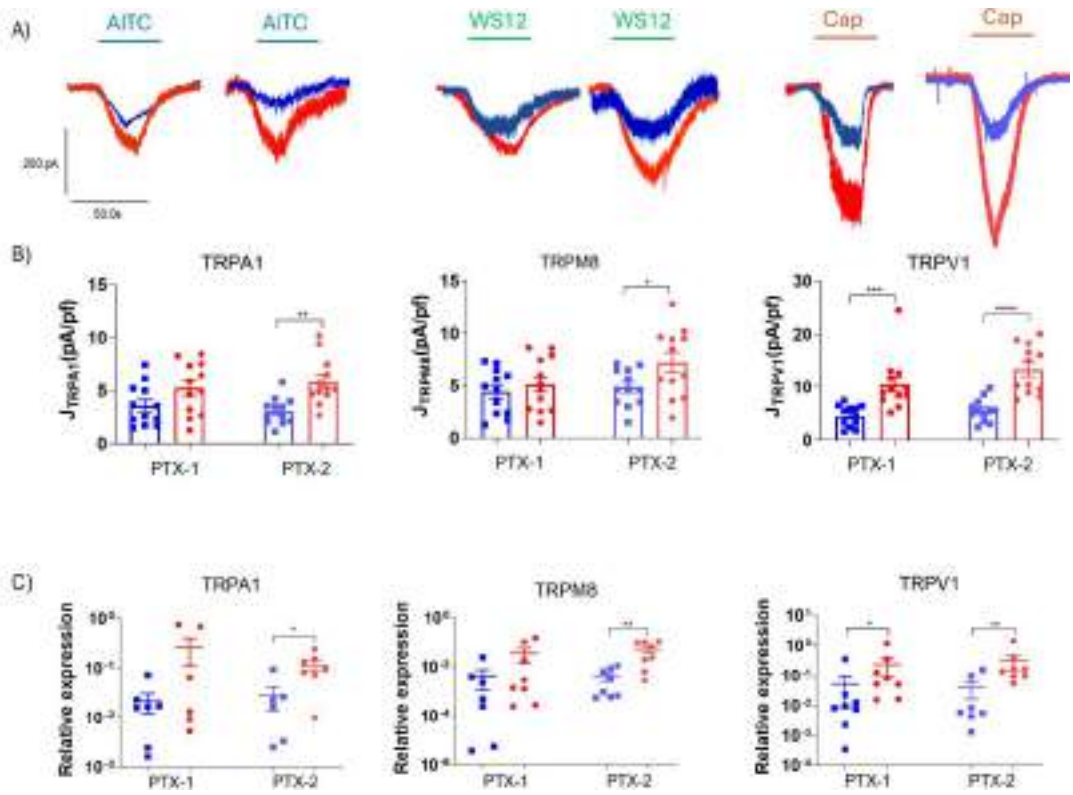

Figure 19. TRPs currents and expressions are increased with a second treatment of Paclitaxel (PTX-2). A) Representative recordings of currents induced by AITC for TRPA1 (left), WS12 for TRPM8 (center), and capsaicin for TRPV1 (right). B) TRPs ion channels current after 48h of treatments normalized based on the capacitance of the cells for TRPA1, TRPM8 and TRPV1. C) Relative quantification of gene expression of TRPA1, TRPM8, TRPV1. Data are presented as mean ± SEM. *P-value<=0.02; **P-value<=0.005; ***P-value<= 0.0005; ***P-value<= 0.0001.

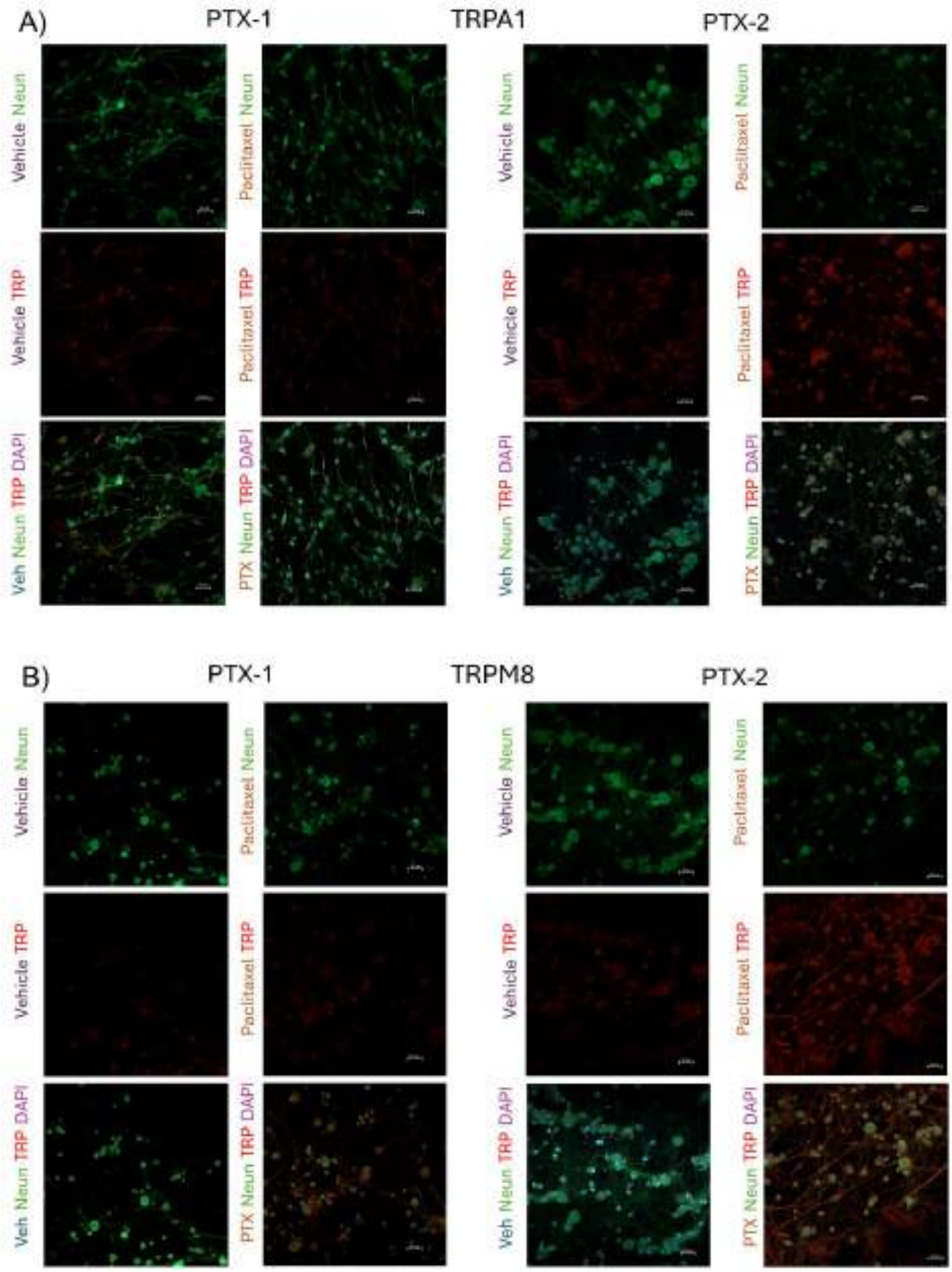
A)
PTX-1
TRPA1
PTX-2
Vehicle Neun
Paclitaxel Neun
Vehicle TRP
Paclitaxel TRP
Veh Neun TRP DAPI
PTX Neun TRP DAPI
B)
PTX-1
TRPM8
PTX-2
Vehicle Neun
Paclitaxel Neun
Vehicle TRP
Paclitaxel TRP
Veh Neun TRP DAPI
PTX Neun TRP DAPI

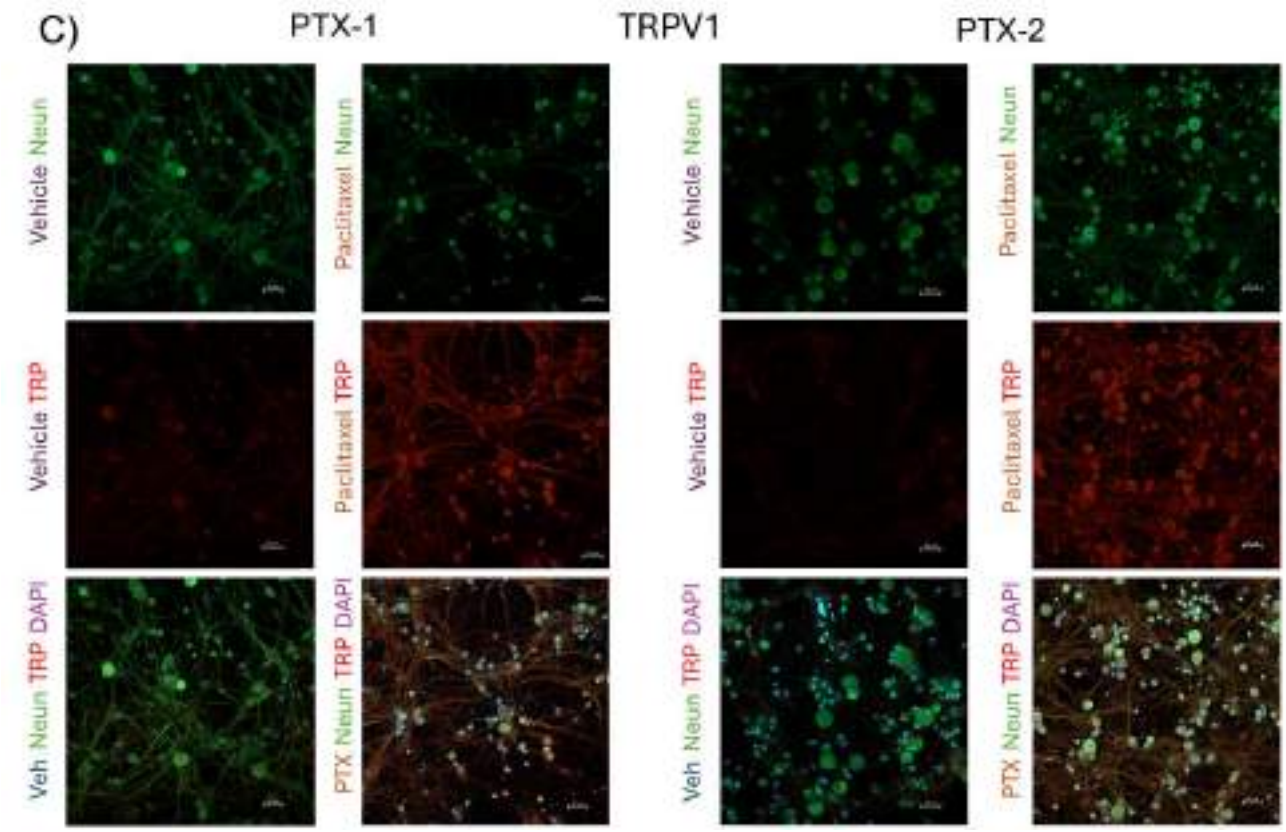

Figure 20. Paclitaxel increased TRPM8 and TRPV1 immunoreactivity in sensory neurons. Immunocytochemical staining of cultured DRG neurons treated with vehicle or paclitaxel using anti-TRPA1, anti-TRPM8 or anti-TRPV1 antibodies along with the neuronal marker NeuN and DAPI staining. Green: Neun; Red: TRP; Blue: DAPI. A-B-C) TRPA1, TRPM8 and TRPV1 representative immunoreactivity picture taken with LSM900 with Airyscan 2 detector confocal microscope. Signal-to-noise ratio is increased 4 to 8 times, and super-resolution reaches up to 120 nm. Scale bar 50 µm.

g. Paclitaxel induced irreversible axonal retraction after the second treatment.

After characterizing the somatic effects of paclitaxel on DRG neurons- including increased excitability, altered sodium and TRP channel activity- we turned our attention to the axonal compartment, given the well-established role of axonopathy in PIPN pathogenesis. Paclitaxel is known to induce axonal retraction and degeneration, which may contribute to long-lasting sensory dysfunction (217). To study these effects in a spatially controlled manner, we employed microfluidic chambers, a compartmentalized culture system that enables the physical separation of neuronal soma from their axons. These devices allow for selective treatment and analysis of axonal processes while preserving the integrity of

the neuronal cell body, making them an ideal tool for investigating axon-specific responses to neurotoxic agents such as paclitaxel.

This approach is particularly relevant in the context of CIPN, where distal axon degeneration often precedes somatic alterations. In line with our findings, Giorgi et al. conducted a detailed study demonstrating that a single treatment with paclitaxel (PTX-1) led to a reversible reduction in axonal density in nociceptor primary cultures (218). Their findings indicated that the most significant decrease in axonal density occurred immediately after the treatment, with full recovery observed by 96 hours post-exposure. This research utilized advanced imaging techniques, specifically using a LSM900 confocal microscope equipped with an Airyscan 2 detector and a 20x objective, to capture high-resolution images of the axonal changes.

Building on Giorgi et al.'s findings, we sought to further investigate the effects of repeated paclitaxel exposure on axonal endings. For this purpose, a second administration of paclitaxel was applied, and the subsequent effects were monitored at different time points. Our results revealed a marked decrease in axonal density at PTX-2, which corresponds to 48 hours after the second paclitaxel treatment. Unlike the initial exposure, this reduction did not show signs of recovery by 96h-PTX-2, indicating a potentially more lasting effect on the neurons (**Fig.21**). The significance of these findings lies in their implications for understanding chemotherapy-induced peripheral neuropathy (CIPN), a common and debilitating side effect of chemotherapy treatments like paclitaxel. CIPN is characterized by sensory disturbances, including pain, tingling, and numbness, often resulting from damage to peripheral nerves. Our observations suggest that repeated exposure to paclitaxel may lead to persistent sensitization and structural changes in neural endings, contributing to the chronic and progressive nature of CIPN.

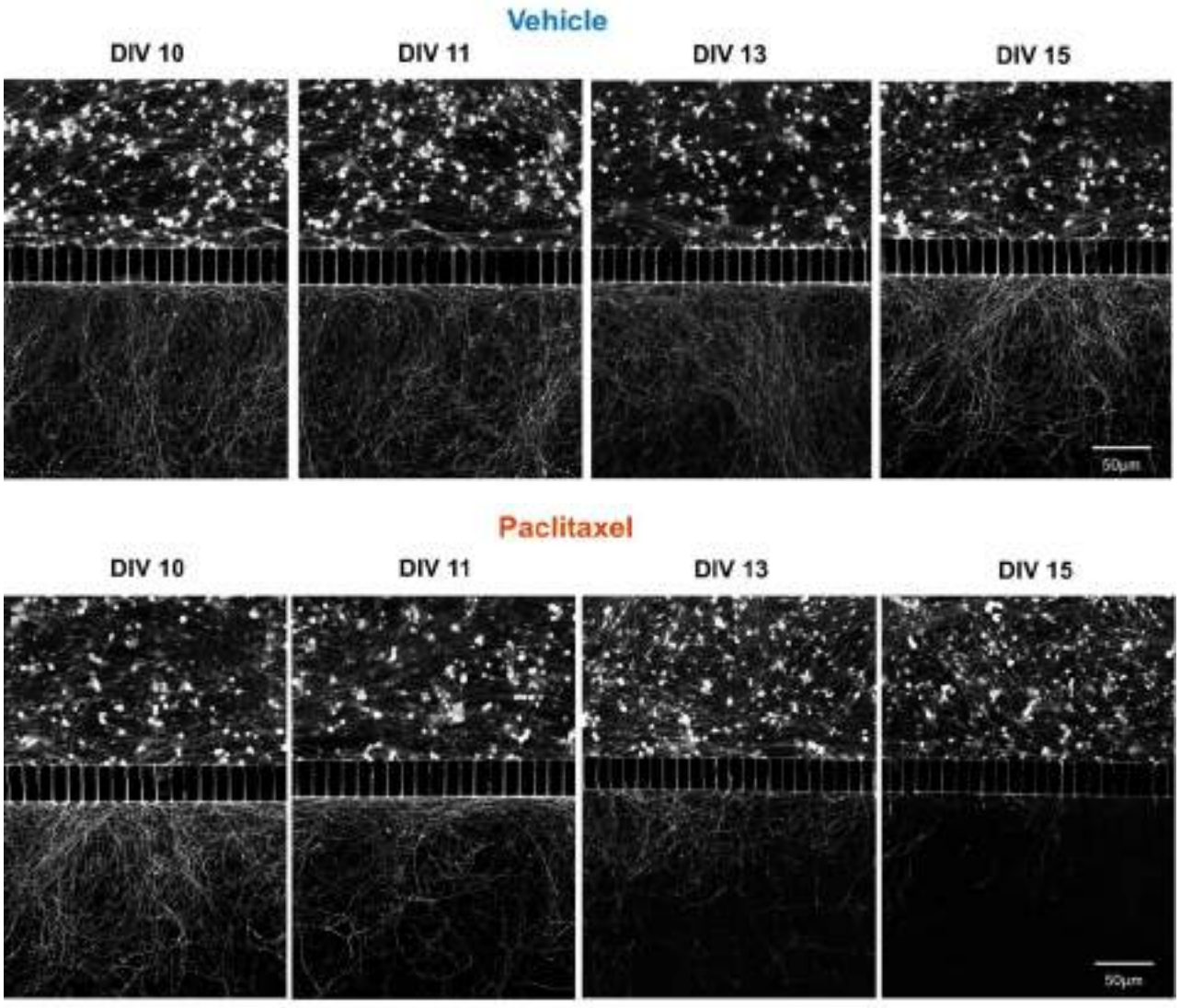

Figure 21. Paclitaxel induced axons retraction with no recovery after the second treatment. Microfluidic chambers (MFC) were used to evaluate the peripheral effect of paclitaxel on axonal density. Representative images of sensory neurons loaded with the calcein fluorescent dye in MFC. Axonal compartment was treated with vehicle (DMSO 0.04%)(top) - or paclitaxel 1 µM (bottom) on DIV10 for 24h, and the density of axonal ends was followed at 0, 48h and 96h post- second treatment (PTX-2). Picture were captured using LSM900 with Airyscan 2 detector confocal microscope, objective 20x. Scale bar 50µm.

h. TRPs channels are augmented in the soma compartment after axon exposure to Paclitaxel

After establishing that paclitaxel enhances excitability and TRP channel activity when applied directly to the soma, we sought to determine whether a similar sensitization could be initiated by targeting only the axonal compartment in the microfluidic chambers.

In this experiment, axons were selectively exposed to 1 µM paclitaxel for 24 hours, followed by a recovery period of up to 96 hours. Calcium imaging was then performed by stimulating axonal terminals with specific TRP agonists- AITC (TRPA1), WS12 (TRPM8), and capsaicin (TRPV1)- while recording responses in the soma. As shown in **Figure 22A**, stimulation of axons 48 hours after the second paclitaxel treatment (PTX-2) resulted in a notable increase in calcium responses in the soma compared to vehicle-treated controls (**Fig. 22B)**.

Quantitative analysis revealed that both the magnitude of the response (normalized fluorescence) and the percentage of responding neurons were significantly increased for TRPM8 and TRPV1, while TRPA1 responses remained largely unchanged (**Fig. 22C–D**). These enhancements peaked at 48h-PTX-2 and showed a partial resolution by 96h-PTX-2 (**Fig. 22E–G**), indicating a transient but robust sensitization of sensory neurons following axonal exposure. Interestingly, these results mirror those obtained when paclitaxel was applied to the soma compartment (**Fig.19**), suggesting that peripheral terminals are not only vulnerable to paclitaxel but are also capable of triggering retrograde signalling that modifies somatic responsiveness.

Altogether, these findings underscore the importance of axonal targets in paclitaxel-induced TRP sensitization and support the idea that chemotherapy-induced neuronal hypersensitivity originates at the peripheral endings. The use of microfluidic chambers was instrumental in revealing this axon-to-soma communication, offering mechanistic insight into the spatial dynamics of sensory neuron sensitization in CIPN.

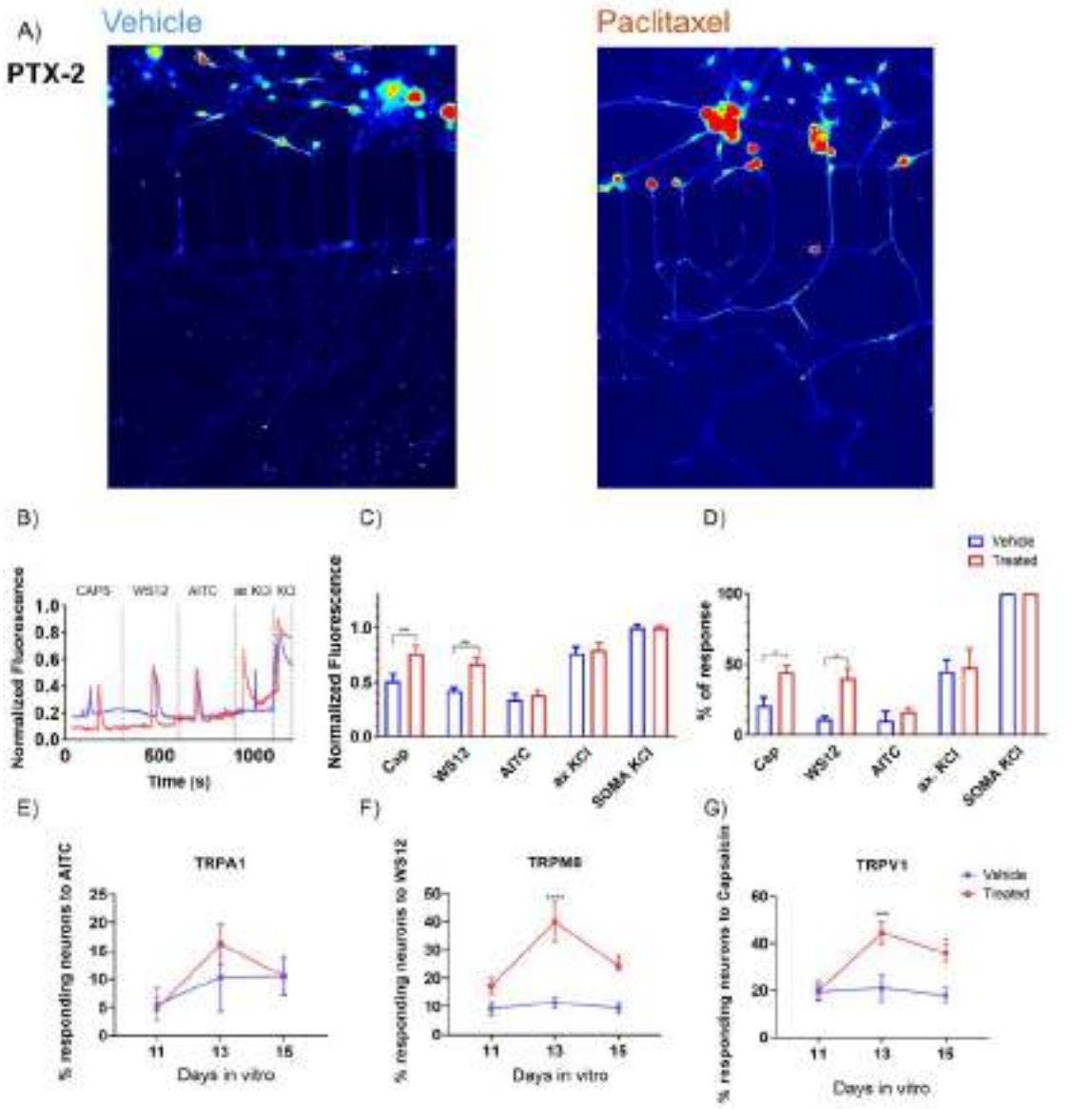

Figure 22. A second treatment of paclitaxel causes axons retraction and increase of TRPs responding neurons. A) Representative pictures of cells responding in the soma compartment of the microfluidic chamber of vehicle (left) or paclitaxel (right) at 48h post second treatment (PTX-2) putting the stimuli in the axonal compartment. B) Representative fluorescent signals recorded in the soma of Did+ neurons following stimulation in the axonal compartment. The Y-axis shows fluorescence normalized to the signal evoked by KCl in the soma compartment. C-D) Size of response and percentage of response normalized to Did+ and somal KCl^+ responsive cells. Data are represented as column of mean ± SEM. E,F and G) Percentage of responding neurons to TRPs agonists at 0 (DIV11), 48 (DIV13) and 96 (DIV15) hours post second-treatment. Responses to AITC, WS12 and Capsaicin were normalized to somal KCl response. Mean ± SEM. N=3; n=6. ****P≤0.0001; ***P≤0.0005; **P≤0.005; *P≤0.01. Mann-Whitney test.

i. Exploring sex-related variability in IB4(+) neurons responses to paclitaxel

After investigating the effects of two sequential paclitaxel treatments, we next sought to explore whether sex differences might influence neuronal responses in our model. Preclinical studies have traditionally used male animals, leaving a significant knowledge gap in understanding how females respond to these neurotoxic treatments. However, recent literature suggests potential sex differences in pain sensitivity, neural plasticity, and response to injury, though findings are often inconsistent and debated.

In this study, we aimed to explore possible sex-dependent differences in sensory neuron responses to paclitaxel treatment.

To investigate whether sex influences nociceptor excitability after paclitaxel exposure, we recorded action potential firing from IB4(+) and IB4(−) DRG neurons at PTX-1 and PTX-2 using stepwise current injections (0–300 pA) (**Fig. 23**).

In both PTX-1 and PTX-2 recordings (**Fig. 23A,C,E,G**), paclitaxel treatment resulted in an overall increase in firing frequency compared to vehicle, suggesting that IB4(−) and IB4 (+) neurons are sensitive to paclitaxel's effects.

However, this increased excitability was observed in both sexes to a similar extent, with no clear difference between male and female neurons. The firing frequency curves, and representative traces show overlapping responses in treated males and females, indicating that sex does not appear to significantly influence IB4(+), nor IB4(−) neurons behavior under these conditions. Interestingly, when comparing across subpopulations, IB4(−) neurons may actually be more sensitive to paclitaxel overall, as their firing rates increased more consistently in both sexes compared to IB4(+).

This supports the interpretation that both IB4(+) and IB4(-) neurons are affected by paclitaxel, but no clear sex-dependent difference emerged in our data. This contrasts with findings by Villalba et al. (150), who reported greater responses in female neurons using a rat model. Given that our study was conducted in mice, the discrepancy may reflect species-specific differences, and further investigation is needed to clarify the role of sex in paclitaxel-induced sensory neuron excitability.

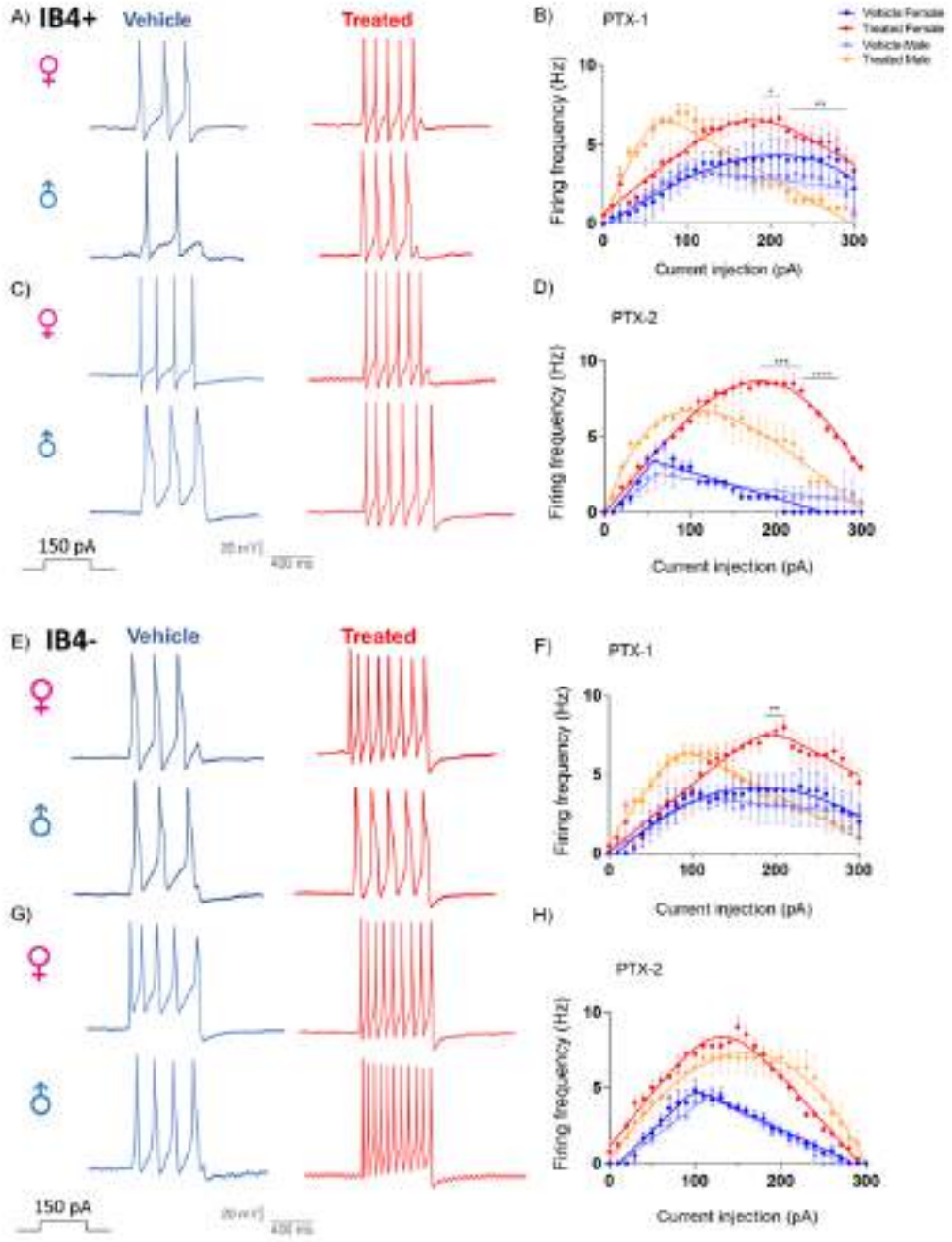

Figure 23. Excitability of IB4(-) and IB4(+) neurons in female mice seems to exhibit greater sensitivity to paclitaxel. A-D) Representative action potential firing of IB4(+) neurons from female and male mice (A,C). Firing frequency of IB4(+) neurons obtained with an injected current in the range of 0 to 300 pA in 10-pA pulses. Firing frequency was obtained counting the number fired APs during the 1 s current pulse at PTX-1 (48h post-first treatment) and PTX-2 (48h post-second treatment) in female and male nociceptors (B,D). E-H) Representative action potential firing of IB4(+) neurons from female and male mice (E,G). Firing frequency of IB4(-) neurons obtained with an injected current in the range of 0 to 300 pA in 10-pA pulses. Firing frequency was obtained counting the number fired APs during the 1 s current pulse at PTX-1 (48h post-first treatment) and PTX-2 (48h post-second treatment) in female and male nociceptors (F,H). Two-way ANOVA test, P-value<=0.005. N=5, n=8-10.

Next, area under the curve (AUC), rheobase and tonic firing analysis were used to further characterize excitability changes for IB4(+) (**Fig.24A,C,E**) and IB4(-) (**Fig.24B,D,F**). Treated female IB4(+) neurons showed a tendency toward lower rheobase and higher AUC values at both timepoints (**Fig. 24A,C**), suggesting they may be more sensitive to paclitaxel-induced changes. Although some trends were observed across sexes, particularly in IB4(+) neurons, the data do not support a consistent or robust sex-dependent difference in response to paclitaxel. Taken together, these results underscore the complexity of nociceptor responses to chemotherapeutic agents and highlight the need for further studies across species, sexes, and neuronal subtypes to better understand the cellular mechanisms underlying paclitaxel-induced neuropathy.

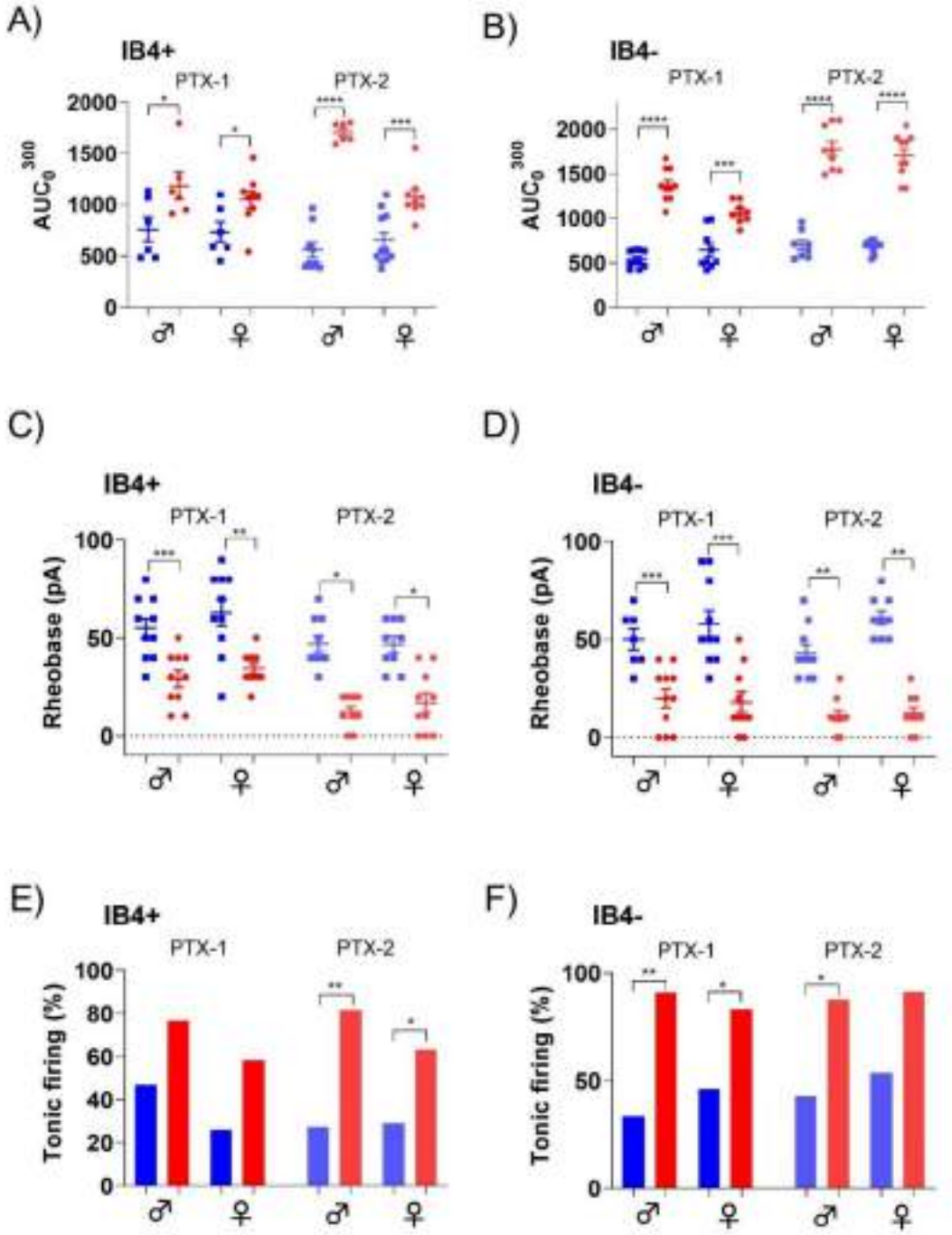

Figure 24. Similar sensitization profiles in male and female DRG neurons following paclitaxel exposure. A-B) The area under the curve ($AUC_{0\text{-}300}$) was calculated by plotting firing frequency against the injected current across the 0 to 300 pA range at 48h-PTX-1 or 48h-PTX-2 for IB4(+) (A) and IB4(-) (B). C-D) Rheobase values were determined for IB4(+) (C) and IB4(-) (D) small DRG neurons exposed to vehicle or paclitaxel at 48h-PTX-1 or 48h-PTX-2. E-F) The percentage of neurons showing tonic firing after vehicle or paclitaxel exposure was recorded at 48h-PTX-1 or 48h-PTX-2 for for IB4(+) (E) and IB4(-) (F). Data are presented as column (E-F) or individual values with ±SEM. Each dot represents the measurements for each recorded cell. Sample sizes were N = 8; n = 10-15. ****P≤0.0001; ***P≤0.0002; **P≤0.001; *P≤0.01. Two way-ANOVA.

3.1.1 Discussion:

The first objective of this research was to examined the direct effects of paclitaxel on the electrogenic properties of dorsal root ganglion (DRG) sensory neurons from male and female mice. Previous findings from Villalba et al., showed that at 48h post a single Paclitaxel administration there is a spontaneous activity and an increased action potential tonic firing in IB4(-) and IB4(+) neurons in both sexes, while at 96h they virtually disappear (150). Furthermore, Paclitaxel upregulated TRPV1 and TRPM8 implying their contribution to cold hypersensitivity in paclitaxel CIPN. Finally, paclitaxel modulated molecularly Na^+ and K^+ ion currents (219–221).

Building on these findings, we extended our study to investigate the effects of two consecutive 24-hour paclitaxel treatments in a long-term (15 days in vitro) culture of DRG neurons from adult mice. This protocol aimed to mimic the cyclical nature of chemotherapy regimens. We employed a long-term (15 days in vitro) primary culture of adult mice dorsal root ganglion (DRG) neurons to examine how dual and consecutive administrations of paclitaxel influence the electrical activity of IB4(+) and IB4(-) sensory neurons of male and female adult mice during sensitization and resolution. The study aimed to elucidate the impact of Paclitaxel, a chemotherapeutic agent, on sensory neurons, particularly focusing on thermoTRP (transient receptor potential) channels and sodium channels.

This pattern closely mirrored the kinetics of pain symptoms observed in patients undergoing paclitaxel treatment, underscoring the translational relevance of our in vitro model. This research revealed findings consistent with prior in vivo studies, including increased TRPV1 activity and nociceptor hyperexcitability (222,223). Notably, paclitaxel-induced hyperexcitability appeared to operate independently of immune system involvement, although autocrine signaling via IL6 and CCK2 might contribute (224,225).

We observed that paclitaxel affected two distinct populations of small DRG neurons, IB4(-) and IB4(+), suggesting that both groups may mediate the altered sensory symptoms associated with PIPN. However, the underlying mechanisms appeared distinct, with TRP channel upregulation restricted to IB4(-) neurons (150) Analysis of action potential (AP) parameters 48 hours after the second paclitaxel treatment (PTX-2) revealed a reduction in the hyperpolarization phase of the AP in both IB4(-) and IB4(+) neurons, potentially

linked to changes in HCN, K2P, and Kir ion channel activity. Supporting this hypothesis, previous studies reported increased HCN1 mRNA expression in paclitaxel-treated rats (226)

Further investigation into Na^+ channel activity demonstrated enhanced $Na_V1.8$ activity in small DRG neurons following paclitaxel exposure. This upregulation may explain the increased repetitive firing of APs and the transition from phasic to tonic firing. These results align with studies suggesting $Na_V1.8$ as a major contributor to paclitaxel-induced hyperexcitability and neuropathic pain (34,227).

On the other hand, in our in vitro model, paclitaxel treatment did not appear to affect potassium channels, which contrasts with other studies that have shown chemotherapy agents like paclitaxel can disrupt potassium channel function and contribute to the development of neuropathic pain (228). Potassium channels are essential for maintaining a stable membrane potential and regulating the repolarization phase of action potentials. When these channels are disrupted, it can lead to hyperexcitability in neurons (90) However, our findings suggest that paclitaxel-induced changes in neuronal excitability might occur through mechanisms that do not involve potassium channels. Instead, other ion channels, particularly sodium and calcium channels, may be more directly involved in the hyperexcitability observed in this model (227)

ThermoTRP channels also played a significant role. Paclitaxel increased TRPV1 and TRPM8 activity, with TRPV1 upregulation likely contributing to heat hyperalgesia and burning pain, as seen in paclitaxel-treated patients (229). TRPM8 activity, meanwhile, could underline cold allodynia, consistent with findings that TRPM8 blockade alleviates cold hyperalgesia (208). Interestingly, no changes in TRPA1 activity were observed with a single Paclitaxel administration, potentially due to the absence of immune-mediated algesic factors in the in vitro model. While TRPA1 current and relative gene expression are significantly increased upon the second treatment.

Building on the findings of Giorgi et al., who demonstrated reversible axonal density reduction after a single paclitaxel treatment, our study revealed that repeated paclitaxel exposure leads to sustained structural damage (218). At PTX-2, corresponding to 48 hours after the second treatment, we observed pronounced axonal retraction that persisted without signs of recovery by 96h-PTX-2. These cumulative structural changes may

underline the chronic and progressive nature of PIPN, emphasizing the need for strategies to mitigate axonal damage (230).

Furthermore, our findings did not reveal clear sex-based differences in nociceptor responses to paclitaxel. Both male and female DRG neurons exhibited similar patterns of sensitization. Unlike previous reports suggesting heightened and prolonged sensitization in female neurons, such as persistent activation after the first treatment, our data showed comparable dynamics across sexes. While this does not align with clinical evidence indicating greater pain sensitivity in women, it highlights the complexity of modeling sex differences in preclinical settings and emphasizes the need for further studies to explore potential species-specific or context-dependent mechanisms (148).

Together, these findings deepen our understanding of the cellular effects of paclitaxel on sensory neurons and provide a foundation for future studies aimed at mitigating chemotherapy-induced neuropathy.

3.2 CHAPTER 2: Optimizing new TRPV1 channel modulators for disease-modifying agents in neuropathy treatment- A dual TRPV1-CB2 agonist.

The results of compound **41**, a dual TRPV1-CB2 agonist, were published in the European Journal of medicinal chemistry. The synthesis and chemical characterization of the compounds were carried out by the group of Prof. Tracey Pirali (Medicinal Chemistry laboratory), while all biological experiments and data analyses were performed by our group (Sensory neurobiology laboratory).

Results obtained from paper 2:

- Lamberti A, Serafini M, et al. The multicomponent Passerini reaction as a means of accessing diversity in structure, activity and properties: soft and hard vanilloid/cannabinoid modulators. 2024;
  doi: https://doi.org/10.1016/j.ejmech.2024.116845.

a. Cross-Talk Between EV and EC Systems: Discovery of Cpd41

Given our previous findings showing a marked upregulation of TRP channels in paclitaxel-induced peripheral neuropathy (PIPN), we subsequently directed our efforts toward exploring their pharmacological modulation. Since these channels play a key role in driving nociceptor hyperexcitability and altered sensory processing in this condition, targeting them may offer a promising therapeutic strategy. By modulating TRP channels activity, we aim to mitigate PIPN symptoms and promote functional sensory recovery in affected individuals. While our investigation has thus far focused on the electrophysiological and structural changes induced by paclitaxel in DRG neurons, including the involvement of specific ion channels and sex-based differences in sensitization, a complementary avenue of research has emerged involving the interplay between endogenous modulatory systems. In particular, the convergence of the endovanilloid and endocannabinoid systems offers new therapeutic possibilities for managing chemotherapy-induced neuropathic pain and other sensory disturbances. This next chapter explores the pharmacological targeting of TRPV1, CB1, and CB2 receptors

through novel synthetic ligands designed to exploit the functional crosstalk between these systems.

Recent research increasingly supports the concept of a functional interplay between the endovanilloid (EV) and endocannabinoid (EC) systems, highlighting their shared ligands, receptors, and regulatory pathways (191). This integrated EV/EC network includes TRPV1 ion channels, cannabinoid receptors CB1 and CB2, their endogenous ligands, and the enzymes involved in their biosynthesis and degradation (186,231). These interconnected systems are implicated in a wide range of physiological and pathological processes, including inflammation, pain modulation, neurodegeneration, as well as disorders affecting the skin and skeletal system.

In collaboration with the medicinal chemistry group led by Professor Tracey Pirali at the University of Eastern Piedmont (UPO), we adopted a diversity-oriented synthetic approach leveraging the Passerini multicomponent reaction. This strategy enabled the generation of a library of α-acyloxycarboxamides, specifically designed to mimic the structural features of endogenous ligands interacting with TRPV1, CB1, and CB2 receptors. The synthesized compounds were screened for their pharmacological activity on TRPV1, CB1, and CB2, and assessed for metabolic stability in skin cells, liver microsomes, and plasma. This screening revealed several candidate molecules with varied bioactivity profiles and metabolic properties, supporting their potential application in both topical and systemic delivery formats.

Among these, compound **41** stood out for its balanced and dual agonistic activity on TRPV1 and CB2, coupled with high selectivity against off-targets such as TRPM8, TRPA1, and CB1. It also demonstrated favorable metabolic stability and synthetic accessibility, making it a promising lead for future therapeutic development.

b. Design and Synthesis of a library of compounds targeting TRPV1 and CB2

To develop the modulators, in the laboratory of medicinal chemistry (UPO) they drew inspiration from known endocannabinoids such as AEA, NADA, and OLDA, which act on the TRPV1 channel, as well as from synthetic cannabinoids reported in the literature as CB2 inverse agonists and dual TRPV1/CB ligands (232,233). They focused on five key hits

bearing the amide substructure suitable for the synthesis of α-acyloxycarboxamide analogues via the Passerini reaction (234,235). These compounds exhibit diverse biological profiles, suggesting the potential for a library of compounds with heterogeneous activities.

Additionally, they introduced an iodide at the 6-position of dopamine derivatives NADA and OLDA to explore if this substitution confers TRPV1 antagonism. Using isocyanides with various substructures, we coupled them with commercially available fatty carboxylic acids and used formaldehyde as the carbonyl component to maintain the desired amide moiety (**Scheme 1**).

The synthesis involved preparing dopamine-based isocyanides, protecting dopamine's hydroxyl groups, and undergoing formylation and dehydration reactions to yield the necessary isocyanides. To synthesize allyl isocyanide 13, a Hofmann isonitrile approach was applied, utilizing benzyltriethylammonium chloride (TEBA) as a lipophilic phase-transfer catalyst. Owing to its limited stability, compound **13** was not isolated and was directly employed in subsequent multicomponent reactions without purification.

The Passerini multicomponent reaction was then carried out using isocyanides (compounds **5**, **7**, **11**, **13**, and the commercially available cyclopropyl isocyanide **14**), together with a set of carboxylic acids (**15–21**) and formaldehyde, following the strategy depicted in Scheme 3. This approach afforded a series of α-acyloxycarboxamides (**22–56**) with yields varying between 18% and 82%. For the synthesis of compounds **22–42**, a final deprotection step was performed by treating the intermediate with tetra-n-butylammonium fluoride (TBAF) and acetic acid, ensuring selective removal of the TBDMS group while preventing ester degradation.

Within this compound library, molecule **41** emerged as a standout candidate. It displayed dual agonist activity toward TRPV1 and CB2, with marked selectivity against TRPM8, TRPA1, and CB1. Additionally, it showed strong metabolic resilience and was straightforward to synthesize. These features position compound **41** as a valuable lead in the development of novel modulators targeting the endovanilloid/endocannabinoid (EV/EC) system.

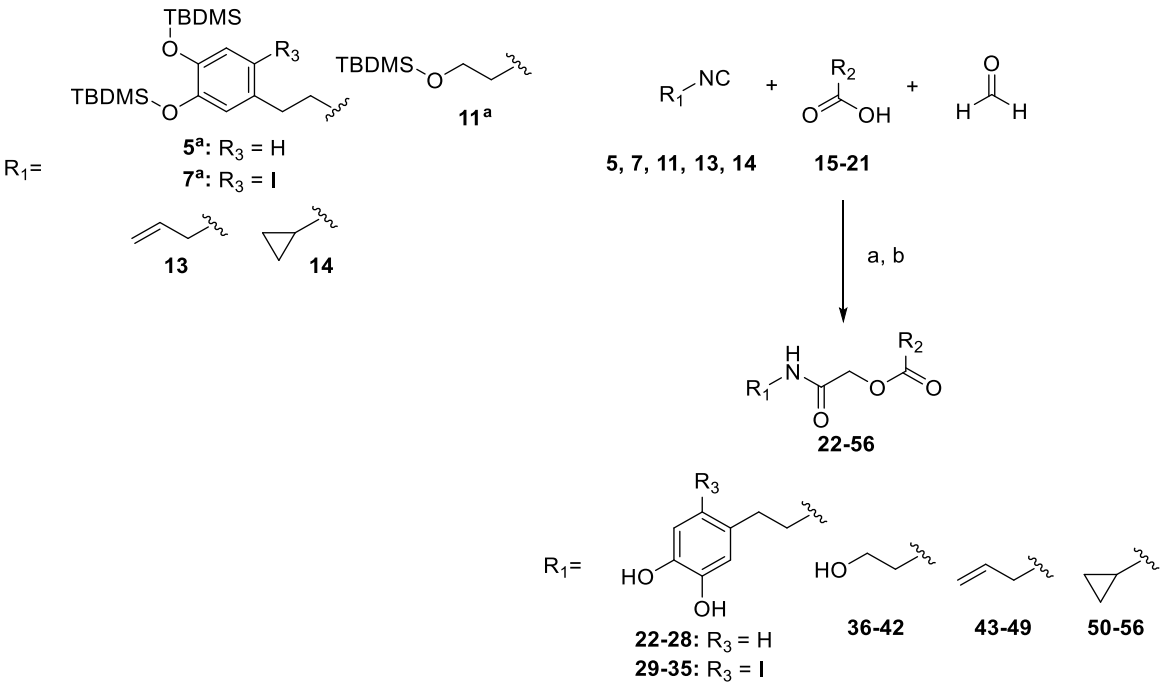

Scheme 1. Overview of the synthetic route using the Passerini reaction followed by deprotection. Reaction conditions: (A) dichloromethane (CH_2Cl_2), 40 °C to room temperature, 2–4 hours, yielding 18–91%; Note: Compounds 22–42 were subjected to an additional deprotection step under the following conditions: (B) acetic acid, TBAF, tetrahydrofuran (THF), 0 °C, 2–3 hours, with yields ranging from 18% to 82%.

c. Highlighting Compound 41: A Balanced TRPV1 and CB2 Agonist.

In this study, they developed two series of compounds inspired by known modulators of the TRPV1 and CB receptors (**Table 6**). These compounds were tested for activity on TRPV1 ion channels and CB receptors using fluorometric assays in HEK293 cells. The first series included NADA and OLDA analogues with dopamine as the polar head, designed to act as either TRPV1 agonists or antagonists based on the presence of hydrogen or iodine.

The second series featured compounds with ethan-1-ol, allyl, or cyclopropyl groups at the polar head, similar to AEA and synthetic cannabinoids. These were paired with the same fatty carboxylic acids used in the first series. Among these, compound **41** stood out due to its balanced agonist activity on both TRPV1 and CB2 receptors. It exhibited an EC_{50} of 26.8 μM for TRPV1 and 37.8 μM for CB2, making it a well-balanced dual agonist. This balanced activity, along with its selectivity and metabolic stability, positions compound

41 as a promising candidate for further development.

Overall, compound **41**'s dual activity and favorable properties highlight its potential as an effective modulator within the EV/EC system, offering therapeutic possibilities for conditions involving TRPV1 and CB2 pathways.

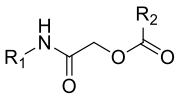

Cpd, Yield	R_1	R_2	hTRPV1		hCB1		hCB2	
			% Activity at 1 µM	EC_{50} (µM)	% Activity at 1 µM	EC_{50} (µM)	% Activity at 1 µM	EC_{50} (µM)
36, 40%	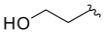	heptyl	15.8 ± 8.8	13.5 ± 1.1	n.a.		n.a.	
37, 49%	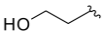	undecyl	10.2 ± 3.3	7.4 ± 1.2	n.a.		n.a.	
38, 20%	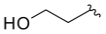	(*R*,*Z*)-11-(2-phenylacetoxy)heptadec-8-en-1-yl	21.0 ± 6.3	3.7 ± 1.1	n.a.		n.a.	
39, 35%	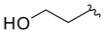	(Z)-heptadec-8-enyl	24.1 ± 9.7	1.9 ± 0.5	n.a.		n.a.	
40, 36%	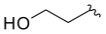	(4*Z*,7*Z*,10*Z*,13*Z*)-nonadeca-4,7,10,13-tetraen-1-yl	38.2 ± 7.2	2.1 ± 0.7	5.2 ± 2.6	30.6 ± 1.3	n.a.	
41, 42%	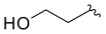	(*E*)-2,6-dimethylhepta-1,5-dien-1-yl	13.2 ± 3.7	26.8 ± 2.4	n.a.		3.7 ± 1.1	37.8 ± 3.6
42, 44%	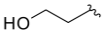	(3*E*,7*E*,11*E*,15*E*)-3,7,12,16,20-pentamethylhenicosa-3,7,11,15,19-pentaen-1-yl	56.5 ± 7.2	0.4 ± 0.1	n.a.		n.a.	
43, 54%	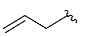	heptyl	14.4 ± 5.2	23.3 ± 3.7	n.a.		n.a.	
44, 50%	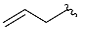	undecyl	16.5 ± 6.4	11.4 ± 1.5	n.a.		n.a.	

Table 6. Second series: AEA, compounds 1 and 2 analogues.

d. Characterization of compound 41.

To confirm direct activation of TRPV1, compound **41** was evaluated using patch-clamp electrophysiology in single HEK293 cells stably expressing human TRPV1. A voltage ramp

protocol was applied, ranging from –120 mV to +120 mV in 20 mV increments, each lasting 100 ms, from a holding potential of 0 mV. Prior to electrophysiological testing, the solubility of compound **41** was assessed in the appropriate buffer up to 100 µM, showing full solubility (refer to material and methods section). Application of 0.5 µM capsaicin induced a prominent, outwardly rectifying current with a reversal potential of approximately 10 mV (10.3 ± 4.1 mV; n = 6), as shown in **Figure 25A**. In contrast, capsaicin produced no response in non-transfected control cells. Co-application with capsazepine, a known TRPV1 inhibitor, effectively suppressed both capsaicin-induced and compound **41**-induced currents, confirming the TRPV1-specific action of derivative **41**.

The capsaicin dose–response curve measured at –60 mV yielded an EC_{50} of 0.3 ± 0.5 µM (**Figure 25B**). Perfusion of 100 µM compound **41** evoked a similarly outwardly rectifying current with a reversal potential close to 0 mV (3.5 ± 3.8 mV; n = 6), as seen in **Figure 25A**. While compound **41** exhibited a significantly lower potency compared to capsaicin (EC_{50} = 47.5 ± 1.1 µM vs 0.2 ± 0.1 µM; n = 7), its efficacy was comparable. Current densities at +80 mV were 333 ± 145 pA/pF for capsaicin and 198 ± 44 pA/pF for compound **41** ($p > 0.05$) (**Figure 25A**), indicating a similar activation profile.

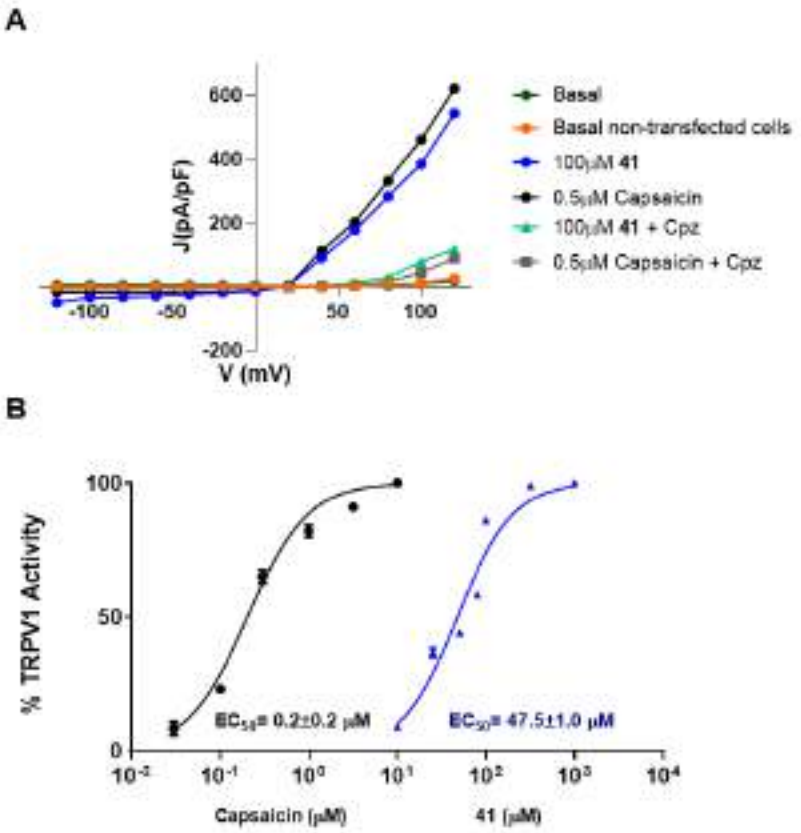

Figure 25. Electrophysiological assessment of compound 41 on human TRPV1 expressed in HEK293 cells. (A) Representative current traces obtained using 100 ms voltage ramps from −120 mV to +120 mV, applied at 4-second intervals. Currents are shown for baseline conditions (dark green), following exposure to 0.5 µM capsaicin (black), 100 µM compound **41** (blue), in non-transfected control cells (orange), or in the presence of 1 µM capsazepine with either capsaicin (gray) or compound **41** (light green). Current amplitudes were normalized to cell size and expressed as pA/pF. (B) Concentration–response relationships for capsaicin and compound **41**. Data were fitted using a sigmoidal dose–response equation: Y = 100 / (1 + 10^((LogEC$_{50}$ − X) × HillSlope)). The fit for capsaicin yielded an EC$_{50}$ of 0.2 µM (95% CI: 0.2–0.35) and a Hill coefficient of 1.3 (95% CI: 0.8–1.7). For compound 41, the EC$_{50}$ was 47.5 µM (95% CI: 40.3–56) with a Hill slope of 1.4 (95% CI: 1–1.77) (n = 5–10).

To further explore the therapeutic relevance of compound **41**, we investigated its capacity to promote desensitization of the human TRPV1 channel in a recombinant expression system. As illustrated in **Figure 26A**, sequential exposure to capsaicin resulted in a marked reduction in TRPV1 responsiveness, with the second stimulus (P2) eliciting a significantly smaller current than the first (P1), yielding a P2/P1 ratio of 0.41 ± 0.1 (n = 6)

(**Fig. 26C**). Similarly, two successive applications of compound **41**, separated by a washout period (**Fig. 26B**), led to a comparable desensitization effect, with a P2/P1 ratio of 0.37 ± 0.05 (n = 6) (**Fig. 26C**). Notably, a prolonged initial exposure to compound **41** triggered a rapid channel inactivation, which showed only partial recovery following removal of the compound.

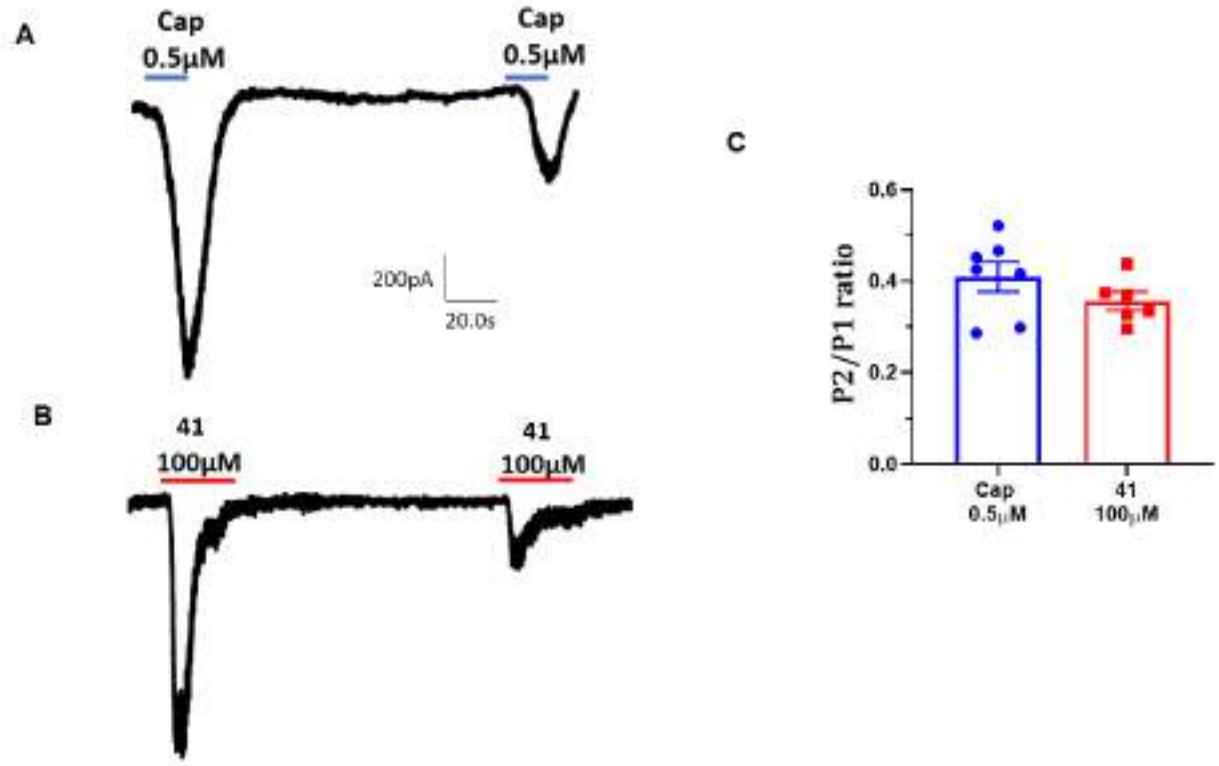

Figure 26. Electrophysiological analysis of TRPV1 desensitization induced by compound 41 in a recombinant expression system. (A, B) Representative current traces recorded at a holding potential of −60 mV in HEK293 cells expressing hTRPV1. Cells were subjected to two successive applications of either capsaicin (0.5 µM; n = 7) (A) or compound **41** (100 µM; n = 6) (B), with a washout period between pulses. The horizontal bars indicate the timing of each agonist application. (C) Quantification of desensitization expressed as the P2/P1 ratio—defined as the amplitude of the second response normalized to the first. Data are presented as mean ± standard deviation. N = 3 independent experiments; n = 8 total recordings.

To assess whether compound **41** exhibits activity on other thermosensitive TRP channels, we conducted patch-clamp recordings in HEK293 cells stably expressing either human TRPM8 or TRPA1 channels. WS12 (1 µM) and AITC (60 µM) served as reference agonists for TRPM8 and TRPA1, respectively. As shown in **Figure 27A** and **27C**, application of 100 µM compound **41** elicited activation of both TRPM8 and TRPA1, though the responses were notably weaker than those evoked by the respective standard agonists

(**Fig. 27A,C**). Importantly, these effects were abolished in the presence of selective antagonists- AMTB for TRPM8 and HC030031 for TRPA1- confirming that **41**'s action was mediated specifically through these channels (**Fig. 27A,C, black traces**).

Quantitative analysis revealed that compound **41** activated each channel to approximately 25% of the response generated by the full agonist (**Fig. 27B,D**), suggesting a relatively high degree of functional selectivity for TRPV1 over TRPM8 and TRPA1.

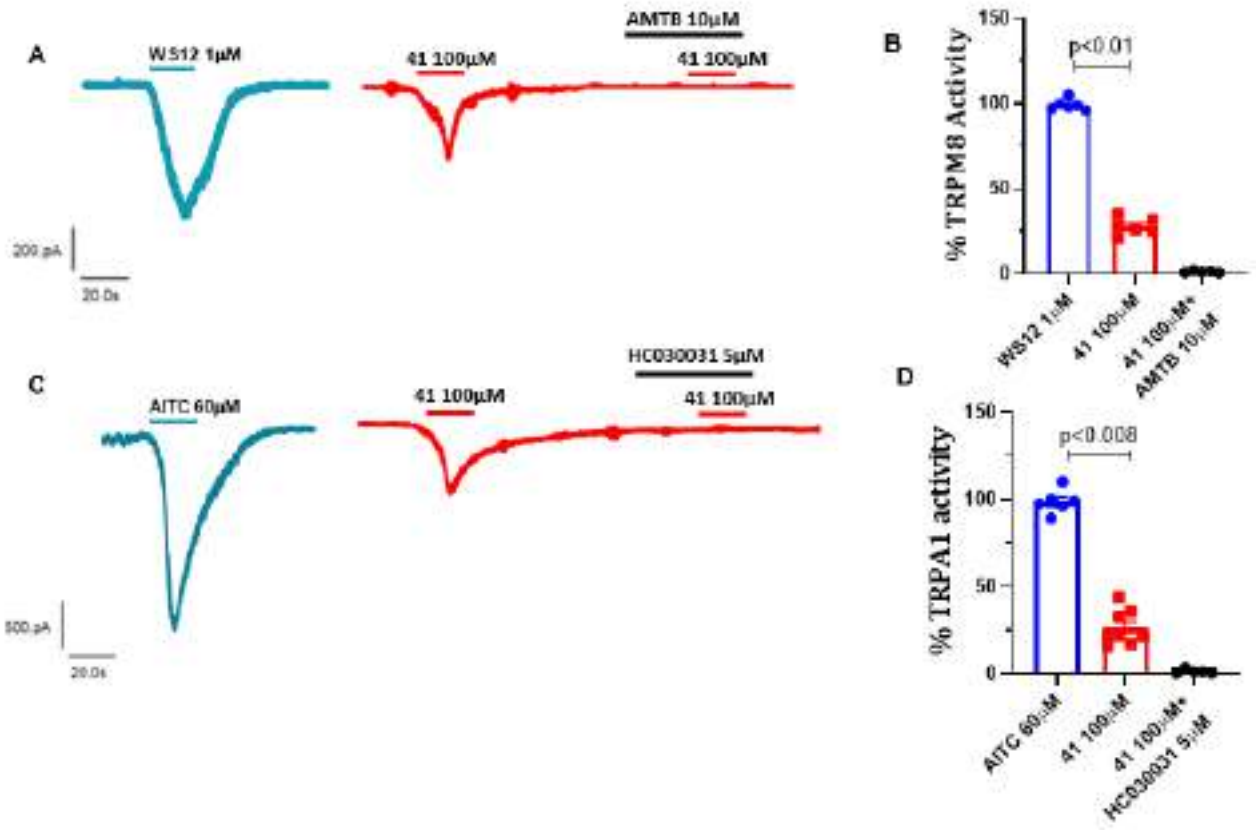

Figure 27. Selectivity profile of compound 41 across thermosensitive TRP channels. (A) Representative inward current traces recorded at a holding potential of −60 mV in HEK293 cells expressing hTRPM8. Cells were exposed to 1 µM WS12 (blue), 100 µM compound **41** (red), or 100 µM compound **41** in the presence of 10 µM AMTB (black), a selective TRPM8 antagonist. (B) Quantitative comparison of hTRPM8 current amplitudes induced by 1 µM WS12 versus 100 µM compound **41**. (C) Inward currents recorded from hTRPA1-expressing cells under stimulation with 60 µM AITC (blue), 100 µM compound **41** (red), or **41** in combination with 10 µM HC030031 (black), a selective TRPA1 blocker. (D) Comparative analysis of hTRPA1 responses to AITC and compound **41**. Statistical significance was assessed using Student's t-test; p-values are reported accordingly. Data are presented as mean ± SEM. N = 3 independent experiments: n = 6–8 cells per group.

e. Computational Binding Studies of Compound 41 to TRPV1 and CB2

Lastly, to investigate how compound **41** binds to TRPV1 and CB2 receptors, computational docking studies were conducted by Professor Gregorio Fernandez (**Fig. 28**). For TRPV1, the docking simulations were based on the human TRPV1 structure (PDB ID: 8GFA) at 2.29 Å resolution, with the capsaicin binding site identified by superimposing it with the squirrel TRPV1 structure (PDB ID: 7LR0). For CB2, docking was done using the activated human CB2 receptor (PDB ID: 6KPF), which was in complex with the agonist AM12033. The docking process involved a total of 500 flexible docking runs, with the simulation search space restricted to a 5 Å box around the known binding sites of capsaicin for TRPV1 and AM12033 for CB2. For TRPV1, compound **41** was observed to bind in a similar manner to capsaicin, with its hydrocarbon tail fitting into the same binding pocket located between the S4, S4-S5 linker segments of one subunit and the S6 TM segment of the adjacent subunit. Capsaicin interacts with the TRPV1 receptor mainly through hydrophobic interactions in the tail and polar/hydrophobic interactions in the vanillyl group. Additionally, a pi-stacking interaction occurs between the vanilloid ring and the residue 511Y. However, when compound **41** binds, it loses some of the hydrogen bond interactions observed in capsaicin's binding, though it still forms hydrogen bonds with the residue N551. The binding energy for capsaicin with TRPV1 was calculated to be 8.29 kcal/mol, while the binding energy for compound **41** was 6.68 kcal/mol. The lower binding energy for compound **41** suggests fewer interactions, particularly hydrophobic and hydrogen bonding, which likely contributes to its lower potency compared to capsaicin.

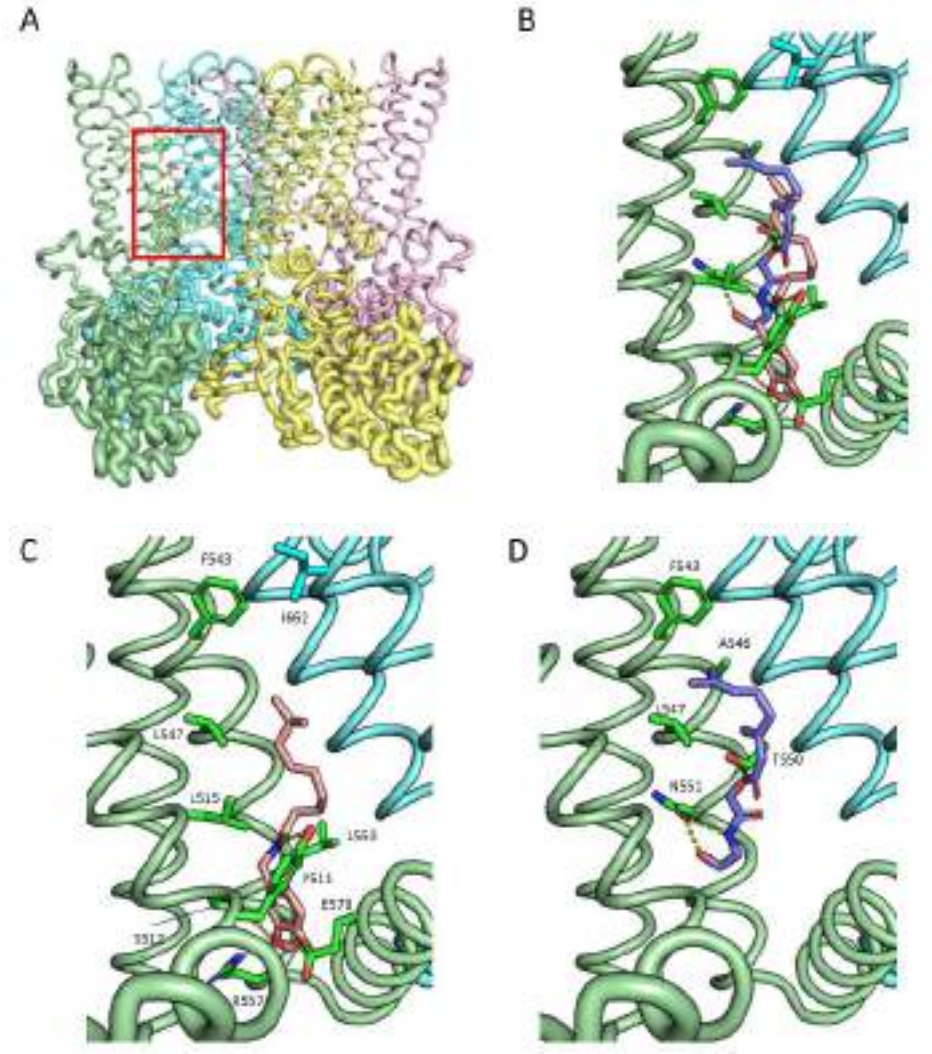

Figure 28. Molecular docking analysis of compound 41 within the human TRPV1 binding site. (A) The cryo-EM structure of human TRPV1 (PDB ID: 8GFA) was employed for docking simulations. The red box outlines the region centered around the capsaicin binding site, with a 5 Å buffer, used as the docking grid to accommodate compound **41**. (B) Close-up view of the ligand-binding pocket showing a superimposition of capsaicin (pink) and compound **41** (blue) to highlight spatial overlap and orientation. (C) Key interactions of capsaicin within the pocket include hydrophobic contacts with L515, F543, L547, L553, and E570 (chain A, shown in green), and I662 (chain B, in cyan). Hydrogen bonding (yellow dashed lines) is observed with Y511, S512, R557, and E570, while a π–π stacking interaction is formed between Y511 and the aromatic vanillyl moiety. (D) Binding mode of compound **41** (blue), which engages in hydrophobic interactions with residues F543, A546, L547, and T550 within the channel pocket.

Previous work on Passerini adducts as topical treatments for inflammatory skin disorders inspired us to explore this approach for targeting the cross-talk between TRPV1 and CB receptors (190). Most existing vanilloid/cannabinoid compounds, particularly natural mediators, have limitations such as low potency, high lipophilicity, unbalanced activity on

CB receptors and TRPV1, and poor synthetic accessibility (186).

Leveraging the Passerini reaction, they aimed to create α-acyloxycarboxamides with diverse chemical structures and tunable metabolic stability. By combining endovanilloid headgroups with various fatty chains, we discovered modulators with varied biological profiles. Three notable compounds with aliphatic heads demonstrated balanced TRPV1 and CB1/CB2 agonism, while compounds with aromatic heads, particularly those with iodine, showed TRPV1 antagonism and CB2 agonism with varying stability.

Given the scarcity of TRPV1/CB2 agonists and the desirability of avoiding CB1-mediated psychoactive effects, we focused on **compound 41**. This compound features an ethanolamine head and a geranyl tail, exhibiting excellent metabolic stability and balanced TRPV1 (EC50 = 26.8 μM) and CB2 (EC50 = 37.8 μM) agonism. In patch-clamp assays, compound **41** showed efficacy similar to capsaicin in activating TRPV1 and inducing desensitization, while maintaining high selectivity over other targets like TRPM8 and TRPA1. Docking simulations predicted its binding at both the capsaicin site of TRPV1 and the orthosteric pocket of CB2.

In summary, the diversity-oriented approach led to the discovery of both single and dual-targeting compounds, suitable for either topical or systemic use. Among these, **compound 41** stands out due to its high synthetic feasibility, optimal stability, and low promiscuity, marking it as a promising candidate for treating pain and inflammatory disorders. Other compounds identified in our study also show potential as chemical probes for further understanding the EV/EC system.

3.2.1 Discussion:

The growing understanding of TRPV1's involvement in neuropathic pain prompted us to consider novel pharmacological approaches, including modulators that simultaneously target TRPV1 and cannabinoid receptors (191). The cross-talk between these systems offers a promising avenue for therapeutic development (186). While most TRPV1/CB dual modulators suffer from limitations such as high lipophilicity, poor metabolic stability, and off-target effects, recent advances using the Passerini reaction have enabled the synthesis of compounds with improved selectivity and tunable profiles (234). These compounds offer the dual advantage of desensitizing TRPV1 to reduce pain while engaging CB receptors to modulate inflammation and neuronal excitability.

Among the dual modulators identified, compound **41** emerges as a particularly promising candidate. It exhibits a well-balanced agonism for TRPV1 (EC50 = 26.8 μM) and CB2 (EC50 = 37.8 μM), with limited activity TRPM8 and TRPA1, two other TRP channels that are also implicated in chemotherapy-induced peripheral neuropathy. While TRPM8 and TRPA1 were not the primary targets in this study, their modest activation profile suggests potential additional contributions to the analgesic effect. Its robust metabolic stability and selective efficacy make it suitable for systemic administration, distinguishing it from previous compounds limited by poor drug-likeness. Moreover, docking simulations revealed that **41** effectively binds the capsaicin site on TRPV1 and the orthosteric pocket of CB2, confirming its dual-targeting mechanism.

The relevance of these findings to the PIPN model is clear. TRPV1 upregulation in IB4(-) neurons during paclitaxel treatment suggests that this channel contributes to the heat hyperalgesia and burning pain often reported by patients. The application of dual TRPV1/CB modulators, such as compound **41**, in this model could mitigate both nociceptor hyperexcitability and neuroinflammation, addressing the multifaceted nature of CIPN. Notably, the selective engagement of CB2 over CB1 minimizes psychoactive effects, enhancing the therapeutic safety profile.

Additionally, compound **41**'s ability to induce TRPV1 desensitization aligns with the resolution phase observed in our study, where nociceptor hyperexcitability subsides after the initial exposure to paclitaxel. Incorporating such modulators into CIPN management could not only alleviate acute symptoms but also prevent the cumulative damage

observed with repeated chemotherapy cycles.

The discovery of compound **41** and similar molecules also offers broader implications for other neuropathic pain conditions and inflammatory disorders. Their capacity to modulate TRPV1, CB1, and CB2 receptors paves the way for developing targeted therapies with minimal side effects. Furthermore, the compounds' chemical diversity and synthetic feasibility allow for their optimization as either soft drugs- compounds designed to be rapidly metabolized into inactive forms to minimize systemic exposure- for topical use or hard drugs, which are chemically stable and suitable for systemic administration, catering to diverse clinical needs (235).

3.3 CHAPTER 2.1: Optimizing new TRPV1 channel modulators for disease-modifying agents in neuropathy treatment – A pegylated TRPV1 antagonist.

Unpublished results of a TRPV1 antagonist, compound **AB9**, and its PEGylation during my secondment in Polypure (Oslo), a research-intensive production company specialized in R&D and manufacturing of uniform polyethylene glycol derivatives with a wide range of applications.

a. Development and evaluation of AB9: a potent TRPV1 antagonist for pain management.

After initially investigating ligands capable of dually modulating TRPV1, CB1, and CB2 receptors, we shifted our focus toward developing more selective strategies targeting TRPV1 alone. This change in direction was driven by the limitations encountered with **AG1529**, a capsaicinoid-based soft drug previously investigated by Nikolaeva et al. (199), to selectively inhibit TRPV1 activation by capsaicin without affecting proton-induced gating. Despite its promising selectivity, **AG1529** proved to be chemically unstable in aqueous environments, undergoing rapid hydrolysis that compromised its usability in therapeutic settings. The lack of aqueous stability not only limited formulation options but also hindered the generation of reproducible pharmacological data, prompting the need for a more stable TRPV1 antagonist with improved chemical robustness and bioavailability. To overcome these drawbacks, we explored two key approaches: the synthesis of a more chemically stable TRPV1 antagonist, and the formulation of PEGylated derivatives to enhance solubility and prolong bioavailability. This led to the development of **AB9**, a stable synthetic analogue of **AG1529** with improved pharmacological characteristics. The synthesis and chemical characterization of the compounds were carried out by the group of Prof. Tracey Pirali (Medicinal Chemistry laboratory), while all biological experiments and data analyses were performed by our group (Sensory neurobiology laboratory).

AB9 was designed as a "hard drug," eliminating the labile ester bond responsible for **AG1529**'s instability, while preserving its TRPV1 antagonistic profile. The pharmacological characterization of **AB9** was carried out in HEK293 cells expressing human TRPV1 (hTRPV1). Using whole-cell patch-clamp recordings, we observed that **AB9** acted as a moderate TRPV1 antagonist, showing measurable inhibitory effects at concentrations starting from 10 μM. A detailed dose-response analysis was conducted to determine its IC_{50}, allowing for a more accurate assessment of its potency. In addition to its TRPV1 activity, we also evaluated the selectivity of **AB9** against other thermoTRP channels, specifically TRPM8 and TRPA1. Although **AG1529** had previously shown minor cross-inhibition of these channels, **AB9** maintained a more selective profile, making it a stronger candidate for further development. To further enhance the solubility and pharmacokinetic properties of **AB9**, we initiated a PEGylation strategy in collaboration with Polypure (Oslo, Norway). The PEGylated derivatives were synthesized with the support of Dr. Erik Agner and Zuzanna Samol. PEG-based hydrogel matrices offer a promising delivery system, ensuring sustained in vitro release while maintaining compound integrity- an important feature in pain management applications (236). Given **AB9**'s pharmacological and structural properties, it represents a viable candidate for PEG-based encapsulation and targeted delivery. Ongoing studies aim to validate the efficacy of PEG-**AB9** formulations by assessing TRPV1 antagonist potency, selectivity, and long-term stability. Preliminary data are encouraging and support the continued development of **AB9** as a novel analgesic agent for treating chemotherapy-induced peripheral neuropathy (PIPN) and other chronic pain syndromes.

b. Synthesis of hard analogues of TRPV1 antagonists 2 and 3.

Given their strong antagonistic effects on TRPV1, different compounds were identified as promising soft drug candidates for further optimization into more chemically stable analogs- suitable for oral formulations aimed at alleviating burning mouth syndrome (BMS). In this context, the labile 2-oxo-ethyl linker was removed, while both the amide moiety and the length of the aliphatic chains were retained, resulting in the synthesis of amide derivative **26** (**AB9**), as shown in **Figure 29**.

The synthetic strategy outlined in **Figure 29** enabled the isolation of these target compounds in excellent overall yields. The key amide bond-forming step involved the coupling of dodecanoic or octanoic acid with the hydrochloride salt of vanillamine, using HATU as the coupling agent and DIPEA as the base. This step provided the intermediate **20** in good yield.

Attempts to liberate vanillamine from its hydrochloride salt using a saturated aqueous sodium carbonate solution followed by THF extraction proved inefficient due to difficulties in isolating the free base from the aqueous layer. As a result, an in-situ desalting strategy was adopted as a more effective alternative. To prevent degradation during the subsequent regioselective iodination, the phenolic hydroxyl group was temporarily protected with a tert-butyldimethylsilyl (TBDMS) group. Due to the reversible nature of this protection, additional quantities of TBDMSCl, DMAP, and imidazole were introduced after two hours to drive the reaction to completion, achieving yields of 85% for the intermediate **22**.

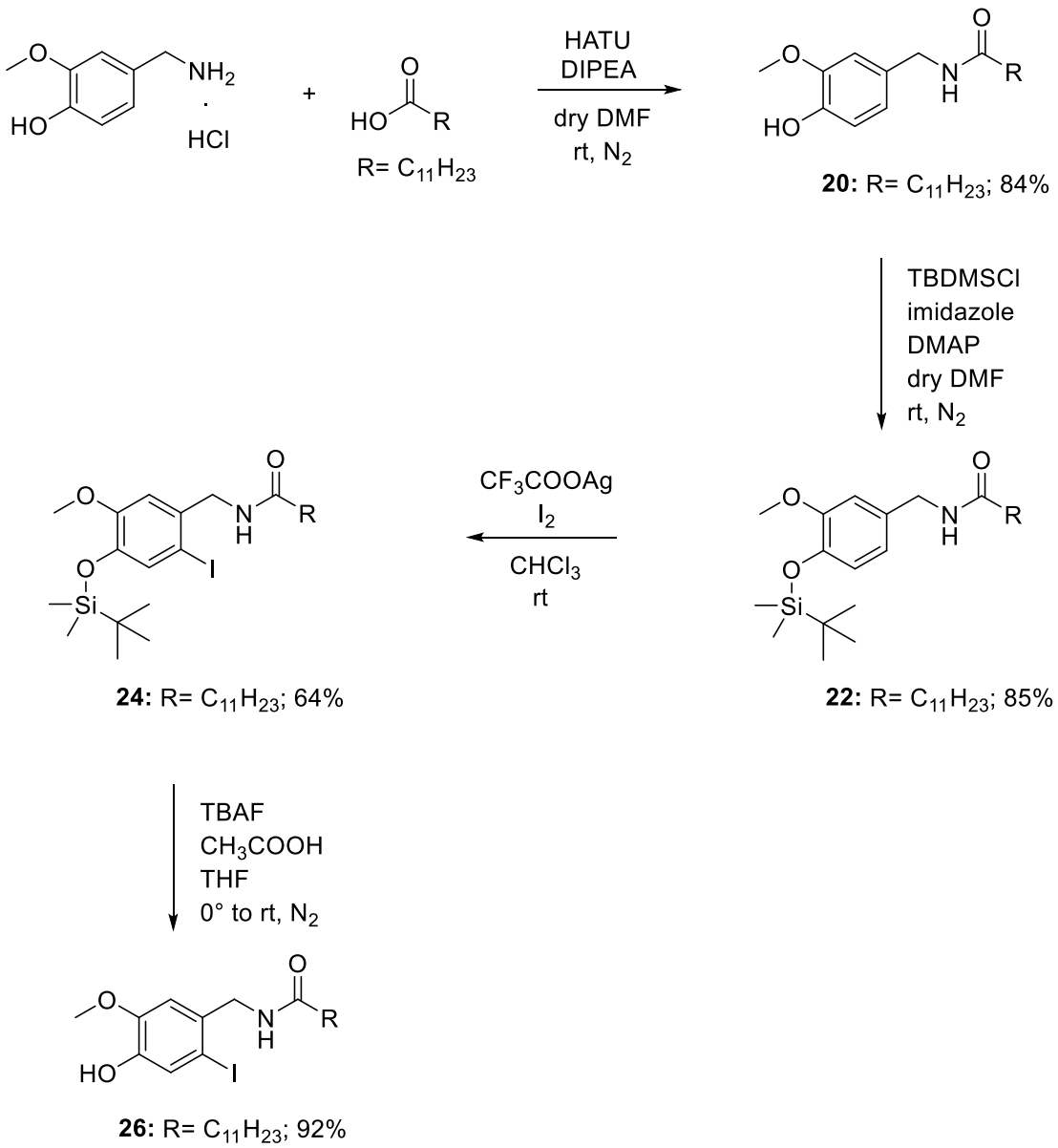

Figure 29: Multistep preparation of hard analogue 26 (AB9).

As previously discussed, selective iodination at position 6 of the vanillamide aromatic ring- located ortho to the benzylic position and para to the methoxy substituent- is a key structural modification known to shift TRPV1 activity from agonism to antagonism. To introduce the iodine atom at this specific site, intermediate **22** was reacted with molecular iodine and silver trifluoroacetate in chloroform, resulting in the formation of iodinated the derivative **24**.

Although full conversion of the starting materials was not achieved, reaction conditions were deliberately not intensified to minimize the risk of side reactions such as

deiodination. Consequently, the yields obtained in this step were slightly reduced compared to other transformations within the synthetic sequence, though they remained within acceptable ranges.

The final step involved the removal of the TBDMS protecting group. Treatment with tetrabutylammonium fluoride (TBAF) in tetrahydrofuran, supplemented with acetic acid to avoid undesired hydrolysis, successfully afforded the target compound **26** (**AB9**).

c. Efficacy of AB9 on hTRPV1 and mTRPV1

In order to evaluate the capacity of AB9 to modulate ion channel activity, we first conducted experiments on mouse dorsal root ganglion (DRG) neurons, a more physiologically relevant system expressing native TRPV1 channels. Initially, we observed that concentrations higher than 10 μM exhibited reduced efficacy compared to 10 μM, likely due to the compound's limited solubility at higher concentrations. To address this, we excluded the higher concentrations and included 0.1 and 0.5 μM. This modification enabled the construction of a dose-response curve (**Fig. 30A**), which revealed an IC_{50} of 0.4 ± 0.5 μM. To confirm these findings and support translational relevance, we performed parallel experiments in HEK cells expressing human TRPV1 (hTRPV1). The compound demonstrates effective interaction with the human TRPV1 channel, although it does not achieve complete inhibition at 10 μM. This partial inhibition is beneficial, considering that the complete inhibition of this pain-related channel is undesirable. Next, we investigated the efficacy of **AB9** on adult mouse neurons, demonstrating an IC_{50} of approximately 0.6 ± 0.2 μM (**Fig. 30B**). Notably, inhibition at 10 μM in these neurons appears to be more effective compared to the inhibition observed in HEK cells expressing the human TRPV1 channel. This suggests a potentially stronger interaction or a more favourable pharmacodynamic profile of the compound in mouse neurons. Together, these results highlight **AB9** as a TRPV1 modulator capable of exerting significant inhibitory effects in both heterologous human cell systems and DRG-mouse sensory neurons. Importantly, the compound's partial inhibition profile may offer a therapeutic advantage by attenuating pathological TRPV1 activity without completely blocking its physiological function, which is essential for maintaining normal thermosensation and protective pain

responses. These findings support the continued investigation of AB9 as a promising candidate for the treatment of TRPV1-related pain conditions.

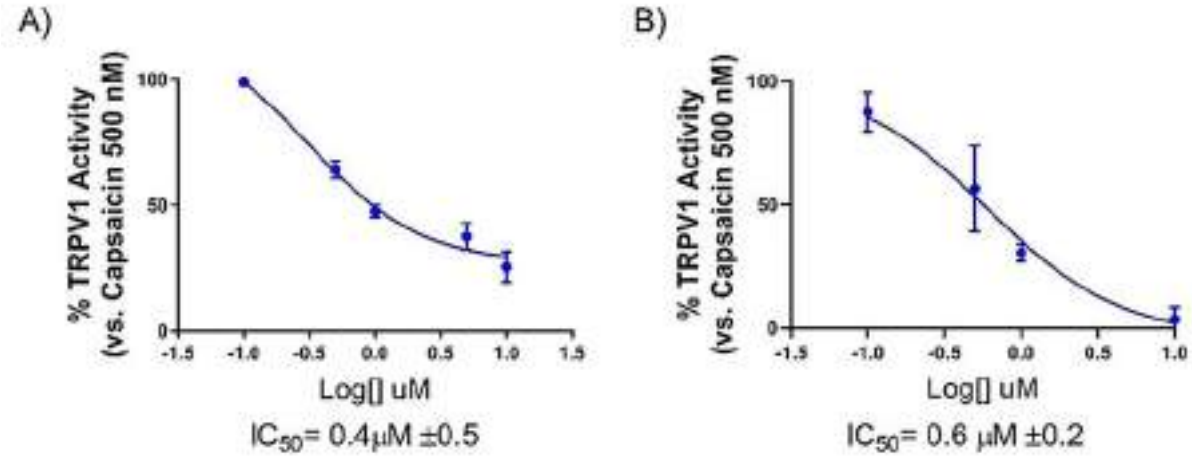

Figure 30. Compound **AB9** blocks Capsaicin-induced TRPV1 activation in HEK cells and murine nociceptors. (A) Dose-response curve for HEK-TRPV1 current blockade at a holding voltage of -60mV. (B) Dose-response curve for mouse TRPV1 current blockade at a holding voltage of -60mV. The line represents fits of the experimental data to the following equation: Y = Min inhibition + (Max inhibition- Min inhibition)/(1 + 10^((X-LogIC_{50}))) with a standard slope of 1.0 (Hill coefficient) and a restriction of the minimum (Top = 100). Each point is the mean ± SEM of n = 8For control conditions (untreated) cells were exposed to two pulses (0.5 µM) of Cap, interspaced by a washing period; whereas treated cells were exposed to one minute of **AB9** before the second pulse of Capsaicin.

d. Broad-Spectrum TRP Channel Inhibition by AB9 and Its Therapeutic Potential

We further investigated the inhibitory effects of **AB9** on other TRP channels using HEK cells expressing human TRPA1 and TRPM8. A single concentration of 10 µM, identified as the most effective on TRPV1, was tested. The results indicate that **AB9** also inhibits TRPA1 and TRPM8 channels (**Fig.31**). This multi-target inhibition, often viewed as a non-specific effect, could be therapeutically advantageous, especially in conditions like neuropathy where TRPA1, TRPM8, and TRPV1 are upregulated. Targeting all three channels with varying degrees of inhibition may offer comprehensive therapeutic benefits.

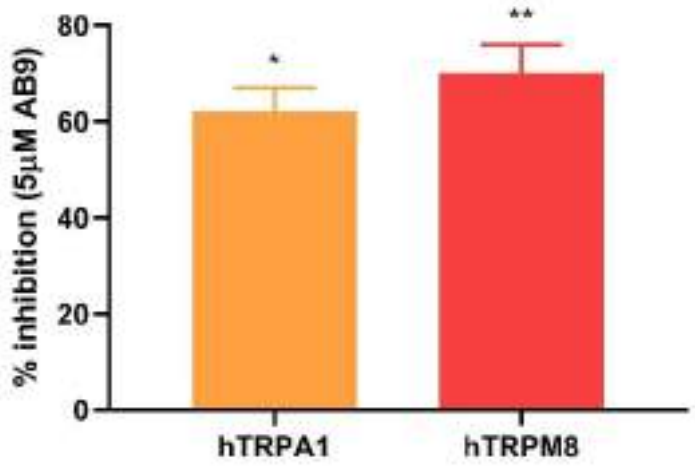

Figure 31. AB9 selectivity over Thermo-TRPs ion channels: 5 µM **AB9** inhibition over TRPA1 activity evoked by 60 µM AITC. (C) 5 µM **AB9** inhibition over TRPM8 activity evoked by 1 µM WS12 AITC considered as 100% of activity. Data were analysed using the non-parametric t-test Student, p-values for statistical differences are indicated for 5 µM **AB9** vs agonists. All data are expressed as mean ± SEM. N = 3; n = 6-8.

e. Pegylation of Capsaicin derivatives.

The secondment plan at Polypure focused on the compound **AB9**, previously studied pharmacologically on HEK cells heterologously expressed human TRPV1 (hTRPV1) and mouse DRGs sensory neurons. The soft antagonist **AG1529** exhibited poor stability in water and underwent hydrolysis when free or encapsulated in liposomes. This chemical instability prevented us from using a traditional water-based encapsulation system. The difference in stability between the hard drug (**AB9**) and the soft drug (**AG1529**) in water can be attributed to their chemical properties and molecular structures. In general, the term "hard drug" is used to describe a compound that is more chemically stable and less prone to degradation or hydrolysis in various environments, including water. For this reason, the objective was to promote the linkation of **AB9** to polyethylene glycol (PEG). First, we started with the pegylation of **AB9** precursor (phenyl-group). **Figure 33A** shows the different structures of the starting precursor, capsaicin (natural and synthetic) and the compound **AB9**. The compound **AB9** differs from the other for the iodin on the vanilloid ring which is crucial to the antagonism. PEG-based hydrogels have shown potential as an in-vitro encapsulation platform for pain relief. Polyethylene glycol (PEG) is commonly used in drug delivery systems, including encapsulation due to its biocompatibility and

versatility. When it comes to pain relief, PEG-based hydrogels have shown promise as effective delivery system for various analgesic drug. Also, it is a non-toxic system which allows a controlled (200). AB9, being more chemically stable ("hard drug"), was a viable candidate for formulation improvements. Given its high hydrophobicity- stemming from its long alkyl chain and amide bond—enhancing water solubility became a key formulation goal. PEGylation, the covalent attachment of polyethylene glycol, was pursued to improve both drug solubility and formulation performance. The rationale for PEGylation includes:

- Enhanced water solubility, due to PEG's hydrophilic and biocompatible properties, allowing better formulation in aqueous systems.
- Extended drug circulation time, as PEGylation can reduce enzymatic degradation and renal clearance.
- Reduced aggregation and improved encapsulation into delivery systems such as hydrogels.
- Preservation of biological activity: by modifying the alkyl chain without altering the hydroxybenzylamine pharmacophore, biological targeting is maintained.

Pegylation method: All compounds in the study feature a long alkyl chain attached via an amide bond, contributing to their high hydrophobicity. The aim was to explore strategies to increase the hydrophilicity of these compounds without compromising their biological activity, particularly their ability to anchor to the receptor. **Figure 32B** shows the pegylation method used to develop a library of PEG-compounds. One approach was to replace the alkyl chain with PEG (polyethylene glycol) conjugates that have alkyl or lipid chains. This involves multiple steps. The first step was to develop a library of PEG derivatives. This library served as a foundation for further modifications. The second step was to attach PEG to hydroxybenzylamine, a cost-effective and readily available reagent that mimics the biologically active part of capsaicin derivatives. This step was crucial for creating compounds that maintain biological activity while improving hydrophilicity. The third step involved using computer modeling to analyze these derivatives. By simulating

their interactions and properties, we can identify the most promising strategies for further development. Once the optimal strategies are identified, we will collaborate with Tracey Pirali's group to synthesize the **AB9** compound with a modified chain, ensuring the new structure enhances hydrophilicity without losing biological efficacy. In the initial stage, PEG-functionalized products of varying lengths were prepared, providing a range of options to test and refine. This approach seeks to optimize both hydrophilicity and bioactivity, potentially improving drug delivery and efficacy in pain management applications.

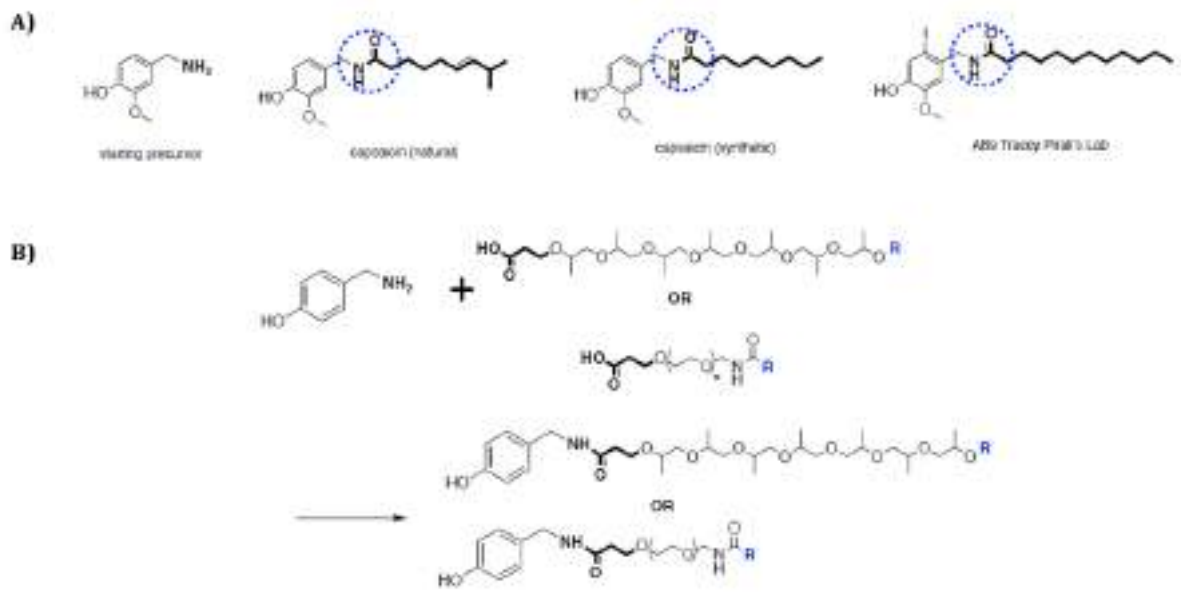

Figure 32. Pegylation method used. (A) Chemical structure of the starting precursor, Capsaicin (natural), Capsaicin (Synthetic), and **AB9**. (B) Chemical reaction used to attach the Capsaicin precursor to different PEG length.

f. PEG-23 seems to be the best compound in terms of solubility

Among the 19 synthesized PEG compounds, including variants such as PEG7, PEG11, and a branched compound PEG14, the C10-amido-PEG23-hydroxybenzylamide emerged as the most soluble. This achievement marks a significant milestone in our pegylation efforts, as the primary objective was to enhance the solubility of the compound. Despite this success, it is important to note that the biological activity of C10-amido-PEG23-hydroxybenzylamide has not yet been confirmed. Further studies will be required to

evaluate whether the increased solubility also translates to maintained or improved biological efficacy. **Figure 33A** shows that the compound C10-PEG23 has a soap-like appearance. Furthermore, as illustrated in **Figure 33B**, it demonstrates complete solubility when dissolved in distilled water.

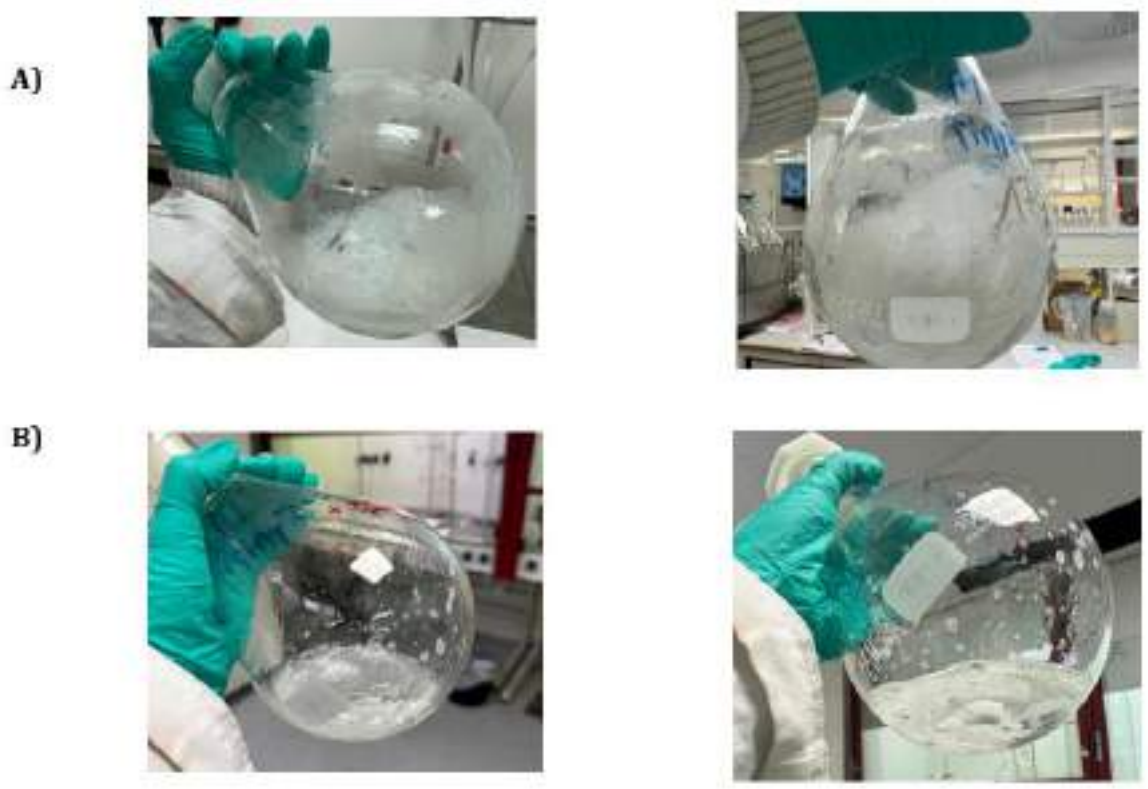

Figure 33. Aspect of C10-PEG23. (A) C10-PEG23 aspect with any solvent. (B) C10-PEG23 aspect after adding distilled water.

g. Docking studies.

After confirming that it was possible to attach PEG of various lengths to the vanilloid ring and achieve more soluble compounds, we conducted modeling studies before proceeding with biological analyses. Indeed, the third step involved using computer modeling to analyze these derivatives (**Fig.34-Table 7**). By simulating their interactions and properties, we aimed to identify the most promising strategies for further development. The docking results, expressed in energy values (kcal/mol), provided valuable insights. Specifically, PEG11 showed the highest binding energy values (5.96 kcal/mol for TRPV1h and 5.12 kcal/mol for TRPV1s), indicating strong interactions. While

longer PEG chains typically resulted in better binding, PEG23 was an exception with lower energy values (4.39 kcal/mol for TRPV1h and 4.58 kcal/mol for TRPV1s). The compounds demonstrated similar binding affinities for both human and squirrel TRPV1. For example, PEG11 bound to TRPV1 with its vanilloid group occupying a pocket equivalent to that of capsaicin, as illustrated by its surface representation with 20% transparency. This binding behavior was observed for PEG11, PEG14b, and PEG23 in TRPV1h, where the vanilloid moiety was buried in the capsaicin pocket. In contrast, other compounds positioned the vanilloid group differently from capsaicin in their top predictions. These findings guide us in selecting and optimizing compounds for further development, with PEG11 showing particular promise due to its effective binding and favorable orientation within the receptor.

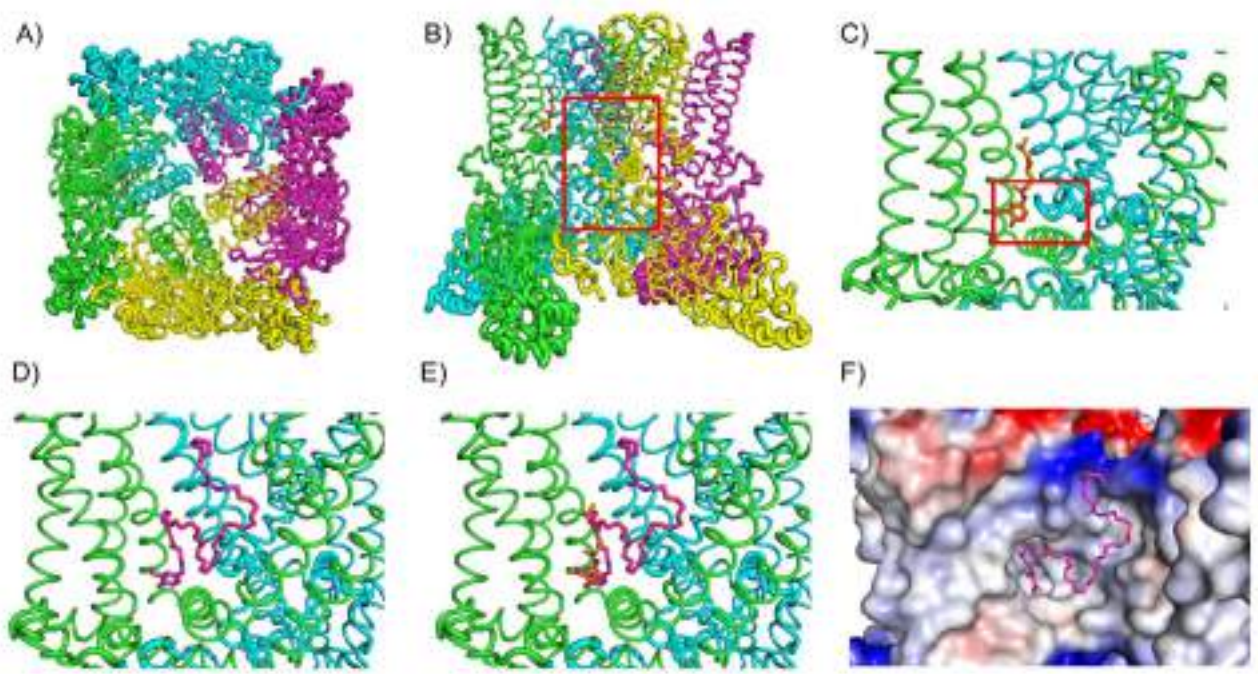

Figure 34. Docking modelling of TRPV1 binding to different length of PEG. A) Squirrel TRPV1 in complex with capsaicin (PDB: 7LR0)- top view. B) Squirrel TRPV1 in complex with capsaicin (PDB: 7LR0)- side view. C) Zoom of capsaicin bound to capsaicin binding site. The vanilloid nucleus is buried in a hydrophobic pocket formed by S3, S4 and S4-S5 linker. D) PEG11 bound to the TRPV1. The vanilloid group occupies an equivalent pocket than capsaicin. This is not the case for all samples: In TRPV1h, the compounds that buried the vanilloid moiety into the capsaicin pocket were: PEG11, PEG14b, and PEG23. E) Comparison between capsaicin and PEG11 location. F) TRPV1 represented as surface with a 20% transparency. PEG11 buries the vanilloid group while the rest of the PEG11 molecule adapts well to the TRPV1 surface.

PEGs length	hTRPV1 (human)	sTRPV1 (squirrel)
PEG7	4.85	5.57
PEG11	5.96	5.12
PEG14b	5.39	5.36
PEG23	4.39	4.58

Table 7: Energy values of ligand receptor interaction in Kcal/mol.

The TRPV1 antagonist, **AB9**, holds significant potential for the treatment of chemotherapy-induced peripheral neuropathy (CIPN) (185,237). Given its moderate efficacy as a TRPV1 antagonist, further exploration is warranted to enhance its therapeutic profile. In our studies, we successfully identified that various PEG lengths could be attached to the vanilloid ring, improving the solubility of the compound. Specifically, PEG11 showed the most promise, exhibiting effective binding and a favorable orientation within the TRPV1 receptor. This finding is pivotal as it guides our future efforts to optimize **AB9** for therapeutic use.

Future investigations will focus on modifying the PEGylated **AB9** structure by introducing an iodine atom on the vanilloid ring. This modification aims to restore the antagonistic properties of **AB9** while maintaining the advantageous solubility and metabolic stability provided by PEG. The resulting compound will be structurally similar to **AB9** but without the PEG moiety, enabling more targeted and effective treatment strategies for CIPN, potentially improving pain management for chemotherapy patients.

3.3.1 Discussion:

Following the in vitro characterization of TRPV1 upregulation in the PIPN model and the investigation of a dual agonist targeting both TRPV1 and CB2, we deemed it essential to further explore the therapeutic potential of TRPV1 antagonism. While agonist activity may offer desensitizing effects, the direct inhibition of TRPV1 represents a complementary strategy aimed at reducing nociceptor hyperexcitability and alleviating neuropathic pain. In this context, we focused on the synthesis and evaluation of compound **AB9**, a rationally designed TRPV1 antagonist, to assess its pharmacological profile and potential use in pain modulation. **AB9**'s development and characterization involved intricate synthesis, biological evaluation, pegylation, and computational modeling, offering insights into its

functionality and therapeutic applicability.

AB9 was identified as a moderate TRPV1 antagonist with an IC_{50} in the sub-micromolar range for both human and mouse TRPV1 channels. While it showed effective inhibition, its partial activity suggests that it may allow channel functionality to recover post-treatment, a characteristic potentially favorable for long-term pain management by avoiding complete desensitization of TRPV1. Cross-inhibition of TRPA1 and TRPM8 by **AB9**, often regarded as a non-selective effect, may be advantageous for managing neuropathic pain, where upregulation of multiple TRP channels is commonly observed. This broad-spectrum activity underscores **AB9**'s therapeutic promise for conditions such as chemotherapy-induced peripheral neuropathy (CIPN) and burning mouth syndrome (BMS). On the other hand, **AB9**'s limited water solubility presented a significant challenge, particularly at concentrations above 10 μM. While calcium imaging suggested no toxicity at higher doses, patch-clamp assays revealed possible cytotoxicity, emphasizing the need for precise and sensitive methods to assess its bioactivity. Furthermore, the instability of its precursor, **AG1529**, highlighted the importance of structural modifications to improve chemical robustness (199) These observations guided the design of **AB9** as a "hard" analogue with improved stability.

To overcome the challenges related to solubility, we explored the use of pegylation, a process that involves attaching polyethylene glycol (PEG) molecules to compounds (200). By testing a range of PEG derivatives, we aimed to improve the compound's water solubility, making it more suitable for therapeutic use. This modification enhances the stability and bioavailability of the drug, which is crucial for ensuring its effectiveness and ease of administration in clinical settings. PEGylation is a well-established strategy in drug development that helps optimize the properties of therapeutic agents, improving their performance while minimizing side effects (236,238). First, we tested a **AB9**-like structure with the vanilloid ring, without the presence of the iodine. The process successfully increased hydrophilicity, with *PEG23* emerging as the most soluble derivative, forming a completely water-dispersible compound. While the biological activity of the pegylated derivatives has yet to be confirmed, these modifications provide a foundation for developing formulations that balance solubility and activity. PEGylation also facilitates controlled drug release, aligning with the needs for sustained analgesia in pain

management. Computational docking studies reinforced the experimental findings, showing favorable binding of PEGylated derivatives, particularly *PEG11*, to the TRPV1 receptor. The positioning of *PEG11*'s vanilloid group in the capsaicin-binding pocket mimics the interaction of capsaicin, maintaining the critical pharmacophore-receptor relationship. This structural alignment provides a strong rationale for prioritizing *PEG11* for further optimization.

3.4 CHAPTER 3: Optimizing new TRPM8 channel modulators for disease-modifying agents in neuropathy treatment – A TRPM8 antagonist.

The results of compound **23**, a TRPM8 antagonist, were published in the FEBS journal. The synthesis and chemical characterization of the compounds were carried out by the group of Prof. Ubaldina Galli (Medicinal Chemistry laboratory), while all biological experiments and data analyses were performed by our group (Sensory neurobiology laboratory). Dr. David Cabañero Ferri performed the in vivo experiments.

Results obtained from paper 3:

- Lamberti A., Aprile S., Cabañero D., Travagin F., Butron L., Fernández-Ballester G., Tron G.C., Fernández-Carvajal A,, Ferrer-Montiel A., Galli U. An adamantane-based ligand as a novel chemical tool for thermosensory TRPM8 channel therapeutic modulation. 2025; **doi:** 10.1111/febs.70065.

a. Design and therapeutic evaluation of TRPM8 antagonists for peripheral neuropathies.

Building upon our previous findings in the in vitro PIPN model, where we observed a significant upregulation not only of TRPV1 but also of TRPM8 channels (**Fig 19**), it becomes evident that TRPM8 may also play a key role in the development of chemotherapy-induced sensory abnormalities, including cold hypersensitivity. This observation guided our subsequent investigation into TRPM8 modulation, expanding our focus beyond TRPV1 to include cold-sensitive pathways. The transient receptor potential melastatin 8 (TRPM8) is a critical ion channel involved in sensing cold temperatures and cooling agents, such as menthol, in peripheral nociceptors (51). Dysfunction of TRPM8 has been linked to sensory disturbances, including cold allodynia, making it a valuable target for therapeutic intervention in various conditions, from peripheral neuropathies to cancer (54,239). Given its broad expression across different tissues, the development of selective TRPM8 modulators is a key area of focus in drug discovery. In this study, we

explore the design of a novel class of TRPM8 modulators using the adamantane ring as a scaffold (240). Leveraging efficient multicomponent reactions, we synthesized a series of compounds that include both TRPM8 agonists and antagonists. Among them, compound **23** emerged as a potent and selective TRPM8 antagonist, demonstrating significant efficacy in reducing TRPM8-induced neuronal firing and offering promising therapeutic potential for treating TRPM8-related peripheral neuropathies, such as oxaliplatin-induced cold allodynia (56).

b. Synthesis and evaluation of TRPM8 agonists and antagonists: insights from Passerini, UGI, and split-UGI reactions.

The study involved synthesizing a series of compounds using the Passerini, Ugi, and split-Ugi multicomponent reactions (**Fig. 35**) (190,234). The key reagent used was 1-isocyanoadamantane (**3**), derived from 1-aminoadamantane (**1**), and reacted with various carboxylic acids and amines in the presence of formaldehyde. The resulting compounds were tested for their activity on the human TRPM8 channel, expressed in HEK293 cells, using Ca2+ microfluorimetry to assess their potential as agonists or antagonists.

For the Passerini reaction, compounds **20-29** were synthesized, with compounds **20, 21, 23, 25,** and **29** identified as TRPM8 antagonists, with compound **23** being the most potent (IC_{50} = 0.2 μM). Compounds **22**, **24**, and **27** exhibited agonistic activity, with potency influenced by changes in the hydrocarbon side chain and the addition of nucleophile atoms like nitrogen and oxygen. The structure-activity relationship suggested that modifications to the aromatic ring altered the ligand-channel interaction and its allosteric effects (**Fig. 35A**).

In the Ugi reaction, compounds **30-41** were synthesized, showing a mix of agonists and antagonists, with agonists being more common. Compounds **33** and **35** showed moderate antagonistic activity, while other compounds, like **31**, displayed potent agonistic activity (EC_{50} = 0.3 μM). The substitution of ester with amide groups did not significantly affect activity but contributed to subtle changes in potency. Notably, compound **32**, an α-aminoacyl amide, was a potent TRPM8 agonist, in contrast to compound **25**, which was an antagonist (**Fig. 35B**).

Finally, the split-Ugi reaction produced four α-acylpiperazino amides (**42-45**), all of which

acted as TRPM8 agonists, though with lower potency compared to the other compounds. For example, compound **42** was compared to compound **30**, while compound **43** displayed agonist activity, albeit at a lower potency (**Fig. 35B**).

In conclusion, the study identified a series of novel TRPM8 agonists and antagonists, highlighting compound **23** as a potent antagonist with therapeutic potential. The structural modifications made to the compounds significantly influenced their biological activity, offering valuable insights into the design of TRPM8-targeting drugs.

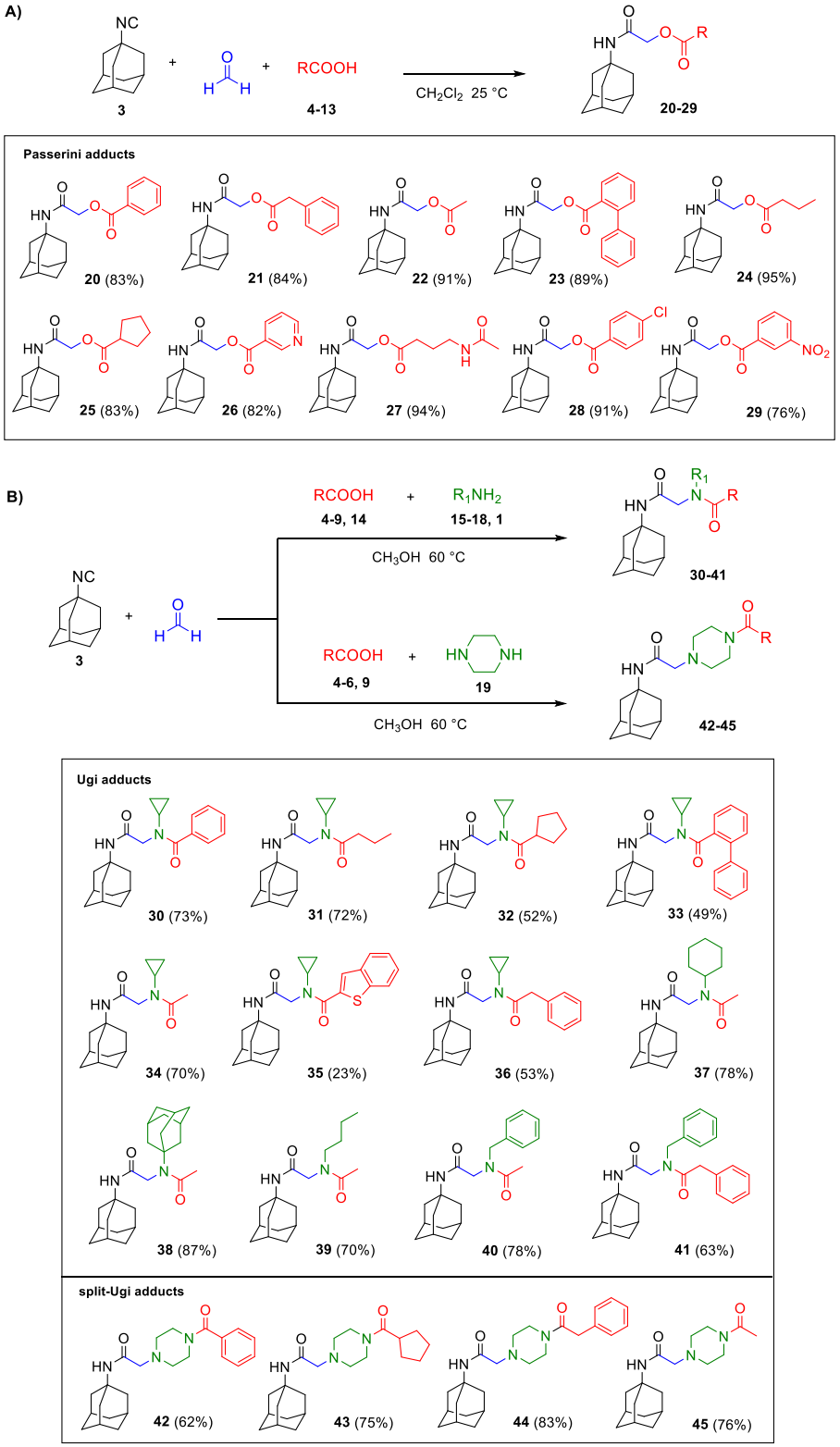

Figure 35. Passerini and Ugi reactions. (A) Preparation of α-acyloxy carboxamides **20-29** *via* Passerini reaction, and compounds obtained. **(B)** Synthesis of α-aminoacyl amides **30-41** and α-acylpiperazino amides **42-45** exploiting the Ugi and split-Ugi reactions respectively, and compounds obtained.

c. α-acyloxy carboxamide 23 is a potent hTRPM8 competitive WS-12 antagonist.

α-Acyloxy carboxamide **23** acts as a potent competitive antagonist against WS-12 at the hTRPM8 receptor (**Fig.36D**). Selected as the strongest antagonist in this study (IC50 = 0.2 ± 1.3 μM), it was further characterized in both in vitro and in vivo tests. Using patch-clamp assays, we evaluated compound **23**'s ability to inhibit WS-12-evoked ionic currents in hTRPM8-HEK293 cells. At a concentration of 1 μM, α-acyloxy carboxamide **23** reduced WS-12-evoked inward currents by over 75%, as shown in **Figure 36A**. This inhibition was reversible, with full recovery of WS-12-evoked currents upon washout (**Fig. 36A**, bottom), thus avoiding potential use-dependent side effects. A dose-response analysis revealed an IC50 of 0.08 ± 0.07 μM and a Hill coefficient of 1 (**Fig. 36B**), confirming its potency as an hTRPM8 antagonist.

To clarify whether the inhibition is competitive, we assessed α-acyloxy carboxamide **23**'s effect on WS-12's potency. By generating WS-12 dose-response curves with and without 80 nM of compound **23** (matching its IC_{50}), we observed a rightward shift of the WS-12 EC_{50} from 3 μM to 15 μM (approximately a five-fold increase) without altering agonist efficacy, as shown in **figure 36C**. This shift suggests α-acyloxy carboxamide **23** competes with WS-12 for the same or nearby binding site on the receptor.

Further evidence of competitive antagonism was provided by a Schild plot, where WS-12 and antagonist **23** were analyzed across four concentrations (0.02, 0.08, 0.1, 0.5 μM) (**Fig. 36D**). The Schild equation Y = 1.003*X + 1.469, with a slope of 1.003, a 1/slope of 0.9973, an R square of 0.9307, and a P value of 0.0353, confirms that compound **23** behaves as a classical competitive antagonist. The slope close to 1 suggests reversible binding at the same site as WS-12 without affecting its maximum response. The high R square value underscores data reliability, while the P value indicates statistical significance. This competitive antagonism is further characterized by a rightward shift in the dose-response curve with no change in maximum response, implying higher agonist concentrations are needed to achieve the same effect in the presence of the antagonist.

To reinforce the competitive nature of the blockade, we tested for voltage dependence of compound **23**'s antagonistic action (**Fig. 36E**). Using 100 ms voltage ramps from -120 mV to 120 mV, we recorded WS-12-activated current in the absence and presence of 80

nM α-acyloxy carboxamide **23**. The current density (J)-V relationships (**Fig. 36E**) for compound **23** and the established TRPM8 antagonist AMTB showed consistent WS-12 inhibition across all tested voltages, indicating a voltage-independent blockade. This observation further supports compound **23**'s competitive and voltage-independent mechanism of action.

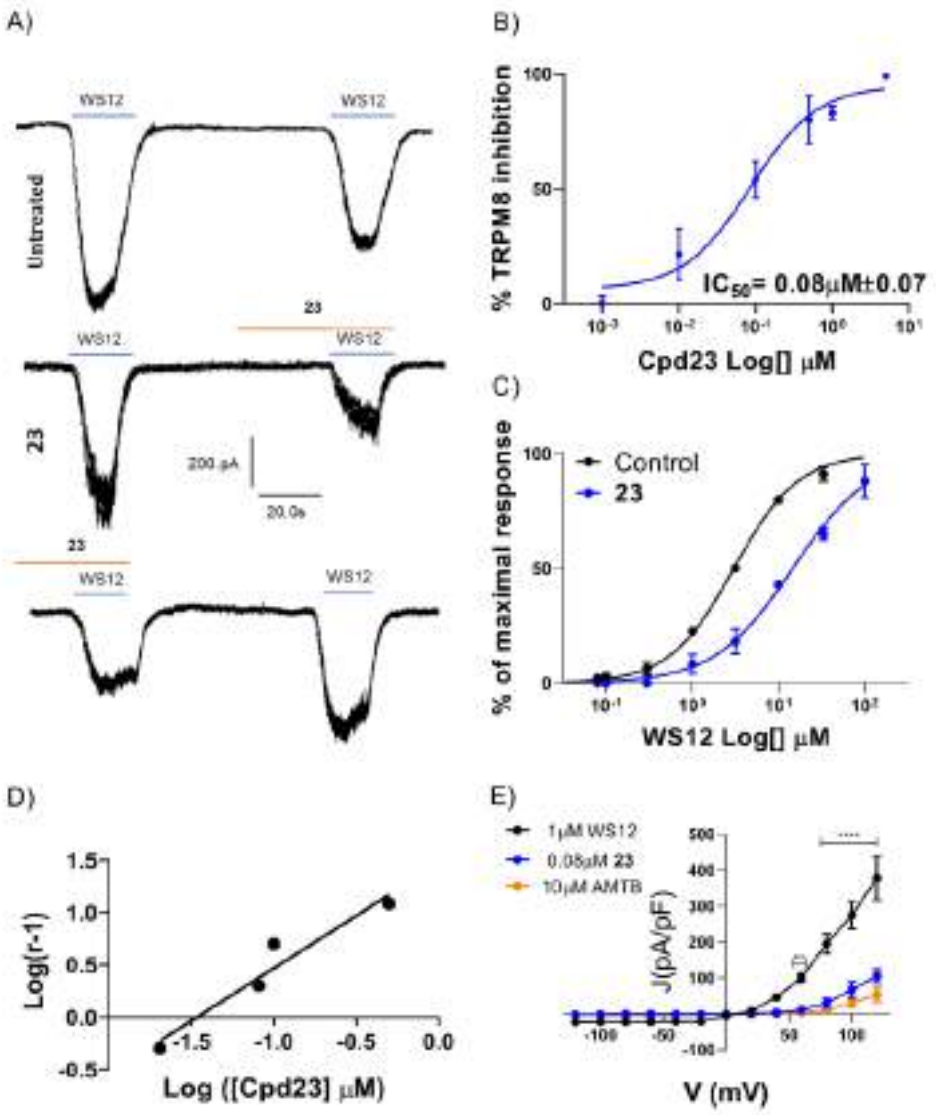

Figure 36. Compound 23 is a hTRPM8 competitive blocker with nanomolar potency. (A) Representative traces of WS-12-evoked ionic currents recorded at a holding potential of -60mV in hTRPM8 HEK cells. (B) Dose-response curve for hTRPM8 current blockade at a holding voltage of -60mV. The line represents the fit of the experimental data to the Hill equation: Y = Bottom + (Top-Bottom)/(1 + 10^((X-LogIC$_{50}$. Each point is the mean ± SEM of n = 10. (**C**) WS-12 dose-response curve in the absence (black) or presence of 0.08 µM compound **23** (blue). The best fitted values for WS-12 EC$_{50}$ value were 3.0 µM (95% CI 2.5-3.68 µM) (n = 18) in the absence of 0.1 µM compound **23** and 15 µM (95% CI 12.8–16.8 µM) in its presence (blue curve, n = 16, Top=100). Hill coefficient in the absence of compound **23** was 1.17 (0.9–1.4) and in its presence was 0.95 (95% CI 0.8–1.0). All data is expressed as mean ± SEM. (**D**) Schild plot derived from the interaction between agonist (WS12) and antagonist (**23**). Equation: Y = 1,003*X + 1,469; Slope: 1.003; 1/Slope: 0.9973; Std. error: 0.1935. R square: 0.9307; P value: 0.0353. **(E)** Representative current density (J)-V curves elicited by a protocol of voltage steps from -120 mV to 120 mV in steps of 20 mV. Each point is the mean ± SEM of n=8. Data were analyzed using a Two-Way ANOVA followed by a Sidak post-hoc test when appropriate, P-value **= 0.0069; **** <0.0001.

d. Compound 23 Shows Limited Activity on TRPV1 and TRPA1

To assess the receptor selectivity of compound **23**, we examined its effects on the hTRPV1 and hTRPA1 channels, expressed in HEK293 cells (**Fig. 37**). These channels, structurally similar to hTRPM8 and expressed in peripheral nociceptive neurons, were chosen due to potential ligand cross-reactivity compound **23** inhibited approximately 50% of hTRPV1 channel activity with an IC_{50} of 1.1 ± 1.02 μM (**Fig. 37A**). At a higher concentration of 5 μM, compound **23** reduced hTRPA1-evoked current by about 40%, yielding an IC_{50} of 3.04 ± 2.01 μM (**Fig. 37B**). In comparison, the reference TRPA1 antagonist HC030031 completely blocked AITC-evoked ionic currents at the same concentration (5 μM, **Fig. 37C-D**). These results suggest that α-acyloxy carboxamide **23** is more selective for hTRPM8, being at least 10 times more potent against hTRPM8 than hTRPV1 and hTRPA1 channels.

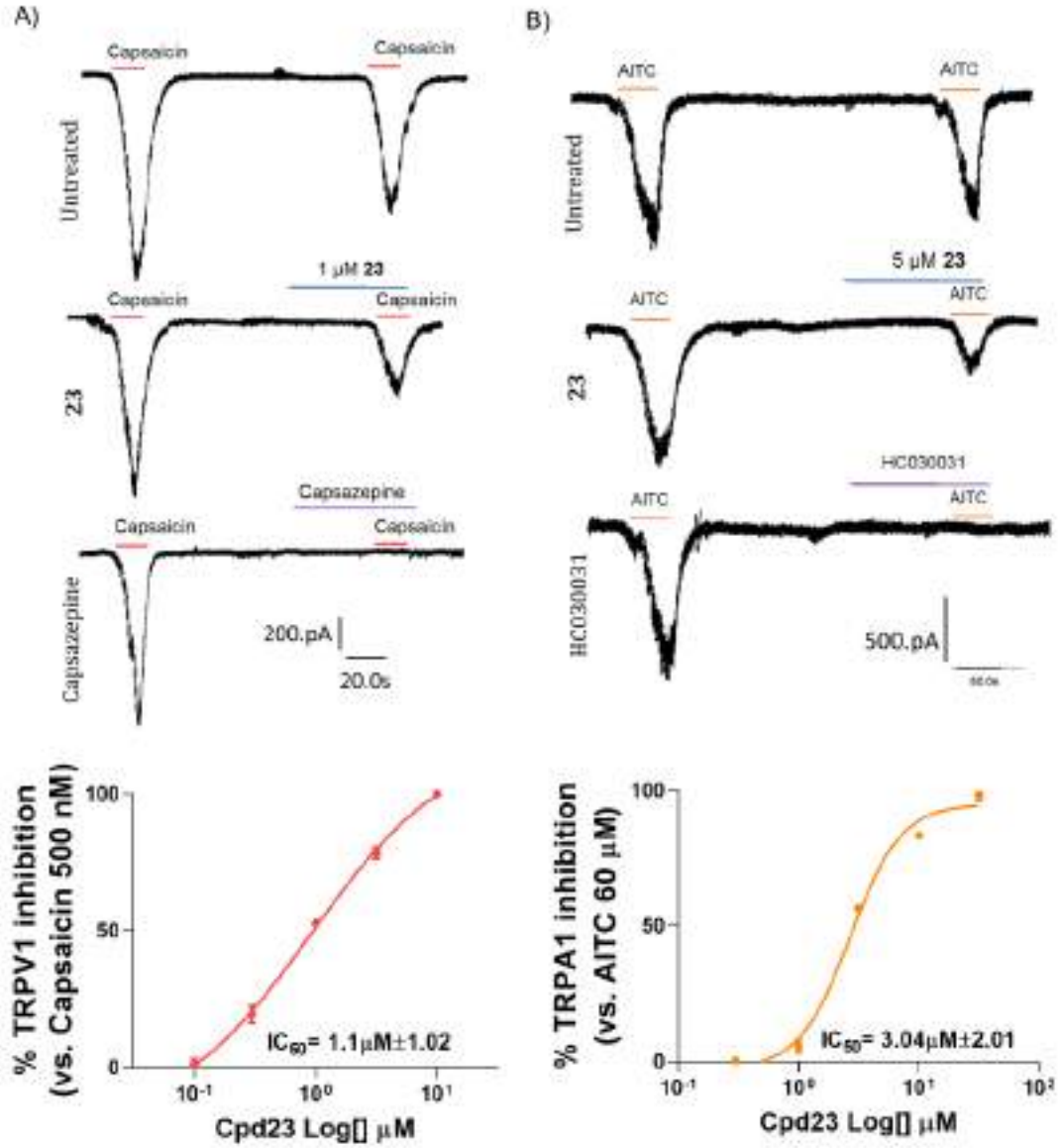

Figure 37. Compound 23 modestly inhibits currents of hTRPV1 and hTRPA1 expressed in HEK293 cells. (A) Representative capsaicin (0.5 µM)-evoked hTRPV1 inward currents recorded at a holding potential of -60mV, for control cells (Untreated) and cells treated with 1 µM compound **23** or 10 µM of Capsazepine. Red lines represent the duration of the capsaicin pulse. (B) Dose-response curve for hTRPV1 current blockade at a holding voltage of -60mV. The line represents the fitted curve of the experimental data to Hill equation. Each point is the mean ± SEM of n = 6. (C) Representative AITC (60 µM) evoked hTRPA1 inward current recorded at a holding potential of -60mV, for control cells (Untreated) and cells treated with 5 µM compound **23** or 5 µM of HC030031. Orange lines represent the duration of AITC pulse. (D) Dose-response curve for hTRPA1 current blockade at a holding voltage of -60mV. The line represents fits of the experimental data to the Hill equation. Each point is the mean ± SEM of n = 8.

e. Compound 23 Inhibits Neuronal TRPM8 and Reduces WS-12-Induced Neuronal Firing

To explore the in vivo effects of compound **23**, we first assessed its inhibition of TRPM8 channels in murine primary nociceptors expressing fluorescently labeled TRPM8, using patch-clamp analysis. As shown in **figure 38A**, 5 μM of compound 23 reduced WS-12-evoked ionic currents by 60% in dorsal root ganglion (DRG) neurons, with a calculated IC50 of 0.43 ± 0.75 μM (**Fig. 38B**). This lower potency against murine TRPM8 compared to the human ortholog may relate to a predicted reduced binding energy or potential differences in channel gating or neuronal environment.

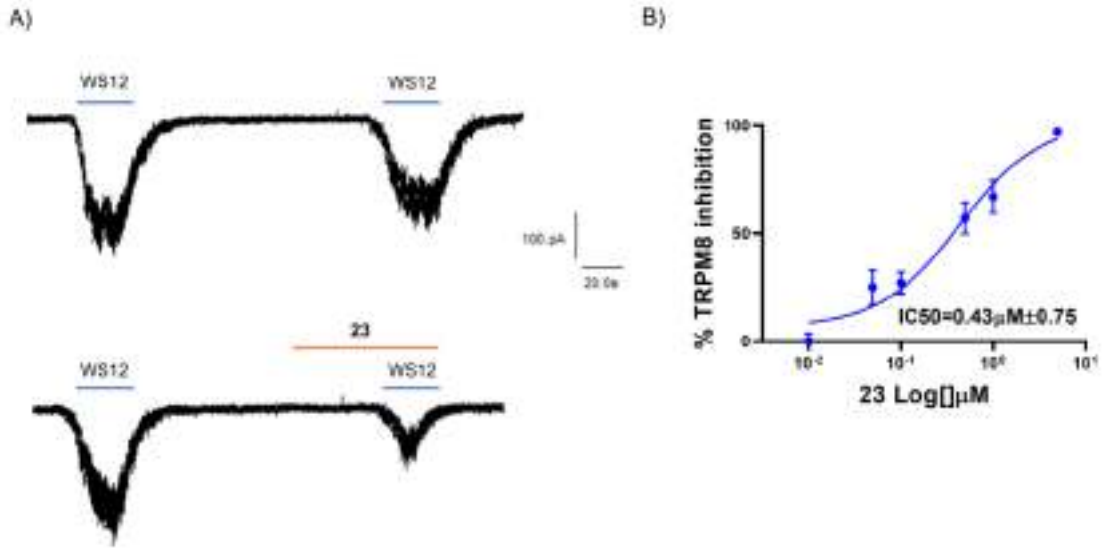

Figure 38. Compound 23 blocks WS-12-induced TRPM8 activation in murine nociceptors. (A) Representative WS-12-evoked currents in DRG neurons of neonatal rats recorded at a holding potential of -60mV. For control conditions (untreated) cells were exposed to two pulses (1 μM) of WS-12, interspaced by a washing period, whereas treated cells were exposed to one minute of compound **23** before the second pulse of WS-12 (B) Dose-response curve for mTRPM8 current blockade at a holding voltage of -60mV. The line represents fits of the experimental data to the Hill equation. The fitted value for IC_{50} was 0.43 μM ± 0.75. Each point is the mean ± SEM of n = 8.

Next, we assessed compound **23**'s effect on WS-12-induced action potentials in murine DRG sensory neurons using multielectrode arrays (MEAs). Applying compound 23 at its IC_{50} (0.43 μM) significantly reduced neuronal firing induced by WS-12, with a sequential protocol used to account for channel desensitization (**Fig. 39A**). Compared to AMTB at 10 μM, compound **23** (0.43 μM) was more effective, reducing action potential frequency by over 75% (**Fig. 39B**).

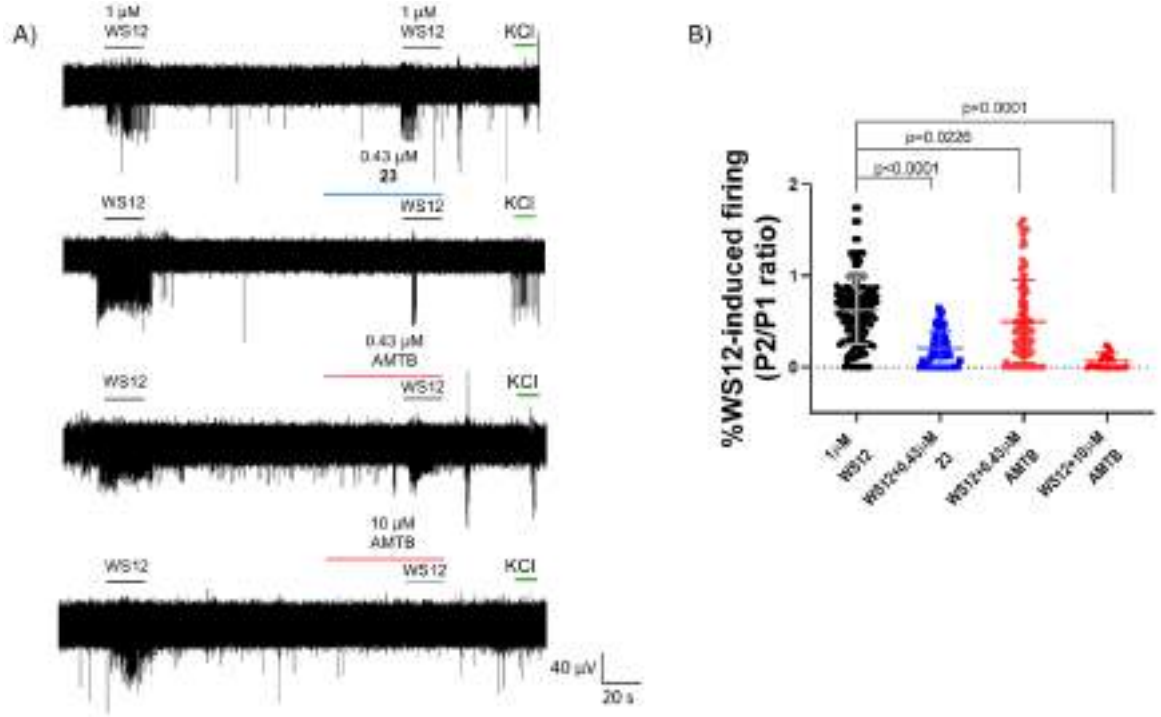

Figure 39. Compound 23 reduces WS-12-induced excitability of murine nociceptors. (A) Multi-Electrode Array (MEA) recordings, with representative traces showing WS-12-evoked action potential (AP) firing under different conditions: control, 0.43 µM compound **23**, 0.43 µM AMTB and 10 µM AMTB. WS-12 (1 µM) was applied in two consecutive pulses, with compounds added 1 minute before the second pulse. The protocol concluded with a 15 s-pulse of 40 mM KCl to ensure neuronal viability. (B) Normalized WS12-induced firing (P2/P1) in the absence (vehicle) and presence of antagonists (0.43 µM compound **23**, 0.43 µM AMTB and 10 µM AMTB) were compared. Data were analyzed with One-Way ANOVA followed by Dunnet test, p-values for statistical differences are indicated. The number of independent experiments (N) was 3, with 60-100 electrodes per condition.

We also tested the influence of compound **23** on capsaicin- and AITC-induced excitability in murine nociceptors, targeting TRPV1 and TRPA1 at their respective IC_{50} concentrations (1 µM for TRPV1 and 5 µM for TRPA1) based on its partial blocking capacity (**Fig. 40**). Employing a dual-pulse protocol, compound **23** was administered one minute prior to and during the second agonist pulse. Results show that compound **23** attenuated capsaicin and AITC responses by 30% and 40%, respectively, demonstrating a primary selectivity for TRPM8 with limited cross-reactivity to TRPV1 and TRPA1 (**Figs. 40B-D**). Overall, α-acyloxy carboxamide **23** emerges as a novel TRPM8 antagonist with a selective blockade of TRPM8 and a reduction in receptor-agonist-induced neuronal excitability.

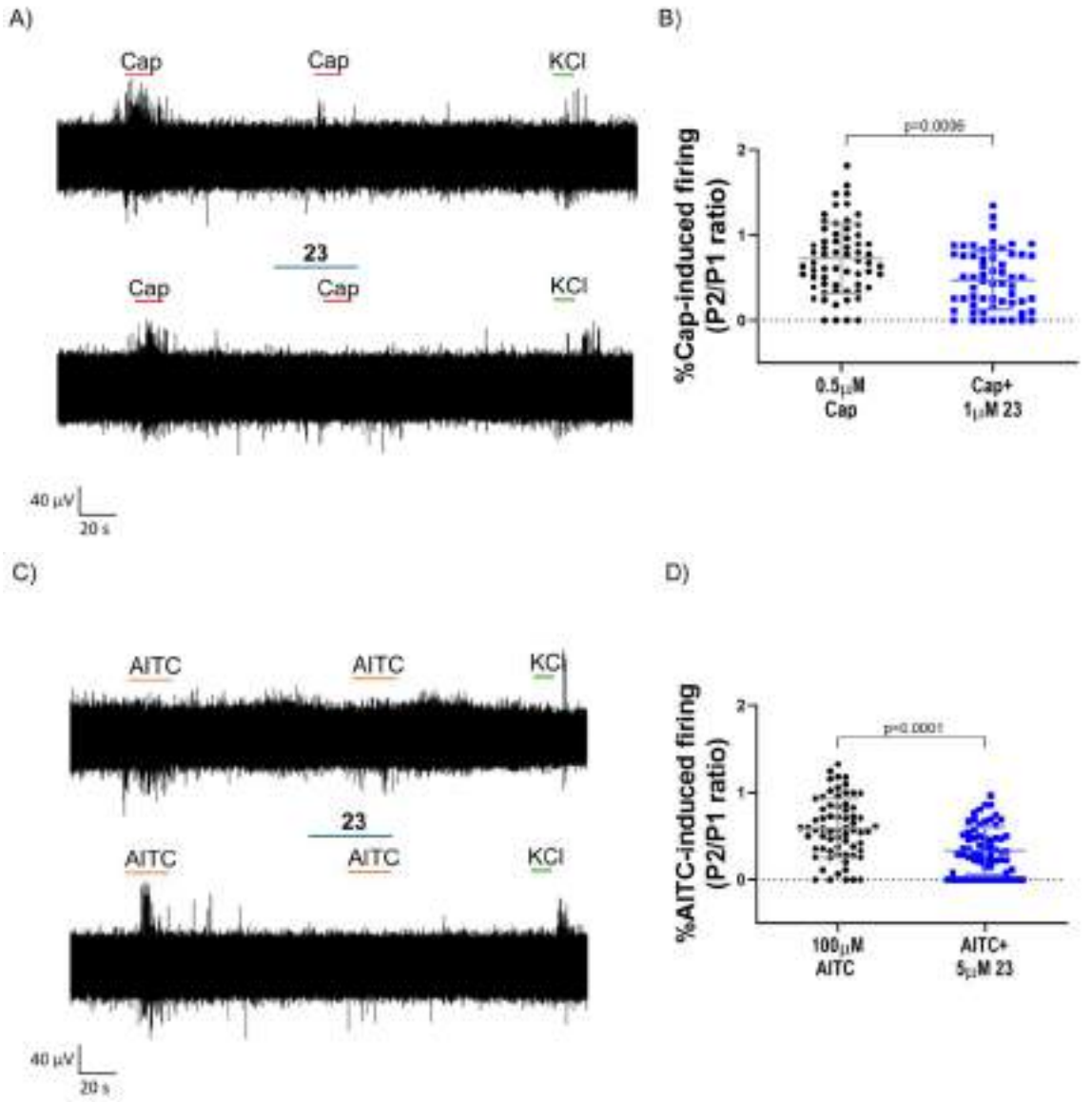

Figure 40. Compound 23 reduces Capsaicin and AITC-induced excitability of murine nociceptors. (A) Multi-Electrode Array (MEA) recordings, with representative traces showing Cap-evoked action potential (AP) firing under different conditions: control and 1 µM Compound **23**. Cap (0.5 µM) was applied in two consecutive pulses, with compounds added 1 minute before the second pulse. The protocol concluded with a 15s-pulse of 40 mM KCl to ensure neuronal culture viability. (B) Normalized capsaicin-induced firing (P2/P1) in the absence (vehicle) and presence of antagonist (1 µM Compound **23**) were compared. (C) Representative traces showing AITC-evoked action potential (AP) firing under different conditions: control and 5 µM Compound **23**. AITC (100 µM) was applied in two consecutive pulses, with compounds added 1 minute before the second pulse. The protocol concluded with a 15s-pulse of 40 mM KCl to ensure neuronal culture viability. (E) Normalized AITC-induced firing (P2/P1) in the absence (vehicle) and presence of antagonist (5 µM Compound **23**) were compared. Data were analyzed with Mann-Whitney test, p-values for statistical differences are indicated. The number of independent experiments (N) was 3, with 60-70 electrodes per condition.

f. Local application of compound 23 mitigates oxaliplatin-induced cold allodynia.

Considering the inhibitory and antinociceptive properties of compound **23**, we conducted behavioral experiments in an oxaliplatin (OXP)-induced neuropathy model to investigate its effect on cold allodynia. Mice were treated with oxaliplatin intraperitoneally (i.p.) over five days, accumulating a total dose of 18 mg/kg. The acetone test, which measures licking duration in response to acetone on the hind paw (**Figs. 41A and 42C**, Before OXP vs. After OXP), showed significantly enhanced cold sensitivity post-oxaliplatin treatment ($P < 0.01$). Additionally, the dry ice test revealed a shortened latency to cold stimulus, indicating increased cold sensitivity (**Fig. 41B**, $P < 0.05$). We then examined the antinociceptive effect of systemic administration of compound **23** (5 mg/kg i.p.) in both the acetone and dry ice tests. Despite administration, compound **23** did not significantly alter the licking response or withdrawal latency compared to the vehicle, likely due to poor systemic pharmacokinetics from ester bond hydrolysis by esterases. To address this, we evaluated local administration in the paw. Local subcutaneous application of compound **23** significantly reduced cold allodynia, evident in the acetone test at both 30 and 90 minutes post-administration ($P < 0.05$ at 30 minutes, $P < 0.01$ at 90 minutes; **Fig. 41C**). These findings suggest that α-acyloxy carboxamide 23 effectively reduces cold sensitivity when applied locally to peripheral sites, whereas its systemic antinociceptive potential is hindered by pharmacokinetic limitations.

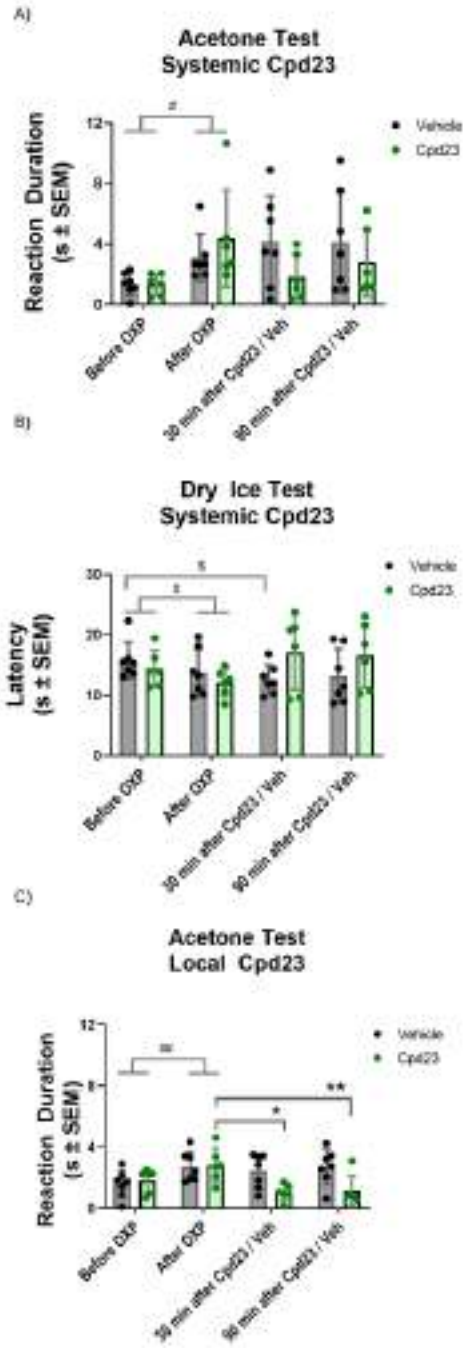

Figure 41. Local administration of compound 23 reduces cold hypersensitivity in an oxaliplatin-induced neuropathy model. (A) Acetone application test on mice (##P < 0.01, before vs. after OXP; two-way ANOVA). Systemic administration of compound **23** via intraperitoneal injection (i.p.) at either 30 or 90 minutes post-treatment. (B) Cold stimulation with dry ice (#P < 0.05, before vs. after OXP; two-way ANOVA). Mice receiving vehicle retained this cold hypersensitivity ($#P < 0.05, before OXP vs. 30 min post-vehicle). Nonetheless, systemic delivery of **23** failed to produce a statistically significant antinociceptive effect. (C) Cold responses triggered by acetone were reduced at both 30 and 90 minutes post-injection (*P < 0.05, **P < 0.01, after OXP vs. post-23 administration; two-way ANOVA followed by Tukey's post hoc test). Data are presented as mean ± SEM. Individual data points for each animal (N = 6–7) are represented as dots.

g. Docking Model of α-Acyloxy Carboxamide 23 in the hTRPM8 Menthol Binding Site

To further investigate the selective blocking mechanism, we performed molecular docking of compound **23** on hTRPM8 (**Fig. 42**). Compound **23** fits well into the menthol binding pocket between the S1-S4 transmembrane domains when the channel is in a closed state (**Figs. 42A-B**). The biphenyl moiety of compound **23** interacts with residues R842, H845, I846 in S4, and W798 in S3, while the adamantane group contacts residues V849, L853 in S4, F738 in S1, and L1001, Y1005 in the TRP helix. Additional stabilizing interactions include a salt bridge with H845 and two π-cation interactions with R842 and H845 in S4 (**Fig. 42C**).

Superimposing compound **23** with WS-12 and AMTB within the receptor's menthol binding pocket reveals partial overlap of the WS-12 site, consistent with compound **23**'s competitive antagonism (**Figs. 42D-E**). The binding energy analysis shows compound **23** has a higher binding affinity (-10.41 kcal/mol) compared to AMTB (-9.93 kcal/mol) and WS-12 (-7.72 kcal/mol). This stronger binding likely results from compound 23's polar and hydrophobic contacts with residues in S4 and the TRP helix, mediated by the biphenyl and adamantane groups. We also modeled compound **23** docking in the menthol binding pocket of mouse TRPM8 (mTRPM8) to compare binding interactions (**Figs. 42F-H**). In mTRPM8, compound **23** interacts differently than in hTRPM8, engaging with residues such as Q785 (S2), D796, W798, N799, D802 in S3, H845 in S4, and E1004 in the TRP helix. Notably, the murine TRPM8 binding site displays fewer hydrophobic interactions, resulting in a lower estimated binding energy (-9.96 kcal/mol) relative to hTRPM8. This lower binding energy implies reduced blocking potency of compound **23** on mTRPM8 compared to its human counterpart.

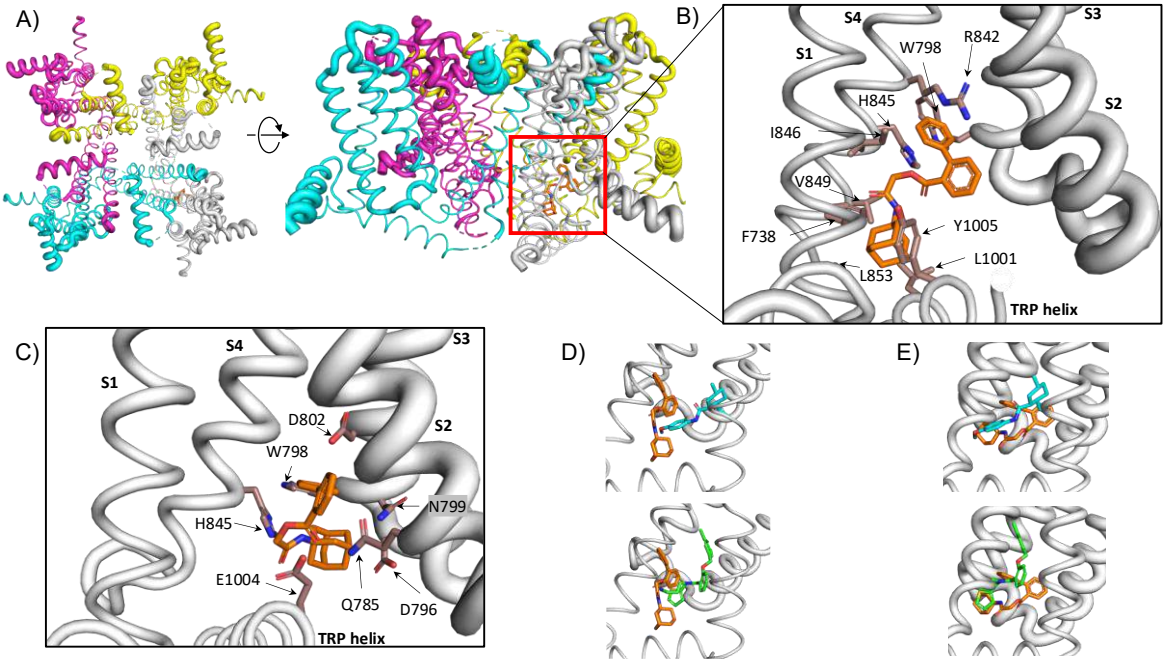

Figure 42. Molecular docking of compound 23 in TRPM8 channels. (A) Side and top view of human TRPM8 structure (PDB ID: 8BDC) used for docking studies. Subunits are colored differently. The red square roughly indicates the simulation box built around menthol binding site to accommodate compound **23**. (B) Detail of the human TRPM8 menthol binding pocket with bound compound **23** (orange color). Residues mainly involved in ligand interactions were F738 (S1), W798 (S3), R842, H845, I846, V849, L853 (S4), and L1001, Y1005 (TRP helix). Interactions are mainly hydrophobic. (C) Detail of compound **23** bound to mouse TRPM8 binding pocket (equivalent view to panel B). Residues interacting with compound **23** (orange) were Q785 (S2), D796, W798, N799, D802 (S3), H845 (S4), and E1004 (TRP helix). (D) Compound **23** (orange) and WS-12 (cyan) or AMTB (green) superimposed in the human TRPM8 menthol binding site for comparison. (E) Compound **23** (orange) and WS-12 (cyan) or AMTB (green) superimposed in the mouse TRPM8 menthol binding site for comparison. Figures were constructed using open source PyMol v3.0 (https://pymol.org/).

In conclusion, our results demonstrate that α-acyloxy carboxamide **23** is a promising TRPM8 antagonist with therapeutic potential for alleviating pathological cold allodynia associated with peripheral neuropathy in cancer patients. Compound **23** exhibits strong in vitro pharmacological properties, including high potency, efficacy, reversible inhibition, and selectivity for TRPM8, with no evidence of use-dependent blockade. Its stability in peripheral tissues further supports its suitability as a candidate for localized treatment of peripheral neuropathies linked to TRPM8 dysfunction.

3.4.1 Discussion:

Following our in vitro findings showing significant TRPM8 upregulation in the PIPN model- alongside TRPV1- and our earlier investigation into a dual CB2/TRPV1 agonist, we turned our attention to an alternative therapeutic strategy: selective TRPM8 antagonism. While TRPV1 is often associated with heat-related pain, TRPM8 plays a key role in the perception of cold and is increasingly recognized for its involvement in pathological cold hypersensitivity, particularly in conditions such as chemotherapy-induced neuropathy. Extensive evidence underscores the role of TRPM8 in mediating both harmless and harmful cold stimuli under normal and pathological conditions (51). Consequently, TRPM8 has emerged as a critical clinical target, with the development of effective modulators representing a key unmet need in the pharmaceutical and medical fields (241). While systemic TRPM8 modulators, akin to TRPV1 antagonists, have faced safety challenges in clinical development, topical formulations targeting receptor overactivity in disorders such as dry eye syndrome and pruritus have shown promise (52). Against this backdrop, the present study introduces a novel approach to designing hTRPM8 ligands with therapeutic potential, leveraging multicomponent reactions like the Ugi and Passerini reactions (234,242)These methodologies facilitate the rapid and sustainable assembly of chemical libraries utilizing the drug-like properties of the adamantane group (233).

Although the Ugi reaction is well-established in drug discovery, the Passerini reaction is underutilized, primarily due to concerns about the enzymatic instability of esters in systemic applications. This property has been beneficial in improving the safety profiles of ester-based soft antagonists, including those targeting vanilloid receptors. Among the tested compounds, α-acyloxy carboxamide **23** stands out as a potent TRPM8 competitive antagonist. A Schild plot analysis confirms its competitive inhibition mechanism, with a slope close to 1 and a statistically significant P value of 0.0353. High blockade potency (IC_{50} of 80 nM) and full efficacy (100% response block) further validates its pharmacological promise. Structural insights suggest that compound **23** stabilizes TRPM8 in its closed state by interacting with the menthol binding site, potentially preventing the allosteric transitions required for channel opening.

Computational docking studies reveal the molecular interactions of compound **23** with

human and murine TRPM8 orthologs, shedding light on species-dependent variations in blockade potency. Interestingly, the observed compatibility with competitive blockade aligns with its ability to selectively bind to the closed state of the channel, possibly obstructing agonist binding at a single site on the tetrameric channel. This aligns with previous findings suggesting that full channel activation requires the occupation of all four binding sites. Nevertheless, further research involving mutagenesis and biophysical analyses is needed to elucidate the structural determinants of this interaction.

A distinguishing feature of α-acyloxy carboxamide **23** is its reversible inhibition, driven by fast on/off kinetics (fast *k_off*), which minimizes use-dependent channel blocking—a property often associated with adverse effects in high-affinity antagonists like TRPV1 blockers or NMDA inhibitors. This reversibility enhances the compound's safety profile, allowing it to preserve TRPM8's physiological functions in body temperature regulation and tissue protection, which are critical to avoiding adverse effects such as hot sensations, gut motility disruptions, or cold burns. Additionally, the compound exhibits high selectivity for TRPM8 over other thermosensory channels such as TRPV1 and TRPA1, which are implicated in peripheral neuropathies. This selectivity reduces off-target effects and highlights its therapeutic potential.

Interestingly, the concept of multitarget cross-reactivity- often considered undesirable- is gaining recognition for its potential benefits in conditions like chemotherapy-induced peripheral neuropathy (CIPN). Given the involvement of TRPM8, TRPV1, and TRPA1 channels in CIPN, a compound that interacts with multiple targets may offer enhanced therapeutic efficacy. Supporting this hypothesis, local application of compound **23** effectively alleviated cold allodynia in a CIPN model, demonstrating significant antinociceptive activity. However, systemic administration failed due to its limited metabolic stability, attributed to oxidative metabolism despite the presence of bulky groups designed to reduce hydrolysis. While this metabolic sensitivity may limit systemic use, it underscores the suitability of compound **23** for local applications, where enzymatic degradation at the dermis can restrict activity to peripheral sites, minimizing systemic side effects.

In conclusion, α-acyloxy carboxamide **23** emerges as a promising TRPM8 antagonist with potent, selective, and reversible inhibitory properties. Its efficacy in mitigating

pathological cold allodynia, combined with its peripheral stability and lack of use-dependent block, positions it as a strong candidate for local therapeutic interventions in peripheral neuropathies, particularly in cancer patients suffering from CIPN. This study not only highlights the therapeutic potential of compound **23** but also provides a framework for advancing its development as a topical treatment for sensory disorders mediated by TRPM8 dysfunction.

DISCUSSION

4. DISCUSSION AND FUTURE DIRECTIONS

Chronic pain is a debilitating condition affecting approximately 1.5 billion individuals globally, with neuropathic pain impacting nearly 4% of the population (21). Beyond its toll on individuals, chronic pain imposes significant societal costs, including increased expenditures on healthcare, disability allowances, lost wages, and decreased productivity (243). Despite these challenges, current treatments for chronic pain remain unreliable, and there is a critical gap in tools to accurately diagnose or visualize the pain process, particularly at the dorsal root ganglia (DRG), key hubs in the pain pathway (16,17).

Within the framework of the PIANO project (PIANO, a H2020 MSCA ITN project), this thesis specifically addresses the objectives of one part of the project, which focused on defining the biophysical profile and TRP channel gating properties of DRG neurons.

These channels are molecular detectors of thermal and chemical stimuli that activate and sensitize sensory neurons, contributing to both acute and persistent pain (244). The research team has demonstrated that pro-inflammatory mediators enhance thermo TRP channel activity by increasing their plasma membrane recruitment and altering channel gating (106,245). Such insights have led to the development of potential analgesics, including Parentide®, currently in Phase Ⅱ clinical trials for inflammatory pain (246).

State-of-the-Art Contributions: Thermo TRP channels have become pivotal markers for distinct subsets of sensory neurons implicated in neuropathic pain (175,216). They enable separate nociceptive pathways for transmitting hot and cold stimuli to the central nervous system. By investigating the pathological dysfunction of these channels in neuropathic conditions, this project in PIANO aims to map pain-related circuitries and identify targets for new analgesic therapies.

As part of PIANO project, this doctoral thesis comprises two main research projects focused on developing and investigating paclitaxel model of chemotherapy-induced peripheral neuropathy (CIPN), alongside testing different TRPs channels modulators to ameliorate neuropathic pain. This thesis explores the key findings, addresses the limitations of the studies, examines the broader implications of the results, and outlines potential future directions for research in pain mechanisms.

Implications and Future Directions: The cumulative effects of paclitaxel on dorsal root ganglion (DRG) neurons underscore the urgent need for therapeutic strategies that can address both electrophysiological and structural disruptions associated with chemotherapy-induced peripheral neuropathy (CIPN). Our findings suggest several potential molecular targets for intervention, the modulation of which may alleviate paclitaxel-induced hyperexcitability and prevent axonal damage. Although sex differences are an important consideration in pain research, our study did not observe significant sex-dependent variations in paclitaxel's effects, suggesting that the mechanisms identified may apply broadly across populations. Future studies should build upon these insights by exploring the molecular mechanisms underlying paclitaxel's cumulative effects on sensory neurons. Particular attention should be paid to intracellular signaling pathways and neuron-glia interactions, as these may play a pivotal role in nociceptor sensitization. Additionally, the involvement of inflammatory mediators such as IL6 and CCK2- potentially contributing to pain independently of immune system activity- warrants in-depth investigation to better understand their contributions to CIPN pathophysiology.

In this context, validating the efficacy of emerging compounds in preclinical models is essential, particularly those aimed at preventing or reversing axonal retraction and functional deficits. Exploring the potential of dual TRPV1/CB modulators- and their effects on other TRP channels such as TRPM8 and TRPA1- could offer a more comprehensive approach to pain modulation, broadening the therapeutic landscape for neuropathic pain.

Further, the promising role of PEGylated derivatives, such as PEG-modified **AB9**, presents a strategic avenue to enhance solubility and metabolic stability while maintaining effective antagonism of TRPV1. Structural modifications, including the reintroduction of iodine on the vanilloid ring, could restore and amplify biological efficacy. These findings position **AB9** as a versatile TRPV1 antagonist, with pegylation emerging as a key strategy to overcome the pharmacokinetic limitations of conventional small molecules. Continued structural optimization and in vivo validation are critical next steps to ensure the clinical viability of these compounds in managing CIPN and other chronic pain conditions.

Additionally, α-acyloxy carboxamide **23** represents another promising candidate,

particularly in the context of TRPM8-targeted therapies. However, its limited systemic efficacy due to metabolic instability necessitates the development of optimized topical delivery systems. Investigating vehicles such as liposomal gels, nanocarriers, or transdermal patches may enhance dermal absorption and localized activity, improving its therapeutic potential. Comprehensive safety assessments, including local tolerability and long-term toxicology studies, are also essential to ensure clinical safety. Moreover, the exploration of potential off-target effects on related thermosensory channels (e.g., TRPV1 and TRPA1) should be prioritized in nonclinical evaluations.

Collectively, these findings aim to refine our understanding of paclitaxel-induced peripheral neuropathy and foster the development of targeted, effective, and personalized pain management strategies. By elucidating the roles of key molecular pathways and optimizing novel pharmacological agents, this research paves the way for innovative interventions that can significantly improve the quality of life for patients undergoing chemotherapy.

CONCLUSIONS - CONCLUSIONES

5. CONCLUSIONS

Based on the initial objectives and results obtained during this thesis, we can conclude that:

- Dual paclitaxel treatments in long-term DRG neuronal cultures alter the electrophysiological properties of both IB4(+) and IB4(–) neurons, inducing sustained hyperexcitability and mimicking clinical pain patterns observed in CIPN.
- Paclitaxel-induced excitability is linked to upregulation of TRPV1, TRPM8, and $Na_V1.8$ channels, while potassium channels appear unaffected in this model, suggesting selective ion channel involvement in sensory neuron sensitization.
- Repeated paclitaxel exposure causes irreversible axonal retraction, supporting its role in progressive structural damage and reinforcing the need for neuroprotective therapeutic strategies.
- No significant sex-based differences in neuronal responses were observed, indicating similar paclitaxel-induced sensitization dynamics in male and female DRG neurons, though further research is needed to resolve discrepancies with clinical data.
- The TRPV1/CB2 dual modulator (Cpd**41**) shows promising therapeutic potential by effectively reducing nociceptor hyperexcitability in vitro and demonstrating favorable selectivity and metabolic stability.
- The TRPV1 antagonist **AB9** demonstrates moderate but broad-spectrum activity, and PEGylation significantly improves its solubility and suitability for sustained-release formulations.
- The compound **23** is a potent and selective TRPM8 antagonist with a competitive and reversible inhibition mechanism. It has great potential for the treatment of cold allodynia in CIPN while minimizing the side effects typically associated with high affinity blockers. Future research should focus on developing optimized topical formulations to overcome limitations related to systemic metabolic instability.

5.1 CONCLUSIONES

Basado en los objetivos iniciales y los resultados obtenidos durante esta tesis, podemos concluir que:

- El tratamiento doble con paclitaxel en cultivos de neuronas DRG a largo plazo altera las propiedades electrofisiológicas de las neuronas IB4(+) y IB4(-), induciendo una hiperexcitabilidad sostenida que podría ser la base subyacente a los patrones de dolor clínico observados en la CIPN.
- La excitabilidad inducida por paclitaxel está vinculada a la sobreexpresión de los canales TRPV1, TRPM8 y $Na_V1.8$, mientras que los canales de potasio parecen no verse afectados en este modelo, lo que sugiere una participación selectiva de los canales iónicos en la sensibilización de las neuronas sensoriales.
- La exposición repetida al paclitaxel causa retracción axonal irreversible, lo que respalda su papel en el daño estructural progresivo y refuerza la necesidad de estrategias terapéuticas neuroprotectoras.
- El protocolo de tratamiento con paclitaxel no produjo diferencias significativas en las respuestas neuronales basadas en el sexo, lo que indica una dinámica de sensibilización inducida por paclitaxel similar en las neuronas DRG de machos y hembras, aunque se necesita más investigación para resolver las discrepancias con los datos clínicos.
- El modulador dual TRPV1/CB2 (Cpd**41**) muestra un gran potencial terapéutico al dirigirse a la hiperexcitabilidad de los nociceptores con alta selectividad y estabilidad metabólica.
- El antagonista TRPV1 **AB9** demuestra una actividad moderada, pero de amplio espectro, y la PEGilación mejora significativamente su solubilidad y adecuación para formulaciones de liberación prolongada.
- El compuesto **23** es un potente y selectivo antagonista de TRPM8 con un mecanismo de inhibición competitivo y reversible, ofreciendo un gran potencial para tratar la alodinia fría en CIPN, minimizando los efectos adversos típicamente asociados con los bloqueadores de alta afinidad. La futura investigación debería centrarse en el desarrollo de formulaciones tópicas optimizadas para superar las limitaciones relacionadas con la inestabilidad metabólica sistémica.

MATERIALS AND METHODS

6. MATERIAL AND METHODS

6.1 **Animals.** All procedures involving animals were approved by the Institutional Animal and Ethical Committee of the University Miguel Hernández de Elche. These procedures complied with guidelines established by the European Economic Community, the National Institutes of Health, and the International Association for the Study of Pain's Committee on Research and Ethical Issues (15). C57BL/6JRccHSd female mice (15-23-week-old, 24-35 g; Harlan, The Netherlands) bred at the animal facility at Universidad Miguel Hernández de Elche (UMH, Elche, Spain) were used to assess the antinociceptive effects of compound **23** on the model of chemotherapy-induced neuropathic pain. Housing conditions were maintained at 21 ± 1 °C and 55 ± 20 % relative humidity in a controlled light/dark cycle (light on between 8:00 a.m. and 8:00 p.m. Care was taken to minimize the number of animals used and the pain and stress they experienced.

6.2 **Culture of DRGs neurons.** Sensory neurons were harvested from adult CD57BL/6J mice aged 8–13 weeks, with both sexes represented. The animals were housed in groups under a 12-hour light-dark cycle (lights on from 8 a.m. to 8 p.m.) and provided unrestricted access to food and water. Euthanasia was performed via cervical dislocation, followed by decapitation. The spinal columns were extracted, and dorsal root ganglia (DRGs) were isolated from the nerve projections. DRGs were immediately placed in ice-cold Neurobasal medium (Gibco) (247). Tissue samples were digested enzymatically with collagenase type XI (0.67 mg/mL, Sigma) and dispase type II (3 mg/mL, Gibco) in INCmix solution (155 mM NaCl, 1.5 mM K2HPO4, 5.6 mM HEPES, 4.8 mM HEPES-Na, 5 mM glucose; Sigma) at 37°C in a 5% CO2 atmosphere for 75 minutes. Post-incubation, the enzymatic solution was removed, and the tissue was mechanically dissociated via pipetting. The resultant suspension was filtered using a 15% bovine serum albumin (BSA) column (prepared in PBS, Sigma) and centrifuged to separate the cells. Cells were resuspended in culture medium, centrifuged again, and subsequently diluted in a complete medium

for plating. Cell culture protocols, including the medium composition, was followed from Giorgi et al. 2023 (218) Paclitaxel treatments, adapted from Villalba et al. (2023), were applied on day in vitro 10 (DIV10), using a concentration of 1 µM for 24 hours alongside 5% fetal bovine serum (FBS), 5 mg/mL NaCl, and additional B27 supplement as in DIV5 (150). Functional assessments were conducted at 24, 48, and 96 hours after the removal of paclitaxel or vehicle (0.04% DMSO).

6.3 **High-throughput assays for activity at human recombinant TRPs ion channel.** HEK-293 cells stably expressing hTRPM8 or hTRPV1, were cultured in a monolayer in Earle's minimum essential medium with Earle's salts supplemented with 10% fetal calf serum, 1% nonessential amino acids, 2 mM L-glutamine, 100 µg streptomycin/mL, 100 U penicillin/mL, and 0.4 µg/mL puromycin (referred to as Puro-EMEM) and kept at 37 ºC in a humidified atmosphere of 5% CO_2 in a suitable incubator (STERI-CyCLE CO_2 Incubator Hepa Class 100, Thermo Electrón Corporation, Waltham, MA, USA). The cell lines were authenticated following the standardization of STR Profiling guidelines (ANSI/ATCC ASN-0002-2022) using the CLA Identifier Plus PCR Amplification Kit (Thermofisher-A44660) to analyze 16 highly variant human STRs. The cells were confirmed to be mycoplasma-free. Cells were stored under liquid nitrogen and used for 15 generations from unfreezing. For fluorometric experiments, HEK-293 cells stably expressing hTRPV1 were detached by means of Trypsin/EDTA solution, resuspended in DMEM-10%FCS and seeded at a concentration of 4 x10^4 cells/mL (207). To measure the effectiveness of the compounds against TRPV1 activity we have used microfluorometry-based calcium flux assays with Fluo-4 NW Ca^{2+} dye and fluorescence as described previously.[52] Briefly human embryonic kidney (HEK) cell line stably transfected with hTRPV1 were seeded in 96-well plates at a cell density of 40.000 cells. After 2 days the medium was replaced with 100 µL of the dye loading solution Fluo-4 NW supplemented with probenecid 2.5 mM and incubated 1 h at 37 º C. The TRP ion channel activity was measured using

a POLASTAR plate reader (BMG Labtech, Ortenberg, Germany) setting the excitation wavelength at 485 nm and emission wavelength at 520 nm. The baseline fluorescence was recorded for 3 cycles before the addition of the vehicle, compound at different concentrations, and the antagonist (ruthenium red, 10 μM). DMSO, at the highest concentration used in the experiment, was added to the control wells. Fluorescence intensity was recorded during 7 more cycles and the agonist (capsaicin, 10 μM) was added. Fluorescence intensity was recorded during 10 more cycles. The maximum possible change detectable by the dye in the fluorescence assay was determined using 4 μM ionomycin in the assay (207,247).

Data analysis: The Z-factor was calculated in each assay using the following equation: (3 x (SDmax + SDmin))/(Mean max - Mean min). In all the experiments, the Z-factor was ≥0.5. The effect of the compounds against TRPV1 activity was determined by normalizing their effect to the maximum fluorescence observed with the application of 10 μM of capsaicin. A decrease in agonist signal was expressed as a percentage of inhibition (%). An increase in the fluorescence intensity at cycle 3 was expressed as a percentage of activation (%). Data are expressed as the concentration exerting a half-maximal inhibition of agonist-induced (Ca^{2+}) elevation (IC_{50}, or concentration exerting a half-maximal activation of agonist-induced (Ca^{2+}) elevation (EC_{50}) which was calculated using GraphPad Prism® software (GraphPad Prism 7, Graphpad Software, San Diego, CA, USA) (Figure S1B, SI). The equation used was Y = Bottom + (Top -Bottom)/(1 + 10((LogEC_{50}-X) x HillSlope)), with the restriction of the minimum (Bottom = 0). All determinations were performed in triplicate (n = 3) in 3 independent experiments (N = 3). All data are expressed as the mean ± standard deviation (SD) (247).

6.4 **Molecular modelling and docking.** Molecular modeling and docking of TRPV1, CB2, and TRPM8 receptors were performed to explore the binding modes and theoretical affinities of specific compounds (247,248). For human TRPV1, the receptor structure was modeled based on the squirrel TRPV1 in

complex with capsaicin (PDB ID: 7LR0, resolution 3.81 Å). Human CB2 was modeled using its complex with the agonist AM12033 (PDB ID: 6KPF, resolution 2.90 Å). Both models enabled the evaluation of compound **41**'s binding interactions at specific sites. For TRPM8, human and mouse receptor structures (PDB IDs: 8BDC and 8E4N) were employed to analyze the binding properties of compound **23**. Docking simulations were carried out using the Autodock4 algorithm implemented in Yasara (249). The docking procedure used a local search confined to a 5 Å box around known ligands—capsaicin and AM12033 for TRPV1 and CB2 (184), and WS-12 and AMTB for TRPM8. Each docking experiment involved 500 flexible docking runs. The resulting ligand-receptor complexes were subjected to simulated annealing minimization, ensuring stabilization at energy minima using the AMBER 99 force field. To preserve pH-dependent bond orders and protonation states, the Yasara pH command was set to 7.0 (250,251). The best binding energy complexes from each cluster were analyzed to identify optimal ligand-receptor orientations. Binding energies were calculated by determining the energy of the complex at the bound state and subtracting the energy at infinite (unbound) distance. Visualizations were generated using PyMol v2.6 (The PyMOL Molecular Graphics System). Non-covalent interactions between macromolecules and ligands were identified using PLIP, an automated web server for analyzing molecular interactions (https://plip-tool.biotec.tu-dresden.de/plip-web/plip/index). This integrated approach allowed for a comprehensive investigation of compound interactions with TRPV1, CB2, and TRPM8 receptors, providing detailed insights into binding dynamics and affinities.

6.5 **Calcium imaging.** Calcium imaging experiments utilized the non-ratiometric fluorescent probe Fluo4-AM (F14201, Thermo Fisher Scientific) and pluronic acid (0.02% p/v, Molecular Probes, Invitrogen). Cells were incubated for 60 minutes at 37°C in a loading buffer containing 6 mg/mL Fluo4-AM and 0.2% w/v pluronic acid dissolved in HBSS (HANKS balanced salt solution) (NaCl 140

mM, KCl 4 mM, $CaCl_2$ 1.8 mM, $MgCl_2$ 1 mM, HEPES 10 mM, and D-glucose 5 mM adjusted to pH 7.4 with NaOH 1M). Excess fluorophore was removed by washing cells with HBSS for at least 20 minutes. Calcium imaging experiments were conducted using an inverted microscope (Axiovert 200/B, ZEISS) equipped with a Hamamatsu Flash 4.0 LT camera (C11440-42U30, Hamamatsu, Sunayama-cho, Japan). Cells were visualized using bright field microscopy, and regions of interest (ROIs) were manually drawn. Fluo4 fluorescence was excited at 480 nm with a rapid-gating shutter (lambda-shutter 10/2, Sutter instruments, Novato, USA), and images were captured every 3 seconds. Mean fluorescence intensity was measured for each cell at each time point using HCimage DIA software (Hamamatsu Photonics). Experiments were conducted 22-26°C. The size of calcium transients was determined by measuring maximum values after agonist application minus fluorescence values at resting state. To ensure comparability, these results were normalized by the positive control in each experiment. Calcium transients were considered positive responses if fluorescence increases were greater than 0.2 arbitrary units. Substances dissolved in HBSS were applied using a perfusion system solution between calcium responses for a period of at least 300 seconds to ensure recovery of basal fluorescence levels. Analysis was conducted in Excel to evaluate the percentage of responses normalized to Ionomycin or KCl, the amplitude of responses relative to Ionomycin, and the area of responding cells. The percentage of responses was determined using Equations 1 and 2 (247,248). If the calculated value was greater than zero, it indicated a positive response to the applied stimulus. The total number of responses was then normalized to Ionomycin or KCl responses to calculate the percentage of responding cells.

- *ΔF=MAX(F90s after stimulus)−MEAN(Fbaseline)*

  [Equation 1, Raw Fluorescence Change: The change in fluorescence (ΔF\Delta FΔF) is defined as the difference between the maximum fluorescence intensity (MAX) recorded after stimulus application and the mean baseline fluorescence intensity

(MEAN) before the stimulus. **MAX(F_{90s})** = peak fluorescence intensity within 90 seconds after stimulus application. **MEAN($F_{(}$baseline$_{)}$)** = average baseline fluorescence intensity before stimulation]

- *ΔFcorrected=ΔF−[SDbaseline×10]*

  [Equation 2, Noise-Corrected Fluorescence: The noise-corrected ΔF\Delta FΔF is calculated by subtracting ten times the standard deviation (DESVEST) of the baseline signal from ΔF\Delta FΔF, ensuring the validity of the response.]

The response amplitude was determined using Equation 3, which normalizes the stimulus-induced response to the magnitude of the response elicited by Ionomycin or KCl:

- Relative Response Amplitude=$\Delta F\ stimulus/\Delta F\ Ionomycin$ or KCl

  [Equation 3, Normalized Response Amplitude: This normalization allowed for inter-experimental comparability. A calcium transient was considered a positive response if the fluorescence increase exceeded 0.2 arbitrary units after noise correction. A minimum recovery interval of 300 seconds was used between stimuli to ensure return to baseline.]

6.6 **Patch clamp recordings from recombinant cells.** Patch-clamp recordings were performed on HEK293 cells cultured in DMEM GlutaMax supplemented with 10% FBS and 1% P/S. The cell lines were authenticated following the standardization of STR Profiling guidelines (ANSI/ATCC ASN-0002-2022) using the CLA Identifier Plus PCR Amplification Kit (Thermofisher-A44660) to analyze 16 highly variant human STRs. The cells were confirmed to be mycoplasma-free. hTRPV1 and hTRPM8 stables transfected lines were used, while hTRPA1 Cells were transiently transfected with plasmids encoding human TRPA1 using Lipofectamine 3000, then seeded on 12 mm Ø glass coverslips pre-treated with poly-L-lysine solution (Sigma Aldrich, Spain). Recordings were conducted 48 hours post-transfection. For experiments with TRPV1, the intracellular pipette solution contained (in mM): 150 NaCl, 5 EGTA, 3 MgCl2, and 10 HEPES (pH adjusted to 7.2 with CsOH). The extracellular solution was composed of (in mM): 150 NaCl, 6 CsCl, 1.5 CaCl2, 1 MgCl2, 10

D-glucose, and 10 HEPES (pH adjusted to 7.4 with NaOH). In dose-response assays, the extracellular Ca^2 concentration was reduced to 0.1 mM to minimize receptor desensitization and achieve accurate EC50 measurements (248). Patch pipettes were fabricated from thin-wall borosilicate capillary glass tubing and pulled using a Micropipette Puller (Model P-97, Sutter Instrument) to a resistance of 2–8 MΩ when filled with the internal solution. Recordings were acquired using an EPC-10 amplifier with PatchMaster software (HEKA Electronics, Germany). Signals were sampled at 10 kHz and low-pass filtered at 3 kHz. Data with leak currents >200 pA or series resistance >20 MΩ were excluded. Voltage-clamp experiments were conducted at a constant holding potential. Agonists or modulators (e.g., capsaicin, compound 23, or compound 41) were applied via a multibarrier concentration-clamp system or a gravity-driven perfusion system. TRPV1 activity was assessed by applying two pulses of 0.5 μM capsaicin or compound **41**, spaced 2 minutes apart. For TRPM8, a voltage-step protocol (from −120 mV to 120 mV in 100 ms steps, holding at 0 mV) was used to study voltage-dependent channel activity. Ionic conductance (G) was calculated using the equation G=I/(V-Vr), where I is the measured ionic current, V is the applied voltage and Vr the reversal potential that for the ionic conditions used was set to 0 mV. Dose-response relationships for agonists (e.g., WS-12 for TRPM8) were normalized to the maximal response at a saturating concentration. In inhibitor studies, responses were normalized to the control response in the absence of blockers. The data were fitted to the Hill equation: Y = Bottom + (Top-Bottom)/(1 + 10^(([ligand]-LogIC50 (or Log(EC50)))) where Top was fixed to 100% for maximal activation or unblocked responses. All experiments were performed at 24–26 °C, and total currents were normalized to the first peak evoked by the activating stimuli. Data analysis, including non-linear regression and EC50/IC50 calculations, was conducted using GraphPad Prism (v8.0 or v9.0). Results were reported as mean ± SEM (N = 3-4; n = 6–12).

6.7 **Patch clamp recording from DRGs sensory neurons.** Dorsal root ganglia

(DRG) neurons were cultured on coverslips and recorded in voltage and current-clamp modes. The coverslips were initially coated with poly-L-lysine (50 µg·mL-1, Sigma-Aldrich) for 1 hour, followed by four washes with deionized water. Subsequently, the coverslips were incubated o/n at 37°C with laminin (10 µg·mL-1, Sigma-Aldrich) diluted in HBSS. After extraction of DRG neurons, the laminin coating was replaced with a drop of cell suspension diluted in Neurobasal medium supplemented with 2% B27 supplement (Gibco) and 1% penicillin-streptomycin (P/S). Patch pipettes were pulled from borosilicate glass and had resistances ranging from 2 to 5 MΩ. The whole-cell configuration was established, with seal-resistance maintained between 200 MΩ and 1.5 GΩ and series resistance compensated to around 80%. The extracellular solution contained (in mM): 140 NaCl, 4 KCl, 2 $CaCl_2$, 2 $MgCl_2$, 10 HEPES, 5 Glucose, adjusted to pH 7.4 with NaOH. The pipette internal solution contained (in mM): 144 KCl, 2 $MgCl_2$, 1 $CaCl_2$, 10 HEPES, 10 EGTA, 110 K-Gluconate, 4 ATP-Na, 0.4 GTP-Na, 4 NaCl adjusted to pH 7.2 with KOH. Recordings were conducted at approximately 22°C. In current-clamp mode, the resting membrane potential (RMP) was determined without any current injection. Neurons with action potential that did not overshoot 0 mV were excluded from analysis. Neurons that fired action potentials in the absence of stimulus were considered as having spontaneous activity (SA). In voltage-clamp recordings, capacitive transients were compensated, and cells with capacitance values higher than 40 pF were excluded from analysis. Current responses to capsaicin, AITC, and WS12 were measured using continuous protocols at -60 mV. Paclitaxel experiments involved sequential activation of TRPA1 and TRPM8, followed by TRPV1 currents (150). Data were acquired using an EPC10 amplifier controlled by Patchmaster software (HEKA Elektronik) at 20 kHz. To distinguish between peptidergic and non-peptidergic DRG neurons, coverslips were incubated with Isolectin-GS-IB4 Alexa Fluor® 568 conjugate (10 µg·mL-1; Invitrogen) before recording. Fluorescence microscopy was used to visualize and classify neurons. Only one cell per dish was recorded and analyzed.

6.8 **Microelectrode array (MEA).** Microelectrode array measurements were conducted using 60-electrode thin MEA chips, featuring 30 µm diameter electrodes and 200 µm inter-electrode spacing, including an integrated reference electrode (Multichannel Systems GmbH). The MEA1060 System (Multi Channel Systems GmbH) and MC Rack software version 4.3.0 was employed to record the electrical activity of primary sensory neurons. Short 30 s-applications (termed P1 and P2) of WS-12 were applied using a continuous perfusion system (2 mL/min) (199,247). Between each stimulus, cells underwent 4 min and 30s washes with external solution. Treated cells were perfused with compound **23**, 1 min before and together with P2. The protocol concluded with the application of 40 mM KCl to confirm neuronal excitability and viability. All measurements were conducted at approximately 34.5 °C using the Multichannel Systems Temperature Controller. For microelectrode array analysis, data were processed using MC_RACK spike sorter with a sample rate of 25 kHz, applying a Butterworth high-pass 2nd order filter with a 200 Hz cutoff. For AITC analysis was applied a cutoff of 500 Hz. An evoked spike was defined when the amplitude of neuronal electrical activity reached a threshold established by automatic estimation at -4.7 µV Std. For AITC analysis an evoked spike was defined when the amplitude of neuronal electrical activity reached a threshold established by automatic estimation at -5 µV Std. Spiking activity was measured for 60 s immediately following the instillation of activating stimuli. Electrodes lacking electrical activity in the first agonist pulse were excluded. The recorded signals were then analyzed to extract the mean spike frequency for each pulse (P1–P2). The ratio P2/P1 of mean spike frequency was calculated and normalized to the vehicle for comparison across different conditions (199).

6.9 **Model of Chemotherapy-Induced Neuropathic Pain.** For the in vivo behavioral experiments evaluating the effects of the TRPM8 antagonist on mice with chemotherapy-induced neuropathy with blind experiments, male C57BL/6JRccHSd mice (15–23 weeks old); Harlan, The Netherlands) were

utilized. The animals were bred and housed at the UMH Animal Facility (Servicio de Experimentación Animal, UMH, Elche, Spain). Chemotherapy-induced sensitization was induced by repeated administration of oxaliplatin (ref#2623, Tocris, Bristol, UK). Oxaliplatin was freshly prepared every day by dissolution in 5% dextrose in warmed distilled water at 37 °C. The chemotherapeutic was administered intraperitoneally every other day for 5 days at a 6 mg/kg and in a volume of 10 mL/kg, reaching an accumulated dose of 18 mg/kg after the three injections (247).

6.10 **Compound 23 treatment.** The systemic effect of compound **23** was assessed after intraperitoneal administration at 5 mg/kg, dissolved in a solution of 2% Cremophor and 5% DMSO in saline, with a volume of 10 mL/kg (247). This dose was chosen based on the relative potency of the compound in the *in vitro* studies when compared to the canonical antagonist AMTB. Nociceptive sensitivity was evaluated for 30- and 90-minutes post-injection using the acetone drop test (7 days after the first oxaliplatin dose) and the dry ice test (9 days after the last oxaliplatin dose). The local effect of compound **23** or its vehicle was assessed 11 days after beginning the oxaliplatin treatment through subcutaneous intraplantar injection of 1 µg compound **23** or vehicle (2% Cremophor and 5% DMSO in saline) in the ventral side of the right hind paw, administered in a volume of 10 µL. This dose was chosen based on previous works [48] and considering the relative potency of the compound in the *in vitro* studies. Nociceptive sensitivity was evaluated 30 and 90 minutes after the intraplantar injection with the acetone test (253).

6.11 **Behavioral assessment of cold sensitivity.** Prior to conducting behavioral experiments, mice underwent a 2-day acclimatization period to the experimental conditions, during which they were handled and habituated to the experimenter Dr. David Cabañero Ferri for a minimum of 2 minutes per day and mouse (253). Additionally, the animals were familiarized with each testing environment 2 hours per day, placed individually in Plexiglas® chambers (10 × 10 × 14 cm). Every day of evaluation, the mice spent an

additional hour of habituation in the testing environment before the measurement of nociceptive sensitivity (247).

6.12 **Acetone drop test.** Mice were placed over a metal grid and allowed to habituate for approximately 1 h. Acetone (179124, Sigma-Aldrich) was applied in 20 µL drops onto the mid-plantar surface of the right hind paw by using a 200 µL pipette with a plastic tip manually curved. Responses were recorded using an iPhone SE camera (Apple, Cupertino, CA, USA) and quantification of paw licking responses was conducted afterwards by a blinded observer (247). The responses were measured for 1 min after acetone application, with a digital stopwatch (Xnote Stopwatch Version 1.63 2011 Dmitry Nikitin) and were averaged for both hindpaws after the systemic treatment with compound **23** or conducted only in the right hind paw after the intraplantar treatment (253). For each measurement, the paws were sampled three times, and the mean was calculated. The interval between each application of acetone was at least 3 min.

6.13 **Dry ice test.** The dry ice test was conducted as previously described[65] with some modifications. Mice underwent a one-hour habituation period on a 6 mm thick glass surface (Flores Valles, Madrid, Spain). Subsequently, a hand-made probe was prepared by cutting the top of a 3 mL syringe (DicoNEX, ZARYS International Group, Zabrze, Poland) and drilling the syringe with a 25G needle (BD Microlance 3, Beckton Dickinson & Co Ltd, Louth, Ireland) to prevent the accumulation of CO_2 gas. Powdered dry ice was used to fill the probe. The ice was compacted by pressing the plunger against the bench until a dense pellet at least 1 cm long was obtained. The flattened pellet was then applied to the glass surface using the probe, targeting the right and left hindpaws. A minimum interval of 5 minutes was maintained between applications. To determine the threshold value for each mouse, the latency to paw withdrawal was recorded for each hindpaw and subsequently averaged. The glass surface was always kept dry (247).

6.14 **Microfluidic chambers.** Dorsal root ganglia (DRGs) were isolated from 15- to 20-week-old adult CD57BL/6J mice. The animals were housed in groups under a 12-hour light/dark cycle, with lights on at 8:00 a.m. and off at 8:00 p.m. They had free access to food and water throughout the study. Both male and female mice were used for the experiments, which received approval from the Institutional Animal and Ethical Committee of Miguel Hernández University of Elche. The study adhered to ethical standards outlined by the European Economic Community, the National Institutes of Health, and the International Association for the Study of Pain (15). DRG cells were plated in microfluidic chambers utilizing the AXIS™ Axon Investigation System—Tissue Culture Ready (AX150 design) from Millipore. These polydimethylsiloxane (PDMS) devices included four microwells (8 mm in diameter each), two microchannels (1.5 mm in length), and approximately 120 microgrooves measuring 150 µm in length. The sterile microfluidic chambers were attached to clean, sterile 24 × 60 mm coverslips coated with poly-L-lysine (0.5 mg/mL; Sigma). Before seeding the DRG cells, the devices were pre-treated with laminin (20 µg/mL; Sigma). A 5-µL suspension of DRG cells (~4 × 10^6 cells/mL) was loaded into the somal compartment. Approximately 30–45 minutes after cell seeding, a complete culture medium supplemented with murine nerve growth factor (mNGF 25s; 100 ng/mL; Promega) and human glial cell line-derived neurotrophic factor (hGDNF; 100 ng/mL; PeproTech) was added. Each well in the somal compartment received 200 µL of medium, while the wells in the axonal compartment were filled with 100 µL to promote axonal extension (218). Media changes occurred every 48h with a gradual reduction in mNGF and hGDNF concentrations in the somal compartment (**Table 8**). Paclitaxel treatments occurred in the axonal compartment on days in vitro 5 and 10 which is removed after 24h. Anti-mitotic agents (uridine and 5-fluoro-2'-deoxyuridine; Sigma) were introduced to limit glial cell proliferation. This protocol was adapted from Giorgi et al., 2023 (218).

DIV	SOMAL COMPARTMENT		AXONAL COMPARTMENT	
0	Neurobasal A (Gibco)		Neurobasal A (Gibco)	
	GlutaMAX (Gibco)	1%	GlutaMAX (Gibco)	1%
	B27 Supplement (Gibco)	2%	B27 Supplement (Gibco)	2%
	Penicillin-Streptomycin (10000 U/mL, Gibco)	1%	Penicillin-Streptomycin (10000 U/mL, Gibco)	1%
	mNGF 25 s (Promega)	100 ng/mL	mNGF 25 s (Promega)	100 ng/mL
	hGDNF (PeproTech)	100 ng/mL	hGDNF (PeproTech)	100 ng/mL
1	Neurobasal A (Gibco)		Neurobasal A (Gibco)	
	GlutaMAX (Gibco)	1%	GlutaMAX (Gibco)	1%
	B27 Supplement (Gibco)	2%	B27 Supplement (Gibco)	2%
	Penicillin-Streptomycin (10000 U/mL, Gibco)	1%	Penicillin-Streptomycin (10000 U/mL, Gibco)	1%
	mNGF 25 s (Promega)	50 ng/mL	mNGF 25 s (Promega)	100 ng/mL
	hGDNF (PeproTech)	50 ng/mL	hGDNF (PeproTech)	100 ng/mL
	Uridine (Sigma)	17,5 µg/mL	Uridine (Sigma)	17,5 µg/mL
	5-fluoro-2'-deoxyuridine (Sigma)	7,5 µg/mL	5-fluoro-2'-deoxyuridine (Sigma)	7,5 µg/mL
Every 48h	Neurobasal A (Gibco)		Neurobasal A (Gibco)	
	GlutaMAX (Gibco)	1%	GlutaMAX (Gibco)	1%
	B27 Supplement (Gibco)	5%	B27 Supplement (Gibco)	5%
	Penicillin-Streptomycin (10000 U/mL, Gibco)	1%	Penicillin-Streptomycin (10000 U/mL, Gibco)	1%
	mNGF 25 s (Promega)	25 ng/mL	mNGF 25 s (Promega)	100 ng/mL
	hGDNF (PeproTech)	25 ng/mL	hGDNF (PeproTech)	100 ng/mL
	Uridine (Sigma)	17,5 µg/mL	Uridine (Sigma)	17,5 µg/mL
	5-fluoro-2'-deoxyuridine (Sigma)	7,5 µg/mL	5-fluoro-2'-deoxyuridine (Sigma)	7,5 µg/mL
	NaCl (Sigma-Aldrich)	5 mg/ml	NaCl (Sigma-Aldrich)	5 mg/ml
	Fetal bovine serum (FBS, Invitrogen)	5%	Fetal bovine serum (FBS, Invitrogen)	5%

Table 8: The medium composition during the days in vitro (DIV) was adjusted to create a neurotrophic gradient that supports axonal growth. The concentrations of NGF and GDNF in the somal compartment were gradually reduced from 100 ng/mL on DIV 1 to 25 ng/mL on DIV 3.

6.15 **Calcium Imaging in Microfluidic Chambers.** Calcium imaging experiments in microfluidic chambers followed the protocol outlined in section 7.14, with modifications to the perfusion system to reduce shear forces by slowing the flow rate to 0.2–0.4 mL/min. To identify neurons with axons extending into the axonal compartment, the axonal compartment was loaded with the fluorescent tracer 1,1'-Dioctadecyl-3,3,3',3'-Tetramethylindodicarbocyanine (DiD, 1:200, Invitrogen) on day 5 and incubated overnight. On day 6, Fluo-4 was introduced into the somal compartment to label calcium-responsive regions. Regions of interest (ROIs) were marked based on the DiD fluorescence image, and Fluo-4 fluorescence intensity was recorded over time (218).

Various stimuli, including capsaicin (100 nM), menthol (100 μM), AITC (100 μM), and KCl (40 mM), were applied to the axonal compartment, while changes in calcium levels were monitored in the somal compartment (218). Data analysis was conducted as described in section 11.6.

6.16 **Quantitative PCR.** Total RNA extraction was performed using the E.Z.N.A.® microElute total RNA kit (Omega Bio-tek). Extracellular RNA samples were assessed for quantity and purity using the NanoDrop 1000 Spectrophotometer (ThermoFisher Scientific). To eliminate any potential contaminating DNA, DNase I treatment (Sigma) was employed prior to reverse transcription of the extracted RNA using the First Strand cDNA Synthesis Kit (ThermoFisher Scientific). Primers specific to mice selective channels were custom-designed. The sequences of the primers used were as follows:

TRPV1:

Forward(Fw):5'-TCACCACGGCTGCTTACTATC-3',

Reverse (Rv): 5'-AACGGTGTTATTCAGCTTATAGGG-3'

TRPA1:

Fw: 5'-GCAGGTGGAACTTCATACCAACT-3',

Rv: 5'-CACTTTGCGTAAGTACCAGAGTGG-3'

TRPM8:

Fw: 5'-CTTTCTAAGCAATGGTATGGAG-3',

Rv: 5'-GGTTTCTTCCTAAATGATACGAG-3'

NaV1.7:

Fw: 5'-CCTTGGCCCCATTAAATCTCT-3',

Rv: 5'-TGCTCCTATGAGTGCGTTGAC-3'

NaV1.8:

Fw: 5'-TTGACACAACCTCGCTCTATTCC-3',

Rv: 5'-ATTTCACCCTGGGTCTTCTCTCA-3'

NaV1.9:

Fw: 5'-CTTCAGGATTGTCCGCTTGG-3',

Rv: 5'-AGAGAGAGGGGAGACATCATCA-3'

GAPDH (housekeeping gene):

Fw: 5'-CCAATGTGTCCGTGGATCT-3',

Rv: 5'-GTTGAAGTCGCAGGAGACAACC-3'

The synthesized complementary DNA (cDNA) was mixed with PowerUp™ SYBR™ Green Master Mix (ThermoFisher Scientific) along with the specific forward and reverse primers and nuclease-free water. Negative controls, including no-template controls and reverse transcriptase minus (RT-) controls, were included to verify the specificity of the amplification. Amplification and quantification of the cDNA were conducted using the QuantStudio3 Real-Time PCR Instrument (Applied Biosystems) with the following thermal cycling conditions: initial denaturation at 95°C for 2 minutes, followed by 40 cycles of denaturation at 95°C for 15 seconds and annealing/extension at 60°C for 1 minute. Final steps included a melt curve analysis with temperature ramping from 95°C to 60°C. The mRNA expression levels were normalized to the housekeeping gene Rpl29 mRNA levels, and the relative expression was determined using the 2^(-ΔΔCt) method (150).

6.17 **Immunofluroescence stain.** DRG neurons cultured on coverslips were gently washed with Dulbecco's Phosphate-Buffered Saline (DPBS) and subsequently fixed in 4% paraformaldehyde (Sigma-Aldrich) for 20 minutes at room temperature. After three washes with DPBS, cells were permeabilized using 0.1% Triton X-100 (Sigma-Aldrich) for 5 minutes and then blocked with 5% normal goat serum (NGS, Sigma-Aldrich) for 1 hour at approximately 22°C (150). Following blocking, cells were incubated overnight at 4°C in DPBS solution with 5% NGS containing primary antibodies against the following targets: NeuN (neuron-specific protein) using a mouse monoclonal antibody at a 1:50 dilution (Millipore, Cat# MAB377C3); TRPV1 with a rabbit polyclonal antibody at a 1:100 dilution (Alomone Labs, Cat# ACC-029); TRPA1 with a rabbit polyclonal antibody at a 1:100 dilution (Alomone Labs, Cat# ACC-037); TRPM8 with a rabbit polyclonal antibody at a 1:100 dilution (Alomone Labs, Cat# ACC-049). The next day, cells were washed with DPBS and then incubated

with secondary antibodies: goat anti-rabbit IgG Alexa Fluor® 488 (1:500 dilution) and goat anti-mouse IgG Alexa Fluor® 568 (1:500 dilution) for 1 hour at approximately 22°C. Following another round of DPBS washes, cells were stained with DAPI (300 nM) for 10 min and mounted onto coverslips using Mowiol®. All antibody dilutions were freshly prepared on the day of the experiment from original stocks stored in individual aliquots at -20°C. Fluorescence images were captured using an inverted microscope (Axiovert 200, Carl Zeiss) equipped with a 10X air objective and Fiji® software was utilized to quantify fluorescence by subtracting the mean background fluorescence from each cell's fluorescence (150).

6.18 **Materials.** Paclitaxel (Taxol®, Tocris Bioscience, Bristol, UK) was dissolved in DMSO to create a stock solution of 25 mM, stored at -20°C, and used within 1 month. Before cell treatment, the stock solution was diluted in Neuorobasal medium, B27 supplement (Gibco) and 1% P/S and filtered through a 0.2-µm filter to achieve a final concentration of 1 µM. Controls were prepared using only DMSO (0.04%) following the same procedure. For electrophysiological experiments, capsaicin, AITC, WS12, and PF04885614 (all from Sigma, St. Louis, MO, USA) were dissolved in DMSO to create stock concentrations of 10 mM, 1 M, 1 M, and 100 µM, respectively. ProTx II (Tocris Bioscience) stock solution was prepared in water to a concentration of 50 µM. On the day of the experiment, these solutions were diluted in the external solution buffer to reach the final concentration specified for each experiment. The final concentration of DMSO was 0.01% of the total volume for capsaicin, AITC, and WS12, and 0.075% for PF04885614. For the Oxaliplatin experiments in the supplementary information, Oxaliplatin treatments were conducted following the protocol described in Villalba-Riquelme et al., 2024 (150).

6.19 **Data and statistical analysis.** For statistical analysis of in vitro studies, data are expressed as mean ± SEM, with the number of replicates noted in figure legends. One-way ANOVA followed by Bonferroni post-hoc tests for multiple comparisons or an unpaired, two-tailed Student's t-test were used for some

experiments, as specified. ANOVA results are presented with F (DFn, DFd) and P values, and the Bonferroni post-hoc test p-values are reported. A significance threshold of 0.05 was applied across analyses. Behavioral experiments were analyzed using GraphPad Prism 9 (GraphPad Software Inc., San Diego, CA, USA). An initial two-factor ANOVA was used to examine the effects of oxaliplatin (OXP) treatment and any baseline differences between treatment groups (within factor: "OXP treatment," between factor: "23 vs Vehicle group"). A subsequent two-way ANOVA assessed compound 23 effects (within factor: "Time Point," between factor: "23 vs Vehicle group"). Tukey's multiple comparisons tests were conducted following significant interactions, with significance set at $p < 0.05$. In further data and statistical analysis, GraphPad Prism® 8.0.0 was used (247). Quantitative variables were assessed for Gaussian distribution using the D'Agostino-Pearson test. Normally distributed data are shown as mean ± SEM and analyzed with unpaired t-tests where appropriate. Given the heterogeneity in DRG neurons and sample size constraints, statistical analysis was limited to treatment and sex-defined groups. Parametric data were analyzed via two-way ANOVA with a Tukey post hoc test, while non-parametric data underwent Kruskal–Wallis with Dunn's test for multiple comparisons. Non-normally distributed data are expressed as median (interquartile range, Q25–Q75) and analyzed using the Mann–Whitney test, with significance set at $P < 0.05$ (150). For patch clamp experiments, 'n' represents cell counts per independent experiment, while 'N' indicates the number of mice. Full statistical methods are detailed in the figure legends.

BIBLIOGRAPHY

7. Bibliography

1. Gadhvi M, Moore MJ, Waseem M. Physiology, Sensory System. StatPearls. 2023;
2. Julius D, Nathans J. Signaling by sensory receptors. Cold Spring Harb Perspect Biol. 2012;4(1).
3. Haberberger RV, Barry C, Dominguez N, Matusica D. Human dorsal root ganglia. Vol. 13, Frontiers in Cellular Neuroscience. 2019.
4. Henley C, Lansing E. FOUNDATIONS OF NEUROSCIENCE Open Edition. 2021.
5. Risch N, Pointeau F, Poquet N. Nociception. Kinesitherapie. 2017;17(186).
6. Terrier LM, Hadjikhani N, Destrieux C. The trigeminal pathways. Vol. 269, Journal of Neurology. 2022.
7. Martinez-Garcia RI, Voelcker B, Zaltsman JB, Patrick SL, Stevens TR, Connors BW, et al. Two dynamically distinct circuits drive inhibition in the sensory thalamus. Nature. 2020;583(7818).
8. Lawson SN. Phenotype and function of somatic primary afferent nociceptive neurones with C-, Aδ- or Aα/β-fibres. Exp Physiol. 2002;87(2).
9. Basbaum AI, Bautista DM, Scherrer G, Julius D. Cellular and Molecular Mechanisms of Pain. Vol. 139, Cell. 2009.
10. Han S. The role of mechanoreceptors in acupuncture. Med Nov Technol Devices. 2023;17.
11. Schepers RJ, Ringkamp M. Thermoreceptors and thermosensitive afferents. Vol. 34, Neuroscience and Biobehavioral Reviews. 2010.
12. Woolf CJ, Ma Q. Nociceptors-Noxious Stimulus Detectors. Vol. 55, Neuron. 2007.
13. Woolf CJ. What is this thing called pain? Vol. 120, Journal of Clinical Investigation. 2010.
14. Daneshjou K, Jafarieh H, Raaeskarami SR. Congenital insensitivity to pain and anhydrosis (CIPA) syndrome; A report of 4 cases. Iran J Pediatr. 2012;22(3).
15. Raja SN, Carr DB, Cohen M, Finnerup NB, Flor H, Gibson S, et al. The revised International Association for the Study of Pain definition of pain: concepts, challenges, and compromises. Vol. 161, Pain. Lippincott Williams and Wilkins; 2020. p. 1976–82.
16. Sabsoob O, Elsaraj SM, Gornitsky M, Laszlo E, Fricton JR, Schiffman EL, et al. Acute and Chronic Temporomandibular Disorder Pain: A critical review of differentiating factors and predictors of acute to chronic pain transition. Vol. 49, Journal of Oral Rehabilitation. 2022.
17. Dragan S, Șerban MC, Damian G, Buleu F, Valcovici M, Christodorescu R. Dietary patterns and interventions to alleviate chronic pain. Vol. 12, Nutrients. 2020.
18. Dagnino APA, Campos MM. Chronic Pain in the Elderly: Mechanisms and Perspectives. Vol. 16, Frontiers in Human Neuroscience. 2022.
19. Armour M, Lawson K, Wood A, Smith CA, Abbott J. The cost of illness and economic

burden of endometriosis and chronic pelvic pain in Australia: A national online survey. Vol. 14, PLoS ONE. 2019.

20. Raffaeli W, Tenti M, Corraro A, Malafoglia V, Ilari S, Balzani E, et al. Chronic pain: What does it mean? a review on the use of the term chronic pain in clinical practice. J Pain Res. 2021;14.
21. Osborne-Crowley L. WHAT IS CHRONIC PAIN? New Sci (1956). 2022;256(3413).
22. Gonzalez-Hermosillo DC, Gonzalez-Hermosillo LM, Villaseñor-Almaraz M, Ballesteros-Herrera D, Moreno-Jimenez S, Corona-Cedillo R, et al. Current Concepts of Pain Pathways: A Brief Review of Anatomy, Physiology, and Medical Imaging. Current Medical Imaging Formerly Current Medical Imaging Reviews. 2023;20.
23. Almeida TF, Roizenblatt S, Tufik S. Afferent pain pathways: A neuroanatomical review. Vol. 1000, Brain Research. 2004.
24. Basbaum A. History of Spinal Cord "Pain" Pathways Including the Pathways Not Taken. Vol. 3, Frontiers in Pain Research. 2022.
25. Melzack R. Gate control theory: On the evolution of pain concepts. Vol. 5, Pain Forum. 1996.
26. Johnson M. Transcutaneous Electrical Nerve Stimulation: Mechanisms, Clinical Application and Evidence. Rev Pain. 2007;1(1).
27. Kricheldorff J, Göke K, Kiebs M, Kasten FH, Herrmann CS, Witt K, et al. Evidence of Neuroplastic Changes after Transcranial Magnetic, Electric, and Deep Brain Stimulation. Vol. 12, Brain Sciences. 2022.
28. Usoskin D, Furlan A, Islam S, Abdo H, Lönnerberg P, Lou D, et al. Unbiased classification of sensory neuron types by large-scale single-cell RNA sequencing. Nat Neurosci. 2015;18(1).
29. Zylka MJ. Nonpeptidergic circuits feel your pain. Vol. 47, Neuron. 2005.
30. Landy MA, Goyal M, Lai HC. Nociceptor subtypes are born continuously over DRG development. Dev Biol. 2021;479.
31. Shiers SI, Sankaranarayanan I, Jeevakumar V, Cervantes A, Reese JC, Price TJ. Convergence of peptidergic and non-peptidergic protein markers in the human dorsal root ganglion and spinal dorsal horn. Journal of Comparative Neurology. 2021;529(10).
32. Stucky CL, Lewin GR. Isolectin B4-positive and -negative nociceptors are functionally distinct. Journal of Neuroscience. 1999;19(15).
33. Lolignier S, Gkika D, Andersson D, Leipold E, Vetter I, Viana F, et al. New insight in cold pain: Role of ion channels, modulation, and clinical perspectives. In: Journal of Neuroscience. Society for Neuroscience; 2016. p. 1435–11439.
34. Zhang J, Yao J, Rong M. Editorial: Role of Ion Channels in Pain. Vol. 13, Frontiers in Pharmacology. Frontiers Media S.A.; 2022.
35. Goodwin G, McMahon SB. The physiological function of different voltage-gated

sodium channels in pain. Vol. 22, Nature Reviews Neuroscience. 2021.
36. Chen I, Lui F. Neuroanatomy, Neuron Action Potential. StatPearls. 2019.
37. Delmas P. SnapShot: Ion Channels and Pain. Vol. 134, Cell. 2008.
38. Gohar O, Ph D. Contribution of Ion Channels in Pain Sensation. Alomone. 2005;19(19).
39. Voets T, Talavera K, Owsianik G, Nilius B. Sensing with TRP channels. Nat Chem Biol. 2005 Jul;1(2):85–92.
40. Vera YMB, Wensel TG. Hot on the trail of TRP channel structure. Vol. 133, Journal of General Physiology. 2009.
41. Clapham DE, Runnels LW, Strübing C. The TRP ion channel family. Vol. 2, Nature Reviews Neuroscience. 2001.
42. Belmonte C, Viana F. Molecular and cellular limits to somatosensory specificity. Vol. 4, Molecular Pain. 2008.
43. Smutzer G, Devassy RK. Integrating TRPV1 Receptor Function with Capsaicin Psychophysics. Vol. 2016, Advances in Pharmacological Sciences. 2016.
44. Bujak JK, Kosmala D, Szopa IM, Majchrzak K, Bednarczyk P. Inflammation, Cancer and Immunity—Implication of TRPV1 Channel. Vol. 9, Frontiers in Oncology. 2019.
45. Meents JE, Neeb L, Reuter U. TRPV1 in migraine pathophysiology. Trends Mol Med. 2010;16(4).
46. Bonezzi C, Costantini A, Cruccu G, Fornasari DMM, Guardamagna V, Palmieri V, et al. Capsaicin 8% dermal patch in clinical practice: an expert opinion. Vol. 21, Expert Opinion on Pharmacotherapy. 2020.
47. Yue WWS, Yuan L, Braz JM, Basbaum AI, Julius D. TRPV1 drugs alter core body temperature via central projections of primary afferent sensory neurons. Elife. 2022;11.
48. Lim SG, Seo SE, Jo S, Kim KH, Kim L, Kwon OS. Highly Efficient Real-Time TRPV1 Screening Methodology for Effective Drug Candidates. ACS Omega. 2022;7(41).
49. Pertusa M, Solorza J, Madrid R. Molecular determinants of TRPM8 function: key clues for a cool modulation. Vol. 14, Frontiers in Pharmacology. Frontiers Media SA; 2023.
50. Palchevskyi S, Czarnocki-Cieciura M, Vistoli G, Gervasoni S, Nowak E, Beccari AR, et al. Structure of human TRPM8 channel. Commun Biol. 2023 Dec 1;6(1).
51. Liu Y, Mikrani R, He Y, Faran Ashraf Baig MM, Abbas M, Naveed M, et al. TRPM8 channels: A review of distribution and clinical role. Vol. 882, European Journal of Pharmacology. Elsevier B.V.; 2020.
52. Fakih D, Baudouin C, Goazigo AR Le, Parsadaniantz SM. TRPM8: A therapeutic target for neuroinflammatory symptoms induced by severe dry eye disease. Int J Mol Sci. 2020 Nov 2;21(22):1–21.
53. Liu H, Liu Q, Hua L, Pan J. Inhibition of transient receptor potential melastatin 8 alleviates airway inflammation and remodeling in a murine model of asthma with

cold air stimulus. Acta Biochim Biophys Sin (Shanghai). 2018 May 1;50(5):499–506.
54. Asuthkar S, Velpula KK, Elustondo PA, Demirkhanyan L, Zakharian E. TRPM8 channel as a novel molecular target in androgen-regulated prostate cancer cells. Oncotarget. 2015 Jul 10;6(19):17221–36.
55. Pérez De Vega MJ, Gómez-Monterrey I, Ferrer-Montiel A, González-Muñiz R. Transient Receptor Potential Melastatin 8 Channel (TRPM8) Modulation: Cool Entryway for Treating Pain and Cancer. Vol. 59, Journal of Medicinal Chemistry. American Chemical Society; 2016. p. 10006–29.
56. Aierken A, Xie YK, Dong W, Apaer A, Lin JJ, Zhao Z, et al. Rational Design of a Modality-Specific Inhibitor of TRPM8 Channel against Oxaliplatin-Induced Cold Allodynia. Advanced Science. 2021 Nov 1;8(22).
57. Ochoa S V., Casas Z, Albarracín SL, Sutachan JJ, Torres YP. Therapeutic potential of TRPM8 channels in cancer treatment. Vol. 14, Frontiers in Pharmacology. Frontiers Media SA; 2023.
58. Zhang H, Wang C, Zhang K, Kamau PM, Luo A, Tian L, et al. The role of TRPA1 channels in thermosensation. Vol. 1, Cell Insight. 2022.
59. Landini L, de Araujo DSM, Titiz M, Geppetti P, Nassini R, De Logu F. TRPA1 Role in Inflammatory Disorders: What Is Known So Far? Vol. 23, International Journal of Molecular Sciences. 2022.
60. Vandewauw I, De Clercq K, Mulier M, Held K, Pinto S, Van Ranst N, et al. A TRP channel trio mediates acute noxious heat sensing. Nature. 2018;555(7698).
61. McKemy DD. How cold is it? TRPM8 and TRPA1 in the molecular logic of cold sensation. Vol. 1, Molecular Pain. 2005.
62. Maglie R, de Araujo DSM, Antiga E, Geppetti P, Nassini R, De Logu F. The role of trpa1 in skin physiology and pathology. Vol. 22, International Journal of Molecular Sciences. 2021.
63. Camino D Del, Murphy S, Heiry M, Barrett LB, Earley TJ, Cook CA, et al. TRPA1 contributes to cold hypersensitivity. Journal of Neuroscience. 2010;30(45).
64. Souza Monteiro de Araujo D, Nassini R, Geppetti P, De Logu F. TRPA1 as a therapeutic target for nociceptive pain. Vol. 24, Expert Opinion on Therapeutic Targets. 2020.
65. De Lera Ruiz M, Kraus RL. Voltage-Gated Sodium Channels: Structure, Function, Pharmacology, and Clinical Indications. Vol. 58, Journal of Medicinal Chemistry. 2015.
66. Bennett DL, Clark XAJ, Huang J, Waxman SG, Dib-Hajj SD. The role of voltage-gated sodium channels in pain signaling. Physiol Rev. 2019;99(2).
67. Shields SD, Deng L, Reese RM, Dourado M, Tao J, Foreman O, et al. Insensitivity to pain upon adult-onset deletion of nav1.7 or its blockade with selective inhibitors. Journal of Neuroscience. 2018;38(47).
68. Bird E V., Christmas CR, Loescher AR, Smith KG, Robinson PP, Black JA, et al.

Correlation of Nav1.8 and Nav1.9 sodium channel expression with neuropathic pain in human subjects with lingual nerve neuromas. Mol Pain. 2013;9(1).

69. Middleton SJ, Perini I, Themistocleous AC, Weir GA, McCann K, Barry AM, et al. Nav1.7 is required for normal C-low threshold mechanoreceptor function in humans and mice. Brain. 2022;145(10).
70. Xue Y, Chidiac C, Herault Y, Gaveriaux-Ruff C. Pain behavior in SCN9A (Nav1.7) and SCN10A (Nav1.8) mutant rodent models. Vol. 753, Neuroscience Letters. 2021.
71. Minett MS, Nassar MA, Clark AK, Passmore G, Dickenson AH, Wang F, et al. Distinct Nav1.7-dependent pain sensations require different sets of sensory and sympathetic neurons. Nat Commun. 2012;3.
72. Minett MS, Falk S, Santana-Varela S, Bogdanov YD, Nassar MA, Heegaard AM, et al. Pain without nociceptors? Nav1.7-independent pain mechanisms. Cell Rep. 2014;6(2).
73. McKerrall SJ, Sutherlin DP. Nav1.7 inhibitors for the treatment of chronic pain. Vol. 28, Bioorganic and Medicinal Chemistry Letters. 2018.
74. Okuda H, Inoue S, Oyamada Y, Koizumi A, Youssefian S. Reduced pain sensitivity of episodic pain syndrome model mice carrying a Nav1.9 mutation by ANP-230, a novel sodium channel blocker. Heliyon. 2023;9(4).
75. Hameed S. Nav1.7 and Nav1.8: Role in the pathophysiology of pain. Vol. 15, Molecular Pain. 2019.
76. Gold MS, Weinreich D, Kim CS, Wang R, Treanor J, Porreca F, et al. Redistribution of Nav1.8 in uninjured axons enables neuropathic pain. Journal of Neuroscience. 2003;23(1).
77. He W you, Zhang B, Xiong Q ming, Yang C xiang, Zhao W cheng, He J, et al. Intrathecal administration of rapamycin inhibits the phosphorylation of DRG Nav1.8 and attenuates STZ-induced painful diabetic neuropathy in rats. Neurosci Lett. 2016;619.
78. Facer P, Punjabi PP, Abrari A, Kaba RA, Severs NJ, Chambers J, et al. Localisation of SCN10A gene product Nav1.8 and novel pain-related ion channels in human heart. Int Heart J. 2011;52(3).
79. Hijma HJ, Siebenga PS, De Kam ML, Groeneveld GJ. A Phase 1, Randomized, Double-Blind, Placebo-Controlled, Crossover Study to Evaluate the Pharmacodynamic Effects of VX-150, a Highly Selective NaV1.8 Inhibitor, in Healthy Male Adults. Pain Medicine (United States). 2021;22(8).
80. Osteen JD, Immani S, Tapley TL, Indersmitten T, Hurst NW, Healey T, et al. Pharmacology and Mechanism of Action of Suzetrigine, a Potent and Selective NaV1.8 Pain Signal Inhibitor for the Treatment of Moderate to Severe Pain. Pain Ther. 2025;
81. Bai Q, Shao J, Cao J, Ren X, Cai W, Su S, et al. Protein kinase C-α upregulates sodium channel Nav1.9 in nociceptive dorsal root ganglion neurons in an inflammatory

arthritis pain model of rat. J Cell Biochem. 2020;121(1).

82. Baker MD, Nassar MA. Painful and painless mutations of SCN9A and SCN11A voltage-gated sodium channels. Vol. 472, Pflugers Archiv European Journal of Physiology. 2020.
83. Brackx W, Collaço R de C, Theys M, Vander Cruyssen J, Bosmans F. Understanding the physiological role of NaV1.9: Challenges and opportunities for pain modulation. Vol. 245, Pharmacology and Therapeutics. 2023.
84. Zu M, Guo WW, Cong T, Ji F, Zhang SL, Zhang Y, et al. SCN11A gene deletion causes sensorineural hearing loss by impairing the ribbon synapses and auditory nerves. BMC Neurosci. 2021;22(1).
85. Touska F, Turnquist B, Vlachova V, Reeh PW, Leffler A, Zimmermann K. Heat-resistant action potentials require TTXresistant sodium channels NaV1.8 and NaV1.9. Journal of General Physiology. 2018;150(8).
86. Kruger LC, Isom LL. Voltage-gated na+ channels: Not just for conduction. Cold Spring Harb Perspect Biol. 2016;8(6).
87. Chong HL, Ruben PC. Interaction between voltage-gated sodium channels and the neurotoxin, tetrodotoxin. Vol. 2, Channels. 2008.
88. Zheng YM, Wang WF, Li YF, Yu Y, Gao ZB. Enhancing inactivation rather than reducing activation of Nav1.7 channels by a clinically effective analgesic CNV1014802. Acta Pharmacol Sin. 2018;39(4).
89. Theile JW, Fuller MD, Chapman ML. The selective Nav1.7 inhibitor, PF-05089771, interacts equivalently with fast and slow inactivated Nav1.7 channels. Mol Pharmacol. 2016;90(5).
90. Tian C, Zhu R, Zhu L, Qiu T, Cao Z, Kang T. Potassium channels: Structures, diseases, and modulators. Chem Biol Drug Des. 2014;83(1).
91. Valiyaveetil FI. Voltage-Gated Potassium Channels. In: Textbook of Ion Channels Volume II: Properties, Function, and Pharmacology of the Superfamilies. 2023.
92. Johnston J. Pharmacology of A-Type K+ Channels. In: Handbook of Experimental Pharmacology. 2021.
93. Tsantoulas C, McMahon SB. Opening paths to novel analgesics: The role of potassium channels in chronic pain. Vol. 37, Trends in Neurosciences. 2014.
94. Staff NP, Grisold A, Grisold W, Windebank AJ. Chemotherapy-induced peripheral neuropathy: A current review. Vol. 81, Annals of Neurology. John Wiley and Sons Inc.; 2017. p. 772–81.
95. Flatters SJL, Dougherty PM, Colvin LA. Clinical and preclinical perspectives on Chemotherapy-Induced Peripheral Neuropathy (CIPN): A narrative review. Vol. 119, British Journal of Anaesthesia. 2017.
96. Zajaczkowską R, Kocot-Kępska M, Leppert W, Wrzosek A, Mika J, Wordliczek J. Mechanisms of chemotherapy-induced peripheral neuropathy. Vol. 20, International Journal of Molecular Sciences. 2019.

97. Desforges AD, Hebert CM, Spence AL, Reid B, Dhaibar HA, Cruz-Topete D, et al. Treatment and diagnosis of chemotherapy-induced peripheral neuropathy: An update. Vol. 147, Biomedicine and Pharmacotherapy. Elsevier Masson s.r.l.; 2022.
98. Tamburin S, Park SB, Schenone A, Mantovani E, Hamedani M, Alberti P, et al. Rehabilitation, exercise, and related non-pharmacological interventions for chemotherapy-induced peripheral neurotoxicity: Systematic review and evidence-based recommendations. Vol. 171, Critical Reviews in Oncology/Hematology. 2022.
99. Argyriou AA, Park SB, Islam B, Tamburin S, Velasco R, Alberti P, et al. Neurophysiological, nerve imaging and other techniques to assess chemotherapy-induced peripheral neurotoxicity in the clinical and research settings. Vol. 90, Journal of Neurology, Neurosurgery and Psychiatry. 2019.
100. Nassini R, Benemei S, Fusi C, Trevisan G, Materazzi S. Transient Receptor Potential Channels in Chemotherapy-Induced Neuropathy. Open Pain J. 2013;6(1).
101. Witting N, Svensson P, Gottrup H, Arendt-Nielsen L, Jensen TS. Intramuscular and intradermal injection of capsaicin: A comparison of local and referred pain. Pain. 2000;84(2–3).
102. Watanabe M, Ueda T, Shibata Y, Kumamoto N, Ugawa S. The role of TRPV1 channels in carrageenan-induced mechanical hyperalgesia in mice. Neuroreport. 2015;26(3).
103. Chung MK, Lee J, Joseph J, Saloman J, Ro JY. Peripheral group i metabotropic glutamate receptor activation leads to muscle mechanical hyperalgesia through TRPV1 phosphorylation in the rat. Journal of Pain. 2015;16(1).
104. Lin SY, Corey DP. TRP channels in mechanosensation. Vol. 15, Current Opinion in Neurobiology. 2005.
105. Yao K, Dou B, Zhang Y, Chen Z, Li Y, Fan Z, et al. Inflammation—the role of TRPA1 channel. Vol. 14, Frontiers in Physiology. 2023.
106. Silverman HA, Chen A, Kravatz NL, Chavan SS, Chang EH. Involvement of Neural Transient Receptor Potential Channels in Peripheral Inflammation. Vol. 11, Frontiers in Immunology. Frontiers Media S.A.; 2020.
107. Servitja S, Castro-Henriques M, Álvarez-Busto I, Díez-Franco C, Medina-Castillo A, Algarra-García MA, et al. A Non-Pharmacological, Nociceutical Formulation Lessens Chemotherapy-Induced Peripheral Neuropathy in Cancer Patients [Internet]. 2024. Available from: http://medrxiv.org/lookup/doi/10.1101/2024.12.29.24319628
108. Asiri YI, Zaheen Hassan M. An overview of ion channels therapeutics in the treatment of pain. Vol. 16, Arabian Journal of Chemistry. Elsevier B.V.; 2023.
109. Hou S, Huh B, Kim HK, Kim KH, Abdi S. Treatment of chemotherapy-induced peripheral neuropathy: Systematic review and recommendations. Vol. 21, Pain Physician. 2018.

110. Hershman DL, Lacchetti C, Dworkin RH, Lavoie Smith EM, Bleeker J, Cavaletti G, et al. Prevention and management of chemotherapy-induced peripheral neuropathy in survivors of adult cancers: American society of clinical oncology clinical practice guideline. Vol. 32, Journal of Clinical Oncology. 2014.
111. Swain SM, Arezzo JC. Neuropathy associated with microtubule inhibitors: Diagnosis, incidence, and management. Vol. 6, Clinical Advances in Hematology and Oncology. 2008.
112. Lipton RB, Apfel SC, Dutcher JP, Rosenberg R, Kaplan J, Berger A, et al. Taxol produces a predominantly sensory neuropathy. Neurology. 1989;39(3).
113. Dougherty PM, Cata JP, Cordella J V., Burton A, Weng HR. Taxol-induced sensory disturbance is characterized by preferential impairment of myelinated fiber function in cancer patients. Pain. 2004;109(1–2).
114. Van Den Bent MJ, Van Raaij-Van Den Aarssen VJM, Verweij J, Doorn PAV, Smitt PAES. Progression of paclitaxel-induced neuropathy following discontinuation of treatment. Muscle Nerve. 1997;20(6).
115. Gill PS, Tulpule A, Espina BM, Cabriales S, Bresnahan J, Ilaw M, et al. Paclitaxel is safe and effective in the treatment of advanced AIDS- related Kaposi's sarcoma. Journal of Clinical Oncology. 1999;17(6).
116. McGuire WP, Rowinsky EK, Rosenhein NB, Grumbine FC, Ettinger DS, Armstrong DK, et al. Taxol: A unique antineoplastic agent with significant activity in advanced ovarian epithelial neoplasms. Ann Intern Med. 1989;111(4).
117. Holmes FA, Walters RS, Theriault RL, Buzdar AU, Frye DK, Hortobagyi GN, et al. Phase II trial of taxol, an active drug in the treatment of metastatic breast cancer. J Natl Cancer Inst. 1991;83(24).
118. Jiang T, Cao YN, Xu JB, Gao F, Zheng LL. Molecular-docking-guided design, palladium-catalyzed synthesis and anticancer activity of paclitaxel-benzoxazoles hybrids. Sci Rep. 2022;12(1).
119. Nogales E, Grayer Wolf S, Khan IA, Ludueña RF, Downing KH. Structure of tubulin at 6.5 Å and location of the taxol-binding site. Nature. 1995;375(6530).
120. Engblom P, Pulkkinen JO, Rantanen V, Hirvonen H, Kulmala J, Grènman R, et al. Effects of paclitaxel with or without cremophor EL on cellular clonogenic survival and apoptosis. Eur J Cancer. 1999;35(2).
121. Eiseman JL, Eddington ND, Leslie J, MacAuley C, Sentz DL, Zuhowski M, et al. Plasma pharmacokinetics and tissue distribution of paclitaxel in CD2F1 mice. Cancer Chemother Pharmacol. 1994;34(6).
122. Lesser GJ, Grossman SA, Eller S, Rowinsky EK. The distribution of systemically administered [3H]-paclitaxel in rats: a quantitative autoradiographic study. Cancer Chemother Pharmacol. 1995;37(1–2).
123. Wozniak KM, Vornov JJ, Wu Y, Nomoto K, Littlefield BA, DesJardins C, et al. Sustained accumulation of microtubule-binding chemotherapy drugs in the

peripheral nervous system: Correlations with time course and neurotoxic severity. Cancer Res. 2016;76(11).

124. Cavaletti G, Tredici G, Braga M, Tazzari S. Experimental peripheral neuropathy induced in adult rats by repeated intraperitoneal administration of taxol. Exp Neurol. 1995;133(1).
125. Xiao WH, Bennett GJ. Chemotherapy-evoked neuropathic pain: Abnormal spontaneous discharge in A-fiber and C-fiber primary afferent neurons and its suppression by acetyl-l-carnitine. Pain. 2008;135(3).
126. Polomano RC, Mannes AJ, Clark US, Bennett GJ. A painful peripheral neuropathy in the rat produced by the chemotherapeutic drug, paclitaxel. Pain. 2001;94(3).
127. Postma TJ, Aaronson NK, Heimans JJ, Muller MJ, Hildebrand JG, Delattre JY, et al. The development of an EORTC quality of life questionnaire to assess chemotherapy-induced peripheral neuropathy: The QLQ-CIPN20. Eur J Cancer. 2005;41(8).
128. Wiernik PH, Schwartz EL, Einzig A, Strauman JJ, Lipton RB, Dutcher JP. Phase I trial of taxol given as a 24-hour infusion every 21 days: Responses observed in metastatic melanoma. Journal of Clinical Oncology. 1987;5(8).
129. Zhang H, Dougherty PM. Enhanced excitability of primary sensory neurons and altered gene expression of neuronal ion channels in dorsal root ganglion in paclitaxel-induced peripheral neuropathy. Anesthesiology. 2014;120(6).
130. Xiao WH, Zheng H, Zheng FY, Nuydens R, Meert TF, Bennett GJ. Mitochondrial abnormality in sensory, but not motor, axons in paclitaxel-evoked painful peripheral neuropathy in the rat. Neuroscience. 2011;199.
131. Cavaletti G, Alberti P, Canta A, Carozzi V, Cherchi L, Chiorazzi A, et al. Translation of paclitaxel-induced peripheral neurotoxicity from mice to patients: the importance of model selection. Pain. 2024 Nov 2;
132. Heimans JJ, Vermorken JB, Wolbers JG, Eeltink CM, Meijer OWM, Taphoorn MJB, et al. Paclitaxel (TAXOL®) concentrations in brain tumor tissue. Annals of Oncology. 1994;5(10).
133. Hershman DL, Unger JM, Crew KD, Minasian LM, Awad D, Moinpour CM, et al. Randomized double-blind placebo-controlled trial of acetyl-L-carnitine for the prevention of taxane-induced neuropathy in women undergoing adjuvant breast cancer therapy. Journal of Clinical Oncology. 2013;31(20).
134. Kleckner IR, Kamen C, Gewandter JS, Mohile NA, Heckler CE, Culakova E, et al. Effects of exercise during chemotherapy on chemotherapy-induced peripheral neuropathy: a multicenter, randomized controlled trial. Supportive Care in Cancer. 2018;26(4).
135. Majithia N, Temkin SM, Ruddy KJ, Beutler AS, Hershman DL, Loprinzi CL. National Cancer Institute-supported chemotherapy-induced peripheral neuropathy trials: outcomes and lessons. Vol. 24, Supportive Care in Cancer. 2016.

136. Argyriou AA, Chroni E, Koutras A, Iconomou G, Papapetropoulos S, Polychronopoulos P, et al. Preventing Paclitaxel-Induced Peripheral Neuropathy: A Phase II Trial of Vitamin E Supplementation. J Pain Symptom Manage. 2006;32(3).
137. Kottschade LA, Sloan JA, Mazurczak MA, Johnson DB, Murphy BP, Rowland KM, et al. The use of vitamin E for the prevention of chemotherapy-induced peripheral neuropathy: Results of a randomized phase III clinical trial. Supportive Care in Cancer. 2011;19(11).
138. Flatters SJL, Xiao WH, Bennett GJ. Acetyl-L-carnitine prevents and reduces paclitaxel-induced painful peripheral neuropathy. Neurosci Lett. 2006;397(3).
139. Gorson KC, Schott C, Herman R, Ropper AH, Rand WM. Gabapentin in the treatment of painful diabetic neuropathy: A placebo controlled, double blind, crossover trial [4]. Vol. 66, Journal of Neurology Neurosurgery and Psychiatry. 1999.
140. Gewandter JS, Mohile SG, Heckler CE, Ryan JL, Kirshner JJ, Flynn PJ, et al. A phase III randomized, placebo-controlled study of topical amitriptyline and ketamine for chemotherapy-induced peripheral neuropathy (CIPN): A University of Rochester CCOP study of 462 cancer survivors. Supportive Care in Cancer. 2014;22(7).
141. Hopkins HL, Duggett NA, Flatters SJL. Chemotherapy-induced painful neuropathy: Pain-like behaviours in rodent models and their response to commonly used analgesics. Vol. 10, Current Opinion in Supportive and Palliative Care. 2016.
142. Reagan-Shaw S, Nihal M, Ahmad N. Dose translation from animal to human studies revisited. The FASEB Journal. 2008;22(3).
143. Griffiths LA, Duggett NA, Pitcher AL, Flatters SJL. Evoked and Ongoing Pain-Like Behaviours in a Rat Model of Paclitaxel-Induced Peripheral Neuropathy. Pain Res Manag. 2018;2018.
144. Imai S, Koyanagi M, Azimi Z, Nakazato Y, Matsumoto M, Ogihara T, et al. Taxanes and platinum derivatives impair Schwann cells via distinct mechanisms. Sci Rep. 2017;7(1).
145. Bartley EJ, Fillingim RB. Sex differences in pain: A brief review of clinical and experimental findings. Br J Anaesth. 2013;111(1):52–8.
146. Mogil JS. Sex differences in pain and pain inhibition: Multiple explanations of a controversial phenomenon. Vol. 13, Nature Reviews Neuroscience. 2012. p. 859–66.
147. Fillingim RB, King CD, Ribeiro-Dasilva MC, Rahim-Williams B, Riley JL. Sex, Gender, and Pain: A Review of Recent Clinical and Experimental Findings. Vol. 10, Journal of Pain. 2009.
148. Cabañero D, Villalba-Riquelme E, Fernández-Ballester G, Fernández-Carvajal A, Ferrer-Montiel A. ThermoTRP channels in pain sexual dimorphism: new insights for drug intervention. Vol. 240, Pharmacology and Therapeutics. 2022.
149. Mizrahi D, Park SB, Li T, Timmins HC, Trinh T, Au K, et al. Hemoglobin, Body Mass Index, and Age as Risk Factors for Paclitaxel- and Oxaliplatin-Induced Peripheral

Neuropathy. JAMA Netw Open. 2021;4(2).
150. Villalba-Riquelme E, de la Torre-Martínez R, Fernández-Carvajal A, Ferrer-Montiel A. Paclitaxel in vitro reversibly sensitizes the excitability of IB4(−) and IB4(+) sensory neurons from male and female rats. Br J Pharmacol. 2022;179(14).
151. Luo X, Chen O, Wang Z, Bang S, Ji J, Lee SH, et al. IL-23/IL-17A/TRPV1 axis produces mechanical pain via macrophage-sensory neuron crosstalk in female mice. Neuron. 2021;109(17).
152. Luo X, Ji J, Ji RR. Sex Differences in Pain with Emphasis on Neuroimmune Interactions. In: Neuroimmune Interactions in Pain: Mechanisms and Therapeutics. 2023.
153. Forsyth KS, Jiwrajka N, Lovell CD, Toothacre NE, Anguera MC. The conneXion between sex and immune responses. Vol. 24, Nature Reviews Immunology. 2024.
154. Gøransson LG, Mellgren SI, Lindal S, Omdal R. The effect of age and gender on epidermal nerve fiber density. Neurology. 2004;62(5).
155. Naji-Esfahani H, Vaseghi G, Safaeian L, Pilehvarian AA, Abed A, Rafieian-Kopaei M. Gender differences in a mouse model of chemotherapy-induced neuropathic pain. Lab Anim. 2016;50(1).
156. Ferrari LF, Araldi D, Green PG, Levine JD. Marked sexual dimorphism in neuroendocrine mechanisms for the exacerbation of paclitaxel-induced painful peripheral neuropathy by stress. Pain. 2020;161(4).
157. Hwang BY, Kim ES, Kim CH, Kwon JY, Kim HK. Gender differences in paclitaxel-induced neuropathic pain behavior and analgesic response in rats. Korean J Anesthesiol. 2012;62(1).
158. Warncke UO, Toma W, Meade JA, Park AJ, Thompson DC, Caillaud M, et al. Impact of Dose, Sex, and Strain on Oxaliplatin-Induced Peripheral Neuropathy in Mice. Frontiers in Pain Research. 2021;2.
159. Wakelee HA, Wang W, Schiller JH, Langer CJ, Sandler AB, Belani CP, et al. Survival differences by sex for patients with advanced non-small cell lung cancer on Eastern Cooperative Oncology Group trial 1594. Journal of Thoracic Oncology. 2006;1(5).
160. Woller SA, Corr M, Yaksh TL. Differences in cisplatin-induced mechanical allodynia in male and female mice. European Journal of Pain (United Kingdom). 2015;19(10).
161. Wongtawatchai T, Agthong S, Kaewsema A, Chentanez V. Sex-related differences in cisplatin-induced neuropathy in rats. Journal of the Medical Association of Thailand. 2009;92(11).
162. Joseph EK, Levine JD. Sexual dimorphism for protein kinase Cε signaling in a rat model of vincristine-induced painful peripheral neuropathy. Neuroscience. 2003;119(3).
163. Legakis LP, Diester CM, Townsend EA, Karim-Nejad L, Negus SS. Comparison of chemotherapy effects on mechanical sensitivity and food-maintained operant responding in male and female rats. Behavioural Pharmacology. 2020;31(5).

164. Martínez JW, Sánchez-Naranjo JC, Londoño-De Los Ríos PA, Isaza-Mejía CA, Sosa-Urrea JD, Martínez-Muñoz MA, et al. Prevalence of peripheral neuropathy associated with chemotherapy in four oncology centers of colombia. Rev Neurol. 2019;69(3).
165. Stockstill K, Wahlman C, Braden K, Chen Z, Yosten GL, Tosh DK, et al. Sexually dimorphic therapeutic response in bortezomib-induced neuropathic pain reveals altered pain physiology in female rodents. Pain. 2020;161(1).
166. Kanbayashi Y, Hosokawa T, Okamoto K, Konishi H, Otsuji E, Yoshikawa T, et al. Statistical identification of predictors for peripheral neuropathy associated with administration of bortezomib, taxanes, oxaliplatin or vincristine using ordered logistic regression analysis. Anticancer Drugs. 2010;21(9).
167. Schmidt R, Baumann F, Hanschmann H, Geissler F, Preiss R. Gender difference in ifosfamide metabolism by human liver microsomes. Eur J Drug Metab Pharmacokinet. 2001;26(3).
168. Brahmer JR, Dahlberg SE, Gray RJ, Schiller JH, Perry MC, Sandler A, et al. Sex differences in outcome with bevacizumab therapy: Analysis of patients with advanced-stage non-small cell lung cancer treated with or without bevacizumab in combination with paclitaxel and carboplatin in the eastern cooperative oncology group trial 4599. Journal of Thoracic Oncology. 2011;6(1).
169. Piedbois P. Toxicity of fluorouracil in patients with advanced colorectal cancer: Effect of administration schedule and prognostic factors. Journal of Clinical Oncology. 1998;16(11).
170. Wagner AD, Grothey A, Andre T, Dixon JG, Wolmark N, Haller DG, et al. Sex and Adverse Events of Adjuvant Chemotherapy in Colon Cancer: An Analysis of 34 640 Patients in the ACCENT Database. J Natl Cancer Inst. 2021;113(4).
171. Unger JM, Vaidya R, Albain KS, Leblanc M, Minasian LM, Gotay CC, et al. Sex Differences in Risk of Severe Adverse Events in Patients Receiving Immunotherapy, Targeted Therapy, or Chemotherapy in Cancer Clinical Trials. Journal of Clinical Oncology. 2022;40(13).
172. Eikeland SA, Smeland KB, Mols F, Fagerli UM, Bersvendsen HS, Kiserud CE, et al. Chemotherapy-induced peripheral neuropathy after modern treatment of Hodgkin's lymphoma; symptom burden and quality of life. Acta Oncol (Madr). 2021;60(7).
173. Davidson M, Wagner AD, Kouvelakis K, Nanji H, Starling N, Chau I, et al. Influence of sex on chemotherapy efficacy and toxicity in oesophagogastric cancer: A pooled analysis of four randomised trials. Eur J Cancer. 2019;121.
174. Yamada Y, Muro K, Takahashi K, Baba H, Komatsu Y, Satoh T, et al. Impact of sex and histology on the therapeutic effects of fluoropyrimidines and oxaliplatin plus bevacizumab for patients with metastatic colorectal cancer in the SOFT trial. Glob Health Med. 2020;2(4).

175. Marwaha L, Bansal Y, Singh R, Saroj P, Bhandari R, Kuhad A. TRP channels: potential drug target for neuropathic pain. Vol. 24, Inflammopharmacology. Birkhauser Verlag AG; 2016. p. 305–17.
176. Takayama Y, Derouiche S, Maruyama K, Tominaga M. Emerging perspectives on pain management by modulation of TRP channels and ANO1. Int J Mol Sci. 2019 Jul 2;20(14).
177. Nilius B. TRP channels in disease. Vol. 1772, Biochimica et Biophysica Acta - Molecular Basis of Disease. 2007.
178. Marini M, Titiz M, Souza Monteiro de Araújo D, Geppetti P, Nassini R, De Logu F. TRP Channels in Cancer: Signaling Mechanisms and Translational Approaches. Vol. 13, Biomolecules. 2023.
179. Koivisto AP, Belvisi MG, Gaudet R, Szallasi A. Advances in TRP channel drug discovery: from target validation to clinical studies. Vol. 21, Nature Reviews Drug Discovery. 2022.
180. Winchester WJ, Gore K, Glatt S, Petit W, Gardiner JC, Conlon K, et al. Inhibition of TRPM8 Channels Reduces Pain in the Cold Pressor Test in Humans. Journal of Pharmacology and Experimental Therapeutics. 2014 Nov;351(2):259–69.
181. Shehab S, Javed H, Johnson AM, Tariq S, Kumar CA, Emerald BS. Unveiling the mechanisms of neuropathic pain suppression: perineural resiniferatoxin targets Trpv1 and beyond. Front Neuroanat. 2023;17.
182. Gao L, Yang P, Qin P, Lu Y, Li X, Tian Q, et al. Selective potentiation of 2-APB-induced activation of TRPV1-3 channels by acid. Sci Rep. 2016;6.
183. McNamara FN, Randall A, Gunthorpe MJ. Effects of piperine, the pungent component of black pepper, at the human vanilloid receptor (TRPV1). Br J Pharmacol. 2005;144(6).
184. Caballero J. A new era for the design of TRPV1 antagonists and agonists with the use of structural information and molecular docking of capsaicin-like compounds. Vol. 37, Journal of Enzyme Inhibition and Medicinal Chemistry. 2022.
185. Brandt MR, Beyer CE, Stahl SM. TRPV1 antagonists and chronic pain: Beyond thermal perception. Vol. 5, Pharmaceuticals. 2012.
186. Storozhuk M V., Zholos A V. TRP Channels as Novel Targets for Endogenous Ligands: Focus on Endocannabinoids and Nociceptive Signalling. Curr Neuropharmacol. 2017;16(2).
187. Diniz CRAF, Biojone C, Joca SRL, Rantamäki T, Castrén E, Guimarães FS, et al. Dual mechanism of TRKB activation by anandamide through CB1 and TRPV1 receptors. PeerJ. 2019;2019(2).
188. Fioravanti B, De Felice M, Stucky CL, Medler KA, Luo MC, Gardell LR, et al. Constitutive activity at the cannabinoid CB1 receptor is required for behavioral response to noxious chemical stimulation of TRPV1: Antinociceptive actions of CB1 inverse agonists. Journal of Neuroscience. 2008;28(45).

189. Goncalves dos Santos G, Li R, Ng MPE, Lemes JBP, Vieira WF, Nagy I, et al. CB1 receptor-dependent desensitisation of TRPV1 channels contributes to the analgesic effect of dipyrone in sensitised primary sensory neurons. Br J Pharmacol. 2020;177(20).
190. Banfi L, Basso A, Lambruschini C, Moni L, Riva R. The 100 facets of the Passerini reaction. Chem Sci. 2021;12(47):15445–72.
191. Maione S, Starowicz K, Palazzo E, Rossi F, Di Marzo V. The endocannabinoid and endovanilloid systems and their interactions in neuropathic pain. Vol. 67, Drug Development Research. 2006.
192. Mizogami M, Tsuchiya H. Membrane Interactivity of Capsaicin Antagonized by Capsazepine. Int J Mol Sci. 2022;23(7).
193. De Blas GA, Darszon A, Ocampo AY, Serrano CJ, Castellano LE, Hernández-Gonzá EO, et al. TRPM8, a versatile channel in human sperm. PLoS One. 2009;4(6).
194. Nguyen TL, Nam YS, Lee SY, Kim HC, Jang CG. Effects of capsazepine, a transient receptor potential vanilloid type 1 antagonist, on morphine-induced antinociception, tolerance, and dependence in mice. Br J Anaesth. 2010;105(5).
195. Valente P, Fernández-Carvajal A, Camprubí-Robles M, Gomis A, Quirce S, Viana F, et al. Membrane-tethered peptides patterned after the TRP domain (TRPducins) selectively inhibit TRPV1 channel activity. The FASEB Journal. 2011;25(5).
196. Ponsati B, Carreño C, Curto-Reyes V, Valenzuela B, Duart MJ, Van Den Nest W, et al. An inhibitor of neuronal exocytosis (DD04107) displays long-lasting in vivo activity against chronic inflammatory and neuropathic pain. Journal of Pharmacology and Experimental Therapeutics. 2012;341(3).
197. Medley Q, YANG J, Demirs JT, Papillon J, Gao Y, Xu Y, et al. In-vitro and In-vivo pharmacology of SAF312 as a TRPV1 inhibitor for ocular surface pain. Invest Ophthalmol Vis Sci. 2021;62(8).
198. Lima CKF, Silva RM, Lacerda RB, Santos BLR, Silva R V., Amaral LS, et al. LASSBio-1135: A dual TRPV1 antagonist and anti-TNF-alpha compound orally effective in models of inflammatory and neuropathic pain. PLoS One. 2014;9(6).
199. Nikolaeva-Koleva M, Butron L, González-Rodríguez S, Devesa I, Valente P, Serafini M, et al. A capsaicinoid-based soft drug, AG1529, for attenuating TRPV1-mediated histaminergic and inflammatory sensory neuron excitability. Sci Rep. 2021;11(1).
200. D'souza AA, Shegokar R. Polyethylene glycol (PEG): a versatile polymer for pharmaceutical applications. Vol. 13, Expert Opinion on Drug Delivery. 2016.
201. Denda M, Tsutsumi M, Denda S. Topical application of TRPM8 agonists accelerates skin permeability barrier recovery and reduces epidermal proliferation induced by barrier insult: role of cold-sensitive TRP receptors in epidermal permeability barrier homoeostasis. Exp Dermatol. 2010;19(9).
202. Yang JM, Li F, Liu Q, Rüedi M, Wei ET, Lentsman M, et al. A novel TRPM8 agonist relieves dry eye discomfort. BMC Ophthalmol. 2017;17(1).

203. Yoon HJ, Kim J, Yang JM, Wei ET, Kim SJ, Yoon KC. Topical trpm8 agonist for relieving neuropathic ocular pain in patients with dry eye: A pilot study. J Clin Med. 2021;10(2).
204. Frasnelli J, Albrecht J, Bryant B, Lundström JN. Perception of specific trigeminal chemosensory agonists. Neuroscience. 2011;189.
205. Caceres AI, Liu B, Jabba S V., Achanta S, Morris JB, Jordt SE. Transient Receptor Potential Cation Channel Subfamily M Member 8 channels mediate the anti-inflammatory effects of eucalyptol. Br J Pharmacol. 2017;174(9).
206. Yin Y, Zhang F, Feng S, Butay KJ, Borgnia MJ, Im W, et al. Activation mechanism of the mouse cold-sensing TRPM8 channel by cooling agonist and PIP_2. Science (1979). 2022 Oct 14;378(6616).
207. Martín-Escura C, Medina-Peris A, Spear LA, de la Torre Martínez R, Olivos-Oré LA, Barahona MV, et al. β-Lactam TRPM8 Antagonist RGM8-51 Displays Antinociceptive Activity in Different Animal Models. Int J Mol Sci. 2022;23(5).
208. Knowlton WM, Daniels RL, Palkar R, McCoy DD, McKemy DD. Pharmacological blockade of TRPM8 ion channels alters cold and cold pain responses in mice. PLoS One. 2011;6(9).
209. Liu T, Fang Z, Wang G, Shi M, Wang X, Jiang K, et al. Anti-tumor activity of the TRPM8 inhibitor BCTC in prostate cancer DU145 cells. Oncol Lett. 2016;11(1).
210. Malkia A, Pertusa M, Fernández-Ballester G, Ferrer-Montiel A, Viana F. Differential role of the menthol-binding residue Y745 in the antagonism of thermally gated TRPM8 channels. Mol Pain. 2009;5.
211. Hammad A, Mohamed M SA, Khalifa M, El-Daly M. Mechanisms of Paclitaxel-induced peripheral neuropathy. Journal of advanced Biomedical and Pharmaceutical Sciences. 2023;6(1).
212. Flatters SJL, Bennett GJ. Studies of peripheral sensory nerves in paclitaxel-induced painful peripheral neuropathy: Evidence for mitochondrial dysfunction. Pain. 2006;122(3).
213. Stage TB, Hu S, Sparreboom A, Kroetz DL. Role for Drug Transporters in Chemotherapy-Induced Peripheral Neuropathy. Vol. 14, Clinical and Translational Science. 2021.
214. Milescu LS, Bean BP, Smith JC. Isolation of somatic Na+ currents by selective inactivation of axonal channels with a voltage prepulse. Journal of Neuroscience. 2010;30(22).
215. Meents JE, Bressan E, Sontag S, Foerster A, Hautvast P, Rösseler C, et al. The role of Nav1.7 in human nociceptors: Insights from human induced pluripotent stem cell-derived sensory neurons of erythromelalgia patients. Pain. 2019;160(6).
216. Caspani O, Zurborg S, Labuz D, Heppenstall PA. The contribution of TRPM8 and TRPA1 channels to cold allodynia and neuropathic pain. PLoS One. 2009 Oct 8;4(10).

217. Gornstein EL, Schwarz TL. Neurotoxic mechanisms of paclitaxel are local to the distal axon and independent of transport defects. Exp Neurol. 2017;288.
218. Giorgi S, Lamberti A, Butrón L, Gross-Amat O, Alarcón-Alarcón D, Rodríguez-Cañas E, et al. Compartmentalized primary cultures of dorsal root ganglion neurons to model peripheral pathophysiological conditions. Mol Pain. 2023;19.
219. Chang W, Berta T, Kim YH, Lee S, Lee SY, Ji RR. Expression and Role of Voltage-Gated Sodium Channels in Human Dorsal Root Ganglion Neurons with Special Focus on Nav1.7, Species Differences, and Regulation by Paclitaxel. Neurosci Bull. 2018;34(1).
220. Li Y, North RY, Rhines LD, Tatsui CE, Rao G, Edwards DD, et al. Drg voltage-gated sodium channel 1.7 is upregulated in paclitaxel-induced neuropathy in rats and in humans with neuropathic pain. Journal of Neuroscience. 2018;38(5).
221. Sałat K, Filipek B. Antinociceptive activity of transient receptor potential channel TRPV1, TRPA1, and TRPM8 antagonists in neurogenic and neuropathic pain models in mice. J Zhejiang Univ Sci B. 2015;16(3).
222. Kamata Y, Kambe T, Chiba T, Yamamoto K, Kawakami K, Abe K, et al. Paclitaxel induces upregulation of transient receptor potential vanilloid 1 expression in the rat spinal cord. Int J Mol Sci. 2020;21(12).
223. Meng J, Qiu S, Zhang L, You M, Xing H, Zhu J. Berberine Alleviate Cisplatin-Induced Peripheral Neuropathy by Modulating Inflammation Signal via TRPV1. Front Pharmacol. 2022;12.
224. Wanderley CWS, Maganin AGM, Adjafre B, Mendes AS, Silva CEA, Quadros AU, et al. PD-1/PD-L1 Inhibition Enhances Chemotherapy-Induced Neuropathic Pain by Suppressing Neuroimmune Antinociceptive Signaling. Cancer Immunol Res. 2022;10(11).
225. Javeed A, Ashraf M, Riaz A, Ghafoor A, Afzal S, Mukhtar MM. Paclitaxel and immune system. Vol. 38, European Journal of Pharmaceutical Sciences. 2009.
226. Zhang J, Rong L, Shao J, Zhang Y, Liu Y, Zhao S, et al. Epigenetic restoration of voltage-gated potassium channel Kv1.2 alleviates nerve injury-induced neuropathic pain. J Neurochem. 2021;156(3).
227. Verma P, Eaton M, Kienle A, Flockerzi D, Yang Y, Ramkrishna D. Examining Sodium and Potassium Channel Conductances Involved in Hyperexcitability of Chemotherapy-Induced Peripheral Neuropathy: A Mathematical and Cell Culture-Based Study. Front Comput Neurosci. 2020;14.
228. Busserolles J, Tsantoulas C, Eschalier A, López García JA. Potassium channels in neuropathic pain. Pain. 2016;157(Supplement 1).
229. Li Y, Adamek P, Zhang H, Tatsui CE, Rhines LD, Mrozkova P, et al. The cancer chemotherapeutic paclitaxel increases human and rodent sensory neuron responses to TRPV1 by activation of TLR4. Journal of Neuroscience. 2015;35(39).
230. Klein I, Lehmann HC. Pathomechanisms of paclitaxel-induced peripheral

neuropathy. Toxics. 2021;9(10).

231. F. R, F. P, D. DP, E. P, C. B, I. M. Endocannabinoid/endovanilloid system as new therapeutic target in osteosarcoma. Pediatr Blood Cancer. 2016;63(Supplement 3).
232. Grillaud M, Bianco A. Multifunctional adamantane derivatives as new scaffolds for the multipresentation of bioactive peptides. Vol. 21, Journal of Peptide Science. John Wiley and Sons Ltd; 2015. p. 330–45.
233. Wanka L, Iqbal K, Schreiner PR. The lipophilic bullet hits the targets: Medicinal chemistry of adamantane derivatives. Vol. 113, Chemical Reviews. 2013. p. 3516–604.
234. Pirali T, Galli U, Serafini M, Griglio A, Genazzani AA, Tron GC. Drug Discovery for Soft Drugs on TRPV1 and TRPM8 Channels Using the Passerini Reaction. In 2019. p. 207–21.
235. Brunelli F, Ceresa C, Fracchia L, Tron GC, Aprile S. Expanding the Chemical Space of Drug-like Passerini Compounds: Can α-Acyloxy Carboxamides Be Considered Hard Drugs? ACS Med Chem Lett. 2022 Dec 8;13(12):1898–904.
236. Fang Y, Xue J, Gao S, Lu A, Yang D, Jiang H, et al. Cleavable PEGylation: a strategy for overcoming the "PEG dilemma" in efficient drug delivery. Vol. 24, Drug Delivery. 2017.
237. Iftinca M, Defaye M, Altier C. TRPV1-Targeted Drugs in Development for Human Pain Conditions. Drugs. 2021;81(1).
238. Di Cesare Mannelli L, Lucarini E, Micheli L, Mosca I, Ambrosino P, Soldovieri MV, et al. Effects of natural and synthetic isothiocyanate-based H2S-releasers against chemotherapy-induced neuropathic pain: Role of Kv7 potassium channels. Neuropharmacology. 2017;121.
239. Andrews MD, Af Forselles K, Beaumont K, Galan SRG, Glossop PA, Grenie M, et al. Discovery of a selective TRPM8 antagonist with clinical efficacy in cold-related pain. ACS Med Chem Lett. 2015 Apr 9;6(4):419–24.
240. Liu J, Obando D, Liao V, Lifa T, Codd R. The many faces of the adamantyl group in drug design. Vol. 46, European Journal of Medicinal Chemistry. 2011. p. 1949–63.
241. Izquierdo C, Martín-Martínez M, Gómez-Monterrey I, González-Muñiz R. Trpm8 channels: Advances in structural studies and pharmacological modulation. Vol. 22, International Journal of Molecular Sciences. MDPI; 2021.
242. Flores-Reyes JC, Islas-Jácome A, González-Zamora E. The Ugi three-component reaction and its variants. Organic Chemistry Frontiers. 2021;8(19):5460–515.
243. Dansie EJ, Turk DC. Assessment of patients with chronic pain. Br J Anaesth. 2013;111(1).
244. Lamas JA, Rueda-Ruzafa L, Herrera-Pérez S. Ion Channels and Thermosensitivity: TRP, TREK, or Both? Vol. 20, International journal of molecular sciences. 2019.
245. Santoni G, Cardinali C, Morelli BB, Santoni M, Nabissi M, Amantini C. Danger- and pathogen-associated molecular patterns recognition by pattern-recognition

receptors and ion channels of the transient receptor potential family triggers the inflammasome activation in immune cells and sensory neurons. J Neuroinflammation. 2015;12(1).

246. EUCTR2016-002846-21-ES. A study to investigate the efficacy, safety, tolerability and pharmacokinetic of PARENTIDE, a new drug for the treatment of inflammatory and neuropathic pain, in patients with neuropathic pain. https://trialsearch.who.int/Trial2.aspx?TrialID=EUCTR2016-002846-21-ES. 2017;
247. Lamberti A, Aprile S, Cabañero D, Travagin F, Butron L, Fernández-Ballester G, et al. An adamantane-based ligand as a novel chemical tool for thermosensory <scp>TRPM</scp> 8 channel therapeutic modulation. FEBS J [Internet]. 2025 Mar 23; Available from: https://febs.onlinelibrary.wiley.com/doi/10.1111/febs.70065
248. Lamberti A, Serafini M, Aprile S, Bhela IP, Goutsiou G, Pessolano E, et al. The multicomponent Passerini reaction as a means of accessing diversity in structure, activity and properties: Soft and hard vanilloid/cannabinoid modulators. Eur J Med Chem. 2024 Dec 5;279.
249. Morris GM, Ruth H, Lindstrom W, Sanner MF, Belew RK, Goodsell DS, et al. Software news and updates AutoDock4 and AutoDockTools4: Automated docking with selective receptor flexibility. J Comput Chem. 2009;30(16).
250. Krieger E, Vriend G. YASARA View—molecular graphics for all devices—from smartphones to workstations. Bioinformatics. 2014 Oct 15;30(20):2981–2.
251. Ozvoldik K, Stockner T, Krieger E. YASARA Model–Interactive Molecular Modeling from Two Dimensions to Virtual Realities. J Chem Inf Model. 2023 Oct 23;63(20):6177–82.
252. Iraci N, Ostacolo C, Medina-Peris A, Ciaglia T, Novoselov AM, Altieri A, et al. In Vitro and In Vivo Pharmacological Characterization of a Novel TRPM8 Inhibitor Chemotype Identified by Small-Scale Preclinical Screening. Int J Mol Sci. 2022 Feb 13;23(4):2070.
253. Martín-Escura C, Bonache MA, Medina-Peris A, Voets T, Ferrer-Montiel A, Fernández-Carvajal A, et al. Phenylalanine-derived β-lactam TRPM8 antagonists: revisiting configuration and new benzoyl derivatives. Exploration of Drug Science [Internet]. 2025 Jan 13; Available from: https://www.explorationpub.com/Journals/eds/Article/100882
254. Brenner DS, Golden JP, Gereau RW. A Novel Behavioral Assay for Measuring Cold Sensation in Mice. PLoS One. 2012 Jun 22;7(6):e39765.

ACKNOWLEDGEMENT

It's not easy to explain what a PhD truly means, until you're living it. People often ask: "What's your research about?". A question that seems simple but rarely is. I've seen uncertainty, exhaustion, and sometimes even disillusionment on the faces of my colleagues trying to answer it. For me, though, talking about my project always came with real, sincere enthusiasm. It still does. Because it was much more than a research project: it was a journey of discovery, of relationships, of growth, of falling and getting back up again. And it's a journey I would take a thousand times over. Every achievement holds a story of effort, smiles, doubts, and breakthroughs. ***This is mine*** :

To Professor Carvajal and Professor Ferrer, the minds behind this project and my guiding lights throughout these years: thank you. To Asia, my anchor in tough moments, when experiments didn't go as planned: thank you for always being ready with a solution. To Antonio, who never hesitated to find solutions to help me, always believing in me and pushing me to grow professionally and personally. Thank both of you also for carefully reviewing this thesis and for your patience throughout this journey.

To my "family" in the PIANO project- an adventure as extraordinary as it was, at times, chaotic. This was more than work and research: it was connection, growth, and unexpected friendships. To those I crossed paths with briefly, and those who stayed until the end: thank you. From day one, we built something genuine, something that still unites us beyond the end of this path. A special thank-you to our "extended Italy" group- you made me feel at home wherever we were. No competition, just a sincere desire to share milestones, fears, and joys, even if just for a few days together. Sofia, Francesca, Georgia, and Marco- thank you for making me feel capable, especially when imposter syndrome tried to take over.

To my travel companions: To Simona- thank you for putting up with me when I talked too much, and for lifting me up when I thought I couldn't go on. To Laura- partners in gossip and laughter- thank you for your invaluable advice. To Maggie, Olivia and Vero- for your presence and your contagious laughter. To Jorge, David, and Jose- the gentlemen of the lab who patiently endured the daily chaos brought by the "geese" surrounding them. To Maria, Lucia, Tania, and Selena-for your overwhelming cheerfulness and tear-inducing laughs. To Jessica- for your sweetness and our "Bardonesse" dates, where we always found the time to vent, reflect, and push each other not to sell ourselves short. To Victor- who showed me the beauty of teaching and sharing knowledge, especially when someone believes in you completely.

But behind the scenes, there has always been my Italy- **My family** and the most important people in my life- because "without roots, the tree falls." First and foremost: Mom, Dad, and Sara- my true roots. Thank you for teaching me the value of sacrifice, determination, and humility. Thank you for always supporting and encouraging me to chase my dreams, even when they were miles away, because "mo devi fare i fossi per terra" ("now you have to go the extra mile"). Your strength and unconditional love have been the engine behind every goal I've reached. Every achievement is yours, too. Thank you for being by my side, never letting me feel alone. This milestone is the result of our journey together.

To my family in Caserta and Novara, my aunts and cousins- just hearing your voices for a few minutes could recharge me with self-esteem, making me feel invincible. To my second mom, my grandmother, who chose my name because all "Angela" are important women. I miss you all every day, but I know that whatever path I take, you'll always be proud of me and ready to support me in every choice I make.

To my best friends: To Regina- my confidant, my anchor. I could write pages just to thank you. "I believe in what we are when we're together," because with you, I can be myself with no filter. I know you'll always be there, ready to visit me anywhere in the world, even if just for a day. To Andrea- friend and confidant- one of the most important people on this journey and in my life. Thank you for always being there, for all the laughter, the endless chats, and the times you found just the right words to help me keep going. To Marta- for always being present in moments of excitement and in times of difficulty, and for your unique way of making everything seem simpler. Thank you for your light, your empathy, and for walking with me every day through our shared podcasts. You all were my safe harbor, the shoulders I leaned on, and I will never be grateful enough for that.

To Ivan- thank you for standing by me during the hardest times and for always finding a way to make me feel capable, strong, and enough. Even if our lives are different now, I'll never forget how essential your presence was in helping me get here.

To Antonio "pequeño"- for your "everything will be fine" that made me feel safe like never before. Thank you for your authentic presence, your ability to understand me without words, the way you see me, hear me, and encourage me- making me feel special and truly seen. Your support, sweetness, and determination were a refuge in uncertain times, helping me believe in myself with a confidence I didn't know I had. Thank you for making this journey even more extraordinary.

To Luna- whose unconditional love brightened every day. Your sweet eyes and quiet affection warmed even the coldest days. Your happy runs, excitement at seeing me, and constant presence taught me the value of small things and living in the moment. Thank you, Lunita, for being my light and my four-legged heart.

This is not just my success- it's the result of all the hands, hearts, and minds that walked this path with me. Thank you, from the bottom of my heart.

Finally, **to me**, because I've discovered how amazing it is when I stop limiting myself, when I begin to take small steps, knowing that great changes grow from them. I've learned that the way to do great work is to love what I do. Success is built with discipline, dedication, and determination. To me- who dared to dream big, without fear of being "too much." And to me- who found the strength to keep going, every single day, with patience and passion, knowing the road is long, but each step brings me closer to who I want to become. Don't call me lucky. I failed more times than you tried. Trust me, I'm a *Doctor* now… not that kind of doctor! :)

AD MAIORA ET MELIORA, SEMPER ✿

ANNEX

8. Annex

ANNEX: PUBLICATION 3 FROM CHAPTER 3.

"An adamantane-based ligand as a novel chemical tool for thermosensory TRPM8 channel therapeutic modulation"

Angela Lamberti, Silvio Aprile, David Cabañero, Fabio Travagin, Laura Butron, Gregorio Fernández-Ballester, Gian Cesare Tron, Asia Fernández-Carvajal, Antonio Ferrer-Montiel and Ubaldina Galli.

The FEBS journal, 2025. ISSN 1742-464X. https://doi.org/10.1111/febs.70065. (https://febs.onlinelibrary.wiley.com)

The FEBS Journal

FEBS PRESS science publishing by scientists

An adamantane-based ligand as a novel chemical tool for thermosensory TRPM8 channel therapeutic modulation

Angela Lamberti[1], Silvio Aprile[2], David Cabañero[1], Fabio Travagin[2], Laura Butron[1], Gregorio Fernández-Ballester[1], Gian Cesare Tron[2], Asia Fernández-Carvajal[1], Antonio Ferrer-Montiel[1] and Ubaldina Galli[2]

1 Instituto de Investigación, Desarrollo e Innovación en Biotecnología Sanitaria de Elche (IDiBE), Universidad Miguel Hernández de Elche, Spain

2 Department of Pharmaceutical Sciences, Università degli Studi del Piemonte Orientale, Novara, Italy

Keywords

cold allodynia; drug discovery; ion channel; medicinal chemistry; neuropathy

Correspondence

U. Galli, Department of Pharmaceutical Sciences, Università degli Studi del Piemonte Orientale, Largo Donegani 2, 28100 Novara, Italy
Tel: (+39) 0321 375856
E-mail: ubaldina.galli@uniupo.it
and
A. Ferrer-Montiel, Instituto de Investigación, Desarrollo e Innovación en Biotecnología Sanitaria de Elche (IDiBE), Universidad Miguel Hernández de Elche, Ed. Torregaitan, Av de la Universidad, s/n, 03202 Elche, Spain
Tel: (+34) 966658727
E-mail: aferrer@umh.es

Angela Lamberti and Silvio Aprile contributed equally to this article.

(Received 22 July 2024, revised 20 November 2024, accepted 5 March 2025)

doi:10.1111/febs.70065

Transient receptor potential cation channel subfamily M member 8 (TRPM8) is a nonselective thermosensory cation channel expressed in peripheral nociceptor terminals where it transduces cold temperatures and cooling agents such as menthol. TRPM8 dysfunction has been involved in disabling sensory symptoms, such as cold allodynia. In addition, its widespread expression has signaled this channel as a pivotal therapeutic target for a variety of diseases, from peripheral neuropathies to cancer. Thus, the design and therapeutic validation of TRPM8 antagonists is an important endeavor in biomedicine. To address this, we used the multicomponent Passerini and Ugi reactions to design a novel family of TRPM8 modulators using as a scaffold the adamantane ring that exhibits drug-like qualities. These green chemistry transformations are ideal for the fast synthesis of libraries of medium complexity with minimal or no generation of waste by-products. We report the identification of a family of TRPM8 agonists and antagonists. Among them, 2-((3S,5S,7S)-adamantan-1-ylamino)-2-oxoethyl [1,1′-biphenyl]-2-carboxylate (referred to as compound **23**) is a potent and selective antagonist that reduces TRPM8-induced neuronal firing in primary nociceptor cultures. Compound **23** exhibits 10-fold higher potency for human TRPM8 (hTRPM8) than for hTRPV1 and hTRPA1 channels. Notably, local administration of compound **23** significantly attenuated oxaliplatin-induced peripheral cold allodynia by modulating epidermal TRPM8 sensory endings. Thus, α-acyloxy carboxamide **23** appears as a promising therapeutic candidate to topically intervene on TRPM8-mediated peripheral neuropathies.

Abbreviations

Ac_2O, acetic anhydride; AITC, allyl isothiocyanate; AMG333, (S)-6-(((3-fluoro-4-(trifluoromethoxy)phenyl)(3-fluoropyridin-2-yl)methyl)carbamoyl) nicotinic acid; AMTB, *N*-(3-aminopropyl)-2-{[(3-methylphenyl)methyl]oxy}(20)-*N*-(2-thienylmethyl)benzamide; AP, action potential; $CDCl_3$, deuterated chloroform; DMSO-d_6, deuterated dimethyl sulfoxide; DRG, dorsal root ganglion; EC_{50}, half-maximal effective concentration; EtOAc, ethyl acetate; HEK293, human embryonic kidney 293 cells; hTRP, human transient receptor potential; IC_{50}, half-maximal inhibitory concentration; LC-HRMS, liquid chromatography coupled to high-resolution mass spectrometry; LC-UV, liquid chromatography coupled to ultraviolet detector; MEA, multielectrode array; MeOH, methanol; MLM, mouse liver microsome; OIPN, oxaliplatin-induced peripheral neuropathy; OXP, oxaliplatin; PE, petroleum ether; PF-05105679, (R)-3-[(1-(4-fluorophenyl)ethyl)(quinolin-3-ylcarbonyl)amino]methylbenzoic acid; $POCl_3$, phosphorus oxychloride; SEM, standard error of the mean; TEA, triethylamine; TRP, transient receptor potential; TRPA1, transient receptor potential cation channel ankyrin 1; TRPM8, transient receptor potential cation channel melastatin 8; TRPV1, transient receptor potential cation channel vanilloid 1; WS12, (1R,2S,5R)-*N*-(4-methoxyphenyl)-5-methyl-2-(propan-2-yl)cyclohexane-1-carboxamide.

The FEBS Journal (2025) © 2025 The Author(s). *The FEBS Journal* published by John Wiley & Sons Ltd on behalf of Federation of European Biochemical Societies.
This is an open access article under the terms of the Creative Commons Attribution License, which permits use, distribution and reproduction in any medium, provided the original work is properly cited.

Introduction

The transient receptor potential melastatin 8 (TRPM8) is a nonselective cation channel expressed in sensory neurons. As a member of the TRP family of ion channels, TRPM8 is involved in thermosensation playing a pivotal role in the perception of environmental cold, and the cooling sensation evoked by menthol [1,2]. TRPM8 is active in the range of 8–28 °C and participates in the transduction of cold allodynia [3]. Structurally, the channel is a tetrameric protein assembled by four identical subunits arranged around a central aqueous pore. Each subunit contains six transmembrane segments (S1–S6) and intracellular N- and C-terminals [4]. Upon activation, TRPM8 transits to an open conformation that allows the influx of cations, such as calcium (Ca^{2+}) and sodium (Na^{+}), favoring neuronal depolarization and action potential firing. Electrical impulses are transmitted through the spinal cord towards the sensory processing areas of the brain to elicit the cold sensation [5,6].

TRPM8 has been involved in inflammation and immune responses in several tissues. For example, TRPM8 influences the release of inflammatory mediators from pulmonary epithelial cells leading to dysregulation of immune responses and chronic inflammation [7,8]. The suppression of TRPM8 activity alleviated respiratory hypersensitivity in individuals with asthma [9]. Additionally, several studies have explored the role of TRPM8 in cancer cell proliferation, migration, and apoptosis [10,11] positioning this channel as a potential target for cancer therapy in combination with other treatment modalities [12]. Furthermore, few studies have suggested that TRPM8 is involved in the perception of itch, modulating the transmission of itch-related neural signals through peripheral pathways [13]. Moreover, the TRPM8 receptor has been also implicated in the etiology of dry eye syndrome, a condition characterized by insufficient tear production or poor tear quality, leading to discomfort and irritation [14,15]. Notably, positive results of the phase 3 COMET trial of AR-15512, a novel formulation of a TRPM8 drug candidate for dry eye syndrome, were announced [16].

TRPM8 has been also signaled as pivotal in the pathophysiology of chronic migraine [17,18] and plays a major role in the pathogenesis of oxaliplatin-induced cold allodynia (OIPN). Its pharmacological modulation has been explored as a potential strategy for pain alleviation [19,20]. Thus, the design and validation of TRPM8 modulators are crucial for advancing our understanding on the contribution of TRPM8 to the etiology of neuropathic pain, inflammatory disorders, pruritus, and cancer and to select novel candidates for therapeutic development. Specifically, therapeutic inhibition of TRPM8 may offer antinociception for conditions characterized by cold-associated pain (i.e., cold allodynia) [21] and provide alternatives to traditional analgesics with unwanted side effects such as opioid drugs [22].

In the past years, the development of TRPM8 modulators has faced challenges due to off-target effects and species-specific structural variations [23]. Compounds such as PF-05105679 and AMG333, both orally active TRPM8 antagonists, progressed into clinical trials with the goal of investigating their potential in cold pain hypersensitivity and alleviating migraine symptoms, respectively [24,25]. However, these promising compounds did not advance beyond phase I trials due to safety concerns. Thus, the discovery and development of therapeutically useful TRPM8 modulators remain a biomedical challenge.

In the pursuit of identifying new TRPM8 ligands with therapeutic potential, we combined the power of multicomponent reactions to readily achieve molecular diversity with adamantane that exhibits therapeutic properties. Its cyclic aliphatic hydrocarbon inspired us to consider it as a 'potential surrogate' for the terpene skeleton of TRPM8 ligands such as menthol, eucalyptol, and camphor. Furthermore, the choice of this caged compound as a potential modulator of the TRPM8 channel was motivated by the fact that the adamantane structure has already been reported capable of inhibiting different ion channels implicated in diseases such as viral infections and neurodegenerative disorders [26,27]. In addition, the adamantyl group has been considered as a 'lipophilic bullet' capable of endowing favorable pharmacokinetic characteristics to molecules, such as a good propensity for crossing biological membranes [27,28]. Beyond increasing partition coefficients (log*P* value) by about 3.1 log units, the adamantyl group has been also found to improve drug-like qualities such as metabolic stability. Of note, the steric bulk of the adamantyl group can impede the access of hydrolytic enzymes (esterases, amidases), thereby increasing the plasma half-life of lead compounds [27]. These unique properties of the adamantane scaffold make it an ideal candidate for modulating ion channels, showcasing its potential in the development of therapeutics for diseases resulting from TRPM8 channel dysregulation [29].

Among the dozens of multicomponent reactions discovered to date [30–33] in terms of versatility, efficiency, exploratory power, and experimental

The FEBS Journal (2025) © 2025 The Author(s). *The FEBS Journal* published by John Wiley & Sons Ltd on behalf of Federation of European Biochemical Societies.

17424658, 0, Downloaded from https://febs.onlinelibrary.wiley.com/doi/10.1111/febs.70065 by Universidad Miguel Hernández De Elche, Wiley Online Library on [16/04/2025]. See the Terms and Conditions (https://onlinelibrary.wiley.com/terms-and-conditions) on Wiley Online Library for rules of use; OA articles are governed by the applicable Creative Commons License

simplicity, the Ugi [34–37] and Passerini reactions [38–41] remain very attractive. In these two isocyanide-mediated reactions, four and three components are respectively reacted together to generate α-aminoacyl amides and α-acyloxy carboxamides. These multicomponent reactions produce focused libraries and have the advantage of minimizing the formation of waste products, thus fulfilling the criteria to be considered green chemistry [40]. In 2006, we discovered a new variant of the Ugi reaction, named split-Ugi, whereby replacing a primary amine with a symmetric secondary diamine yielded a new drug-like molecular scaffold [42].

Here, we report a family of adamantane-based TRPM8 agonists and antagonists that increase the channel pharmacopeia. Among all ligands tested, the acyloxy carboxamide **23** (referred to as compound **23**) is a potent hTRPM8 antagonist showing a >10-fold blockade preference over the structurally related thermosensory channels TRPV1 and TRPA1. Furthermore, compound **23** reduced nociceptor excitability and locally attenuated oxaliplatin-induced *in vivo* cold allodynia.

Results

Synthesis of compounds using the Passerini, Ugi, and split-Ugi reactions

To employ the three multicomponent reactions, we utilized 1-isocyanoadamantane (**3**) as a lipophilic warhead. This reagent was prepared from 1-aminoadamantane (**1**) through the intermediate 1-adamantylformamide (**2**), as described previously [43] (Fig. 1). 1-Isocyanoadamantane (**3**) was reacted with various commercially available carboxylic acids (**4–14**) and amines (**15–19**, **1**) (Fig. 1), always employing formaldehyde as the carbonyl component to avoid the introduction of a stereogenic center.

For the Passerini reaction, we mixed isocyanide **3**, formaldehyde, and a carboxylic acid (**4–13**) in dichloromethane and stirred the three-component mixture at room temperature. We obtained 10 α-acyloxy carboxamides (**20–29**) with excellent yields (Fig. 2A). Employing the Ugi reaction, we obtained 12 α-aminoacyl amides (**30–41**) by mixing the 4 components (isocyanide **3**, formaldehyde, a carboxylic acid **4–9**, **14** and a primary amine **1**, **15–18**) in methanol and stirring them at 60 °C (Fig. 2B). Finally, we carried out the split-Ugi reaction [42] to prepare 4 α-acylpiperazino amides (**42–45**) using carboxylic acids **4–6** and **9** (Fig. 2B). In this variant of the Ugi reaction, piperazine **19** was added to the other 3 components, instead of a primary amine, maintaining the same experimental conditions. ^{1}H-NMR, ^{13}C-NMR spectra, and HRMS spectra of final compounds **20–45** are reported in Figs S1–S78.

Ca^{2+}-microfluorometry to screen for agonist/antagonist activity of synthesized compounds

We first evaluated the series of compounds **20–29** synthesized using the Passerini-Adamantane reaction. All compounds were screened for channel agonism and antagonism on recombinant human TRPM8 stably expressed in HEK293 cells (hTRPM8-HEK293) with Ca^{2+} microfluorimetry. For agonistic activity, we directly assessed compound-induced Ca^{2+} influx into hTRPM8-HEK293 cells and compared it with the activity of WS-12, a well-known potent hTPRM8 agonist. Compound-induced TRPM8-mediated Ca^{2+} influx was confirmed using untransfected HEK293 cells and the channel blocker AMTB. For antagonistic activity, modulation of WS-12-induced Ca^{2+} influx was evaluated. The concentration of compounds to reach half of channel activation (EC_{50}) or to block half-channel activity evoked by WS-12 (IC_{50}) are reported in Table 1, along with the percentage of maximal activation or blockade (Efficacy).

We found that compounds **20**, **21**, **23**, **25**, and **29** behave as hTRPM8 antagonists, blocking WS-12 responses with potencies ranging from 0.2 to 45 μM (Table 1). The most potent antagonist was compound **23** that exhibited an IC_{50} value of 0.2 ± 1.3 μM and 100% efficacy. The lowest activity was observed in compound **25**, suggesting that a bulky aromatic group at position R was important for potent antagonistic activity. Compounds **22**, **24**, and **27** exhibited an agonistic activity with potency ranging from 0.6 to 19 μM. Data show that increasing the hydrocarbon side chain (**22** and **24**) produced a decrease in potency, that can be compensated if the increase in size is accompanied by the addition of nucleophile atoms such as nitrogen and oxygen (**27**). Interestingly, compounds **26** and **28**, containing an aromatic group at the R position, displayed agonist activity contrasting with the antagonistic action of compounds **20** and **29**. This suggests that changes in the aromatic ring modulated the interaction of these ligands with molecular determinants of the channel binding site, differentially impacting the allosteric conformational changes needed for channel activation. These results provide a novel family of hTRPM8 agonists and antagonists and signal to α-acyloxy carboxamide **23** as a potent TRPM8 antagonist with potential therapeutic value.

17424658, 0, Downloaded from https://febs.onlinelibrary.wiley.com/doi/10.1111/febs.70065 by Universidad Miguel Hernández De Elche, Wiley Online Library on [16/04/2025]. See the Terms and Conditions (https://onlinelibrary.wiley.com/terms-and-conditions) on Wiley Online Library for rules of use; OA articles are governed by the applicable Creative Commons License

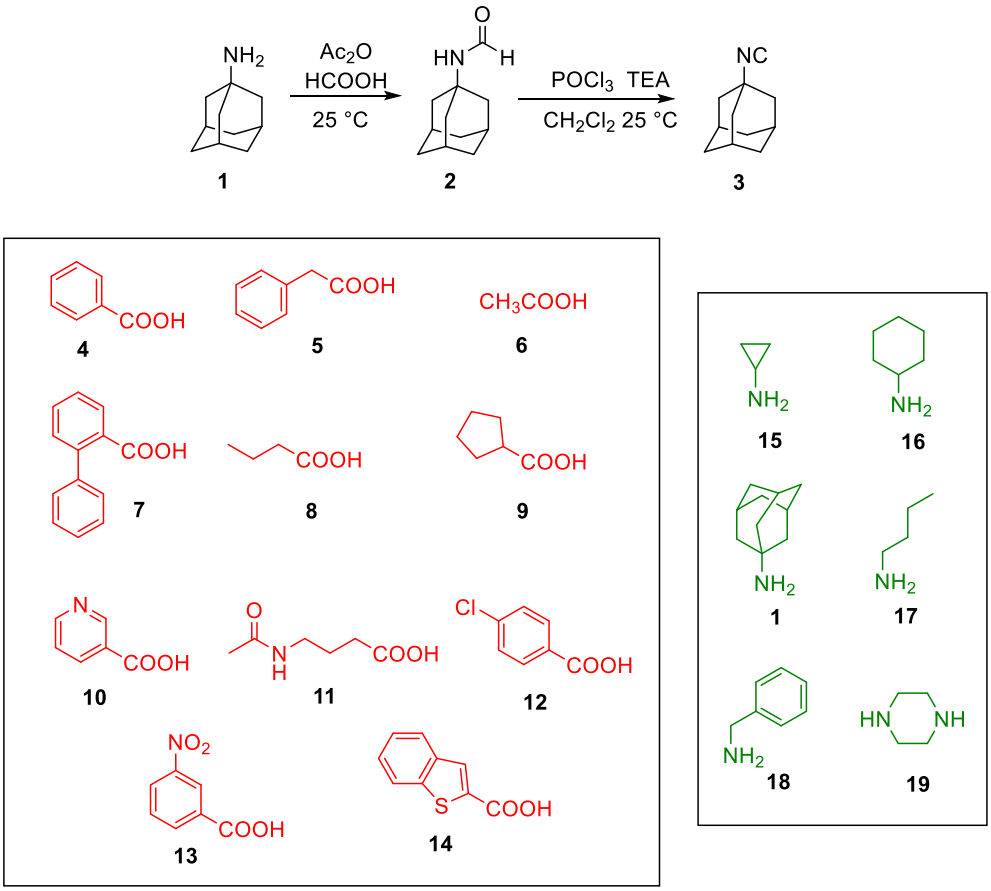

Fig. 1. Preparation reaction of 1-isocyanoadamantane 3 and chemical structure of carboxylic acids **4–14** (red color) and amines **15–19**, **1** (green color) used in this study.

We next evaluated the α-aminoacyl amides **30–41** exploiting the Ugi reaction (Table 1). We also found a mixture of agonists and antagonists within this family of compounds, although more enriched in agonists. Hence, compounds **33** and **35** displayed moderate antagonistic activity with IC_{50} in the low micromolar range. Compound **33** is closely related to compound **23**, indicating that the substitution of the ester by an amide did not drastically alter the activity of the compound, substantiating the importance for antagonistic activity of the bulky aromatic rings. Additional support is provided by compound **35**. All other α-aminoacyl amides exhibited agonistic activity with potencies ranging from 0.2 to 5 μM. Again, the substitution of the ester by an amide modestly affected the potency of most compounds (see **22** with **34**, **37**, **39**, and **40**). A significant increase in potency was observed for compound **31** ($EC_{50} = 0.3 \pm 1.9$ μM) as compared with the ester-containing counterpart **24** ($EC_{50} = 19 \pm 2.0$ μM). Most notably, at variance with the antagonistic activity of the α-acyloxy carboxamide **25** ($IC_{50} = 45 \pm 2.0$ μM), the α-aminoacyl amide **32** acted as a potent hTRPM8 agonist ($EC_{50} = 0.4 \pm 1.7$ μM).

Last, functional evaluation of the four α-acylpiperazino amides (**42–45**) revealed an agonistic activity on hTRPM8 channels, with lower micromolar potency than the α-acyloxy carboxamide and α-aminoacyl amides (Table 1). To highlight specific

Fig. 2. Passerini and Ugi reactions. (A) Preparation of α-acyloxy carboxamides **20–29** via the Passerini reaction and compounds obtained. (B) Synthesis of α-aminoacyl amides **30–41** and α-acylpiperazino amides **42–45** exploiting the Ugi and split-Ugi reactions, respectively, and compounds obtained (black color refers to isocyanide component, blue color refers to aldehyde component, red color refers to carboxylic acid component, and green color refers to amine component).

The FEBS Journal (2025) © 2025 The Author(s). *The FEBS Journal* published by John Wiley & Sons Ltd on behalf of Federation of European Biochemical Societies.

17424658, 0, Downloaded from https://febs.onlinelibrary.wiley.com/doi/10.1111/febs.70065 by Universidad Miguel Hernández De Elche, Wiley Online Library on [16/04/2025]. See the Terms and Conditions (https://onlinelibrary.wiley.com/terms-and-conditions) on Wiley Online Library for rules of use; OA articles are governed by the applicable Creative Commons License

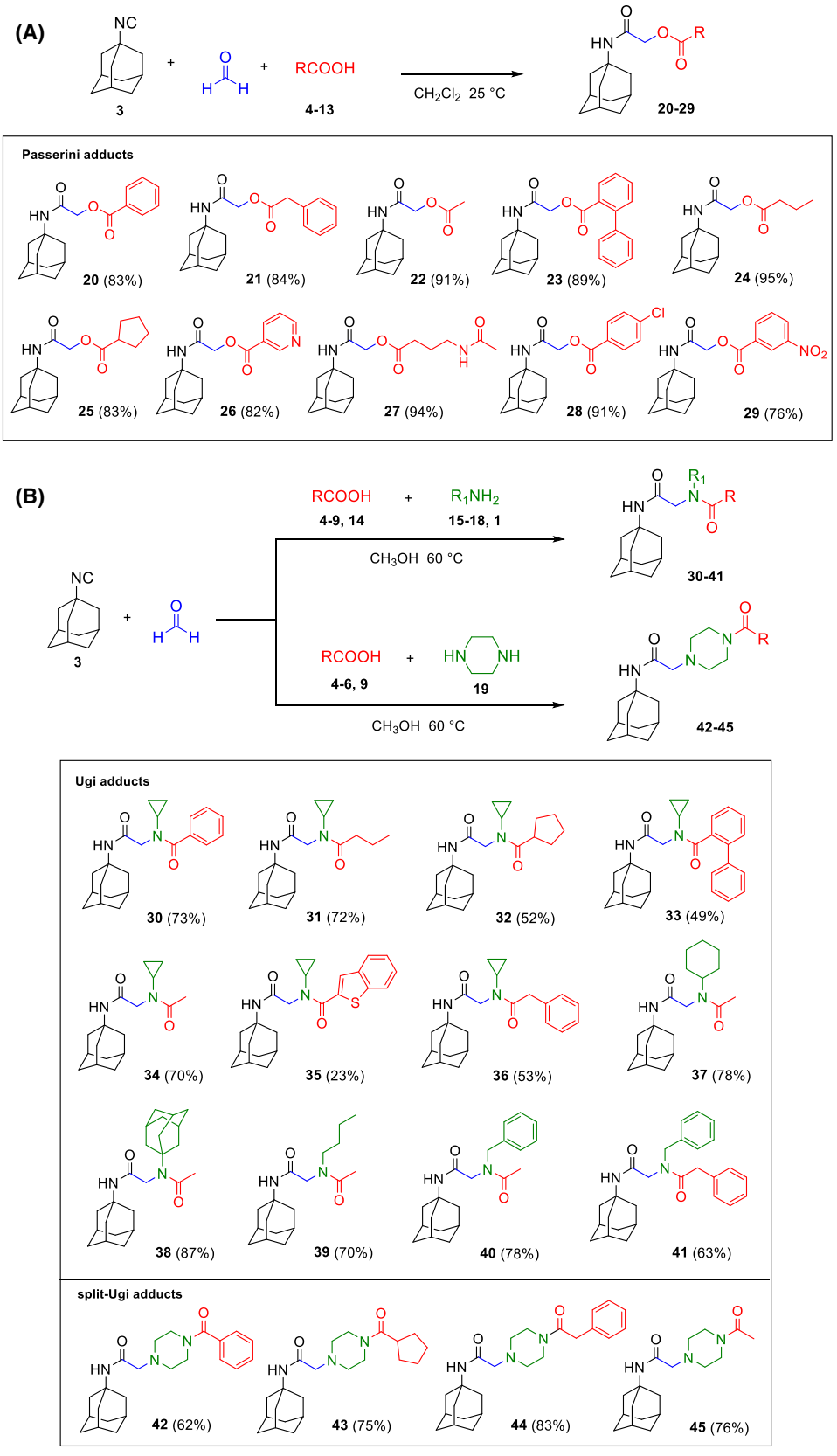

17424658, 0, Downloaded from https://febs.onlinelibrary.wiley.com/doi/10.1111/febs.70065 by Universidad Miguel Hernández De Elche, Wiley Online Library on [16/04/2025]. See the Terms and Conditions (https://onlinelibrary.wiley.com/terms-and-conditions) on Wiley Online Library for rules of use; OA articles are governed by the applicable Creative Commons License

Table 1. Screening for agonist/antagonist activity of synthesized compounds **20–45**. The experiments were conducted three times independently ($N = 3$), with each determination performed in triplicate ($n = 3$). The data are presented as the mean value accompanied by the standard deviation (SD).

	hTRPM8					
Compound	R	Activity	EC_{50} (μM)	IC_{50} (μM)	Hill coefficient	Efficacy (%)
20		Antagonist		1.8 ± 1.1	0.4 ± 1.2	60
21		Antagonist		1.5 ± 1.1	0.5 ± 2.3	44
22	-CH_3	Agonist	1.1 ± 1.5		0.4 ± 1.3	64
23	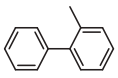	Antagonist		0.2 ± 1.3	0.5 ± 0.9	100
24	-$CH_2CH_2CH_3$	Agonist	19 ± 2.0		0.6 ± 0.2	19
25		Antagonist		45 ± 2.0	0.8 ± 3.0	57
26		Agonist	1.9 ± 1.6		0.4 ± 6.4	72
27	-$CH_2CH_2CH_2$-NH-CO-CH_3	Agonist	0.6 ± 1.2		0.3 ± 1.6	60
28	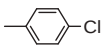	Agonist	1.2 ± 1.2		0.1 ± 0.2	87
29	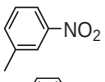	Antagonist		2.3 ± 1.1	0.5 ± 3.0	69
30		Agonist	1.5 ± 1.5		0.7 ± 1.6	92
31	-$CH_2CH_2CH_3$	Agonist	0.3 ± 1.9		0.7 ± 2.5	72
32		Agonist	0.4 ± 1.7		0.2 ± 1.5	56
33	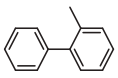	Antagonist		1.1 ± 1.2	2.0 ± 7.8	48
34	-CH_3	Agonist	0.2 ± 1.9		0.3 ± 14	54
35	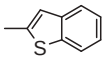	Antagonist		0.6 ± 1.2	2.0 ± 4.3	40
36		Agonist	4.9 ± 1.7		2.3 ± 2.6	47
37	-CH_3	Agonist	0.2 ± 3.0		0.9 ± 9.2	48
38	-CH_3	Agonist	2.0 ± 1.4		0.3 ± 3.6	65
39	-CH_3	Agonist	0.5 ± 1.4		0.4 ± 9.1	64
40	-CH_3	Agonist	1.4 ± 1.4		0.7 ± 2.4	86
41		Agonist	0.9 ± 1.1		2.1 ± 1.0	49
42		Agonist	5.4 ± 1.5		0.4 ± 4.3	73
43		Agonist	9.3 ± 1.5		0.6 ± 1.8	82
44		Agonist	9.6 ± 1.5		0.7 ± 4.0	69
45	-CH_3	Agonist	2.3 ± 1.6		0.7 ± 2.1	54

comparisons: compound **42** can be directly compared to compound **30**; compound **44** to compound **36**; and compound **45** to compounds **22**, **34**, **37**, **39**, and **40**. Akin to α-aminoacyl amide **32**, the α-acylpiperazino amide **43** also behaves as a TRPM8 agonist although with > 10-fold lower potency.

The FEBS Journal (2025) © 2025 The Author(s). *The FEBS Journal* published by John Wiley & Sons Ltd on behalf of Federation of European Biochemical Societies.

17424658, 0, Downloaded from https://febs.onlinelibrary.wiley.com/doi/10.1111/febs.70065 by Universidad Miguel Hernández De Elche, Wiley Online Library on [16/04/2025]. See the Terms and Conditions (https://onlinelibrary.wiley.com/terms-and-conditions) on Wiley Online Library for rules of use; OA articles are governed by the applicable Creative Commons License

α-Acyloxy carboxamide 23 is a potent hTRPM8 competitive WS-12 antagonist

We selected α-acyloxy carboxamide **23** as the most potent antagonist ($IC_{50} = 0.2 \pm 1.3$ μM) for further *in vitro* and *in vivo* characterization. We first used patch-clamp to investigate the potency and blockade mechanism of compound **23** inhibiting WS-12 evoked ionic currents in hTRPM8-HEK293 cells. As shown in Fig. 3A, 1 μM of α-acyloxy carboxamide **23** reduced ≥ 75% WS-12 evoked inward current. This blockade activity was reversible as virtually all WS-12-evoked ionic current could be recovered upon washout (Fig. 3A, bottom panel), thus preventing a use-dependent side effect. A dose–response curve revealed an IC_{50} of 0.08 ± 0.07 μM, and a Hill coefficient of 1 (Fig. 3B), suggesting that compound **23** is a potent hTRPM8 antagonist.

To unveil the underlying mechanism of channel blockade (competitive vs noncompetitive) we evaluated the effect of the α-acyloxy carboxamide **23** on WS-12 activating potency. For this purpose, we obtained the WS-12 dose response in the absence and presence of 80 nM compound **23** (corresponding to its IC_{50} value). As depicted in Fig. 3C, the WS-12 dose response was right-shifted to higher concentrations in the presence of compound **23** increasing up to five-fold the WS-12 EC_{50} value from 3 to 15 μM, without altering the agonist efficacy, suggesting a competitive blockade mechanism. In support of this tenet, a Schild plot to evaluate the effect of increasing concentrations of compound **23** in the blockade efficacy of WS-12 revealed a linear relationship (slope of 1.0) consistent with a competitive inhibitory mechanism (Fig. 3D). Thus, these results suggest that α-acyloxy carboxamide **23** and WS-12 binding to the same or nearby site in the receptor.

To further substantiate the competitive mechanism of channel blockade, we examined the voltage dependency of compound **23** antagonistic activity (Fig. 3E). For this purpose, we run 100 ms voltage ramps from −120 to 120 mV activated by WS-12 in the absence and presence of 80 nM α-acyloxy carboxamide **23**. Figure 3E shows the current density (J)-V relationships for compound **23** and the well-known TRPM8 competitive antagonist **AMTB**. Both compounds inhibited WS-12 in the entire range of depolarizing voltages, indicating channel blockade was not voltage dependent as it would be expected for an uncompetitive antagonist. Thus, these data further support a competitive, voltage-independent blockade mechanism for compound **23**.

Compound 23 marginally blocks TRPV1 and TRPA1 activity

To evaluate receptor selectivity, we investigated the activity of compound **23** on recombinant hTRPV1 and hTRPA1 channels recombinantly expressed in HEK293 cells (Fig. 4). We choose these thermosensory channels because of their structural similarity and expression in peripheral nociceptive terminals. In addition, some ligand cross-interaction within these channels has been reported [44]. At 1 μM, compound **23** blocked ≈ 50% of hTRPV1-channel activity (Fig. 4A, top panel), showing an IC_{50} of 1.1 ± 1.02 μM (Fig. 4A, bottom panel). Similarly, at 5 μM compound **23** blocked ≈ 60% of hTRPA1-evoked current (Fig. 4B, top panel), exhibiting an IC_{50} of 3.04 ± 2.01 μM (Fig. 4B, bottom panel). For comparison, 2-(1,3-Dimethyl-2,6-dioxo-1,2,3,6-tetrahydro-7H-purin-7-yl)-*N*-(4-isopropylphenyl)acetamide (HC030031), a reference TRPA1 antagonist [45], completely abrogated AITC-evoked ionic currents at 5 μM (Fig. 4B, top panel). Collectively, these data indicate that α-acyloxy carboxamide **23** is ≥ 10-fold more potent blocking hTRPM8 than hTRPV1 and hTRPA1 channels, denoting a preferential selectivity for hTRPM8.

Modeling of α-acyloxy carboxamide 23 docking in the menthol WS-12 site of the hTRPM8 channel

To further support the blocking mechanism and selectivity, we performed molecular docking of compound **23** on the hTRPM8 channel (Fig. 5). Notably, compound **23** readily accommodates into the menthol binding pocket located between the S1, S2, S3, and S4 transmembrane domains in the closed conformation (Fig. 5A,B). The biphenyl group of compound **23** interacts with residues R842, H845, and I846 in S4, and W798 in S3 of hTRPM8. Similarly, the adamantane group contacts V849 and L853 in S4, F738 in S1, and L1001 and Y1005 in the TRP helix. Additional interactions are a salt bridge with H845 and two π-cation involving R842 and H845 in S4 (Fig. 5C).

The superimposition of compound **23**, **WS-12**, and **AMTB** bound to the receptor menthol binding pocket (Fig. 5D) shows that compound **23** partially occupies the site of **WS-12**, consistent with the observed competitive mechanism of channel blockade. The estimated binding energies to the hTRPM8 receptor reveal that the largest value corresponds to compound **23** (-10.41 kcal·mol^{-1} vs. -9.93 kcal·mol^{-1} for AMTB and -7.72 kcal·mol^{-1} for WS-12). The higher binding energy of compound **23** as compared to WS-12 may be due to the polar and

17424658, 0, Downloaded from https://febs.onlinelibrary.wiley.com/doi/10.1111/febs.70065 by Universidad Miguel Hernández De Elche, Wiley Online Library on [16/04/2025]. See the Terms and Conditions (https://onlinelibrary.wiley.com/terms-and-conditions) on Wiley Online Library for rules of use; OA articles are governed by the applicable Creative Commons License

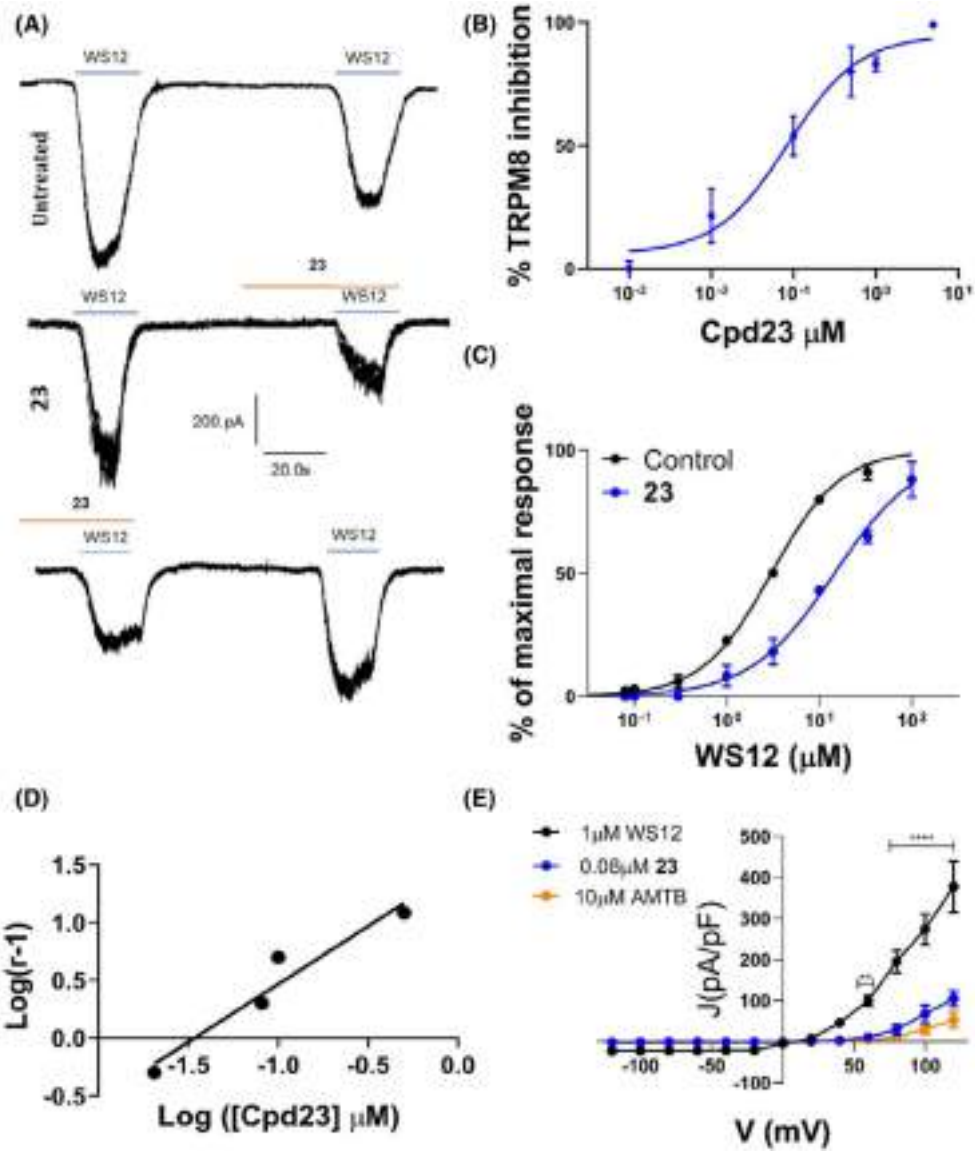

Fig. 3. Compound **23** is a hTRPM8 competitive blocker with nanomolar potency. (A) Representative traces of WS-12-evoked ionic currents recorded at a holding potential of −60 mV in HEK293 cells heterologously expressing hTRPM8. Control cells (upper panel) were exposed to two pulses (1 μM) of WS-12, interspaced by a washing period whereas compound **23**-treated cells (middle panel) were exposed before to 1 min of compound **23** (1 μM) and then to 30s of compound **23** during the second pulse of WS-12. In the lower panel, the recovery of WS-12-evoked currents after compound **23** treatment is shown, indicating a reversible effect of the compound on hTRPM8 activity. (B) Dose–response curve for hTRPM8 current blockade at a holding voltage of −60 mV. The line represents the fit of the experimental data to the Hill equation: $Y = \text{Bottom} + (\text{Top} - \text{Bottom})/\left(1 + 10^{(X - \text{LogIC}_{50})}\right)$ with a standard slope of 1.0 (Hill coefficient) and a restriction Top (= 100). The fitted value for IC_{50} was 0.08 ± 0.07 μM. Each point is the mean ± SEM of $N = 3$, $n = 10$. (C) WS-12 dose–response curve in the absence (black) or presence of 0.08 μM compound **23** (blue). The best fitted values for WS-12 EC_{50} value were 3.0 μM (95% CI 2.5–3.68 μM) ($n = 18$) in the absence of 0.1 μM compound **23** and 15 μM (95% CI 12.8–16.8 μM) in its presence (blue curve, $n = 16$, Top = 100). Hill coefficient in the absence of compound **23** was 1.17 (0.9–1.4) and in its presence was 0.95 (95% CI 0.8–1.0). All data are expressed as mean ± SEM. $N = 3$. (D) Schild plot derived from the interaction between agonist (WS12) and antagonist (compound **23**) at four different concentrations: 0.02, 0.08, 0.1, 0.5 μM. Equation: $Y = 1003 \times X + 1469$; Slope: 1.003; 1/Slope: 0.9973; Std. error: 0.1935. *R* square: 0.9307; *P* value: 0.0353. $N = 3$, $n = 10$. (E) Representative current density (*J*)-*V* curves elicited by a protocol of voltage steps from −120 to 120 mV in steps of 20 mV in the absence (control) or presence of 0.08 μM compound **23** ($n = 10$) or 10 μM AMTB ($n = 8$). In the control condition, an additional pulse of WS-12 was used to consider channel desensitization. Data were analyzed with two-way ANOVA, $N = 3$. Each point is the mean ± SEM. Data were analyzed using a two-way ANOVA followed by a Sidak *post hoc* test when appropriate, ***P* value = 0.0069; *****P* value < 0.0001.

The FEBS Journal (2025) © 2025 The Author(s). *The FEBS Journal* published by John Wiley & Sons Ltd on behalf of Federation of European Biochemical Societies.

17424658, 0, Downloaded from https://febs.onlinelibrary.wiley.com/doi/10.1111/febs.70065 by Universidad Miguel Hernández De Elche, Wiley Online Library on [16/04/2025]. See the Terms and Conditions (https://onlinelibrary.wiley.com/terms-and-conditions) on Wiley Online Library for rules of use; OA articles are governed by the applicable Creative Commons License

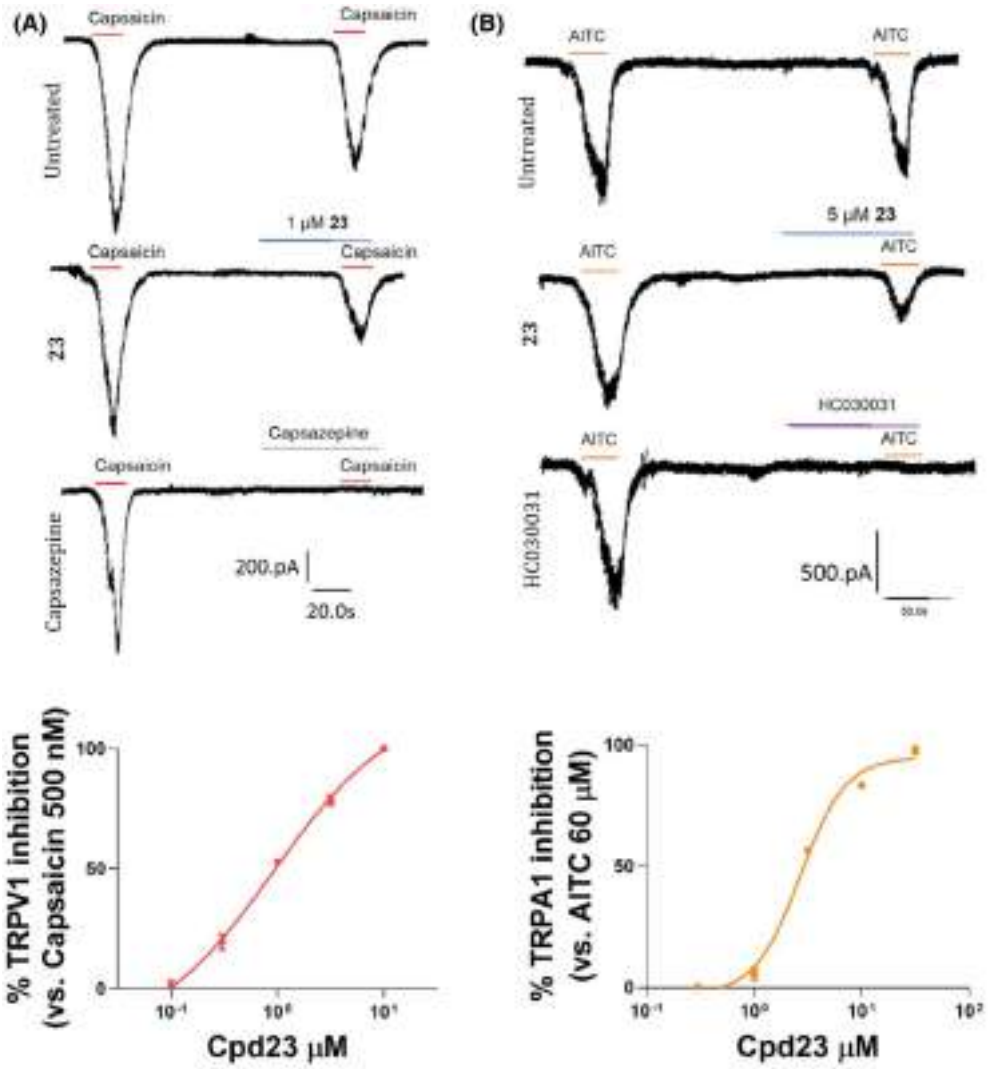

Fig. 4. Compound **23** modestly inhibits currents of hTRPV1 and hTRPA1 expressed in HEK293 cells. (A) Representative capsaicin (0.5 μM)-evoked hTRPV1 inward currents recorded at a holding potential of −60 mV, for control cells (untreated) and cells treated with 1 μM compound **23** or 10 μM of Capsazepine. Red lines represent the duration of the capsaicin pulse (top panel). Dose–response curve for hTRPV1 current blockade at a holding voltage of −60 mV. The line represents the fitted curve of the experimental data to the Hill equation. The fitted value for IC_{50} was 1 μM ± 1.02. Each point is the mean ± SEM of $n = 6$ (bottom panel). (B) Representative AITC (60 μM) evoked hTRPA1 inward current recorded at a holding potential of −60 mV, for control cells (untreated) and cells treated with 5 μM compound **23** or 5 μM of HC030031. Orange lines represent the duration of the AITC pulse (top panel). Dose–response curve for hTRPA1 current blockade at a holding voltage of −60 mV. The line represents fits of the experimental data to the Hill equation. The fitted value for IC_{50} was 3.04 μM ± 2.01. Each point is the mean ± SEM of $n = 8$ (bottom panel).

hydrophobic contacts with residues located mainly in S4 and the TRP helix that involve both the biphenyl and the adamantane groups of compound **23**.

For comparison, we also modeled the interaction of compound **23** with the menthol binding site of mouse TRPM8 (mTRPM8, Fig. 5E). Docking of compound **23** into this binding site appears to involve slightly different interactions than those observed in the human ortholog. At variance with hTRPM8, where compound **23** accommodates into a faintly polar environment with the biphenyl and the adamantane groups closer to S2 and S3 transmembrane domains, in the murine TRPM8 compound **23** interacts with Q785 (S2), D796, W798, N799, D802 in S3, H845 in S4, and E1004 in the TRP helix. The reduced hydrophobic interactions noticed in the mTRPM8 binding site may underlie the lower binding energy estimated ($-9.96\ kcal{\cdot}mol^{-1}$) as compared to the human ortholog. This lower binding

17424658, 0, Downloaded from https://febs.onlinelibrary.wiley.com/doi/10.1111/febs.70065 by Universidad Miguel Hernández De Elche, Wiley Online Library on [16/04/2025]. See the Terms and Conditions (https://onlinelibrary.wiley.com/terms-and-conditions) on Wiley Online Library for rules of use; OA articles are governed by the applicable Creative Commons License

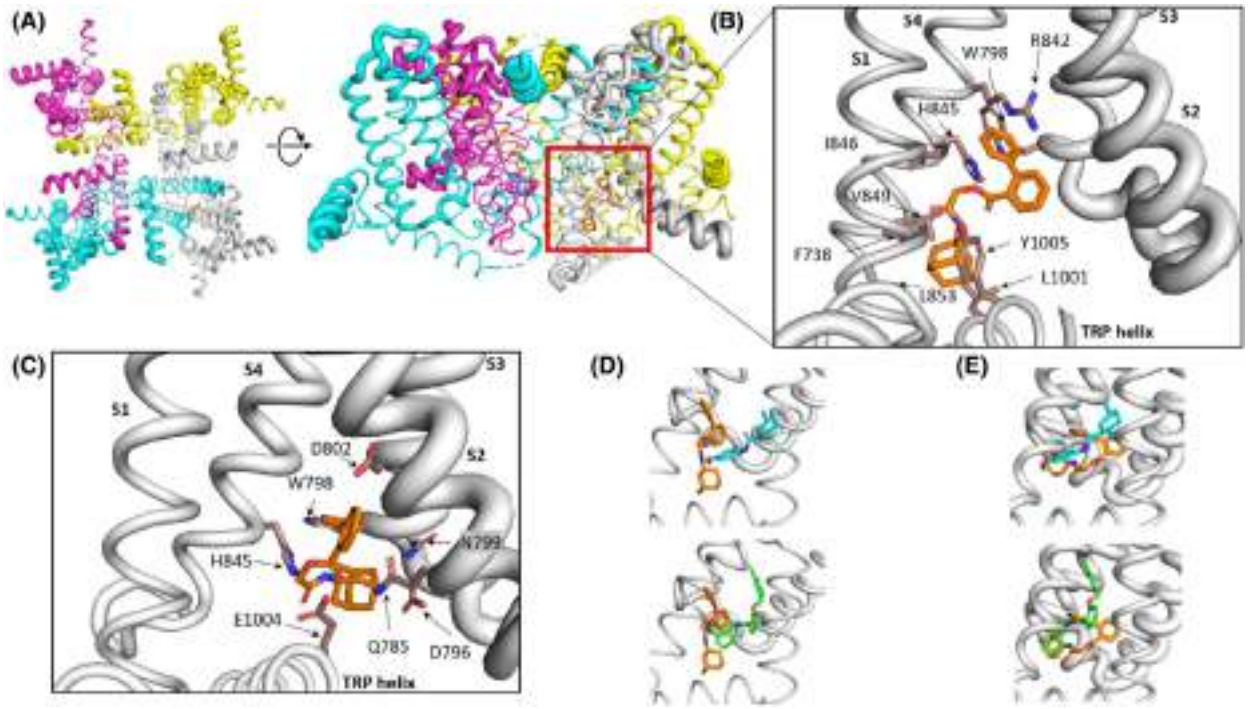

Fig. 5. Molecular docking of compound **23** in TRPM8 channels. (A) Side and top view of human TRPM8 structure (PDB ID: 8BDC) used for docking studies. Subunits are colored differently. The tetrameric nature of the channel and the pore are clearly seen. The red square roughly indicates the simulation box built around the menthol binding site to accommodate compound **23**. (B) Detail of the human TRPM8 menthol binding pocket with bound compound **23** (orange color). Residues mainly involved in ligand interactions were F738 (S1), W798 (S3), R842, H845, I846, V849, L853 (S4), and L1001, Y1005 (TRP helix). Interactions are mainly hydrophobic, although a salt bridge and π-cation interactions are also observed. (C) Detail of compound **23** bound to the mouse TRPM8 binding pocket (equivalent view to panel B). Residues interacting with compound **23** (orange) were Q785 (S2), D796, W798, N799, D802 (S3), H845 (S4), and E1004 (TRP helix). (D) Compound **23** (orange) and WS-12 (cyan) or AMTB (green) superimposed in the human TRPM8 menthol binding site for comparison. (E) Compound **23** (orange) and WS-12 (cyan) or AMTB (green) superimposed in the mouse TRPM8 menthol binding site for comparison. Figures were constructed using open-source PYMOL v3.0 (https://pymol.org/).

energy suggests a lower blocking potency of compound **23** blocking mTRPM8.

Compound 23 blocks neuronal TRPM8 and modulates WS-12-induced neuronal firing

To examine the *in vivo* activity of compound **23**, we first investigated its inhibitory potency on neuronal TRPM8 channels expressed in murine primary nociceptor cultures by patch-clamp. As seen in Fig. 6A, 5 μM of compound **23** blocked 60% of WS-12-evoked ionic currents in primary cultures of dorsal root ganglion neurons. A dose–response curve revealed an IC_{50} of 0.43 ± 0.75 μM (Fig. 6B). This result indicates a lower potency of compound **23** inhibiting the murine TRPM8 as compared with the human ortholog consistent with the predicted lower binding energy to mTRPM8. Alternatively, it could also be due to distinct gating mechanisms of both orthologs or the influence of the neuronal environment.

Complementarily, we examined the effect of compound **23** on WS-12-evoked action potentials in primary cultures of murine DRG sensory neurons. For this task, we recorded neuronal excitability using multielectrode arrays (MEAs). The IC_{50} value corresponding to 0.43 μM was used to examine compound **23** induced inhibition of neuronal excitability. A protocol of two sequential pulses of WS-12 interspersed with a washing pulse was applied to correct for channel desensitization (Fig. 7A, upper recording). Compounds **23** and **AMTB** (0.43 and 10 μM, respectively) were applied 1 min before and during the second WS-12 pulse (Fig. 7A, second, third, and fourth recordings). As depicted in Fig. 7B, compound **23** virtually abolished action potential firings induced by WS-12 application in murine primary afferent neurons (≥ 75%). Thus, compound **23** appears to be a potent inhibitor of WS12-evoked firing frequency, even surpassing the efficacy of AMTB at equimolar concentrations (Fig. 7B).

The FEBS Journal (2025) © 2025 The Author(s). *The FEBS Journal* published by John Wiley & Sons Ltd on behalf of Federation of European Biochemical Societies.

17424658, 0, Downloaded from https://febs.onlinelibrary.wiley.com/doi/10.1111/febs.70065 by Universidad Miguel Hernández De Elche, Wiley Online Library on [16/04/2025]. See the Terms and Conditions (https://onlinelibrary.wiley.com/terms-and-conditions) on Wiley Online Library for rules of use; OA articles are governed by the applicable Creative Commons License

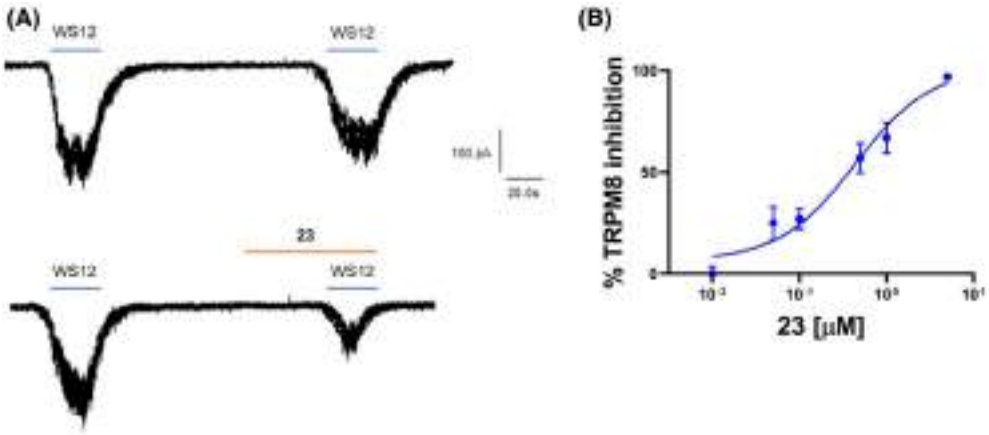

Fig. 6. Compound **23** blocks WS-12-induced TRPM8 activation in murine nociceptors. (A) Representative WS-12-evoked currents in DRG neurons of neonatal rats recorded at a holding potential of −60 mV. For control conditions (untreated) cells were exposed to two pulses (1 μM) of WS-12, interspaced by a washing period, whereas treated cells were exposed before to 1 min of compound **23** (1 μM) and then to 30 s of compound **23** during the second pulse of WS-12. (B) Dose–response curve for mTRPM8 current blockade at a holding voltage of −60 mV. The line represents fits of the experimental data to the Hill equation. The fitted value for IC_{50} was 0.43 μM ± 0.75. Each point is the mean ± SEM of $N = 3$, $n = 8$.

Additionally, we investigated the effect of compound **23** on capsaicin and AITC-induced excitability in murine nociceptors. Employing an IC_{50} value of 1 μM for TRPV1 and 5 μM for TRPA1 of firing inhibition by compound **23** (Fig. 4), we interrogated its ability to modulate neuronal excitability. As for TRPM8, our experimental design involved a protocol of dual agonist pulses interspersed with a washing pulse to minimize agonist-induced channel desensitization. Compound **23** was administered 1 min prior to and during the second agonist pulse. Figure 7C–F show that compound **23** attenuated capsaicin and AITC responses by 30% and 40%, respectively, consistent with a more potent blockade of TRPM8 channels and a mild cross-reactivity with TRPV1 and TRPA1 akin to other modulators of this channel family [46]. Collectively, these results indicate that α-acyloxy carboxamide **23** is a novel TRPM8 antagonist that potently and selectively blocks TRPM8 channel activity and reduces neuronal excitability induced by receptor agonists.

Local application of compound 23 reduces oxaliplatin-induced peripheral cold allodynia

Given the inhibitory activity of compound **23** and the antinociceptive effects of TRPM8 antagonists described in models of oxaliplatin (OXP)-induced neuropathy [47–49], we conducted a behavioral experiment in mice to assess the antinociceptive effects of compound **23** after repeated oxaliplatin administration. Oxaliplatin was intraperitoneally (i.p.) administered every other day for 5 days at 6 $mg \cdot kg^{-1}$, reaching a total accumulative dose of 18 $mg \cdot kg^{-1}$. The acetone test, based on the duration of the licking response after the application of acetone drops to the hind paws (Fig. 8A–C, Before OXP vs. After OXP), revealed a significant enhancement in the nociceptive response to cold after OXP treatment (Fig. 8A–C, $P < 0.01$ Before OXP vs. After OXP). The OXP-induced sensitization to cold stimuli was also evident with the dry ice test, as evidenced by the significant reduction in the latency to cold stimulation through the application of a dry ice pellet against the paw on a glass surface (Fig. 8B, $P < 0.05$ Before OXP vs. After OXP).

We next investigated the antinociceptive effect of systemic compound **23** (5 $mg \cdot kg^{-1}$ i.p.) as compared to its vehicle in both the acetone and the dry ice tests. Measurements were conducted 30 and 90 min after compound **23** or vehicle i.p. administration. As shown in Fig. 8A,B, instillation of compound **23** did not significantly affect the licking response to acetone drops nor the withdrawal latencies to dry ice application as compared to vehicle. This unexpected lack of antinociceptive activity may be because of poor pharmacokinetic due to the metabolic instability of the ester bond that is susceptible to esterase hydrolysis.

To circumvent the potential systemic metabolic instability, we investigated if a local application in the animal paw produced antinociceptive activity. As illustrated in Fig. 8C, local subcutaneous application of compound **23** produced a significant antinociceptive

17424658, 0, Downloaded from https://febs.onlinelibrary.wiley.com/doi/10.1111/febs.70065 by Universidad Miguel Hernández De Elche, Wiley Online Library on [16/04/2025]. See the Terms and Conditions (https://onlinelibrary.wiley.com/terms-and-conditions) on Wiley Online Library for rules of use; OA articles are governed by the applicable Creative Commons License

effect in the acetone test, evident at 30 and 90 min after compound administration ($P < 0.05$ at 30 min, $P < 0.01$ at 90 min, After OXP vs. 30 and 90 min after compound **23**). Collectively, these results suggest that α-acyloxy carboxamide **23** exhibits a significant antinociceptive effect following local application to the peripheral endings, substantiating that systemic treatment is limited by a poor pharmacokinetics of the antagonist.

Compound 23 exhibits mild metabolic stability

Because of the lack of systemic activity of compound **23**, we evaluated the *in vitro* plasmatic and hepatic metabolic stability. To this aim, compound **23** was exposed to mouse plasma and mouse liver microsome (MLM) fractions, and the residual substrate was measured after 1 h. Under these conditions, the residual substrate was about 97% and 90% in plasma and microsomes, respectively, denoting that this molecule suffers from mild hydrolysis of the ester group. However, when the microsomal monooxygenase system was activated by the NADPH regenerating system, the residual substrate dropped about 42% suggesting a susceptibility towards oxidative metabolism.

Metabolic biotransformation of compound **23** was investigated by tandem high-resolution mass spectrometry using the software COMPOUND DISCOVERER 3.2™. Alongside enzymatic hydrolysis giving M1a and M1b metabolites, mono and multi-aliphatic oxidation was the predominant biotransformation occurring on the adamantane ring M2–M9 (Table 2; Fig. 9) and (Tables S1 and S2, Figs S79 and S80 for full spectral data) also demonstrate by the relative abundancy of some of them estimated based on the total ion current (TIC) measurement. Notably, the susceptibility of the adamantane ring to undergo microsomal oxidation is consistent with previous published findings [50,51]. Indeed, some synthetic cannabinoid mono-, di-, and even tri-hydroxylate derivatives of the adamantane group were revealed after hepatic phase I biotransformation.

Discussion

Cumulative evidence supports a role of TRPM8 in transducing both innocuous and harmful cold thermal signals under physiological and pathological conditions [52–54]. Accordingly, TRPM8 is considered a pivotal clinical target, and the development of therapeutically useful modulators is a significant pharmaceutical and medical unmet goal. Akin to TRPV1 antagonists, most of systemic TRPM8 modulators tested have failed clinical development due to safety concerns. However, topical formulations of TRPM8 modulators directed to attenuate receptor pathological overactivity in conditions such as dry eye syndrome [14] or pruritus [23] have reported promising results. In this context, the salient contribution of this study is the design of hTRPM8 ligands with potential therapeutic properties based on multicomponent reactions such as the Ugi and Passerini reactions that capitalize on the drug-like properties of the adamantane group. These reactions enable the rapid assembly of focused chemical libraries using green chemistry criteria [40]. Although medicinal chemists have extensively utilized the Ugi reaction in drug discovery [32], the Passerini reaction has been less popular. This reluctance stems from the apprehension

Fig. 7. Compound **23** reduces WS-12-induced excitability of murine nociceptors. (A) Multielectrode array (MEA) recordings, with representative traces showing WS-12-evoked action potential (AP) firing under different conditions: control, 0.43 μM compound **23**, 0.43 μM AMTB, and 10 μM AMTB. WS-12 (1 μM) was applied in two consecutive pulses, with compounds added 1 min before and during the second pulse. The protocol concluded with a 15 s pulse of 40 mM KCl to ensure neuronal viability. (B) Normalized WS12-induced firing (P2/P1) in the absence (vehicle) and presence of antagonists (0.43 μM compound **23**, 0.43 μM AMTB and 10 μM AMTB) were compared. Data were analyzed with one-way ANOVA followed by Dunnett's test; *P* values for statistical differences are indicated. The number of independent experiments (*N*) was 3, with 94 electrodes per condition. The data points are plotted with error bars representing the standard deviation (SD). (C) Multielectrode array (MEA) recordings, with representative traces showing Cap-evoked action potential (AP) firing under different conditions: control and 1 μM compound **23**. Cap (0.5 μM) was applied in two consecutive pulses, with compounds added 1 min before and during the second pulse. The protocol concluded with a 15 s pulse of 40 mM KCl to ensure neuronal culture viability. (D) Normalized capsaicin-induced firing (P2/P1) in the absence (vehicle) and presence of antagonist (1 μM compound **23**) were compared. The data points are plotted with error bars representing the standard deviation (SD). The number of independent experiments (*N*) was 3, with 63 electrodes per condition. Data were analyzed with Mann–Whitney test; *P* values for statistical differences are indicated. (E) Representative traces showing AITC-evoked action potential (AP) firing under different conditions: control and 5 μM compound **23**. AITC (100 μM) was applied in two consecutive pulses, with compounds added 1 min before and during the second pulse. The protocol concluded with a 15 s pulse of 40 mM KCl to ensure neuronal culture viability. (F) Normalized AITC-induced firing (P2/P1) in the absence (vehicle) and presence of antagonist (5 μM compound **23**) were compared. Data were analyzed with Mann–Whitney test; *P* values for statistical differences are indicated. The data points are plotted with error bars representing the standard deviation (SD). The number of independent experiments (*N*) was 3, with 67 electrodes per condition.

The FEBS Journal (2025) © 2025 The Author(s). *The FEBS Journal* published by John Wiley & Sons Ltd on behalf of Federation of European Biochemical Societies.

17424658, 0, Downloaded from https://febs.onlinelibrary.wiley.com/doi/10.1111/febs.70065 by Universidad Miguel Hernández De Elche, Wiley Online Library on [16/04/2025]. See the Terms and Conditions (https://onlinelibrary.wiley.com/terms-and-conditions) on Wiley Online Library for rules of use; OA articles are governed by the applicable Creative Commons License

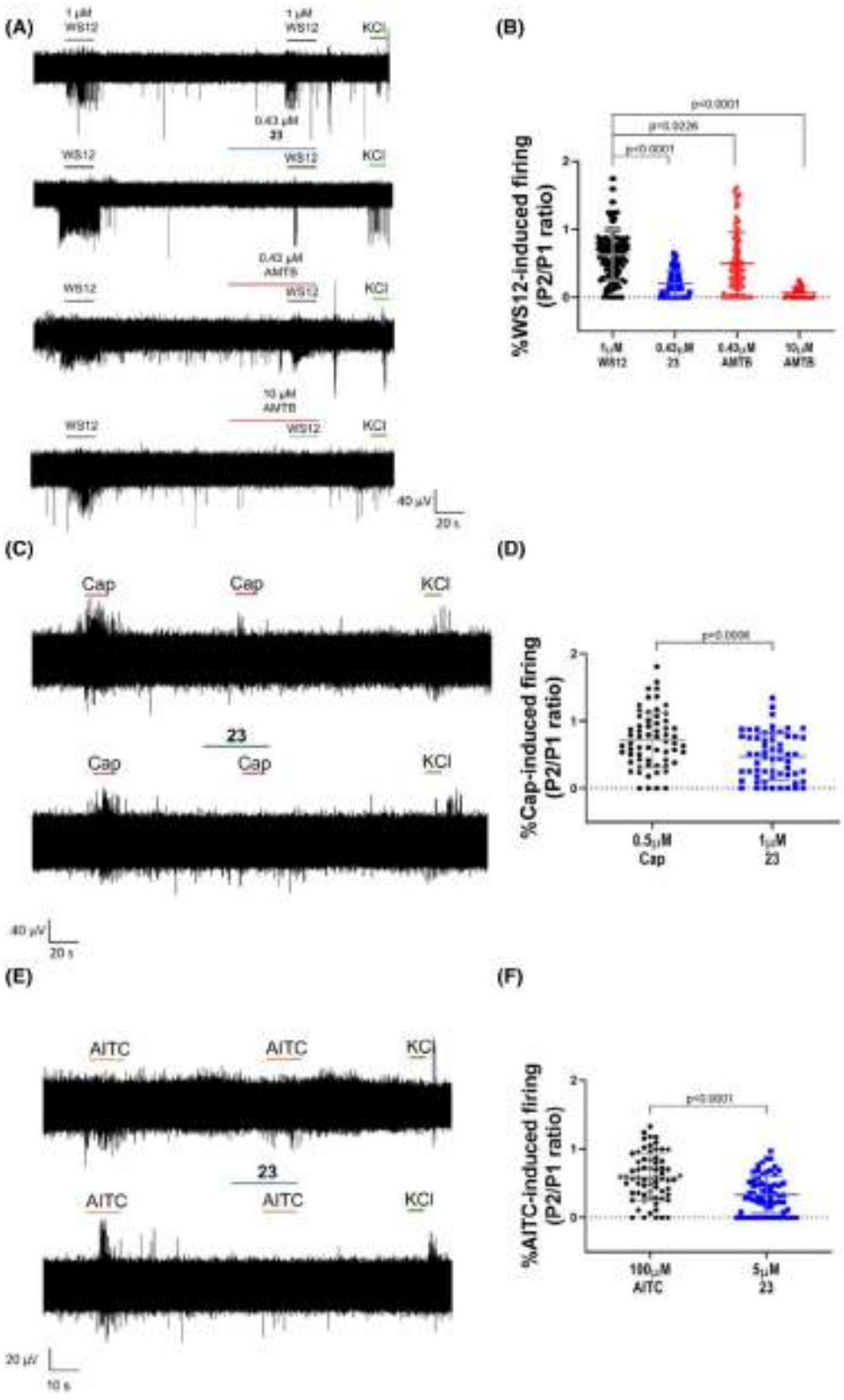

17424658, 0, Downloaded from https://febs.onlinelibrary.wiley.com/doi/10.1111/febs.70065 by Universidad Miguel Hernández De Elche, Wiley Online Library on [16/04/2025]. See the Terms and Conditions (https://onlinelibrary.wiley.com/terms-and-conditions) on Wiley Online Library for rules of use; OA articles are governed by the applicable Creative Commons License

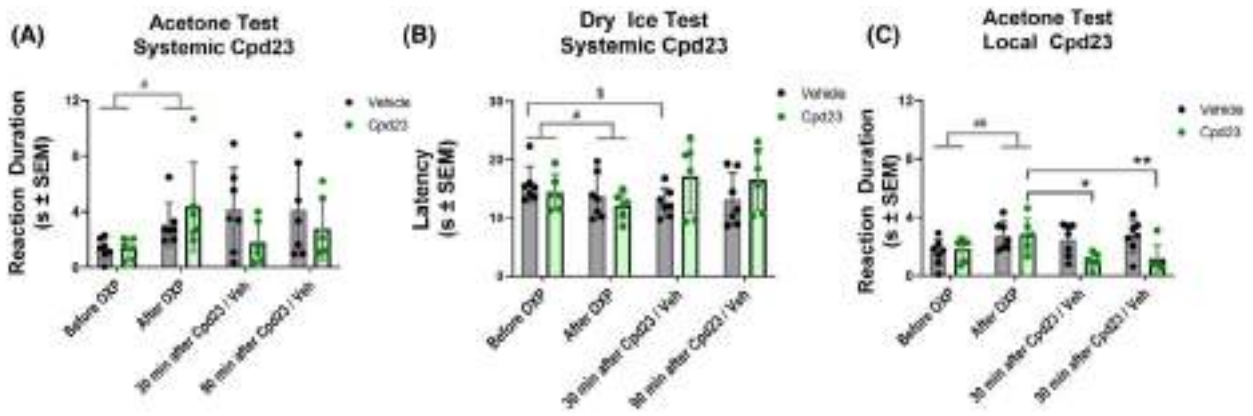

Fig. 8. Local application of **23** alleviates oxaliplatin-induced sensitivity to cold. (A) Repeated administration of oxaliplatin increased the duration of responses to cold induced by acetone application (A, $^{\#}P < 0.05$ Before vs After OXP, two-way ANOVA). However, no significant effect of systemic **23** was found 30 or 90 min after its intraperitoneal (i.p.) administration. (B) Oxaliplatin induced a significant decrease in the withdrawal latency to cold induced by dry ice application (B, $^{\#}P < 0.05$ Before vs After OXP, two-way ANOVA). Vehicle-treated mice retained significant cold sensitization after i.p. treatment (B, $^{\$,\#}P < 0.05$, Before OXP vs 30 min after Vehicle, two-way ANOVA), whereas this difference was not evident in **23**-treated mice. However, **23** did not exhibit cold antinociceptive effects following systemic treatment. (C) Oxaliplatin increased the duration of the responses to acetone-induced cold (C, $^{\#\#}P < 0.01$ Before vs After OXP, two-way ANOVA) and **23** alleviated oxaliplatin-induced cold sensitivity 30 and 90 min after its local subcutaneous administration in the paw (i.pl., $^{*}P < 0.05$ After OXP vs. 30 min after **23**, $^{**}P < 0.01$ After OXP vs. 90 min after **23**). Two-way ANOVA followed by Tukey *post hoc* test when appropriate. Bars represent average values and error bars represent SEM. Dots are the individual values of each mouse ($N = 6$–7).

Table 2. Phase I metabolites of the compound **23** incubated in mouse liver microsomes and detected by LC-HRMS analysis.

	Retention time (min)	Theoretical $[M + H]^+$	Measured $[M + H]^+$	Δ Da p.p.m.	Metabolite relative abundancy %
23	10.71	390.20637	390.20584	1.36	–
M1a	4.87	210.14886	210.14871	0.71	18.7
M1b	6.07	199.07536	199.07563	1.36	n.d.[a]
M2	6.94	406.20129	406.20118	0.27	11.5
M3	4.42	422.19620	422.19601	0.45	14.2
M4	4.82	422.19620	422.19602	0.43	1.5
M5	5.34	422.19620	422.19598	0.52	6.2
M6	5.67	422.19620	422.19577	1.02	12.8
M7	3.36	438.19111	438.19092	0.43	4.5
M8	4.20	438.19111	438.19077	0.78	29.0
M9	7.02	420.18055	420.18018	0.88	1.5

[a]Not determined due to poor ionization in positive ion modality.

of medicinal chemists towards esters, which are considered enzymatically unstable and unsuitable for systemic drug administration. In contrast to this belief, we have demonstrated that depending on the nature of the carboxylic acid utilized, Passerini adducts can be obtained that are resistant to plasma and hepatic esterases [55]. Nonetheless, these ester-containing soft compounds have been shown useful in improving the safety of topically acting vanilloid-based soft antagonists [56].

Among all compounds tested, α-acyloxy carboxamide **23** stems as a potent TRPM8 competitive antagonist, substantiated by Schild plot analysis. Furthermore, compound **23** exhibited high blockade potency (IC_{50} of 80 nM) and efficacy (100% response block). Structurally, α-acyloxy carboxamide **23** displays a bulky moiety that readily fits into the menthol binding site of the receptor stabilizing the channel in the closed state, most likely by restricting the movement of the S4 and TRP domains necessary to drive the allosteric conformation that leads to the opening of the inner channel gate [57]. Computational docking studies show the potential binding interactions of compound **23** to hTRPM8 and mTRPM8 orthologs and provide evidence for the lower blockade potency on the murine channel. These differences appear to be

The FEBS Journal (2025) © 2025 The Author(s). *The FEBS Journal* published by John Wiley & Sons Ltd on behalf of Federation of European Biochemical Societies.

17424658, 0, Downloaded from https://febs.onlinelibrary.wiley.com/doi/10.1111/febs.70065 by Universidad Miguel Hernández De Elche, Wiley Online Library on [16/04/2025]. See the Terms and Conditions (https://onlinelibrary.wiley.com/terms-and-conditions) on Wiley Online Library for rules of use; OA articles are governed by the applicable Creative Commons License

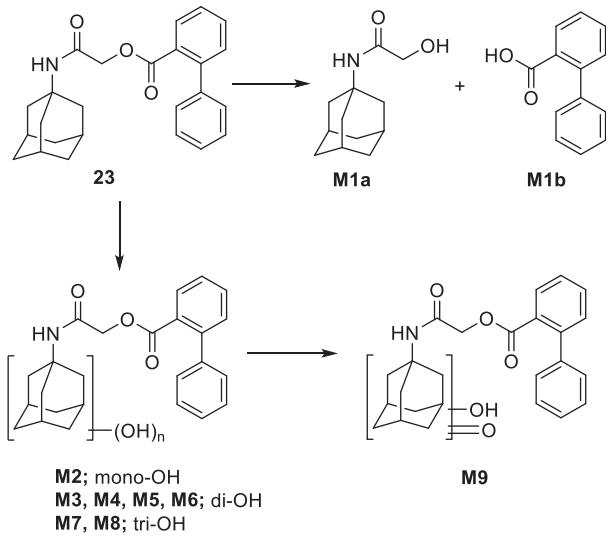

Fig. 9. Proposed *in vitro* phase I metabolic scheme for the compound **23**.

mediated by a slightly different orientation of the compound within the receptor binding site that impacts the binding energy and consequently the blockade potency. Interestingly, the capacity of compound **23** to effectively bind to the channel closed state is compatible with a competitive blockade mechanism, as this site is readily accessible for agonists to bind and trigger the allosteric conformation to the open state. It is also tempting to hypothesize that occupancy of a binding site of the four available in the native tetrameric channel may suffice to prevent channel opening by the agonist, as suggested by the estimated hill coefficient from the dose–response curves. In this regard, it has been reported that efficient opening of TRPM8 channels requires occupancy of the four binding sites [58] thus interference with a single binding site by antagonists may suffice to lock the channel in the closed state. Nonetheless, additional experiments are needed to unveil the structural determinants of compound **23** binding, including site-specific mutagenesis, along with biophysical analysis of its blockade activity.

Fast unblocking kinetics of α-acyloxy carboxamide **23** unblock, that is, fast k_{off}, ensures reversible activity, which is important to reduce a use-dependent channel block. This property is associated with high-affinity antagonists exhibiting a slow unblockage kinetics, which limits their therapeutic utility because of undesirable side effects, as exemplified by the high affinity of TRPV1 blockers [59] or the NMDA blocker MK-801 [60]. In this regard, compounds endowed of fast on/off kinetics appear to be safer for therapeutic applications. As TRPM8 is a physiologically relevant channel transducing environmental temperature detection for proper body temperature homeostasis and prevention of tissue damage, preservation of this physiological activity is crucial to prevent alterations in body temperature unwanted effects described with previous antagonists including hot sensation, gut motility deficits, and cold burns [61,62]. Absence of use-dependent block minimizes the manifestation of unwanted side effects, increasing the safety profile of drug candidates.

A complementary property of α-acyloxy carboxamide **23** is represented by its channel selectivity, as evidenced by its preferential action on TRPM8 channels, and lower interaction with structurally related thermosensory channels such as TRPV1 and TRPA1, which are also highly expressed in nociceptive neurons and contribute to the etiology of peripheral neuropathies. Interestingly, cross-reactivity of agonists and antagonists of these thermosensory channels has been reported [46]. For instance, an interaction of capsaicin with TRPM8 and menthol with TRPV1 and TRPA1 channels has been described [46]. This cross-recognition is due to conserved similarities between the receptor membrane domain structuring the ligand binding sites, which have evolved to preferentially recognize one ligand but conserve the essential features to be mildly recognized by others.

Drug-off target effects may raise safety concerns in contrast to highly selective drugs. However, it should be noted that although drug selectivity has been considered a pivotal goal for therapeutic leads and long pursued by medicinal chemistry programs, it is being realized that some cross-reactivity of drugs with structurally similar receptors may enhance their therapeutic value as peripheral neuropathies involve the participation of various thermosensory receptors.

Absence of use-dependency also in off-target interactions minimizes the appearance of side effects that could compromise the therapeutic index. Furthermore, a multitarget cross-activity may be beneficial in cancer patients treated with chemotherapy that develop a distal peripheral neuropathy, where a contribution of TRPM8, TRPV1, and TRPA1 channels has been reported [63]. The possibility of differentially targeting all three channels with a single compound could be a promising therapeutic strategy to target this disease. In support of this tenet, local application of α-acyloxy carboxamide **23** exhibited significant antinociceptive activity attenuating OIPN-induced cold allodynia.

A systemic administration of compound **23**, however, failed to reduce the cold allodynia that accompanies OIPN. This lack of therapeutic effect is most likely due to a low *in vivo* metabolic stability of compound **23** that resulted in poor pharmacokinetics. In this regard, although the bulky aromatic groups

17424658, 0, Downloaded from https://febs.onlinelibrary.wiley.com/doi/10.1111/febs.70065 by Universidad Miguel Hernández De Elche, Wiley Online Library on [16/04/2025]. See the Terms and Conditions (https://onlinelibrary.wiley.com/terms-and-conditions) on Wiley Online Library for rules of use; OA articles are governed by the applicable Creative Commons License

present in the molecule slowed the hydrolysis when exposed to plasma and microsomal fractions, it did not fully prevent the breakdown of the ester under oxidative metabolism when the microsomal monooxygenase system was activated. Though this metabolic instability may be seen as a therapeutic limitation, metabolically sensitive soft drugs are ideal candidates for local applications whereby the therapeutic activity needs to be peripherally restricted to avoid potential interference with a pharmacological treatment, such as in cancer patients suffering OIPN. In addition, this lack of systemic distribution helps to reduce any potential off-target effect on physiologically acting thermosensory channels in other tissues, which would raise safety concerns. Thus, drugs that act epidermally and are enzymatically hydrolyzed at the dermis appear relevant for therapeutic interventions of peripheral neuropathies. In this regard, the anti-allodynic local activity of compound **23** paves the way to develop this compound for the topical treatment of this disabling sensory condition suffered by cancer patients.

In conclusion, our findings indicate that α-acyloxy carboxamide **23** is a potential therapeutic TRPM8 antagonist that attenuates pathological cold allodynia arising from a common peripheral neuropathy in cancer patients. The *in vitro* pharmacological properties of compound **23**, that is, its potency and efficacy, reversible inhibition, receptor selectivity, lack of use-dependent block, and relative peripheral stability, make it a potential drug candidate for local therapeutic intervention of peripheral neuropathies mediated by dysfunctional TRPM8 channels.

Materials and methods

Chemistry

General experimental methods

Commercially available reagents and solvents were purchased from Sigma-Aldrich (Merck Life Science, Milan, Italy) or Alfa Aesar (Thermo Fisher Scientific, Monza, Italy) and were used without further purification. Melting points were determined in open glass capillary with a Stuart scientific SMP3 apparatus and are uncorrected. Infrared spectra were acquired with a FT-IR Thermo-Nicolet Avatar. ^{1}H-NMR and ^{13}C-NMR spectra were recorded on a JEOL ECP 300 MHz spectrometer (JEOL, Basiglio, Italy). Chemical shifts (δ) are reported in parts per million (p.p.m.) referenced to the residual solvent peak. The multiplicity of each signal is designated using the following abbreviations: s (singlet), d (doublet), t (triplet), q (quadruplet), quint (quintuplet), m (multiplet), br s (broad singlet), dd (doublet of doublets). Coupling constants (J) are reported in Hertz (Hz). High-resolution ESI-MS spectra were acquired on a Thermo Scientific Q-Exactive™ Plus Hybrid Quadrupole-Orbitrap™ mass spectrometer. The spectra were recorded by infusion into the ESI source using methanol as the solvent. Flash column chromatography was performed on silica gel (Merck Kieselgel 60, 230–400 mesh ASTM, Milan, Italy). Thin layer chromatography (TLC) was carried out on plates with a layer thickness of 0.25 mm (Merck Silica gel 60 F_{254}); when necessary, they were developed with $KMnO_4$ reagent or Dragendorff reagent. 1-Isocyanoadamantane **3** was synthesized as described previously [43]. Compounds **1**, **4–14**, and **15–19** were commercially available. The purity of final compounds was ≥ 95% and was determined by high-performance liquid chromatography coupled with an ultraviolet–visible detector using the instrumentation and methods reported in Figs S81–S92.

General procedure A for the synthesis of α-acyloxy carboxamides 20–29

To a solution of the corresponding carboxylic acid (0.62 mmol, 1 equiv) in dichloromethane (2 mL), 37% aqueous formaldehyde solution (2.48 mmol, 4 equiv) and 1-isocyanoadamantane (**3**) (0.62 mmol, 1 equiv) were added. The reaction mixture was stirred at 25 °C for 18 h. After completion of the reaction, water was added, and the product was extracted with dichloromethane (x2). The combined organic layers were washed with aqueous saturated Na_2CO_3 solution (x1), brine (x1) and dried over sodium sulfate. After evaporation of the solvent under reduced pressure, the crude material was purified by flash column chromatography.

2-((3*S*,5*S*,7*S*)-adamantan-1-ylamino)-2-oxoethyl benzoate (20)

The title compound was prepared from 1-isocyanoadamantane (**3**), 37% aqueous formaldehyde solution, and benzoic acid (**4**) according to general procedure A. After extraction, the crude was purified by flash column chromatography using PE/EtOAc 9 : 1 as eluent to give a white solid; yield 83%; mp 155–157 °C; IR (KBr) $\tilde{\nu}$ 3275, 3090, 2916, 2853, 1727, 1657, 1271, 1129, 709 cm^{-1}; ^{1}H-NMR (300 MHz, $CDCl_3$) δ 8.05 (d, J = 8.3 Hz, 2H), 7.62 (t, J = 7.3 Hz, 1H), 7.49 (d, J = 7.5 Hz, 2H), 5.79 (br s, 1H), 4.70 (s, 2H), 2.09 (br s, 3H), 2.04 (br s, 6H), 1.68 (br s, 6H) p.p.m.; ^{13}C-NMR (75 MHz, $CDCl_3$) δ 165.9, 165.2, 133.7, 129.8, 129.2, 128.8, 63.7, 52.2, 41.7, 36.3, 29.5 p.p.m.; HRMS (ESI$^+$): m/z = 314.17464 $[M+H]^+$; calcd. for $C_{19}H_{23}O_3N + H^+$: 314.17507.

2-((3*S*,5*S*,7*S*)-adamantan-1-ylamino)-2-oxoethyl 2-phenylacetate (21)

The title compound was prepared from 1-isocyanoadamantane (**3**), 37% aqueous formaldehyde

The FEBS Journal (2025) © 2025 The Author(s). *The FEBS Journal* published by John Wiley & Sons Ltd on behalf of Federation of European Biochemical Societies.

17424658, 0, Downloaded from https://febs.onlinelibrary.wiley.com/doi/10.1111/febs.70065 by Universidad Miguel Hernández De Elche, Wiley Online Library on [16/04/2025]. See the Terms and Conditions (https://onlinelibrary.wiley.com/terms-and-conditions) on Wiley Online Library for rules of use; OA articles are governed by the applicable Creative Commons License

solution and phenylacetic acid (**5**) according to general procedure A. After extraction, the crude was purified by flash column chromatography using PE/EtOAc 8 : 2 as eluent to give a white solid; yield 84%; mp 78–80 °C; IR (KBr) $\tilde{\nu}$ 3292, 3065, 2911, 2851, 1750, 1671, 1544, 1234, 1134 cm^{-1}; ^{1}H-NMR (300 MHz, $CDCl_3$) δ 7.33–7.25 (m, 5H), 5.47 (br s, 1H), 4.39 (s, 2H), 3.66 (s, 2H), 1.99 (br s, 3H), 1.81 (br s, 6H), 1.60 (br s, 6H) p.p.m.; ^{13}C-NMR (75 MHz, $CDCl_3$) δ 169.6, 165.6, 133.4, 129.1, 128.8, 127.4, 63.1, 51.8, 41.3, 41.2, 36.1, 29.3 p.p.m.; HRMS (ESI^+): $m/z = 328.19034$ $[M + H]^+$; calcd. for $C_{20}H_{25}O_3N + H^+$: 328.19072.

2-((3*S*,5*S*,7*S*)-adamantan-1-ylamino)-2-oxoethyl acetate (22)

The title compound was prepared from 1-isocyanoadamantane (**3**), 37% aqueous formaldehyde solution and acetic acid (**6**) according to general procedure A. After extraction, the product is obtained as a white solid; yield 91%; mp 102–104 °C; IR (KBr) $\tilde{\nu}$ 3292, 3077, 2909, 2849, 1745, 1662, 1558, 1225, 1095, 999, 605 cm^{-1}; ^{1}H-NMR (300 MHz, $CDCl_3$) δ 5.83 (br s, 1H), 4.31 (s, 2H), 2.03 (br s, 3H), 1.96 (br s, 3H), 1.90 (br s, 6H), 1.56 (br s, 6H) p.p.m.; ^{13}C-NMR (75 MHz, $CDCl_3$) δ 169.3, 165.6, 63.0, 51.9, 41.3, 36.1, 29.2, 20.6 p.p.m.; HRMS (ESI^+): $m/z = 252.15916$ $[M + H]^+$; calcd. for $C_{14}H_{21}O_3N + H^+$: 252.15942.

2-((3*S*,5*S*,7*S*)-adamantan-1-ylamino)-2-oxoethyl [1,1′-biphenyl]-2-carboxylate (23)

The title compound was prepared from 1-isocyanoadamantane (**3**), 37% aqueous formaldehyde solution and [1,1′-biphenyl]-2-carboxylic acid (**7**) according to general procedure A. After extraction, the product is obtained as a colorless oil which taken up with methanol precipitated as a white solid, yield 89%; mp 53–55 °C; IR (KBr) $\tilde{\nu}$ 3059, 2908, 2850, 1734, 1685, 1533, 1273, 1132, 747 cm^{-1}; ^{1}H-NMR (300 MHz, $CDCl_3$) δ 7.83 (d, $J = 7.7$ Hz, 1H), 7.52 (t, $J = 7.5$ Hz, 1H), 7.42–7.27 (m, 7H), 5.27 (br s, 1H), 4.32 (s, 2H), 2.00 (br s, 3H), 1.81 (br s, 6H), 1.60 (br s, 6H) p.p.m.; ^{13}C-NMR (75 MHz, $CDCl_3$) δ 167.3, 165.0, 141.9, 140.9, 131.7, 130.6, 130.1, 129.8, 128.4, 128.0, 127.5, 127.3, 63.6, 51.6, 41.0, 36.1, 29.2 p.p.m.; HRMS (ESI^+): $m/z = 390.20607$ $[M + H]^+$; calcd. for $C_{25}H_{27}O_3N + H^+$: 390.20637.

2-((3*S*,5*S*,7*S*)-adamantan-1-ylamino)-2-oxoethyl butyrate (24)

The title compound was prepared from 1-isocyanoadamantane (**3**), 37% aqueous formaldehyde solution and butanoic acid (**8**) according to general procedure A. After extraction, the product is obtained as a colorless oil; yield 95%; IR (KBr) $\tilde{\nu}$ 3297, 3073, 2908, 2849, 1749, 1664, 1551, 1421, 1170, 1109 cm^{-1}; ^{1}H-NMR (300 MHz, $CDCl_3$) δ 5.78 (br s, 1H), 4.32 (s, 2H), 2.27 (t, $J = 7.3$ Hz, 2H), 1.96 (br s, 3H), 1.90 (br s, 6H), 1.57 (br s, 8H), 0.86 (t, $J = 7.5$ Hz, 3H) p.p.m.; ^{13}C-NMR (75 MHz, $CDCl_3$) δ 171.9, 165.8, 62.8, 51.8, 41.3, 36.1, 35.7, 29.2, 18.2, 13.5 p.p.m.; HRMS (ESI^+): $m/z = 280.19042$ $[M + H]^+$; calcd. for $C_{16}H_{25}O_3N + H^+$: 280.19072.

2-((3*S*,5*S*,7*S*)-adamantan-1-ylamino)-2-oxoethyl cyclopentane carboxylate (25)

The title compound was prepared from 1-isocyanoadamantane (**3**), 37% aqueous formaldehyde solution and cyclopentanecarboxylic acid (**9**) according to general procedure A. After extraction, the crude was purified by flash column chromatography using PE/EtOAc 9 : 1 as eluent to give a white solid; yield 83%; mp 104–106 °C; IR (KBr) $\tilde{\nu}$ 3280, 2910, 2851, 1743, 1673, 1558, 1153, 1096, 997, 814 cm^{-1}; ^{1}H-NMR (300 MHz, $CDCl_3$) δ 5.76 (br s, 1H), 4.34 (s, 2H), 2.73 (quint, $J = 7.6$ Hz, 1H), 1.98 (br s, 3H), 1.91 (br s, 6H), 1.88–1.49 (m, 14H) p.p.m.; ^{13}C-NMR (75 MHz, $CDCl_3$) δ 175.0, 165.9, 62.8, 51.8, 43.4, 41.4, 36.1, 29.9, 29.3, 25.7 p.p.m.; HRMS (ESI^+): $m/z = 306.20594$ $[M + H]^+$; calcd. for $C_{18}H_{27}O_3N + H^+$: 306.20637.

2-((3*S*,5*S*,7*S*)-adamantan-1-ylamino)-2-oxoethyl nicotinate (26)

The title compound was prepared from 1-isocyanoadamantane (**3**), 37% aqueous formaldehyde solution and nicotinic acid (**10**) according to general procedure A. After extraction, the crude was purified by flash column chromatography, using PE/EtOAc 5 : 5 as eluent to give a white solid; yield 82%; mp 155–157 °C; IR (KBr) $\tilde{\nu}$ 3273, 3094, 2913, 2852, 1732, 1658, 1568, 1271, 1134, 741 cm^{-1}; ^{1}H-NMR (300 MHz, $CDCl_3$) δ 9.13 (s, 1H), 8.70 (d, $J = 3.4$ Hz, 1H), 8.22 (d, $J = 8.0$ Hz, 1H), 7.33 (dd, $J = 8.0/4.9$ Hz, 1H), 5.95 (br s, 1H), 4.63 (s, 2H) 1.97 (br s, 3H), 1.92 (d, $J = 2.1$ Hz, 6H), 1.56 (br s, 6H) p.p.m.; ^{13}C-NMR (75 MHz, $CDCl_3$) δ 165.2, 164.0, 153.8, 150.7, 137.1, 125.2, 123.4, 63.6, 52.1, 41.4, 36.1, 29.2 p.p.m.; HRMS (ESI^+): $m/z = 315.16979$ $[M + H]^+$; calcd. for $C_{18}H_{22}O_3N_2 + H^+$: 315.17032.

2-((3*S*,5*S*,7*S*)-adamantan-1-ylamino)-2-oxoethyl 4-acetamidobutanoate (27)

The title compound was prepared from 1-isocyanoadamantane (**3**), 37% aqueous formaldehyde solution and 4-acetamidobutanoic acid (**11**) according to general procedure A. After extraction, the product is obtained as a white solid; yield 94%; mp 102–104 °C; IR (KBr) $\tilde{\nu}$

17424658, 0, Downloaded from https://febs.onlinelibrary.wiley.com/doi/10.1111/febs.70065 by Universidad Miguel Hernández De Elche, Wiley Online Library on [16/04/2025]. See the Terms and Conditions (https://onlinelibrary.wiley.com/terms-and-conditions) on Wiley Online Library for rules of use; OA articles are governed by the applicable Creative Commons License

3560, 3415, 3074, 2908, 2850, 1742, 1697, 1547, 1361, 1175 cm^{-1}; ^{1}H-NMR (300 MHz, $CDCl_3$) δ 7.03 (br s, 1H), 6.25 (br s, 1H), 4.32 (s, 2H), 3.14 (q, $J = 6.1$ Hz, 2H), 2.31 (t, $J = 6.9$ Hz, 2H), 1.93 (br s, 3H), 1.88 (br s, 6H), 1.83 (s, 3H), 1.73 (quint, $J = 6.7$ Hz, 2H), 1.53 (br s, 6H) p.p.m.; ^{13}C-NMR (75 MHz, $CDCl_3$) δ 171.9, 170.7, 166.0, 62.7, 52.0, 41.2, 38.4, 36.0, 31.3, 29.2, 24.6, 22.7 p.p.m.; HRMS (ESI^+): $m/z = 337.21169$ $[M + H]^+$; calcd. for $C_{18}H_{28}O_4N_2 + H^+$: 337.21218.

2-((3*S*,5*S*,7*S*)-adamantan-1-ylamino)-2-oxoethyl 4-chlorobenzoate (28)

The title compound was prepared from 1-isocyanoadamantane (**3**), 37% aqueous formaldehyde solution and 4-chlorobenzoic acid (**12**) according to general procedure A. After extraction, the crude was purified by flash column chromatography, using PE/EtOAc 7 : 3 as eluent to give a white solid; yield 91%; mp 165–167 °C; IR (KBr) $\tilde{\nu}$ 3307, 3074, 2906, 2849, 1720, 1658, 1552, 1117, 855, 764, 686 cm^{-1}; ^{1}H-NMR (300 MHz, $CDCl_3$) δ 7.94 (d, $J = 8.3$ Hz, 2H), 7.40 (d, $J = 8.6$ Hz, 2H), 5.81 (br s, 1H), 4.64 (s, 2H), 2.03 (br s, 3H), 1.98 (br s, 6H), 1.63 (br s, 6H) p.p.m.; ^{13}C-NMR (75 MHz, $CDCl_3$) δ 165.6, 164.4, 140.1, 131.1, 129.0, 127.6, 63.7, 52.2, 41.6, 36.2, 29.4 p.p.m.; HRMS (ESI^+): $m/z = 348.13573$ $[M + H]^+$; calcd. for $C_{19}H_{22}O_3ClN + H^+$: 348.13610.

2-((3*S*,5*S*,7*S*)-adamantan-1-ylamino)-2-oxoethyl 3-nitrobenzoate (29)

The title compound was prepared from 1-isocyanoadamantane (**3**), 37% aqueous formaldehyde solution and 3-nitrobenzoic acid (**13**) according to general procedure A. After extraction, the crude was purified by flash column chromatography, using PE/EtOAc 9 : 1 and PE/EtOAc 7 : 3 as eluents to give a white solid; yield 76%; mp 122–124 °C; IR (KBr) $\tilde{\nu}$ 3282, 3083, 2905, 2848, 1729, 1533, 1352, 1263, 1143, 715 cm^{-1}; ^{1}H-NMR (300 MHz, $CDCl_3$) δ 8.78 (s, 1H), 8.39–8.32 (m, 2H), 7.64 (t, $J = 8.0$ Hz, 1H), 5.89 (br s, 1H), 4.70 (s, 2H), 2.01 (br s, 3H), 1.98 (br s, 6H), 1.61 (br s, 6H) p.p.m.; ^{13}C-NMR (75 MHz, $CDCl_3$) δ 165.1, 163.4, 148.2, 135.4, 131.0, 129.9, 127.8, 124.6, 64.0, 52.3, 41.5, 36.2, 29.3 p.p.m.; HRMS (ESI^+): $m/z = 359.15987$ $[M + H]^+$; calcd. for $C_{19}H_{22}O_5N_2 + H^+$: 359.16015.

General procedure B for the synthesis of α-aminoacyl amides 30–41

To a solution of 1-isocyanoadamantane (**3**) (0.070 g, 0.40 mmol, 1 equiv) in methanol (3 mL), paraformaldehyde (0.026 g, 0.60 mmol, 1.5 equiv), the corresponding amine (0.40 mmol, 1 equiv) and the corresponding carboxylic acid (0.40 mmol, 1 equiv) were added. The reaction mixture was stirred at 60 °C for 4 h. After completion of the reaction, water was added and the product was extracted with dichloromethane (x2). The combined organic layers were washed with water (x1), NaOH 2 M (x1), brine (x1) and dried over sodium sulfate. After evaporation of the solvent under reduced pressure, the crude material was purified by flash column chromatography.

N-(2-(((3*S*,5*S*,7*S*)-adamantan-1-yl)amino)-2-oxoethyl)-*N*-cyclopropylbenzamide (30)

The title compound was prepared from 1-isocyanoadamantane (**3**), paraformaldehyde; cyclopropylamine (**15**) and benzoic acid (**4**) according to general procedure B. After extraction, the crude was purified by flash column chromatography, using PE/EtOAc 8 : 2 as eluent to give a white solid; yield 73%; mp 71–72 °C; IR (KBr) $\tilde{\nu}$ 3445, 3316, 3066, 2906, 2849, 1645, 1626, 1548, 1426, 728, 702 cm^{-1}; ^{1}H-NMR (300 MHz, $CDCl_3$) δ 7.55–7.34 (m, 5H), 6.05 (br s, 1H), 4.06 (s, 2H), 2.96–2.88 (m, 1H), 2.05 (br s, 3H), 1.98 (br s, 6H), 1.65 (br s, 6H), 0.60–0.50 (m, 4H) p.p.m.; ^{13}C-NMR (75 MHz, $CDCl_3$) δ 173.4, 168.5, 136.7, 130.0, 128.2, 127.4, 53.5, 52.0, 41.6, 36.4, 33.6, 29.5, 9.8 p.p.m.; HRMS (ESI^+): $m/z = 353.22214$ $[M + H]^+$; calcd. for $C_{22}H_{28}O_2N_2 + H^+$: 353.22235.

N-(2-(((3*S*,5*S*,7*S*)-adamantan-1-yl)amino)-2-oxoethyl)-*N*-cyclopropylbutyramide (31)

The title compound was prepared from 1-isocyanoadamantane (**3**), paraformaldehyde; cyclopropylamine (**15**) and butanoic acid (**8**) according to general procedure B. After extraction, the crude was purified by flash column chromatography, using PE/EtOAc 7 : 3 and PE/EtOAc 5 : 5 as eluents to give an off-white solid; yield 72%; mp 126–127 °C; IR (KBr) $\tilde{\nu}$ 3312, 3073, 2906, 2849, 1679, 16 345, 1554, 1428, 1362, 1290, 1275, 744 cm^{-1}; ^{1}H-NMR (300 MHz, $CDCl_3$) δ 5.87 (br s, 1H), 3.85 (s, 2H), 2.81–2.73 (m, 1H), 2.52 (t, $J = 7.3$ Hz, 2H), 2.01 (br s, 3H), 1.91 (br s, 6H), 1.73–1.61 (m, 8H), 0.94 (t, $J = 7.3$ Hz, 3H), 0.91–0.81 (m, 4H) p.p.m.; ^{13}C-NMR (75 MHz, $CDCl_3$) δ 176.8, 169.0, 53.2, 51.8, 41.6, 36.4, 35.9, 31.7, 29.5, 18.5, 14.1, 9.3 p.p.m.; HRMS (ESI^+): $m/z = 319.23778$ $[M + H]^+$; calcd. for $C_{19}H_{30}O_2N_2 + H^+$: 319.23800.

N-(2-(((3*S*,5*S*,7*S*)-adamantan-1-yl)amino)-2-oxoethyl)-*N*-cyclopropylcyclopentanecarboxamide (32)

The title compound was prepared from 1-isocyanoadamantane (**3**), paraformaldehyde; cyclopropylamine (**15**) and cyclopentanecarboxylic acid (**9**) according to general procedure B. After extraction, the crude was purified by flash column chromatography, using PE/EtOAc

The FEBS Journal (2025) © 2025 The Author(s). *The FEBS Journal* published by John Wiley & Sons Ltd on behalf of Federation of European Biochemical Societies.

17424658, 0, Downloaded from https://febs.onlinelibrary.wiley.com/doi/10.1111/febs.70065 by Universidad Miguel Hernández De Elche, Wiley Online Library on [16/04/2025]. See the Terms and Conditions (https://onlinelibrary.wiley.com/terms-and-conditions) on Wiley Online Library for rules of use; OA articles are governed by the applicable Creative Commons License

9 : 1 and PE/EtOAc 8 : 2 as eluents to give a white solid; yield 52%; mp 152–153 °C; IR (KBr) $\tilde{\nu}$ 3407, 3321, 2906, 2849, 1681, 1630, 1546, 1429, 1361, 1273 cm^{-1}; ^{1}H-NMR (300 MHz, $CDCl_3$) δ 5.91 (br s, 1H), 3.85 (s, 2H), 3.42–3.32 (m, 1H), 2.83–2.76 (m, 1H), 1.99–1.54 (m, 23H), 0.86–0.80 (m, 4H) p.p.m.; ^{13}C-NMR (75 MHz, $CDCl_3$) δ 180.5, 169.0, 53.3, 51.6, 41.5, 41.4, 36.3, 31.5, 30.6, 29.4, 26.3, 9.1 p.p.m. HRMS (ESI^+): $m/z = 345.25329$ $[M + H]^+$; calcd. for $C_{21}H_{32}O_2N_2 + H^+$: 345.25365.

N-(2-(((3*S*,5*S*,7*S*)-adamantan-1-yl)amino)-2-oxoethyl)-*N*-cyclopropyl-[1,1′-biphenyl]-2-carboxamide (33)

The title compound was prepared from 1-isocyanoadamantane (**3**), paraformaldehyde; cyclopropylamine (**15**) and [1,1′-biphenyl]-2-carboxylic acid (**7**) according to general procedure B. After extraction, the crude was purified by flash column chromatography, using PE/EtOAc 8 : 2 and PE/EtOAc 7 : 3 as eluents to give a white solid; yield 49%; mp 83–84 °C; IR (KBr) $\tilde{\nu}$ 3313, 3060, 2906, 2850, 1683, 1629, 1542, 1453, 745, 701 cm^{-1}; ^{1}H-NMR (300 MHz, DMSO-d_6 75 °C) δ 7.48–7.35 (m, 9H), 6.94 (br s, 1H), 3.76 (br s, 2H), 3.30 (br s, 1H), 2.01–1.84 (m, 9H), 1.64 (br s, 6H), 0.56–0.24 (m, 4H) p.p.m.; ^{13}C-NMR (75 MHz, DMSO-d_6 75 °C) δ 172.0, 167.0, 139.7, 137.6, 136.5, 129.0, 128.6, 128.1, 128.0, 127.2, 127.1, 126.7, 51.9, 50.3, 40.9, 35.8, 31.4, 28.6, 7.5 p.p.m.; HRMS (ESI^+): $m/z = 429.25359$ $[M + H]^+$; calcd. for $C_{28}H_{32}O_2N_2 + H^+$: 429.25365.

N-((3*S*,5*S*,7*S*)-adamantan-1-yl)-2-(*N*-cyclopropylacetamido)acetamide (34)

The title compound was prepared from 1-isocyanoadamantane (**3**), paraformaldehyde; cyclopropylamine (**15**) and acetic acid (**6**) according to general procedure B. After extraction, the crude was purified by flash column chromatography, using PE/EtOAc 7 : 3 and PE/EtOAc 5 : 5 as eluents to give a white solid; yield 70%; mp 73–74 °C; IR (KBr) $\tilde{\nu}$ 3330, 3053, 2906, 2849, 1660, 1544, 1422, 1360, 1291, 1030 cm^{-1}; ^{1}H-NMR (300 MHz, $CDCl_3$) δ 5.86 (br s, 1H), 3.82 (s, 2H), 2.81–2.74 (m, 1H), 2.19 (s, 3H), 1.97 (br s, 3H), 1.90 (br s, 6H), 1.59 (br s, 6H), 0.83–0.76 (m, 4H) p.p.m.; ^{13}C-NMR (75 MHz, $CDCl_3$) δ 174.3, 168.6, 52.7, 51.8, 41.4, 36.3, 32.3, 29.4, 22.4, 9.1 p.p.m.; HRMS (ESI^+): $m/z = 291.20628$ $[M + H]^+$; calcd. for $C_{17}H_{26}O_2N_2 + H^+$: 291.20670.

N-(2-(((3*S*,5*S*,7*S*)-adamantan-1-yl)amino)-2-oxoethyl)-*N*-cyclopropylbenzo[b]thiophene-2-carboxamide (35)

The title compound was prepared from 1-isocyanoadamantane (**3**), paraformaldehyde; cyclopropylamine (**15**) and benzo[b]thiophene-2-carboxylic acid (**14**) according to general procedure B. After extraction, the crude was purified by flash column chromatography, using PE/EtOAc 7 : 3 and PE/EtOAc 5 : 5 as eluents to give a white solid; yield 23%; mp 193–194 °C; IR (KBr) $\tilde{\nu}$ 3411, 3309, 3142, 2907, 2851, 1666, 1600, 1515, 1390, 1288, 961, 760 cm^{-1}; ^{1}H-NMR (300 MHz, $CDCl_3$) signals are referred to the main rotamer, δ 7.89–7.79 (m, 3H), 7.44–7.33 (m, 2H), 6.04 (br s, 1H), 4.10 (s, 2H), 3.22–3.14 (m, 1H), 2.14–1.97 (m, 9H), 1,71–1.63 (m, 6H), 0.89–0.82 (m, 4H) p.p.m.; ^{13}C-NMR (75 MHz, $CDCl_3$) signals are referred to the main rotamer, δ 168.3, 166.5, 141.0, 138.8, 137.7, 127.9, 126.3, 125.2, 124.8, 122.4, 54.6, 52.1, 41.6, 36.4, 33.4, 29.5, 10.7 p.p.m.; HRMS (ESI^+): $m/z = 409.19433$ $[M + H]^+$; calcd. for $C_{24}H_{28}O_2N_2 + H^+$: 409.19443.

N-(2-(((3*S*,5*S*,7*S*)-adamantan-1-yl)amino)-2-oxoethyl)-*N*-cyclopropyl-2-phenylacetamide (36)

The title compound was prepared from 1-isocyanoadamantane (**3**), paraformaldehyde; cyclopropylamine (**15**) and phenylacetic acid (**5**) according to general procedure B. After extraction, the crude was purified by flash column chromatography, using PE/EtOAc 7 : 3 as eluent to give an off-white solid; yield 53%; mp 119–120 °C; IR (KBr) $\tilde{\nu}$ 3329, 3025, 2905, 2851, 1723, 1689, 1639, 1454, 1300, 1042, 742, 696 cm^{-1}; ^{1}H-NMR (300 MHz, $CDCl_3$) δ 7.29–7.20 (m, 5H), 5.84 (br s, 1H), 3.92 (s, 2H), 3.88 (s, 2H), 2.77–2.69 (m, 1H), 2.00 (br s, 3H), 1.85 (br s, 6H), 1.61 (br s, 6H), 0.89–0.81 (m, 4H) p.p.m.; ^{13}C-NMR (75 MHz, $CDCl_3$) δ 174.6, 168.5, 135.0, 129.1, 128.7, 126.9, 53.1, 51.7, 41.4, 41.1, 36.3, 32.0, 29.4, 9.5 p.p.m.; HRMS (ESI^+): $m/z = 367.23767$ $[M + H]^+$; calcd. for $C_{23}H_{30}O_2N_2 + H^+$: 367.23800.

N-((3*S*,5*S*,7*S*)-adamantan-1-yl)-2-(*N*-cyclohexylacetamido)acetamide (37)

The title compound was prepared from 1-isocyanoadamantane (**3**), paraformaldehyde; cyclohexylamine (**16**) and acetic acid (**6**) according to general procedure B. After extraction, the crude was purified by flash column chromatography, using PE/EtOAc 7 : 3 and PE/EtOAc 5 : 5 as eluents to give a white solid; yield 78%; mp 77–78 °C; IR (KBr) $\tilde{\nu}$ 3309, 2907, 2851, 1669, 1627, 1538, 1453, 1416, 1359, 1241, 976 cm^{-1}; ^{1}H-NMR (300 MHz, $CDCl_3$) signals are referred to the main rotamer, δ 6.36 (br s, 1H), 3.74 (s, 2H), 3.50–3.41 (m, 1H), 2.10 (s, 3H), 1.99–1.87 (m, 9H), 1.80–1.46 (m, 12H), 1.33–1.16 (m, 4H) p.p.m.; ^{13}C-NMR (75 MHz, $CDCl_3$) signals are referred to the main rotamer, δ 171.3, 169.6, 58.7, 51.4, 48.4, 47.4, 41.4, 36.3, 31.1, 30.4, 29.3, 25.8, 25.0, 21.7 p.p.m.; HRMS (ESI^+): $m/z = 333.25320$ $[M + H]^+$; calcd. for $C_{20}H_{32}O_2N_2 + H^+$: 333.25365.

17424658, 0, Downloaded from https://febs.onlinelibrary.wiley.com/doi/10.1111/febs.70065 by Universidad Miguel Hernández De Elche, Wiley Online Library on [16/04/2025]. See the Terms and Conditions (https://onlinelibrary.wiley.com/terms-and-conditions) on Wiley Online Library for rules of use; OA articles are governed by the applicable Creative Commons License

N-((3*S*,5*S*,7*S*)-adamantan-1-yl)-2-(*N*-((3*S*,5*S*,7*S*)-adamantan-1-yl)acetamido)acetamide (38)

The title compound was prepared from 1-isocyanoadamantane (**3**), paraformaldehyde, (3S,5S,7S)-adamantan-1-amine (**1**), and acetic acid (**6**) according to general procedure B. After extraction, the crude was purified by flash column chromatography, using PE/EtOAc 7 : 3 and PE/EtOAc 5 : 5 as eluents to give a white solid; yield 87%; mp 239–240 °C; IR (KBr) $\tilde{\nu}$ 3302, 3064, 2908, 2849, 1691, 1623, 1549, 1414, 1359, 988, 902 cm^{-1}; ^{1}H-NMR (300 MHz, $CDCl_3$) δ 5.80 (br s, 1H), 3.78 (s, 2H), 2.11 (br s, 6H), 2.02–1.92 (m, 15H), 1.61 (br s, 12H) p.p.m.; ^{13}C-NMR (75 MHz, $CDCl_3$) δ 172.1, 168.8, 59.2, 52.1, 49.6, 41.6, 40.0, 36.2, 36.1, 30.1, 29.3, 25.8 p.p.m.; HRMS (ESI^+): $m/z = 385.28461$ $[M + H]^+$; calcd. for $C_{24}H_{36}O_2N_2 + H^+$: 385.28495.

N-((3*S*,5*S*,7*S*)-adamantan-1-yl)-2-(*N*-butylacetamido) acetamide (39)

The title compound was prepared from 1-isocyanoadamantane (**3**), paraformaldehyde, butan-1-amine (**17**), and acetic acid (**6**) according to general procedure B. After extraction, the crude was purified by flash column chromatography, using PE/EtOAc 7 : 3 and PE/EtOAc 5 : 5 as eluents to give a white solid; yield 70%; mp 124–125 °C; IR (KBr) $\tilde{\nu}$ 3296, 2907, 2853, 1644, 1537, 1414, 1305, 1245, 985, 708 cm^{-1}; ^{1}H-NMR (300 MHz, $CDCl_3$) signals are referred to the main rotamer, δ 6.20 (br s, 1H), 3.75 (s, 2H), 3.26 (t, $J = 7.4$ Hz, 2H), 2.05–1.87 (m, 12H), 1.60–1.46 (m, 8H), 1.24–1.20 (m, 2H), 0.85 (t, $J = 7.0$ Hz, 3H) p.p.m.; ^{13}C-NMR (75 MHz, $CDCl_3$) signals are referred to the main rotamer, δ 171.2, 168.5, 52.0, 50.4, 47.1, 41.4, 36.2, 30.6, 29.3, 21.1, 19.9, 13.7 p.p.m.; HRMS (ESI^+): $m/z = 307.23759$ $[M + H]^+$; calcd. for $C_{18}H_{30}O_2N_2 + H^+$: 307.23800.

N-((3*S*,5*S*,7*S*)-adamantan-1-yl)-2-(*N*-benzylacetamido) acetamide (40)

The title compound was prepared from 1-isocyanoadamantane (**3**), paraformaldehyde, benzylamine (**18**), and acetic acid (**6**) according to general procedure B. After extraction, the product was obtained as a white solid; yield 78%; mp 195–196 °C; IR (KBr) $\tilde{\nu}$ 3312, 3030, 2920, 2854, 1642, 1533, 1409, 1344, 1004, 722, 693 cm^{-1}; ^{1}H-NMR (300 MHz, $CDCl_3$) signals are referred to the main rotamer, δ 7.35–7.26 (m, 5H), 5.90 (br s, 1H), 4.62 (s, 2H), 3.83 (s, 2H), 2.16–1.61 (m, 18H) p.p.m.; ^{13}C-NMR (75 MHz, $CDCl_3$) signals are referred to the main rotamer, δ 171.7, 167.9, 136.2, 129.1, 127.9, 126.8, 53.5, 52.0, 51.3, 41.7, 36.5, 29.6, 21.5 p.p.m.; HRMS (ESI^+): $m/z = 341.22196$ $[M + H]^+$; calcd. for $C_{21}H_{28}O_2N_2 + H^+$: 341.22235.

N-(2-(((3*S*,5*S*,7*S*)-adamantan-1-yl)amino)-2-oxoethyl)-*N*-benzyl-2-phenylacetamide (41)

The title compound was prepared from 1-isocyanoadamantane (**3**), paraformaldehyde, benzylamine (**18**), and phenylacetic acid (**5**) according to general procedure B. After extraction, the crude was purified by flash column chromatography, using PE/EtOAc 7 : 3 as eluent to give a white solid; yield 63%; mp 60–61 °C; IR (KBr) $\tilde{\nu}$ 3300, 3063, 3029, 2906, 2849, 1681, 1632, 1545, 1453, 1359, 724, 697 cm^{-1}; ^{1}H-NMR (300 MHz, $CDCl_3$) signals are referred to the main rotamer, δ 7.31–7.26 (m, 10H), 5.98 (br s, 1H), 4.60 (s, 2H), 3.84 (s, 2H), 3.77 (s, 2H), 2.02–1.60 (m, 15H) p.p.m.; ^{13}C-NMR (75 MHz, $CDCl_3$) signals are referred to the main rotamer, δ 172.2, 167.6, 135.8, 134.6, 129.0, 128.9, 128.6, 127.9, 127.1, 126.7, 52.5, 51.8, 51.2, 41.4, 40.7, 36.3, 29.4 p.p.m.; HRMS (ESI^+): $m/z = 417.25337$ $[M + H]^+$; calcd. for $C_{27}H_{32}O_2N_2 + H^+$: 417.25365.

General procedure C for the synthesis of α-acylpiperazino amides 42–45

To a solution of piperazine (**19**) (0.037 g, 0.40 mmol, 1 equiv) in methanol (3 mL) were added paraformaldehyde (0.031 g, 0.60 mmol, 1.5 equiv), the corresponding carboxylic acid (0.40 mmol, 1 equiv) and 1-isocyanoadamantane (**3**) (0.070 g, 0.40 mmol, 1 equiv) sequentially at room temperature. The reaction mixture was heated at 60 °C for 3 h, and the solvent was evaporated. The crude material was purified by flash column chromatography.

N-((3*S*,5*S*,7*S*)-adamantan-1-yl)-2-(4-benzoylpiperazin-1-yl)acetamide (42)

The title compound was prepared from 1-isocyanoadamantane (**3**), paraformaldehyde, piperazine (**19**), and benzoic acid (**4**) according to general procedure C. The crude was purified by flash column chromatography using EtOAc as eluent to give a white solid; yield 62%; mp 141–142 °C; IR (KBr) $\tilde{\nu}$ 3346, 3019, 2909, 2848, 1668, 1638, 1530, 1458, 1428, 1138, 1017, 715 cm^{-1}; ^{1}H-NMR (300 MHz, $CDCl_3$) δ 7.35 (br s, 5H), 6.75 (br s, 1H), 3.72–3.44 (m, 4H), 2.88 (s, 2H), 2.50 (br s, 4H), 2.03–1.94 (m, 9H), 1.64 (br s, 6H) p.p.m.; ^{13}C-NMR (75 MHz, $CDCl_3$) δ 170.4, 168.3, 135.6, 129.8, 128.6, 127.0, 62.2, 53.3 (4C), 51.2, 41.7, 36.3, 29.4 p.p.m.; HRMS (ESI^+): $m/z = 382.24859$ $[M + H]^+$; calcd. for $C_{23}H_{31}O_2N_3 + H^+$: 382.24890.

N-((3*S*,5*S*,7*S*)-adamantan-1-yl)-2-(4-(cyclopentanecarbonyl)piperazin-1-yl)acetamide (43)

The title compound was prepared from 1-isocyanoadamantane (**3**), paraformaldehyde, piperazine

17424658, 0, Downloaded from https://febs.onlinelibrary.wiley.com/doi/10.1111/febs.70065 by Universidad Miguel Hernández De Elche, Wiley Online Library on [16/04/2025]. See the Terms and Conditions (https://onlinelibrary.wiley.com/terms-and-conditions) on Wiley Online Library for rules of use; OA articles are governed by the applicable Creative Commons License

(**19**), and cyclopentanecarboxylic acid (**9**) according to general procedure C. The crude was purified by flash column chromatography using EtOAc as eluent to give a white solid; yield 75%; mp 118–119 °C; IR (KBr) $\tilde{\nu}$ 3270, 3062, 2907, 2852, 2811, 1672, 1644, 1552, 1514, 1452, 1239, 814, 715 cm^{-1}; ^{1}H-NMR (300 MHz, $CDCl_3$) δ 6.80 (br s, 1H), 3.56 (br s, 2H), 3.47 (br s, 2H), 2.90–2.74 (m, 3H), 2.46–2.40 (m, 4H), 2.01–1.91 (m, 9H), 1.76–1.48 (m, 14H) p.p.m.; ^{13}C-NMR (75 MHz, $CDCl_3$) δ 174.6, 168.5, 62.0, 53.4, 53.0, 51.2, 45.4, 41.8, 41.6, 40.9, 36.2, 30.0, 29.3, 25.9 p.p.m.; HRMS (ESI$^+$): $m/z = 374.27984$ $[M + H]^+$; calcd. for $C_{22}H_{35}O_2N_3 + H^+$: 374.28020.

N-((3*S*,5*S*,7*S*)-adamantan-1-yl)-2-(4-(2-phenylacetyl) piperazin-1-yl)acetamide (44)

The title compound was prepared from 1-isocyanoadamantane (**3**), paraformaldehyde, piperazine (**19**), and phenylacetic acid (**5**) according to general procedure C. The crude was purified by flash column chromatography, using EtOAc as eluent to give a white solid; yield 83%; mp 145–146 °C; IR (KBr) $\tilde{\nu}$ 3321, 3019, 2908, 2848, 1664, 1630, 1511, 1456, 1241, 1143, 736, 723 cm^{-1}; ^{1}H-NMR (300 MHz, $CDCl_3$) δ 7.28–7.15 (m, 5H), 6.70 (br s, 1H), 3.67 (s, 2H), 3.59 (br s, 2H), 3.40–3.37 (m, 2H), 2.78 (s, 2H), 2.41–2.38 (m, 2H), 2.26–2.23 (m, 2H), 2.02–1.91 (m, 9H), 1.61 (br s, 6H) p.p.m.; ^{13}C-NMR (75 MHz, $CDCl_3$) δ 169.4, 168.2, 134.8, 128.7, 128.4, 126.8, 62.0, 53.0, 52.8, 51.1, 46.0, 41.7, 41.6, 40.9, 36.2, 29.3 p.p.m.; HRMS (ESI$^+$): $m/z = 396.26419$ $[M + H]^+$; calcd. for $C_{24}H_{33}O_2N_3 + H^+$: 396.26455.

2-(4-acetylpiperazin-1-yl)-*N*-((3*S*,5*S*,7*S*)-adamantan-1-yl)acetamide (45)

The title compound was prepared from 1-isocyanoadamantane (**3**), paraformaldehyde, piperazine (**19**), and acetic acid (**6**) according to general procedure C. The crude was purified by flash column chromatography, using EtOAc/MeOH 95 : 5 as eluent to give a white solid; yield 76%; mp 135–136 °C; IR (KBr) $\tilde{\nu}$ 3322, 3008, 2915, 2848, 2901, 1667, 1654, 1512, 1427, 1273, 1245, 1006, 990 cm^{-1}; ^{1}H-NMR (300 MHz, $CDCl_3$) δ 6.73 (br s, 1H), 3.55 (br s, 2H), 3.41 (br s, 2H), 2.84 (s, 2H), 2.47–2.39 (m, 4H), 2.02–1.92 (m, 12H), 1.61 (br s, 6H) p.p.m.; ^{13}C-NMR (75 MHz, $CDCl_3$) δ 168.9, 168.2, 62.1, 53.2, 52.9, 51.2, 46.2, 41.6, 41.4, 36.2, 29.3, 21.3 p.p.m.; HRMS (ESI$^+$): $m/z = 320.23295$ $[M + H]^+$; calcd. for $C_{18}H_{29}O_2N_3 + H^+$: 320.23325.

Biology

Animals

C57BL/6JRccHSd female mice (15-23-week-old, 24–35 g; Harlan, the Netherlands) bred at the animal facility at Universidad Miguel Hernández de Elche (UMH, Elche, Spain) were used to assess the antinociceptive effects of compound **23** on the model of chemotherapy-induced neuropathic pain. Housing conditions were maintained at 21 ± 1 °C and 55 ± 20% relative humidity in a controlled light/dark cycle (light on between 8:00 a.m. and 8:00 p.m). Care was taken to minimize the number of animals used and the pain and stress they experienced. Animal experimentation procedures were conducted under the approval of the Institutional Animal and Ethical Committee at UMH, following the guidelines of the European Community (2010/63/EU), and the Committee for Research and Ethical Issues of the International Association for the Study of Pain [64]. The study protocol received approval from the Ethical Committee of Universidad Miguel Hernández de Elche (UMH, Elche, Spain) and the regional government (approval code: 2022 VSC PEA 0078-2). For the *in vivo* behavioral experiments evaluating the effects of the TRPM8 antagonist on mice with chemotherapy-induced neuropathy, male C57BL/6JRccHSd mice (15–23 weeks old; Harlan, the Netherlands) were utilized. The animals were bred and housed at the UMH Animal Facility (Servicio de Experimentación Animal, UMH, Elche, Spain). The experimental protocol was reviewed and approved by the Institutional Animal and Ethical Committee of UMH.

Primary cultures of dorsal root ganglia neurons

Primary cultures of neonatal dorsal root ganglia were used for multielectrode array (MEA) and patch-clamp experiments following established methodologies previously described [65]. Neonatal dorsal root ganglia (DRGs) were obtained from Wistar rats (3–5 days old) and were isolated and digested with 0.25% (w/v) collagenase (type IA) in DMEM GlutaMax with 1% (v/v) penicillin/streptomycin (P/S) solution for 1 h at 37 °C in a 5% CO_2 Thermo Scientific incubator. Following digestion, DRGs were mechanically dissociated and passed through a 100 µm cell strainer to obtain single-cell suspensions. Suspensions were washed with DMEM GlutaMax with 10% (v/v) fetal bovine serum (FBS) and 1% (v/v) penicillin/streptomycin (P/S). Cells were then seeded in microelectrode array chambers coated with poly-L-lysine (8.3 µg·mL^{-1}) and laminin (5 µg·mL^{-1}). After 1 h, the medium was replaced with DMEM GlutaMax, 10% (v/v) FBS, and 1% (v/v) P/S, supplemented with mouse 2.5S NGF 50 ng·mL^{-1} and 1.25 µg·mL^{-1} cytosine arabinoside. Isolated mouse cells were incubated with 0.67% (w/v) collagenase type XI and 3% (w/v) dispase (Gibco) in INC mix medium (in mM): 155 NaCl, 1.5 K_2HPO_4, 5.6 HEPES, 4.8 NaHEPES, and 5 glucose for 1 h (37 °C, 5% 3 CO_2). Primary cultures of mouse DRGs were used for patch-clamp experiments. Mouse DRG were mechanically dissociated using a glass Pasteur pipette. Single-cell suspensions were passed through a 100 µm cell strainer and washed with DMEM GlutaMax plus 10%

17424658, 0, Downloaded from https://febs.onlinelibrary.wiley.com/doi/10.1111/febs.70065 by Universidad Miguel Hernández De Elche, Wiley Online Library on [16/04/2025]. See the Terms and Conditions (https://onlinelibrary.wiley.com/terms-and-conditions) on Wiley Online Library for rules of use; OA articles are governed by the applicable Creative Commons License

FBS (Invitrogen (Thermo Fisher Scientific), Barcelona, Spain) and 1% P/S. For each experiment, cells were seeded at the required density on 12 mm coverglass slides in a 24-well plate or microelectrode array chambers previously coated with poly-L-lysine ($8.33\,\mu g{\cdot}mL^{-1}$) and laminin ($5\,\mu g{\cdot}mL^{-1}$). After 2 h, the medium was replaced with DMEM GlutaMax, 10% FBS, and 1% P/S, supplemented with mouse 2.5 s NGF $50\,ng{\cdot}mL^{-1}$ (Promega). All experiments in patch-clamp were conducted 48 h after cell seeding.

Calcium microfluorimetric assay

Assays were conducted to assess the channel activity of the recombinant hTRPM8 stably expressed in HEK-293 cells. HEK-293-hTRPM8 cells were cultured in a monolayer using a DMEM GlutaMax with 10% FBS and 1% P/S and maintained at 37 °C in 5% CO_2. For experiments, cells were prepared and seeded at the indicated densities. To evaluate compound effectiveness against hTRPM8 activity, microfluorometry-based calcium flux assays were performed using Fluo-4 NW Ca^{2+} dye and fluorescence detection. HEK cell lines expressing hTRPM8 were seeded in 96-well plates and incubated with the dye-loading solution. Ion channel activity was measured using a plate reader, and fluorescence intensity changes were recorded following the addition of vehicle, compound at varying concentrations, and antagonist (10 μM AMTB). Data analysis included calculating the Z-factor for each assay and normalizing compound effects to capsaicin-induced fluorescence. Data were analyzed to determine the concentration exerting half-maximal inhibition (IC_{50}) or activation (EC_{50}) of agonist-induced calcium elevation, using GRAPHPAD PRISM8® software (Boston, MA, USA). All experiments were conducted in triplicate, and results are presented as mean ± standard deviation.

Patch-clamp recordings from recombinant cells

Recording through patch-clamp techniques was performed on HEK293 cells cultured in DMEM GlutaMax with 10% FBS and 1% P/S. The cell lines were authenticated following the standardization of STR Profiling guidelines (ANSI/ATCC ASN-0002-2022) using the CLA Identifier Plus PCR Amplification Kit (Thermo Fisher-A44660) to analyze 16 highly variant human STRs. The cells were confirmed to be mycoplasma-free. These cells were transiently transfected with plasmids encoding hTRPV1, hTRPM8, or hTRPA1 using Lipofectamine 3000. Transfected cells were seeded on 12 mm Ø glass coverslips treated with poly-L-lysine solution and recorded 2 days post-transfection. The intracellular pipette solution included (in mM) 150 NaCl, 3 $MgCl_2$, 5 EGTA, and 10 HEPES, pH 7.2 with CsOH, while the extracellular solution contained (in mM) 150 NaCl, 6 CsCl, 1 $MgCl_2$, 1.5 $CaCl_2$, 10 glucose, and 10 HEPES, pH 7.4 with NaOH. An EPC-10 amplifier with Patchmaster software was used in whole-cell experiments. Patch pipettes, created from thin-wall borosilicate capillary glass tubing, were pulled with a Micropipette puller to a final resistance of 2–8 MΩ when filled with the internal solution. Recordings were acquired at 10 kHz and low-pass filtered at 3 kHz, discarding recordings with leak currents > 200pA or series resistance > 20 MΩ. In voltage-clamp recordings, cells were held at a constant potential, and the application of modulators was carried out using a gravity-driven perfusion system. Total currents were normalized to the first current peak evoked by the activating stimuli. To study the effect of compound **23** on TRPM8 voltage dependence, a voltage step protocol from −120 to 120 mV was used with 100 ms steps of 20 mV from a holding potential at 0 mV. Leak currents were not subtracted, and conductance was calculated using the equation: $G = I/(V - V_r)$, where I is the measured ionic current, V is the applied voltage, and V_r is the reversal potential that for the ionic conditions used was set to 0 mV.

Dose–response relationships for WS-12 channel activation were normalized to the response of the channel to a saturating concentration of the agonist. Similarly, dose–response curves for blockade activity were normalized with respect to the response in the absence of the blocker. The experimental data were fitted to the Hill equation: $Y = \text{Bottom} + (\text{Top} - \text{Bottom})/(1 + 10^{([\text{ligand}] - \text{LogIC}_{50}(\text{or Log}(\text{EC}_{50})))})$ using PRISM 9 software. Top was fixed to 100, as the unblocked response or the maximal response for WS-12.

Patch-clamp recordings from DRG nociceptors

Two days after being seeded on 12 mm Ø glass coverslips treated with poly-L-lysine solution and Laminin (Sigma-Aldrich), whole-cell patch-clamp recordings were conducted on sensory DRG neurons from adult mice. The intracellular pipette solution consisted of (in mM): 4 NaCl, 110 K gluconate, 1 $CaCl_2$, 30 KCl, 2 $MgCl_2$, 10 HEPES, 4 ATP, 0.4 GTP, and 10 EGTA, with a pH of 7.2 adjusted with KOH. The extracellular solution comprised (in mM): 140 NaCl, 4 KCl, 2 $CaCl_2$, 2 $MgCl_2$, 10 HEPES, 5 glucose, and 20 mannitol, with a pH of 7.4 adjusted with NaOH.

Microelectrode array (MEA)

Microelectrode array measurements were conducted using 60-electrode thin MEA chips, featuring 30 μm diameter electrodes and 200 μm inter-electrode spacing, including an integrated reference electrode (Multi Channel Systems GmbH, Reutlingen, Germany). The MEA1060 System (Multi Channel Systems GmbH) and MC RACK software version 4.3.0 were employed to record the electrical activity of primary sensory neurons. Short 30 s applications (termed P1 and P2) of WS-12 were applied using a continuous perfusion system ($2\,mL{\cdot}min^{-1}$). Between each stimulus, cells

The FEBS Journal (2025) © 2025 The Author(s). *The FEBS Journal* published by John Wiley & Sons Ltd on behalf of Federation of European Biochemical Societies.

17424658, 0, Downloaded from https://febs.onlinelibrary.wiley.com/doi/10.1111/febs.70065 by Universidad Miguel Hernández De Elche, Wiley Online Library on [16/04/2025]. See the Terms and Conditions (https://onlinelibrary.wiley.com/terms-and-conditions) on Wiley Online Library for rules of use; OA articles are governed by the applicable Creative Commons License

underwent 4 min and 30 s washes with external solution. Treated cells were perfused with compound **23**, 1 min before and together with P2. The protocol concluded with the application of 40 mM KCl to confirm neuronal excitability and viability. All measurements were conducted at approximately 34.5 °C using the Multichannel Systems Temperature Controller. For microelectrode array analysis, data were processed using MC_RACK spike sorter with a sample rate of 25 kHz, applying a Butterworth high-pass 2nd order filter with a 200 Hz cutoff. For AITC analysis, a cutoff of 500 Hz was applied. An evoked spike was defined when the amplitude of neuronal electrical activity reached a threshold established by automatic estimation at −4.7 μV Std. For AITC analysis, an evoked spike was defined when the amplitude of neuronal electrical activity reached a threshold established by automatic estimation at −5 μV Std. Spiking activity was measured for 60 s immediately following the instillation of activating stimuli. Electrodes lacking electrical activity in the first agonist pulse were excluded. The recorded signals were then analyzed to extract the mean spike frequency for each pulse (P1–P2). The ratio P2/P1 of mean spike frequency was calculated and normalized to the vehicle for comparison across different conditions.

Model of chemotherapy-induced neuropathic pain

Chemotherapy-induced sensitization was induced by repeated administration of oxaliplatin (ref#2623; Tocris, Bristol, UK). Oxaliplatin was freshly prepared every day by dissolution in 5% dextrose in warmed distilled water at 37 °C. The chemotherapeutic was administered intraperitoneally every other day for 5 days at a 6 $mg \cdot kg^{-1}$ and in a volume of 10 $mL \cdot kg^{-1}$, reaching an accumulated dose of 18 $mg \cdot kg^{-1}$ after the three injections.

Compound 23 treatment

The systemic effect of compound **23** was assessed after intraperitoneal administration at 5 $mg \cdot kg^{-1}$, dissolved in a solution of 2% Cremophor and 5% DMSO in saline, with a volume of 10 $mL \cdot kg^{-1}$. This dose was chosen based on the relative potency of the compound in the *in vitro* studies when compared to the canonical antagonist AMTB. Nociceptive sensitivity was evaluated for 30- and 90-min postinjection using the acetone drop test (7 days after the first oxaliplatin dose) and the dry ice test (9 days after the last oxaliplatin dose).

The local effect of compound **23** or its vehicle was assessed 11 days after beginning the oxaliplatin treatment through subcutaneous intraplantar injection of 1 μg compound **23** or vehicle (2% Cremophor and 5% DMSO in saline) in the ventral side of the right hind paw, administered in a volume of 10 μL [66]. This dose was chosen based on previous works [48] and considering the relative potency of the compound in the *in vitro* studies. Nociceptive sensitivity was evaluated 30 and 90 min after the intraplantar injection with the acetone test [66].

Behavioral assessment of cold sensitivity

Prior to conducting behavioral experiments, mice underwent a 2-day acclimatization period to the experimental conditions, during which they were handled and habituated to the male experimenter for a minimum of 2 min per day and mouse [66]. Additionally, the animals were familiarized with each testing environment 2 h per day, placed individually in Plexiglas® chambers (10 × 10 × 14 cm). Every day of evaluation, the mice spent an additional hour of habituation in the testing environment before the measurement of nociceptive sensitivity.

Acetone drop test

Mice were placed over a metal grid and allowed to habituate for approximately 1 h. Acetone (179124; Sigma-Aldrich) was applied in 20 μL drops onto the mid-plantar surface of the right hind paw by using a 200 μL pipette with a plastic tip manually curved [66]. Responses were recorded using an iPhone SE camera (Apple, Cupertino, CA, USA), and quantification of paw-licking responses was conducted afterwards by a blinded observer. The responses were measured for 1 min after acetone application, with a digital stopwatch (Xnote Stopwatch Version 1.63 2011 Dmitry Nikitin) and were averaged for both hindpaws after the systemic treatment with compound **23** or conducted only in the right hind paw after the intraplantar treatment. For each measurement, the paws were sampled three times, and the mean was calculated. The interval between each application of acetone was at least 3 min [66].

Dry ice test

The dry ice test was conducted as previously described [67] with some modifications. Mice underwent a 1-h habituation period on a 6 mm thick glass surface (Flores Valles, Madrid, Spain). Subsequently, a hand-made probe was prepared by cutting the top of a 3 mL syringe (DicoNEX; ZARYS International Group, Zabrze, Poland) and drilling the syringe with a 25 G needle (BD Microlance 3; Beckton Dickinson & Co Ltd, Louth, Ireland) to prevent the accumulation of CO_2 gas. Powdered dry ice was used to fill the probe. The ice was compacted by pressing the plunger against the bench until a dense pellet at least 1 cm long was obtained. The flattened pellet was then applied to the glass surface using the probe, targeting the right and left hindpaws. A minimum interval of 5 min was maintained between applications. To determine the threshold value for each mouse, the latency to paw withdrawal was recorded for each hindpaw and subsequently averaged. The glass surface was always kept dry.

17424658, 0, Downloaded from https://febs.onlinelibrary.wiley.com/doi/10.1111/febs.70065 by Universidad Miguel Hernández De Elche, Wiley Online Library on [16/04/2025]. See the Terms and Conditions (https://onlinelibrary.wiley.com/terms-and-conditions) on Wiley Online Library for rules of use; OA articles are governed by the applicable Creative Commons License

Statistical analysis

For the analysis of *in vitro* studies, all data are expressed as mean ± SEM. The number of replicates is indicated in the figure legends. *In vitro* data were statistically analyzed using one-way ANOVA followed by the Bonferroni *post hoc* test of multiple comparisons as indicated, or unpaired, two-tailed Student *t*-test for some experiments are also indicated. For one-way ANOVA, we report the F (DFn, DFd) and the P value, along with the P values derived from the Bonferroni *post hoc* test. The P value for all the analyses was set at 0.05, and the value obtained is reported.

For the analysis of behavioral experiments, GRAPHPAD PRISM 9 was used (GraphPad Software Inc., San Diego, CA, USA). An ANOVA with two factors (Within Factor 'OXP treatment', between factor '**23** vs Vehicle group') and their interaction was first used to assess the effect of the oxaliplatin treatment and to assess possible baseline differences between treatment groups. A subsequent two-way ANOVA was used to study the effects of compound **23** treatment (Within Factor 'Time Point', between factor '**23** vs Vehicle group' and their interaction). *Post hoc* Tukey's multiple comparisons tests were run whenever the interaction was significant and differences were considered statistically significant when P value was below 0.05.

Metabolic stability

Incubation in mouse plasma

The standard incubation mixture (100 µL final volume) was carried out by dissolving the tested substrate (100 µM) in DMSO (5% final volume) in preincubated plasma at 37 °C. The mixture was shaken for 60 min at 37 °C. Control incubations were carried out without substrate. Each incubation was stopped by addition of 200 µL of ice-cold acetonitrile, vortexed, and centrifuged at 13 000 r.p.m. for 10 min. The supernatants were analyzed by LC-UV [68].

Incubation in mouse liver microsomes

The standard incubation mixture (250 µL final volume) was carried out in a 50 mM Tris (tris[hydroxymethyl]aminomethane) buffer (pH 7.4) containing 150 mM KCl, 1.5 mM, 3.3 mM $MgCl_2$, 1.3 mM $NADPNa_2$, 3.3 mM glucose 6-phosphate, 0.4 units·mL^{-1} glucose 6-phosphate dehydrogenase, acetonitrile as cosolvent (1% of total volume), and the substrate (50 µM). After pre-equilibration of the mixture, an appropriate volume of MLM suspension was added to give a final protein concentration of 1.0 mg·mL^{-1}. The mixture was shaken for 60 min at 37 °C using a horizontal shaking thermostatic bath while protecting the samples from light. Control incubations were carried out without the presence of substrate, or NADPH regenerating system, or microsomes. Each incubation was stopped by the addition of 250 µL of ice-cold acetonitrile, vortexed, and centrifuged at 13 000 r.p.m. for 5 min [68]. The supernatants were analyzed by LC-UV and LC-HRMS equipment (see Tables S1 and S2, Fig. S79 for full parameters setting in the Supporting Information).

Data processing

The metabolic stability of the compound **23** was determined *in vitro* by measuring the residual peak area after incubation by LC-UV analysis. Samples were further processed by LC-HRMS equipment for metabolite profiling. Raw data files were processed using both XCALIBUR® and COMPOUND DISCOVERER 3.2® software (Thermo Scientific) using a customized workflow for the detection and identification of the expected and unknown metabolites (Fig. S80).

Molecular modeling and docking

Human and mouse TRPM8 structures (PDB ID 8BDC, 8E4N) [4,69] were used to explore the binding of compound **23**. The docking procedure was performed with the AutoDock4 algorithm [70] implemented in Yasara [71,72]. Briefly, a local docking procedure was accomplished using either human or mouse TRPM8 structures, and compound **23**. The search space was limited to a simulation box built around the well-known agonist or antagonist ligands (WS-12, AMTB). A total of 500 flexible docking runs were set and clustered around the selected binding sites. The program performs a simulated annealing minimization of the complexes, which moves the structure to a stable energy minimum, by using the implemented AMBER 99 (Assisted Model Building with Energy Refinement) force field [73]. The Yasara pH command was set to 7.0, to ensure that molecules preserved their pH dependency of bond orders and protonation patterns. The best binding energy complex in each cluster was stored, analyzed, and used to select the best orientation of the interacting partners. The theoretical affinities of ligands at its binding site were determined by calculating the binding energy of the ligand-receptor complex. The binding energy was obtained by measuring the energy at infinite distance (the unbound state) and subtracting from that value the energy of the complex at the bound state. Figures were drawn using the open-source PYMOL v2.6 (The PyMOL Molecular Graphics System, at http://www.pymol.org/). Interactions were determined in PLIP (https://plip-tool.biotec.tu-dresden.de/plip-web/plip/index), a fully automated web server [74] to identify noncovalent interactions between macromolecules and ligands. The same molecular modeling methodology was used by Lamberti *et al.* [75].

Acknowledgements

AL received funding from the European Union's Horizon 2020 research and innovation program under the Marie Skłodowska-Curie Actions (no. 956477);

17424658, 0, Downloaded from https://febs.onlinelibrary.wiley.com/doi/10.1111/febs.70065 by Universidad Miguel Hernández De Elche, Wiley Online Library on [16/04/2025]. See the Terms and Conditions (https://onlinelibrary.wiley.com/terms-and-conditions) on Wiley Online Library for rules of use; OA articles are governed by the applicable Creative Commons License

Financial support from the Spanish Ministry of Science, Innovation and Universities (PID2021-126423OB-C21), from Generalitat Valenciana (GVA-PROMETEO/2021/031), and Miguel Hernández University of Elche (UMH-PAR2019) was granted to AF-C and AF-M. Free access to University of Piemonte Orientale (Novara) scientific infrastructures and equipment, is gratefully acknowledged. Open access publishing facilitated by Universita degli Studi del Piemonte Orientale Amedeo Avogadro, as part of the Wiley - CRUI-CARE agreement.

Conflict of interest

The authors declare no conflict of interest.

Author contributions

UG, AF-M, GCT, and AF-C wrote and revised the manuscript with input from all the authors, drafting the work or reviewing it critically for important intellectual content. UG and FT synthesized the compounds. SA performed metabolic stability, HRMS analysis, and purity of final compounds. AL performed the biological evaluation, patch-clamp, and MEA experiments and wrote the manuscript. DC performed *in vivo* experiments and wrote and revised the manuscript. LB performed MEA experiments and revised the manuscript. GFB performed docking simulations. All the authors have approved the final version of the manuscript.

Peer review

The peer review history for this article is available at https://www.webofscience.com/api/gateway/wos/peer-review/10.1111/febs.70065.

Data availability statement

The authors confirm that the data supporting the findings of this study are available within the main text and the Supporting Information. The data that support the findings of this study are available from the corresponding authors upon reasonable request.

References

1 Kashio M & Tominaga M (2022) TRP channels in thermosensation. *Curr Opin Neurobiol* **75**, 102591.
2 Pertusa M, Solorza J & Madrid R (2023) Molecular determinants of TRPM8 function: key clues for a cool modulation. *Front Pharmacol* **14**, 1213337.
3 Lolignier S, Gkika D, Andersson D, Leipold E, Vetter I, Viana F, Noël J & Busserolles J (2016) New insight in cold pain: role of ion channels, modulation, and clinical perspectives. *J Neurosci* **36**, 1435–11439.
4 Palchevskyi S, Czarnocki-Cieciura M, Vistoli G, Gervasoni S, Nowak E, Beccari AR, Nowotny M & Talarico C (2023) Structure of human TRPM8 channel. *Commun Biol* **6**, 1065.
5 Peier AM, Moqrich A, Hergarden AC, Reeve AJ, Andersson DA, Story GM, Earley TJ, Dragoni I, Mcintyre P, Bevan S *et al.* (2002) A TRP channel that senses cold stimuli and menthol. *Cell* **108**, 705–715.
6 Plaza-Cayón A, González-Muñiz R & Martín-Martínez M (2022) Mutations of TRPM8 channels: unraveling the molecular basis of activation by cold and ligands. *Med Res Rev* **42**, 2168–2203.
7 Khalil M, Alliger K, Weidinger C, Yerinde C, Wirtz S, Becker C & Engel MA (2018) Functional role of transient receptor potential channels in immune cells and epithelia. *Front Immunol* **9**, 174.
8 Silverman HA, Chen A, Kravatz NL, Chavan SS & Chang EH (2020) Involvement of neural transient receptor potential channels in peripheral inflammation. *Front Immunol* **11**, 590261.
9 Liu H, Liu Q, Hua L & Pan J (2018) Inhibition of transient receptor potential melastatin 8 alleviates airway inflammation and remodeling in a murine model of asthma with cold air stimulus. *Acta Biochim Biophys Sin* **50**, 499–506.
10 Bidaux G, Borowiec A-S, Dubois C, Delcourt P, Schulz C, Vanden Abeele F, Lepage G, Desruelles E, Bokhobza A, Dewailly E *et al.* (2016) Targeting of short TRPM8 isoforms induces 4TM-TRPM8-dependent apoptosis in prostate cancer cells. *Oncotarget* **7**, 29063–29080.
11 Ochoa SV, Casas Z, Albarracín SL, Sutachan JJ & Torres YP (2023) Therapeutic potential of TRPM8 channels in cancer treatment. *Front Pharmacol* **14**, 1098448.
12 Pérez De Vega MJ, Gómez-Monterrey I, Ferrer-Montiel A & González-Muñiz R (2016) Transient receptor potential melastatin 8 channel (TRPM8) modulation: cool entryway for treating pain and cancer. *J Med Chem* **59**, 10006–10029.
13 Mahmoud O, Soares GB & Yosipovitch G (2023) Transient receptor potential channels and itch. *Int J Mol Sci* **24**, 420.
14 Fakih D, Baudouin C, Réaux-Le Goazigo A & Mélik Parsadaniantz S (2020) TRPM8: a therapeutic target for neuroinflammatory symptoms induced by severe dry eye disease. *Int J Mol Sci* **21**, 8756.
15 Parra A, Madrid R, Echevarria D, Del Olmo S, Morenilla-Palao C, Acosta MC, Gallar J, Dhaka A, Viana F & Belmonte C (2010) Ocular surface wetness is

17424658, 0, Downloaded from https://febs.onlinelibrary.wiley.com/doi/10.1111/febs.70065 by Universidad Miguel Hernández De Elche, Wiley Online Library on [16/04/2025]. See the Terms and Conditions (https://onlinelibrary.wiley.com/terms-and-conditions) on Wiley Online Library for rules of use; OA articles are governed by the applicable Creative Commons License

regulated by TRPM8-dependent cold thermoreceptors of the cornea. *Nat Med* **16**, 1396–1399.
16 Wirta DL, Senchyna M, Lewis AE, Evans DG, McLaurin EB, Ousler GW & Hollander DAA (2022) Randomized, vehicle-controlled, phase 2b study of two concentrations of the TRPM8 receptor agonist AR-15512 in the treatment of dry eye disease (COMET-1). *Ocul Surf* **26**, 166–173.
17 Dussor G & Cao YQ (2016) TRPM8 and migraine. *Headache* **56**, 1406–1417.
18 Alarcón-Alarcón D, Cabañero D, de Andrés-López J, Nikolaeva-Koleva M, Giorgi S, Fernández-Ballester G, Fernández-Carvajal A & Ferrer-Montiel A (2022) TRPM8 contributes to sex dimorphism by promoting recovery of normal sensitivity in a mouse model of chronic migraine. *Nat Commun* **13**, 6304.
19 Wu B, Su X, Zhang W, Zhang YH, Feng X, Ji YH & Tan ZY (2021) Oxaliplatin depolarizes the IB4 – dorsal root ganglion neurons to drive the development of neuropathic pain through TRPM8 in mice. *Front Mol Neurosci* **14**, 690858.
20 Aierken A, Xie YK, Dong W, Apaer A, Lin JJ, Zhao Z, Yang S, Xu ZZ & Yang F (2021) Rational design of a modality-specific inhibitor of TRPM8 channel against oxaliplatin-induced cold allodynia. *Adv Sci* **8**, 2101717.
21 Weyer-Menkhoff I & Lötsch J (2018) Human pharmacological approaches to TRP-ion-channel-based analgesic drug development. *Drug Discov Today* **23**, 2003–2012.
22 Beccari AR, Gemei M, Monte ML, Menegatti N, Fanton M, Pedretti A, Bovolenta S, Nucci C, Molteni A, Rossignoli A *et al.* (2017) Novel selective, potent naphthyl TRPM8 antagonists identified through a combined ligand- and structure-based virtual screening approach. *Sci Rep* **7**, 10999.
23 Fernández-Carvajal A, González-Muñiz R, Fernández-Ballester G & Ferrer-Montiel A (2020) Investigational drugs in early phase clinical trials targeting thermotransient receptor potential (ThermoTRP) channels. *Expert Opin Investig Drugs* **29**, 1209–1222.
24 Horne DB, Biswas K, Brown J, Bartberger MD, Clarine J, Davis CD, Gore VK, Harried S, Horner M, Kaller MR *et al.* (2018) Discovery of TRPM8 antagonist (S)-6-(((3-Fluoro-4-(trifluoromethoxy)phenyl)(3-fluoropyridin-2-yl)methyl)carbamoyl)nicotinic acid (AMG 333), a clinical candidate for the treatment of migraine. *J Med Chem* **61**, 8186–8201.
25 Andrews MD, Forselles KA, Beaumont K, Galan SRG, Glossop PA, Grenie M, Jessiman A, Kenyon AS, Lunn G, Maw G *et al.* (2015) Discovery of a selective TRPM8 antagonist with clinical efficacy in cold-related pain. *ACS Med Chem Lett* **6**, 419–424.
26 Wu S, Huang J, Gazzarrini S, He S, Chen L, Li J, Xing L, Li C, Chen L, Neochoritis CG *et al.* (2015) Isocyanides as influenza a virus subtype H5N1 wild-type M2 channel inhibitors. *ChemMedChem* **10**, 1837–1845.
27 Liu J, Obando D, Liao V, Lifa T & Codd R (2011) The many faces of the adamantyl group in drug design. *Eur J Med Chem* **46**, 1949–1963.
28 Wanka L, Iqbal K & Schreiner PR (2013) The lipophilic bullet hits the targets: medicinal chemistry of adamantane derivatives. *Chem Rev* **113**, 3516–3604.
29 Grillaud M & Bianco A (2015) Multifunctional adamantane derivatives as new scaffolds for the multipresentation of bioactive peptides. *J Pept Sci* **21**, 330–345.
30 Dömling A, Wang W & Wang K (2012) Chemistry and biology of multicomponent reactions. *Chem Rev* **112**, 3083–3135.
31 Zhu J, Wang Q & Wang MX (2014) Multicomponent Reactions in Organic Synthesis. Wiley, Weinheim.
32 Hulme C & Gore V (2003) Multi-component reactions: emerging chemistry in drug discovery 'from xylocain to crixivan'. *Curr Med Chem* **10**, 51–80.
33 Ruijter E & Orru RVA (2013) Multicomponent reactions – opportunities for the pharmaceutical industry. *Drug Discov Today Technol* **10**, e15–e20.
34 Ugi I, Meyr U, Fetzer U & Steinbrückner C (1959) Versuche mit isonitrilen. *Angew Chem* **71**, 386–388.
35 Dömling A & Ugi I (2000) Multicomponent reactions with isocyanides. *Angew Chem* **39**, 3168–3210.
36 Ugi I & Werner B (2007) Methods and Reagents for Green Chemistry: An Introduction (Tundo P, Perosa A & Zecchini F, eds), pp. 1–22. Wiley, Hoboken, NJ. doi: 10.1002/9780470124086
37 Flores-Reyes JC, Islas-Jácome A & González-Zamora E (2021) The Ugi three-component reaction and its variants. *Org Chem Front* **8**, 5460–5515.
38 Passerini M (1921) Isonitrili, I. Composti del p-isonitrileazobenzene con acetone ed acido acetico. *Gazz Chim Ital* **51**, 126–129.
39 Banfi L, Basso A, Lambruschini C, Moni L & Riva R (2021) The 100 facets of the Passerini reaction. *Chem Sci* **12**, 15445–15472.
40 Pirali T, Galli U, Serafini M, Griglio A, Genazzani AA & Tron GC (2019) Drug discovery for soft drugs on TRPV1 and TRPM8 channels using the Passerini reaction. In TRP Channels: Methods and Protocols, *Methods in Molecular Biology* (Ferrer-Montiel A & Hucho T, eds), 1987, pp. 207–221. Springer, New York, NY.
41 Banfi L & Riva R (2005) The Passerini reaction. In Organic Reactions, pp. 1–140. Wiley, Hoboken, NJ. doi: 10.1002/0471264180.or065.01
42 Giovenzana GB, Tron GC, Di Paola S, Menegotto IG & Pirali T (2006) A mimicry of primary amines by bis-secondary diamines as components in the Ugi four-component reaction. *Angew Chem Int Ed* **45**, 1099–1102.

The FEBS Journal (2025) © 2025 The Author(s). *The FEBS Journal* published by John Wiley & Sons Ltd on behalf of Federation of European Biochemical Societies.

17424658, 0, Downloaded from https://febs.onlinelibrary.wiley.com/doi/10.1111/febs.70065 by Universidad Miguel Hernández De Elche, Wiley Online Library on [16/04/2025]. See the Terms and Conditions (https://onlinelibrary.wiley.com/terms-and-conditions) on Wiley Online Library for rules of use; OA articles are governed by the applicable Creative Commons License

43 Galli U, Tron GC, Purghè B, Grosa G & Aprile S (2020) Metabolic fate of the isocyanide moiety: are isocyanides pharmacophore groups neglected by medicinal chemists? *Chem Res Toxicol* **33**, 955–966.

44 Voets T, Talavera K, Owsianik G & Nilius B (2005) Sensing with TRP channels. *Nat Chem Biol* **1**, 85–92.

45 Eid SR, Crown ED, Moore EL, Liang HA, Choong KC, Dima S, Henze DA, Kane SA & Urban MO (2008) HC-030031, a TRPA1 selective antagonist, attenuates inflammatory- and neuropathy-induced mechanical hypersensitivity. *Mol Pain* **4**, 48.

46 Takaishi M, Uchida K, Suzuki Y, Matsui H, Shimada T, Fujita F & Tominaga M (2016) Reciprocal effects of capsaicin and menthol on thermosensation through regulated activities of TRPV1 and TRPM8. *J Physiol Sci* **66**, 143–155.

47 Bertamino A, Ostacolo C, Medina A, Di Sarno V, Lauro G, Ciaglia T, Vestuto V, Pepe G, Basilicata MG, Musella S *et al.* (2020) Exploration of TRPM8 binding sites by β-carboline-based antagonists and their in vitro characterization and in vivo analgesic activities. *J Med Chem* **63**, 9672–9694.

48 Iraci N, Ostacolo C, Medina-Peris A, Ciaglia T, Novoselov AM, Altieri A, Cabañero D, Fernández-Carvajal A, Campiglia P, Gómez-Monterrey I *et al.* (2022) In vitro and in vivo pharmacological characterization of a novel TRPM8 inhibitor chemotype identified by small-scale preclinical screening. *Int J Mol Sci* **23**, 2070.

49 Martín-Escura C, Bonache MÁ, Medina JA, Medina-Peris A, De Andrés-López J, González-Rodríguez S, Kerselaers S, Fernández-Ballester G, Voets T, Ferrer-Montiel A *et al.* (2023) β-Lactam TRPM8 antagonists derived from phe-phenylalaninol conjugates: structure–activity relationships and antiallodynic activity. *Int J Mol Sci* **24**, 14894.

50 Gandhi AS, Wohlfarth A, Zhu M, Pang S, Castaneto M, Scheidweiler KB & Huestis MA (2015) High-resolution mass spectrometric metabolite profiling of a novel synthetic designer drug, N-(adamantan-1-yl)-1-(5-fluoropentyl)-1H-indole-3-carboxamide (STS-135), using cryopreserved human hepatocytes and assessment of metabolic stability with human liver microsomes. *Drug Test Anal* **7**, 187–198.

51 Gandhi AS, Zhu M, Pang S, Wohlfarth A, Scheidweiler KB, Liu H & Huestis MA (2013) First characterization of AKB-48 metabolism, a novel synthetic cannabinoid, using human hepatocytes and high-resolution mass spectrometry. *AAPS J* **15**, 1091–1098.

52 Lelis Carvalho A, Treyball A, Brooks DJ, Costa S, Neilson RJ, Reagan MR, Bouxsein ML & Motyl KJ (2021) TRPM8 modulates temperature regulation in a sex-dependent manner without affecting cold-induced bone loss. *PLoS One* **16**, e0231060.

53 Asuthkar S, Velpula KK, Elustondo PA, Demirkhanyan L & Zakharian E (2015) TRPM8 channel as a novel molecular target in androgen-regulated prostate cancer cells. *Oncotarget* **6**, 17221–17236.

54 Zhang L & Barritt GJ (2004) Evidence that TRPM8 is an androgen-dependent Ca^{2+} channel required for the survival of prostate cancer cells. *Cancer Res* **64**, 8365–8373.

55 Brunelli F, Ceresa C, Fracchia L, Tron GC & Aprile S (2022) Expanding the chemical space of drug-like Passerini compounds: can α-acyloxy carboxamides be considered hard drugs? *ACS Med Chem Lett* **13**, 1898–1904.

56 Nikolaeva-Koleva M, Butron L, González-Rodríguez S, Devesa I, Valente P, Serafini M, Genazzani AA, Pirali T, Fernández-Ballester G, Fernández-Carvajal A *et al.* (2021) A capsaicinoid-based soft drug, AG1529, for attenuating TRPV1-mediated histaminergic and inflammatory sensory neuron excitability. *Sci Rep* **11**, 246.

57 Diaz-Franulic I, Poblete H, Miño-Galaz G, González C & Latorre R (2016) Allosterism and structure in thermally activated transient receptor potential channels. *Annu Rev Biophys* **45**, 371–398.

58 Janssens A & Voets T (2011) Ligand stoichiometry of the cold- and menthol-activated channel TRPM8. *J Physiol* **589**(Pt 20), 4827–4835.

59 Garami A, Shimansky YP, Pakai E, Oliveira DL, Gavva NR & Romanovsky AA (2010) Contributions of different modes of TRPV1 activation to TRPV1 antagonist-induced hyperthermia. *J Neurosci* **30**, 1435–1440.

60 Williamson JM & Lothman EW (1989) The effect of MK-801 on kindled seizures: implications for use and limitations as an antiepileptic drug. *Ann Neurol* **26**, 85–90.

61 Winchester WJ, Gore K, Glatt S, Petit W, Gardiner JC, Conlon K, Postlethwaite SPP, Roberts S, Gosset JR, Matsuura T *et al.* (2014) Inhibition of TRPM8 channels reduces pain in the cold pressor test in humans. *J Pharm Exp Ther* **351**, 259–269.

62 Shulman RJ, Chumpitazi BP, Abdel-Rahman SM, Garg U, Musaad S & Kearns GL (2022) Randomised trial: peppermint oil (menthol) pharmacokinetics in children and effects on gut motility in children with functional abdominal pain. *Br J Clin Pharmacol* **88**, 1321–1333.

63 Singh R, Adhya P & Sharma SS (2021) Redox-sensitive TRP channels: a promising pharmacological target in chemotherapy-induced peripheral neuropathy. *Expert Opin Ther Targets* **25**, 529–545.

64 Zimmermann M (1983) Ethical guidelines for investigations of experimental pain in conscious animals. *Pain* **16**, 109–110.

17424658, 0, Downloaded from https://febs.onlinelibrary.wiley.com/doi/10.1111/febs.70065 by Universidad Miguel Hernández De Elche, Wiley Online Library on [16/04/2025]. See the Terms and Conditions (https://onlinelibrary.wiley.com/terms-and-conditions) on Wiley Online Library for rules of use; OA articles are governed by the applicable Creative Commons License

65 Bonache MÁ, Martín-Escura C, de la Torre Martínez R, Medina A, González-Rodríguez S, Francesch A, Cuevas C, Roa AM, Fernández-Ballester G, Ferrer-Montiel A *et al.* (2020) Highly functionalized β-lactams and 2-ketopiperazines as TRPM8 antagonists with antiallodynic activity. *Sci Rep* **10**, 14154.
66 Martín-Escura C, Bonache MA, Medina-Peris A, Voets T, Ferrer-Montiel A, Fernández-Carvajal A & González-Muñiz R (2025) Phenylalanine-derived β-lactam TRPM8 antagonists: revisiting configuration and new benzoyl derivatives. *Explor Drug Sci* **3**, 100882.
67 Brenner DS, Golden JP & Gereau RW (2012) A novel Behavioral assay for measuring cold sensation in mice. *PLoS One* **7**, e39765.
68 Brunelli F, Ceresa C, Aprile S, Coppo L, Castiglioni B, Bosetti M, Fracchia L & Tron GC (2023) Isocyanides in med chem: a scaffold hopping approach for the identification of novel 4-isocyanophenylamides as potent antibacterial agents against methicillin-resistant *Staphylococcus aureus*. *Eur J Med Chem* **246**, 114950.
69 Yin Y, Zhang F, Feng S, Butay KJ, Borgnia MJ, Im W & Lee SY (2022) Activation mechanism of the mouse cold-sensing TRPM8 channel by cooling agonist and PIP2. *Science* **378**, eadd1268.
70 Morris GM, Huey R, Lindstrom W, Sanner MF, Belew RK, Goodsell DS & Olson AJ (2009) AutoDock4 and AutoDockTools4: automated docking with selective receptor flexibility. *J Comput Chem* **30**, 2785–2791.
71 Krieger E & Vriend G (2014) YASARA view—molecular graphics for all devices—from smartphones to workstations. *Bioinformatics* **30**, 2981–2982.
72 Ozvoldik K, Stockner T & Krieger E (2023) YASARA model–interactive molecular modeling from two dimensions to virtual realities. *J Chem Inf Model* **63**, 6177–6182.
73 Duan Y, Wu C, Chowdhury S, Lee MC, Xiong G, Zhang W, Yang R, Cieplak P, Luo R, Lee T *et al.* (2003) A point-charge force field for molecular mechanics simulations of proteins based on condensed-phase quantum mechanical calculations. *J Comput Chem* **24**, 1999–2012.
74 Adasme MF, Linnemann KL, Bolz SN, Kaiser F, Salentin S, Haupt VJ & Schroeder M (2021) Expanding the scope of the protein–ligand interaction profiler to DNA and RNA. *Nucleic Acids Res* **49**, W530–W534.
75 Lamberti A, Serafini M, Aprile S, Bhela IP, Goutsiou G, Pessolano E, Fernández-Ballester G, Ferrer-Montiel A, Di Martino RMC, Fernández-Carvajal A *et al.* (2024) The multicomponent Passerini reaction as a means of accessing diversity in structure, activity and properties: soft and hard Vanilloid/cannabinoid modulators. *Eur J Med Chem* **279**, 116845.

Supporting information

Additional supporting information may be found online in the Supporting Information section at the end of the article.

Figs S1–S78. ^{1}H-NMR, ^{13}C-NMR and HRMS spectra of final compounds **20–45**.

Figs S79–S80. LC-UV methods for purity and metabolic stability evaluation and LC-HRMS metabolic profile of compound **23** in mouse liver microsomes.

Figs S81–S92. Purity of selected active compounds.

Tables S1–S2. LC-UV methods for purity and metabolic stability evaluation and LC-HRMS metabolic profile of compound **23** in mouse liver microsomes.

The FEBS Journal (2025) © 2025 The Author(s). *The FEBS Journal* published by John Wiley & Sons Ltd on behalf of Federation of European Biochemical Societies.

17424658, 0, Downloaded from https://febs.onlinelibrary.wiley.com/doi/10.1111/febs.70065 by Universidad Miguel Hernández De Elche, Wiley Online Library on [16/04/2025]. See the Terms and Conditions (https://onlinelibrary.wiley.com/terms-and-conditions) on Wiley Online Library for rules of use; OA articles are governed by the applicable Creative Commons License